Yasmine Guendouz, M.Sc.

Exploring the Role of Neovascularisation in Carotid Plaque Vulnerability

---

Trinity College Dublin, January 2025

A thesis submitted to the University of Dublin in partial fulfilment of the requirements for the degree of

Doctor in Philosophy

Supervisors: Prof. Caitríona Lally, Dr. Catherine Mooney

Internal examiner: Prof. Ciaran Simms

External examiner: Prof. Craig Goergen

Declaration

I declare that this thesis has not been submitted as an exercise for a degree at this or any other university and it is entirely my own work. I agree to deposit this thesis in the University's open access institutional repository or allow the library to do so on my behalf, subject to Irish Copyright Legislation and Trinity College Library conditions of use and acknowledgment.

Yasmine Guendouz
January 31st, 2025

Summary

Non-invasive ultrasound imaging is a valuable tool for disease diagnosis and treatment monitoring. In cardiovascular diseases, identifying reliable clinical indicators of vulnerable carotid plaques is vital for improving outcomes. This thesis examines the mechanical behaviour and rupture risk of atherosclerotic plaques, focusing on neovascularisation as a potential marker of vulnerability, using mechanical testing, ultrasound imaging, histology, immunohistochemistry, and computational modelling.

To replicate the physiological loading conditions of plaques, polyvinyl alcohol cryogel phantoms were designed, developed, and tested using a custom-built inflation rig. This setup was complemented by the integration of ultrasound imaging and inverse finite element modelling. This study offered valuable insights into the mechanical behaviour of diseased vessels' surrogates, establishing a critical foundation framework for plaque testing. The workflow was then applied to fresh human atherosclerotic plaques obtained during endarterectomy surgeries. Controlled inflation allowed to subsequently study plaque biomechanics and assess the role of neovascularisation. Immunohistochemistry was then employed, enabling the visualisation of neovessels within the plaques. This offered valuable insights into the potential role of neovascularisation in plaque mechanical behaviour. Of note, plaques tended to show increased neovascularisation as their microstructural complexity increased. Uniaxial tensile testing further demonstrated that plaques with higher neovascularisation failed at lower ultimate tensile strains, highlighting a relationship between neovessels and reduced mechanical integrity.

These findings highlight neovascularisation as a potential marker for plaque vulnerability. This research paves the way for future studies to bridge the gap between research and clinical practice. By leveraging non-invasive imaging techniques like contrast-enhanced ultrasound, future work could explore *in vivo* neovascularisation, improving the identification of high-risk plaques and enhancing cardiovascular risk assessment.

Acknowledgements

Firstly, I would like to express my deepest gratitude to my supervisors, Professor Caitríona Lally and Professor Catherine Mooney. Tríona, your drive, enthusiasm, and guidance throughout my PhD have been instrumental in shaping me into the researcher that I am today. Your mentorship has been invaluable, and I am profoundly grateful for your support in helping me complete this journey. Being part of the Lally Lab has been an incredible experience; it is a truly supportive environment where people uplift one another, and I am honoured to have been a part of it. I would also like to thank Research Ireland for funding this work and making it possible. I am sincerely grateful to my committee members, Professor Ciaran Simms and Professor Craig Goergen, for taking the time to read this thesis.

To my collaborators, I extend my heartfelt thanks, especially to Dr Moein Mozzafardeh and Professor Chris de Korte, for their contributions to the ultrasound data analysis. I am also grateful to the Cruinn Diagnostic team and Siemens Healthineers for their technical support, which played a pivotal role in this work.

A special thanks to the vascular surgical team at Galway Clinic, with heartfelt appreciation to Dr. Niamh Hynes for her kindness, enthusiasm, and warmth, which made me feel like an integral part of the surgical team. Dr. Cleona Gray from the Mater Hospital deserves my deepest thanks for training me on the ultrasound machine and enabling me to work independently. Your guidance has been indispensable, and I will always cherish your support.

During my internship at Erasmus MC in Rotterdam, I had the privilege of working with incredible people. A special mention to Professor Ali Akylidiz for warmly welcoming me into the lab and making me feel at home. To the ultrasound research group, particularly Lucy, Anton, and Fox, thank you for patiently answering my questions and for your expertise. Thank you to Robert, your technical advice on inflation testing and ultrasound imaging was immensely helpful. Kim van Gaalen, your assistance with immunohistochemistry – a critical part of my PhD – was invaluable. I would like to specially thank Su. You were the loveliest mentor I could have asked for during my time in Rotterdam. Thank you for your patience and guidance, especially while you were finishing your own PhD.

This journey would not have been possible without the incredible support I received

at Trinity. To the team in Parsons – Peter O'Reilly, Alex Kearns, Rob Dunbar, Mick Reilly, Gerard Byrne, Owen Hughes, Mark Jordan, and Brendan Caffrey – thank you for the laughter, camaraderie, and the joy you brought to those years. Special thanks to Gordon O'Brien, whose expertise made the inflation testing possible.

To my lab colleagues, thank you for fostering an environment where challenges and successes were shared and celebrated. Alix, even though our time together was brief, I truly appreciated our discussions and coffee breaks. Niall, thank you for sharing your surgical suturing knowledge with me – it played a crucial role in my PhD. Rob Johnston, you have been my Yoda in the office, with your thought-provoking conversations and great sense of humour. I will miss your Irish slang. Brooke Tornifoglio, you have been a wonderful friend and guide throughout this journey. I am incredibly grateful for your unwavering support and encouragement.

To my friends, thank you for being my pillars of strength:

Liza, you have been my rock through thick and thin. Your joy, support, and advice have been a constant source of comfort. I am so lucky to have you in my life – you are the sister I chose. Inès, your passion and strength inspire me every day. I am so grateful to have met you in engineering school. Sharing our PhD journeys together has been incredibly special, and I cannot wait to see the amazing future ahead of you. Jessica, even from Brazil, your positivity and warmth made me feel like you were always close. Thank you for everything, Gata. Alexandra, I am so glad I randomly spoke to you in Mines de Saint-Étienne. Your supportive texts and calls always lifted my spirits. Assim, thank you for being my Frenchie friend in Dublin; it was wonderful to share this journey with you. Sophia, thank you for your unwavering support and friendship. You have been such a great friend, and I am truly grateful to have you by my side throughout this journey. Mary and Tobi, your board game nights brought so much joy. I am forever grateful. Moh and Flavia, you have been my second family in Dublin. Thank you for always taking care of me. Success, your friendship made my final year of this PhD so memorable. I am forever thankful.

To my family:

Mima, my beloved grandmother, your unwavering support and positive energy have been a constant source of inspiration. Rabah, my late grandfather, I wish you were here to celebrate this moment. Your memory motivates me, and I hope I have made you proud. To my sister Safia, "ma frère," you are my anchor and my purest source of joy. Thank you for being there for me throughout this journey – your presence means the world to me. Thank you for existing. To Amine and Djibril, you are the best brothers I could ever wish for, and I am so grateful for your support.

To my parents, Nabila and Redha, there are no words to express how much you mean to me. Your unconditional love and support have been the foundation of everything I have achieved. This journey was challenging, but knowing you were always there to

guide me made all the difference. I hope to return even a fraction of what you have given me. Thank you for everything.

Finally, I thank الله for always watching over me and guiding me through every challenge.

List of publications, conference proceedings and awards

Awards

- Granted a **Trinity College Postgraduate Travel Fund** to attend research conferences, Dublin, Ireland (2023).
- Recipient of **Outstanding Poster Award** at the Gordon Research Conference in Biomechanics in Vascular Biology and Disease, Boston, USA (2023).
- **1st prize for Best Paper** at the 25th Sir Bernard Crossland Symposium, Galway, Ireland (2022).

Conferences proceedings

- **Guendouz, Y.**, Tornifoglio, B., Sultan, S., Hynes, N., Gray, C., Guvenir, S., Mozaffarzadeh, M., de Korte, C., Gijsen, F., Akyilidiz, A., Lally, C. (2024) 'Exploring the Link Between Neovascularisation and Carotid Plaque Mechanics', in the 2024 IEEE Ultrasonics, Ferroelectrics, and Frequency Control Joint Symposium, Taipei, Taiwan.
- **Guendouz, Y.**, Tornifoglio, B., Sultan, S., Hynes, N., Gray, C., Guvenir, S., Mozaffarzadeh, M., de Korte, C., Gijsen, F., Akyilidiz, A., Lally, C. (2023) 'Investigating the Relationship between Carotid Plaque Mechanical Behavior and Neovascularisation', in the 28th Congress of the European Society of Biomechanics, Edinburgh, Scotland.
- Participated at the 'Journée de l'Imagerie Cardiovasculaire' and 'Workshop échocardiographie pré-clinique', 2023, Paris, France.
- **Guendouz, Y.**., Tornifoglio, B., Sultan, S., Hynes, N., Gray, C., Guvenir, S., Mozaffarzadeh, M., de Korte, C., Gijsen, F., Akyilidiz, A., Lally, C. (2023) 'In-

flation Testing of Atherosclerotic Plaques using Ultrasound Imaging', at the Inaugural School of Engineering Research Symposium, Dublin, Ireland.

- **Guendouz, Y.**, Tornifoglio, B., Sultan, S., Hynes, N., Gray, C., Guvenir, S., Mozaffarzadeh, M., de Korte, C., Gijsen, F., Akyilidiz, A., Lally, C. (2023) 'Characterising Carotid Atherosclerotic Plaque Using Ultrasound Imaging and Inflation Testing', in Biomechanics in Vascular Biology and Disease, Gordon Research Conference. South Hadley, Massachusetts, USA.

- **Guendouz, Y.**, Tornifoglio, B., Sultan, S., Hynes, N., Gray, C., Guvenir, S., Mozaffarzadeh, M., de Korte, C., Gijsen, F., Akyilidiz, A., Lally, C. (2023) 'Ultrasound Imaging to Characterise Inflated Atherosclerotic Plaques', in Summer Biomechanics, Bioengineering and Biotransport Conference. Vail, Colorado, USA.

- **Guendouz, Y.**, Tornifoglio, B., Sultan, S., Hynes, N., Gray, C., Guvenir, S., Mozaffarzadeh, M., de Korte, C., Gijsen, F., Akyilidiz, A., Lally, C. (2022) 'Mechanical Characterisation of Atherosclerotic Plaques through Inflation Testing and Non-Invasive Ultrasound Imaging', at Trinity Center of Bioengineering Research Day, Dublin, Ireland.

- **Guendouz, Y.**, Johnston, R. D., Razif, A., Bernasconi, F., Lally, C., (2022) 'Inverse Finite Element Framework Combining Ultrasound Imaging and Inflation Testing of PVA Phantoms' at the 25th annual Sir Bernard Crossland Symposium. Galway, Ireland.

- **Guendouz, Y.**, Bernasconi, F., Johnston, R. D., Lally, C., (2022) 'Combined ultrasound imaging, inflation testing and inverse FE to assess the stiffness of PVA-c phantoms as analogue atherosclerotic vessels', in the 11^{th} European Solid Mechanics Conference. Galway, Ireland.

- **Guendouz, Y.**, Tornifoglio, B., Sultan, S., Hynes, N., Gray, C., Lally, C., (2022) 'Inflation Testing of Atherosclerotic Plaques Using Ultrasound Imaging', in the Proceedings of the 27^{th} Bioengineering in Ireland. Galway, Ireland.

- **Guendouz, Y.**, Tornifoglio, B., Sultan, S., Hynes, N., Gray, C., Lally, C., (2022) 'Ultrasound-based Method to Characterize Atherosclerotic Vessel Mimicking PVA-c Based Phantoms', in the 17^{th} international symposium on Biomechanics in Vascular Biology and Cardiovascular Disease. Rotterdam, Netherlands.

- **Guendouz, Y.**, Bernasconi, F., Johnston, R. D., Lally, C., (2021) 'Inverse FEA Framework Using Ultrasound Imaging and Inflation Testing of PVA-c Phantoms', in the Proceedings of the 26^{th} Bioengineering in Ireland, Ireland.

Publications

- **Guendouz, Y.**, Digeronimo, F., Tornifoglio, B., & Lally, C. (2024). Low ultimate tensile strain in atherosclerotic plaques is linked to presence of neovascularisation: insights from *ex vivo* uniaxial tensile testing. [In preparation].

- Tornifoglio, B., Hughes, C., Digeronimo, F., **Guendouz, Y.**, Johnston, R. D., & Lally, C. (2024). Imaging the microstructure of the arterial wall – *ex vivo* to *in vivo* potential. Acta Biomaterialia.[Submitted].

- **Guendouz, Y.**, Razif, N. A. M., Bernasconi, F., O'Brien, G., Johnston, R. D., & Lally, C. (2024). Simulating atherosclerotic plaque mechanics using polyvinyl alcohol (PVA) cryogel artery phantoms, ultrasound imaging and inverse finite element analysis. Physics in Medicine & Biology, 69(24), doi: 245020.10.1088/1361-6560/ad9a4b.

- A. M., Antoniadi, Du, Y., **Guendouz, Y.**., Wei, L., Mazo, C., Becker, B. A., & Mooney, C. (2021). Current Challenges and Future Opportunities for XAI in Machine Learning-Based Clinical Decision Support Systems: A Systematic Review. Applied Sciences, 11(11), 5088. https://doi.org/10.3390/app11115088.

Contents

List of Figures

List of Tables

Nomenclature

AHA American Heart Association

BMT Best medical therapy

CAS Carotid stenting

CCA Common carotid artery

CEA Carotid endarterectomy

CEUS Contrast enhanced ultrasound

CTA Computed tomography angiography

DIC Digital image correlation

ECA External carotid artery

ECST European Symptomatic Carotid Surgery Trial

FEA Finite element analysis

FE Finite element

FTCs Freeze-thaw cycles

FTIR Fourier Transformed Infrared

Haematoxylin and Eosin H&E

ICA Internal carotid artery

iFEA Inverse finite element analysis

iFEM Inverse finite element modelling

IPH Intraplaque haemorrhage

IPN Intraplaque neovascularisation

IVUS Intravascular ultrasound

MRI Magnetic resonance imaging

NASCET North American Symptomatic Carotid Endarterectomy Trial

NPCaA Native porcine carotid artery

OCT Optical coherence tomography

PBS Phosphate buffer saline

PLA Polylactic acid

PSV Peak systolic velocity

PVA Polyvinyl alcohol

RF Radiofrequency

SAEI Small arterial elasticity index

SD Standard deviation

SEM Scanning electron microscopy

SMC Smooth muscle cell

SMI Superb microvasculature imaging

SNR Signal-to-noise ratio

SSD Sum of squared differences

SWE Shear wave elastography

TFC Thin fibrous cap

ULM Ultrasound localisation microscopy

US Ultrasound imaging

UT Ultimate Tensile

VEGF Vascular endothelial growth factor

Chapter 1

Introduction

1.1 Research Motivation

Cardiovascular diseases are the leading cause of death globally, responsible for 18.6 million deaths in 2019, with ischaemic heart disease and stroke being the major contributors [1]. Atherosclerosis, in particular, is a major driver of vascular disease worldwide [2]. More specifically, carotid artery disease accounts for 10–20% of ischaemic strokes [3]. Rupture of atherosclerotic plaques in the carotid arteries often triggers thrombus formation, leading to ischaemic stroke [4]. Atherosclerosis is characterised by the thickening of the arterial wall in vulnerable regions [5]. Chronic inflammation in the arterial wall leads to the formation of atherosclerotic plaques, which narrow the lumen and, when ruptured, can trigger thrombosis and stroke. Plaques at higher risk of rupture are known as 'vulnerable plaques'.

Current clinical guidelines for determining whether a patient should undergo carotid endarterectomy (surgical removal of plaque) are based primarily on the degree of stenosis, which measures lumen narrowing [6]. However, vulnerable plaques are often characterised by a lipid-rich core and a thin fibrous cap, features that are not captured by the percentage of stenosis alone. Studies have demonstrated that mechanical characterisation of plaques provides pivotal information about their integrity and rupture risk, suggesting that stenosis alone may be an insufficient risk criterion [7], [8]. Recent evidence highlights that incorporating plaque morphology into clinical assessments could improve risk stratification, identifying patients with significant rupture potential despite low-degree stenosis [9].

Plaques are subjected to a complex loading environment arising from pulsatile blood pressure and vascular motion. This loading induces a multi-axial stress field that includes circumferential stress (σ_c), longitudinal stress (σ_L), and wall shear stress (τ_w). Circumferential stress, driven by systolic pressure, is typically the dominant component and acts to stretch the vessel wall radially. Longitudinal stress arises from both

luminal pressure (σ_{L-P}) and axial tethering (σ_{L-T}) due to anatomical constraints, contributing to axial loading along the vessel. Wall shear stress is generated by blood flow acting tangentially on the endoluminal surface. These combined stresses interact with plaque morphology and composition, influencing local mechanical behaviour and potentially contributing to failure. A schematic representation of these physiological stress components is shown in Fig. 1.1 [10].

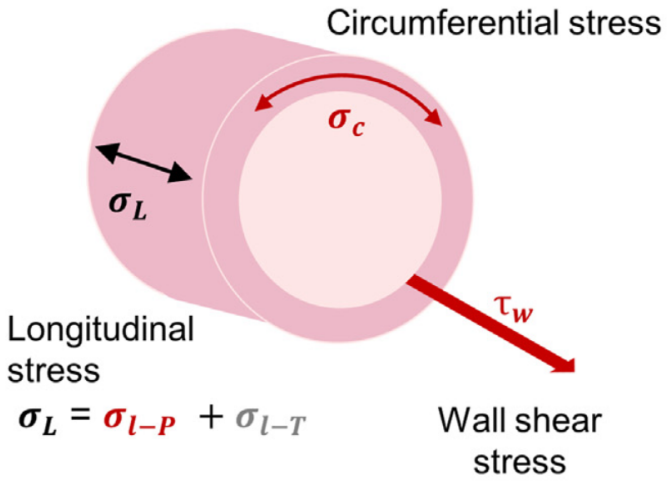

Figure 1.1: Schematic representation of the main physiological stresses acting on the vascular wall. Circumferential stress (σ_c), longitudinal stress (σ_L), and wall shear stress (τ_w) represent the primary components of the loading environment. Longitudinal stress is composed of a component due to luminal pressure (σ_{L-P}) and a component due to axial tethering (σ_{L-T}). Adapted from [10].

Plaque rupture occurs when the stress within the plaque exceeds the mechanical strength of the overlying fibrous cap, leading to structural failure and exposure of the lipid core to circulating blood [11]. While full-thickness rupture of the cap is the most widely recognised failure mode, other forms of surface disruption, such as plaque fissures, have also been identified. Fissures are partial tears or separations between distinct tissue layers within the plaque, often localised near the shoulder region, and are frequently associated with intraplaque haemorrhage [12]. These different modes of failure highlight the need for a deeper understanding of how plaque composition contribute to plaque vulnerability

A schematic diagram of a rupture-prone plaque is presented in Fig. 1.2 extracted from [13] illustrating key features such as a thin fibrous cap, lipid-rich core which are critically involved in plaque vulnerability.

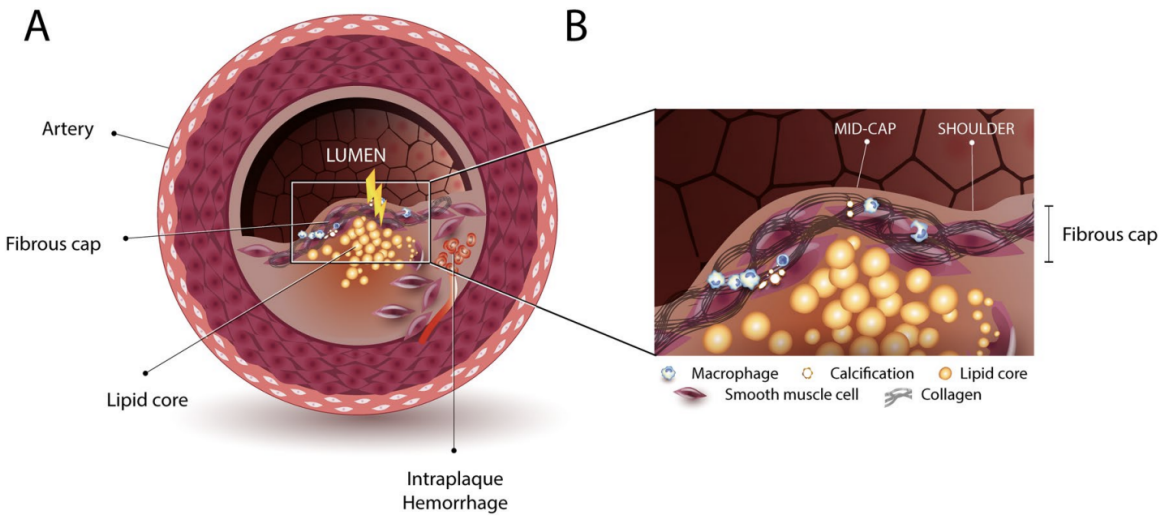

Figure 1.2: Schematic representation of a vulnerable atherosclerotic plaque. (A) Cross-sectional view of the carotid artery showing the lumen, lipid core, fibrous cap, and regions of intraplaque haemorrhage. (B) Magnified view of the fibrous cap region highlighting inflammatory cells (macrophages), smooth muscle cells, calcification, and collagen. This morphological configuration, particularly the presence of a thin fibrous cap overlying a lipid-rich core, is strongly associated with plaque rupture risk. Adapted from [13].

Magnetic resonance imaging (MRI) is considered the gold standard for assessing atherosclerotic plaque composition, however its high cost and time demands limit its use [14]. In contrast, ultrasound (US) imaging offers a faster, more cost-effective alternative that can easily be integrated into clinical workflows and is most widely used [15].

Previous studies have successfully used US imaging to assess plaque mechanical properties, and recent work has highlighted the potential of combining multiple US parameters to identify vulnerable plaques [16]–[18]. Understanding microstructural features within plaque is crucial for advancing diagnostic tools for plaque vulnerability [19]–[22]. Imaging biomarkers sensitive to plaque microstructures, have the potential to transform the current diagnostic criteria and provide a more comprehensive assessment of plaque vulnerability [23]. Neovascularisation, in particular, holds significant potential to enhance current diagnostic criteria for assessing plaque instability [23], [24]. Despite its critical role in plaque progression and rupture risk, its predictive value remains under explored.

1.2 Objectives

The fundamental goal of this thesis is to address this gap by investigating the potential of neovascularisation as a clinical marker for plaque vulnerability. By conducting *ex vivo* mechanical testing of both surrogate plaque models and human atherosclerotic plaques, combined with US imaging and histology, this work aims to provide novel insights into the biomechanical and morphological characteristics of plaques. Ultimately,

this thesis demonstrates the potential of US-based neovascularisation assessment as a valuable clinical tool for carotid atherosclerosis management. A graphical summary of the chapters in this thesis is presented in Figure 1.3.

1. Gain insights into the mechanical behaviour of atherosclerotic plaques through the development and validation of polyvinyl alcohol (PVA) cryogel phantoms, integrating inflation testing, inverse finite element modelling (iFEM), and US imaging.

2. Extend the framework developed for PVA phantoms to inflate human plaques using highly compliant balloons, enabling the investigation of the mechanical response of surgically excised carotid plaques under physiological conditions.

3. Investigate the mechanical behaviour of inflated plaques and their associated neovascularisation using US imaging, iFEM, and immunohistochemistry to deepen the understanding of the interplay between neovessel presence and plaque behaviour.

4. Explore the relationship between mechanical properties and neovascularisation in atherosclerotic plaques by performing uniaxial tensile testing until failure, providing insights into neovascularisation as a potential biomarker of plaque rupture.

Altogether, **these objectives aim to assess the potential of neovascularisation as a clinical tool** for evaluating the vulnerability of plaques to rupture.

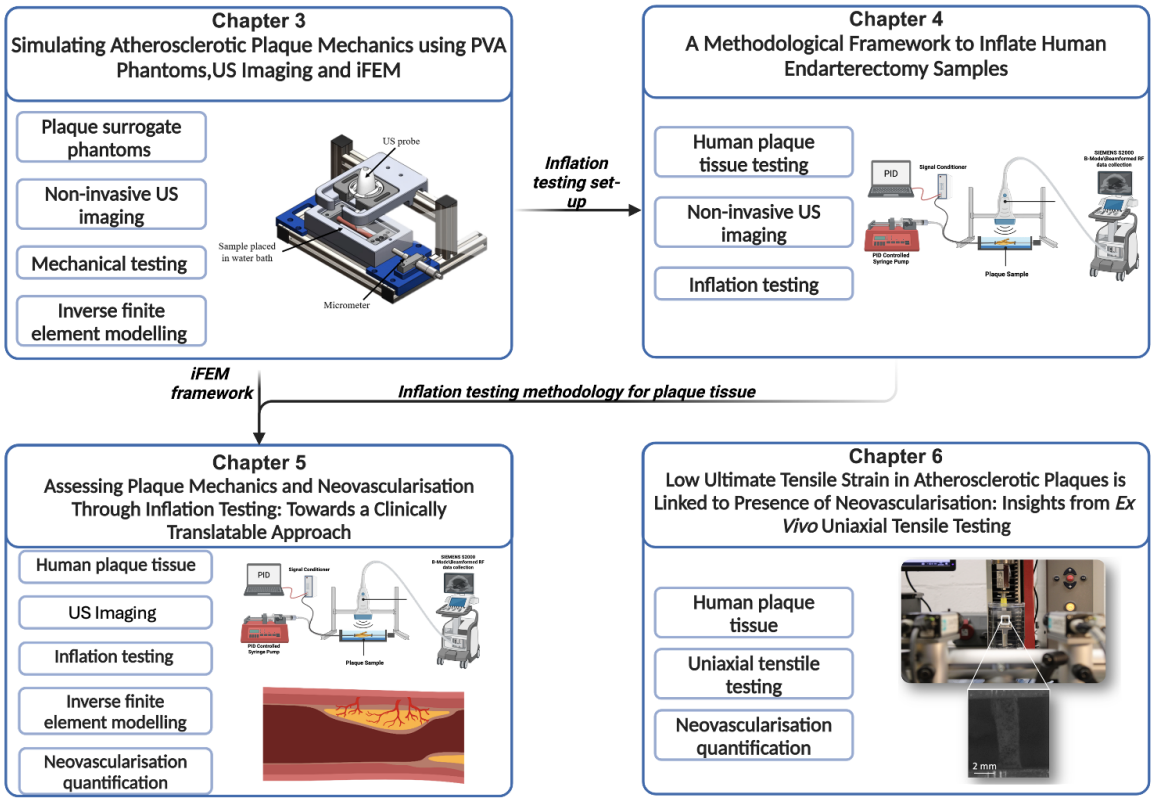

Figure 1.3: Graphical summary of the thesis chapters. The arrows indicate what specific methodologies and insights from one chapter are integrated into the subsequent chapters.

1.3 Thesis structure

This thesis consists of eight chapters that are centred around four main studies. From these studies, two first-author journal papers will emanate (one published, one in preparation). A brief description of each chapter is outlined below:

Chapter 1: Introduces the motivation for the research and outlines the key objectives that will be addressed in later chapters.

Chapter 2: Provides a comprehensive review of cardiovascular anatomy and the pathology of atherosclerosis, with a focus on the mechanisms of plaque vulnerability. The chapter further explores existing imaging techniques, with particular attention given to US imaging and the current limitations in assessing plaque instability. The potential of neovascularisation as a clinical tool is introduced in this context.

Chapter 3: Details the development and validation of PVA cryogel phantoms designed to replicate diseased vessels, including lipid inclusions, under physiological loading. Chapter 3 also introduces an iFEM framework based on boundary matching derived from US imaging, enabling further mechanical characterisation.

Chapter 4: Describes the establishment of a novel experimental framework for inflating plaques using highly compliant balloons fabricated in-house. This framework is applied to human plaques harvested after endarterectomy surgery.

Chapter 5: Utilises the previously developed inflation framework developed from Chapter 4, incorporating iFEM from Chapter 3, to investigate neovascularisation within plaques following inflation testing. The chapter explores how neovessel presence and distribution contribute to plaque mechanics.

Chapter 6: Focuses on the uniaxial tensile testing of plaque strips, linking mechanical properties to neovascularisation. This chapter highlights the importance of neovascularisation in determining plaque rupture risk and its potential role in clinical assessments of plaque vulnerability.

Chapter 7 and Chapter 8: Conclude with a general discussion that synthesises the findings from Chapters 3–6. The chapters also address the limitations of this work, provide suggestions for future research, and discusse the broader implications of using neovascularisation as a clinical marker, particularly in the context of advances in US, which hold significant potential for translating these research findings into clinical practice.

Chapter 2

Literature review

2.1 Cardiovascular system

The cardiovascular system consists of the heart and the blood vessels namely arteries, veins, and capillaries. Its main role is to supply oxygen and nutrients to the organs through the blood while removing carbon dioxide and waste. Blood is pumped by the heart throughout the whole body. The circulatory system is divided into two subsystems which are [25] :

- the systemic circulation conveying oxygen rich blood to the organs;
- the pulmonary circulation bringing poor oxygenated blood to the lungs.

Figure 2.1 depicts how the circulatory system is organised [26].

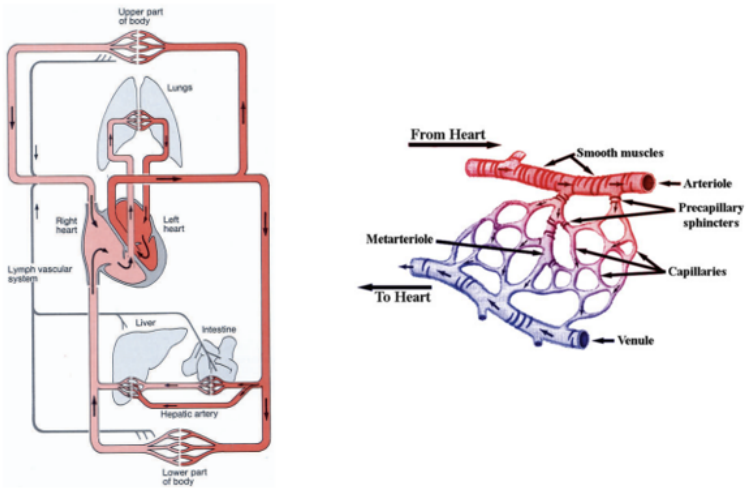

Figure 2.1: Schematic of the circulatory system (left) and capillary beds (right) taken from [26].

Oxygenated blood travels from the left ventricle through the aorta and will reach the different organs of the body through secondary arteries, getting increasingly smaller and becoming arterioles. Arterioles branch to create capillary beds where a multitude

of exchanges between blood and cells as well as the surrounding tissue occur. The blood charged in carbon dioxide travels back to the right ventricle after passing through the venous system.

2.1.1 Carotid arteries

A major part of the blood supply to the brain, head and neck is done through the carotid arteries, see Figure 2.2.

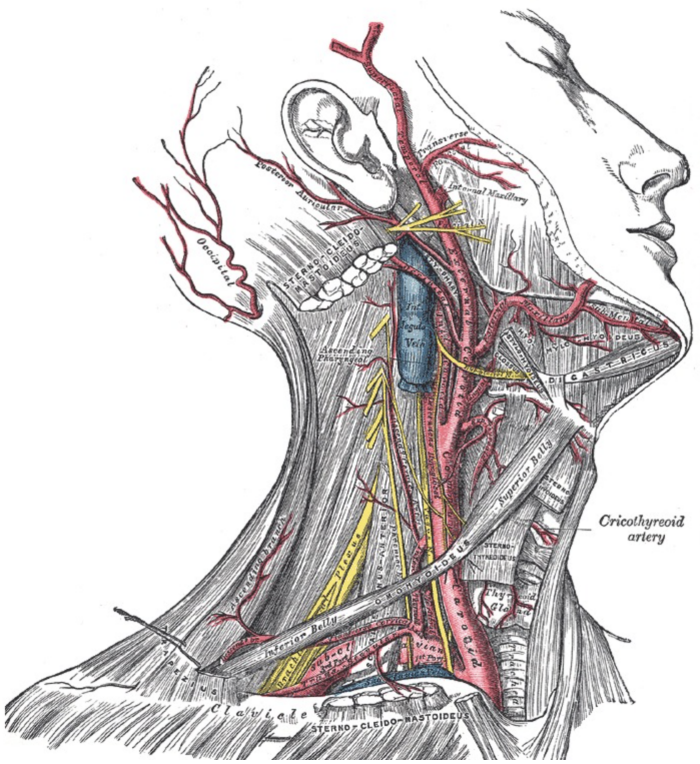

Figure 2.2: Arteries of the head and neck, external carotid, internal jugular Vein, external maxillary. Taken from Gray's Anatomy Plates.

Carotid arteries are situated in the front part of the neck. Along with the vertebral arteries, they arise from the Circle of Willis. The left common carotid artery emerges from the aortic arch while the right common carotid artery comes from the brachiocephalic arterial trunk [27]. The common carotid arteries (CCA) bifurcate, at the location of the carotid bulb, into the internal (ICA) and external carotid arteries (ECA). The ECA mainly supplies the head, neck, and face while the internal carotid artery supplies the brain with blood.

The carotid bulb is usually anatomically located using the thyroid when performing US imaging protocols. The external carotid artery possesses a cervical and a cephalic part. In the study by Krejza et al., US examination of the carotid arteries of 500 patients with a mean age of 52 $\pm$15 years ($\pm$standard deviation, SD) were performed [28]. Carotid artery diameter measurements were assessed, and results show that the

mean ICA diameter of female patients (4.66 ±0.78 mm (±SD)) was significantly lower than for the male patients (5.11±0.8 mm (±SD)). Similarly, the mean CCA diameter measured in women is 6.10 ±0.80 mm and 6.52 ±0.98 mm (±SD), for male patients. In addition, the diameter of the ICA is generally greater than the diameter of the ECA which features branches [29]. These characteristics allow clinicians to distinguish between the ICA and the ECA [29]. Carotid arteries have a pivotal role in maintaining the necessary blood supply to the brain. However, depositions such as cholesterol or calcification can occur in the carotid artery, mostly at the location of the bifurcation creating plaque build-up and stenosis. The arterial lumen can thus be partially or totally obstructed. The risk is that atherosclerotic plaques can in turn rupture leading to lethal complications.

2.1.2 Structure of arteries

The structure of the arterial vessel wall differs depending on its location along the vascular tree. The arteries are divided into two main categories:

- elastic arteries which have a large diameter and are situated close to the heart (aorta, carotid arteries);

- muscular arteries which are located next to the capillaries.

Some arteries nonetheless demonstrate both elastic and muscular properties [30]. The arterial wall is divided into three layers namely the intima, media and adventitia [31], see Figure 2.3 .

The intimal layer, the innermost layer, is constituted of a one-cell-thick layer of endothelial cells maintained by a basal membrane. In healthy arteries, the mechanical contribution of the intima can be considered negligible. However, some diseases such as atherosclerosis can be correlated with changes in the intima layer consequently altering its mechanical properties. The media layer consists of smooth muscle cells (SMCs) embedded in elastin, collagen fibres and ground gel matrix. In elastic arteries, the SMCs are oriented in the circumferential direction and organised in a concentric manner divided by elastic laminae. The medial layer is separated from the intima and adventitia respectively by the internal and external elastic lamina. In muscular arteries, the media is characterized by a thick smooth muscle cell layer. In the media layer, elastin, collagen fibres, SMCs and the elastic laminae have a helical structure giving rise to its resistance to high loads. Finally, the adventitia is the outermost layer and is mostly composed of fibroblasts and collagen fibres and is enveloped in connective tissue. The orientation of the collagen fibres in the adventitia and their waviness induces its higher stiffness at higher pressures.

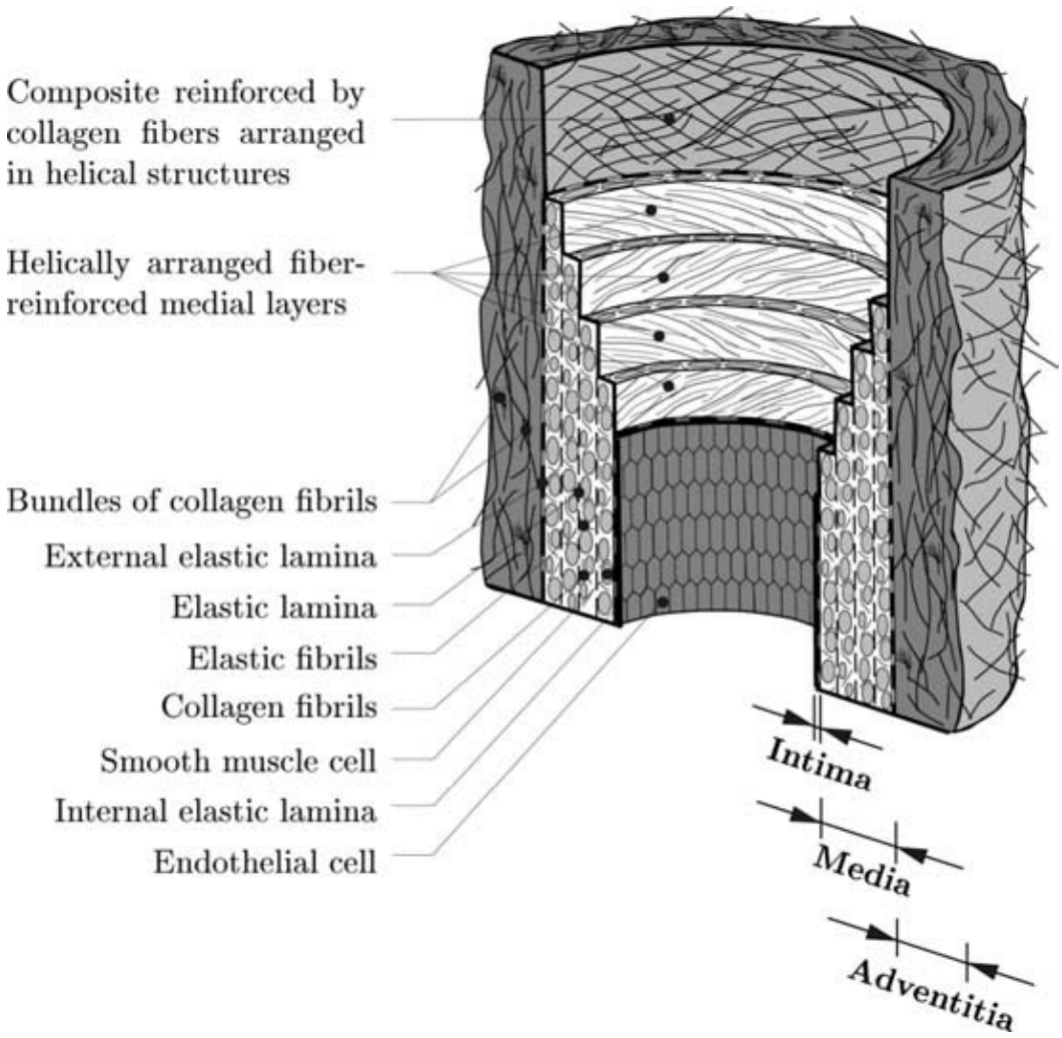

Figure 2.3: Microstructure of the arterial wall from [31].

2.2 Mechanical properties of arterial tissue

As highlighted in the above section, soft tissues can be considered as having fibre-reinforced arrangements. Collagen (specifically collagen I being predominant in soft tissues) is the most significant-load bearing constituent of blood vessels [32]. Its intramolecular cross-linking provides the necessary strength to soft tissues to bear physiological loads. Collagen fibrils are arranged in fibres having a hierarchical structure. Those fibres are characterised by their waviness providing elasticity to blood vessels. Elastin is another protein that plays a major role in the mechanical properties of soft tissue. It is one of the main components of the extracellular matrix of soft tissues. The behaviour of elastin can be described using entropic elasticity due to the random distribution of elastin molecules. When uniaxial tension is applied to elastin fibres, the random arrangement of molecules decreases thus decreasing its entropy [32]. Elastin can undergo large elastic deformations. The mechanical properties of soft tissues thus highly depend on elastin and collagen distribution [33]. The non-linear behaviour of

soft tissues can be depicted in the following J-shaped stress-strain curve:

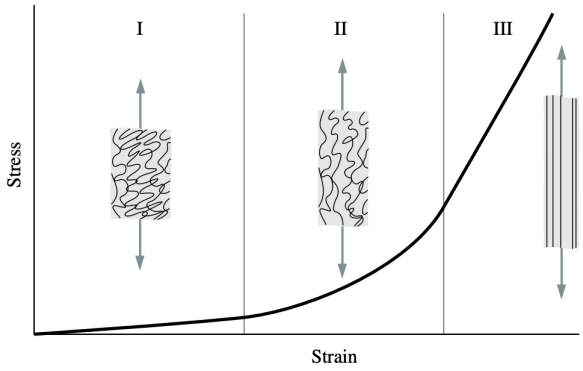

Figure 2.4: J-shaped stress-strain curve taken from [32].

Three major phases can be observed in Figure 2.4. Phase I is usually named the toe-region where low stresses are experienced with increasing strains. At low strains, the collagen fibres are still arranged in their initial crimped configuration. In the second phase, namely the elastic region, the collagen fibres start aligning along the tensile load as strain increases. This region allows recoil of the collagen fibres. Finally, at higher strains, the collagen fibres fully uncrimp leading to a higher stiffness of the tissue and resistance to the applied load. Higher stress values ultimately lead to the failure of the fibres. The viscoelastic properties of arterial tissues can be described by a nonlinear exponential stiffening curve as depicted in Figure 2.5 below [31]. The inelastic part of the curve situated between point I and II refers to permanent damage and changes in the tissue. Arterial tissue can be pre-conditioned by applying repetitive loading-unloading cycles. This induces stress-softening until reaching a repeatable behaviour.

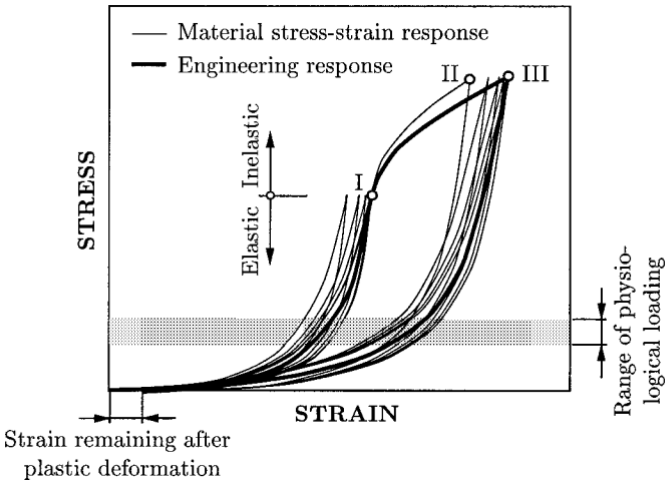

Figure 2.5: Typical stress-strain curve of soft tissue from [31].

The arrangement of the load bearing collagen fibres gives rise to the anisotropic behaviour of the arterial wall. Holzapfel et al. studied the layer-specific mechanical

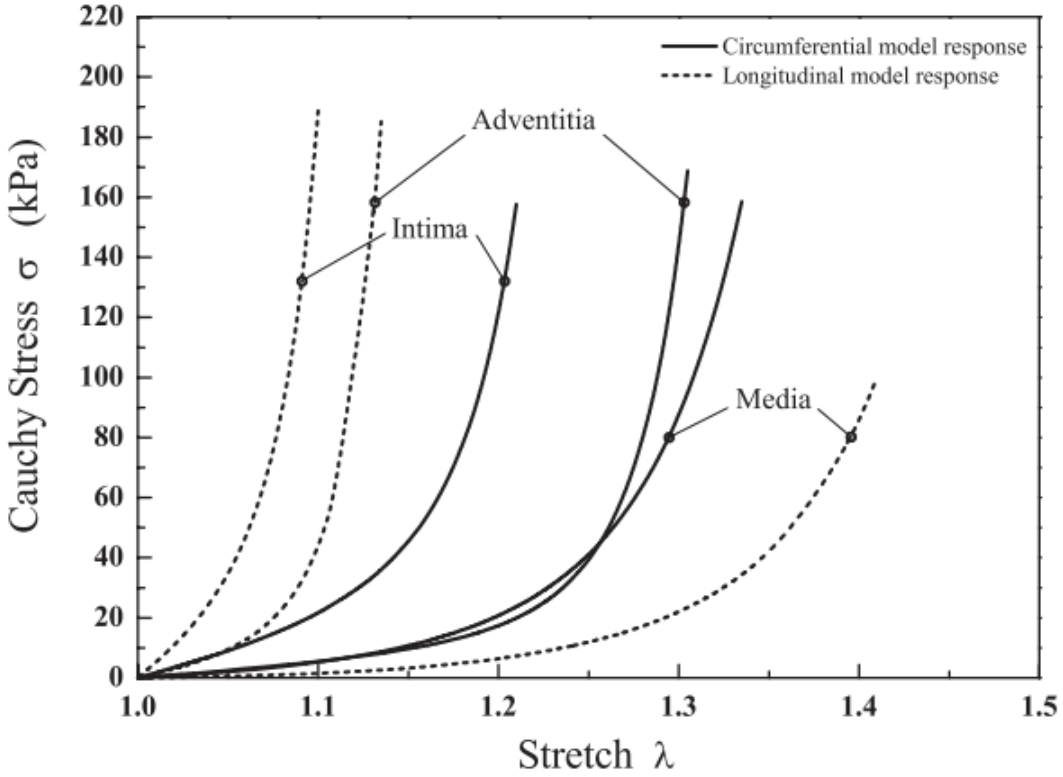

Figure 2.6: Stress-Stretch mean responses of arterial wall layers from [34].

properties of coronary arteries in both axial and circumferential directions [34]. This study demonstrates the variable mechanical responses between the different coronary arteries' layers by performing uniaxial tensile tests. Figure 2.6 highlights the anisotropy of arterial tissue by displaying the mean circumferential and longitudinal response of the intima, media, and adventitia. The media layer being the softest in both the circumferential and longitudinal directions.

2.3 Atherosclerosis

As mentioned previously, atherosclerosis is a progressive disease characterised by the build-up of plaques within arterial walls, is a leading cause of cardiovascular complications [3]. In the carotid arteries, this plaque accumulation can lead to stenosis which could lead to stroke and other cerebrovascular events [4].

Carotid endarterectomy (CEA), depicted in Figure 2.7, is the preferred choice of medical treatment for symptomatic patients with a carotid stenosis percentage between 70-99% [35]. This procedure is very invasive and risky for patients as it consists of the removal of the plaque by making a cut on the side of the neck and opening the carotid artery. Moreover, when it comes to the optimal treatment choice for asymptomatic patients, whether to perform CEA or not remains debatable [36].

2.3.1 Management of atherosclerosis

The management of carotid artery stenosis can be tackled with different treatment measures. The best medical therapy (BMT) consists of managing the major risk factors of carotid disease. This is done by administering anti-platelet therapy, anti-thrombotic therapy, statins, and angiotensin-converting enzyme inhibitors to control hypertension. Lifestyle changes are also part of the BMT involving recommendations such as quitting smoking, diet changes and exercising regularly [37]. In other patients, direct management of the carotid atherosclerotic plaque is required such as CEA, carotid stenting (CAS) or carotid angioplasty. Major studies have demonstrated a benefit for CEA against medical management for patients with stenosis of 70% or greater. Carotid endarterectomy is the commonly chosen surgical procedure. Figure 2.7 illustrates the procedure. Usually, an incision is made along the neck to cut the carotid open. Once the plaque is exposed, it is removed, and the artery is stitched together again.

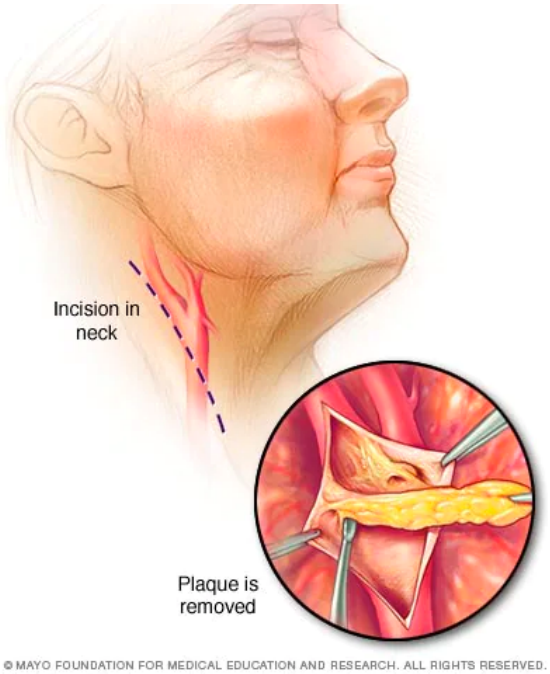

Figure 2.7: Schematic of endarterectomy procedure [38].

Carotid stenting and carotid angioplasty are endovascular procedures. A catheter is inserted and guided using X-ray. This procedure is chosen if the plaque is difficult to reach. The patient is sedated, and a balloon is then inserted in the artery to either widen, for an angioplasty procedure, or to insert and expand a stent, see Figure 2.8. However, the use of stents in this region has decreased due to concerns about the risk of plaque rupture and embolisation. Greater understanding of plaque vulnerability is needed to refine patient selection and improve treatment strategies, ensuring safer and more effective interventions [39].

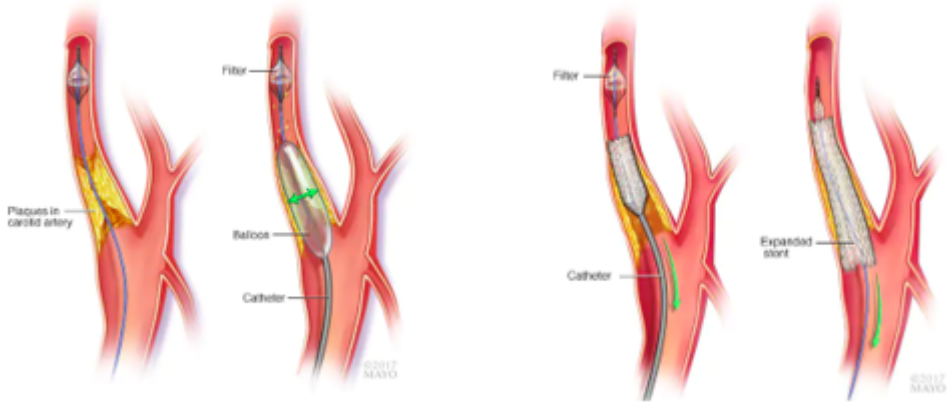

Figure 2.8: Schematic of carotid angioplasty (left) [40] and stenting (right) procedure from [41].

2.3.2 Disease description

Atherosclerosis is defined by the thickening of the arterial wall causing stenosis of the arterial lumen [5]. Left untreated, stenosis can result in ischaemic events and even lethal occlusions. Atherosclerosis is a progressive disease which initiates in the intima but ultimately reaches the media and adventitia layers. Different major steps in the evolution of atherosclerosis can be described:

- Early fatty streak development caused by lipids accumulation.
- Early fibroatheroma where cellular debris are accumulated and can form lipid-rich necrotic cores. A thin fibrous cap (TFC) surrounds this core to form a fibrous cap lesion.
- Advancing atheroma during which a thin fibrous cap atheroma forms and may rupture.

More complex lesions can be observed when ruptured TFCs heal through the development of additional fibrous tissue. Those complex lesions are also prone to rupture or can cause thrombosis. The above-described lesion types can be identified through histopathology.

Figure 2.9 illustrates the progressive stages of a carotid atherosclerotic plaque until rupture:

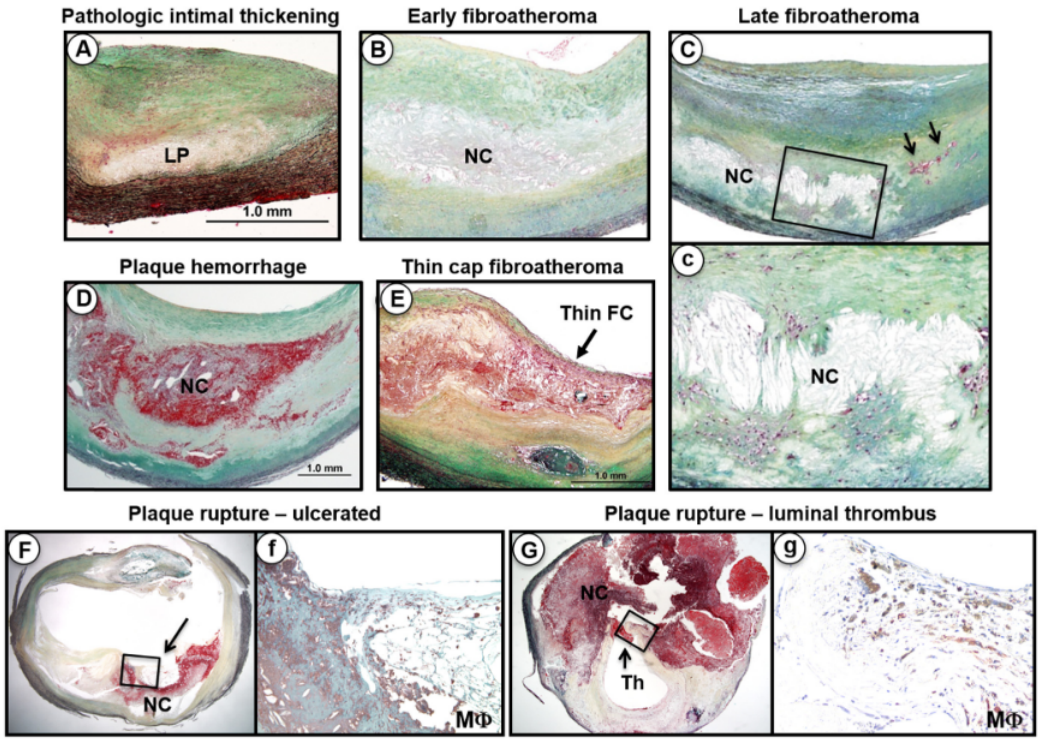

Figure 2.9: (A) Early lipid pool lesion. (B) Early and (C) late necrotic cores. (D) Intraplaque haemorrhage. (E) Thin-cap fibroatheroma. (F) Ulcerated plaque rupture and (G) Luminal thrombus. Figure taken from [42].

In 1995, the American Heart Association (AHA) submitted a detailed report differentiating plaque lesion types with Roman numerals [43]. The following schematic illustrates those lesion types on cross section drawings of left anterior coronary arteries, see Figure 2.10.

These classification guidelines were refined in 2000 by Stary et al. adding type VII and type VIII lesions [44]. In these guidelines, atherosclerotic lesion types are associated with histopathological structures. Type I lesions occur in the early stage of life and are associated with lipid foam cells deposited in the intima layers [44]. Type II lesions are characterized by fatty streaks. Type I and II lesions are considered early lesions. Intermediate or type III is known as a transitional stage to a more "advanced" lesion. Consequently, type III lesions are described as pre-atheroma with extracellular lipid pools. Moreover, extracellular lipid particles can interfere with the normal functioning of smooth muscle cells in the intima layer. Type IV lesions feature a large core of extracellular lipid pool named lipid core or necrotic core within the intima. These changes in type IV lesions are correlated with major structural changes of the intima layer caused by an increase of fibrous tissue. Subsequently, type V or fibroatheroma lesions occur when the lipid core is largely covered by a thick layer of fibrous tissue. Further structural modifications can appear such as disruptions, haemorrhage or thrombotic deposits leading to a type VI lesion. The presence or absence of those pre-

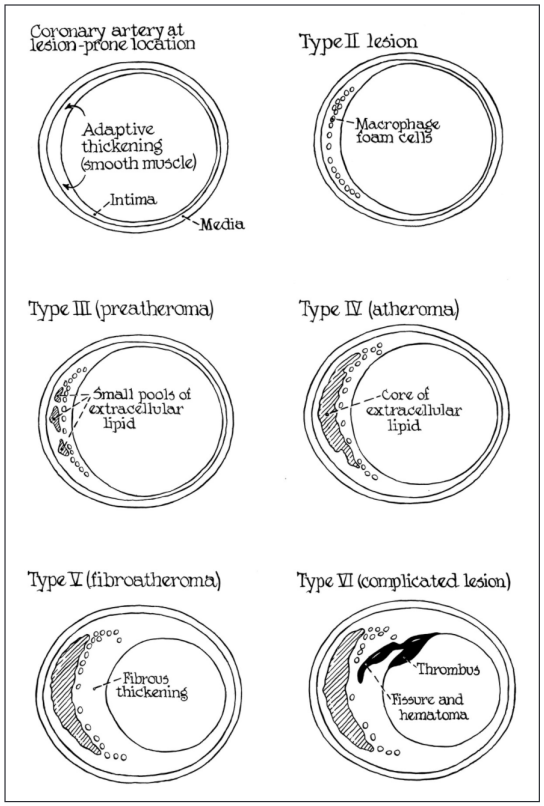

Figure 2.10: Cross-section drawings of coronary arteries with different lesion types taken from [43].

viously cited features lead to further subdivision in type VI lesions. In 2000, the AHA provides supplementary information on the evolution of atherosclerotic lesions and subdivided paths. Type Vb (calcified plaque) and Vc (fibrotic plaque without lipid core) are respectively replaced by lesion types VII and VIII. The AHA lesion type classification and description can be resumed in the following Table 2.1 taken adapted from [45]:

Table 2.1: AHA Classification adapted from [45].

AHA Classification
Type I: initial lesions with foam cells
Type II: fatty streak with multiple foam cell layers
Type III: pre-atheroma with extracellular lipid pools
Type IV: atheroma with a confluent lipid core
Type V: fibroatheroma
Type VI: complex plaque with possible surface defect, hemorrhage, or thrombus
Type VII: calcified plaque
Type VIII: fibrotic plaque without lipid core

Atherosclerotic lesions are classified histologically based on their structural characteristics and progression. Table 2.2 is reproduced from Stary et al., summarising the

different lesion types, with their corresponding histological classification [46].

Table 2.2: Classification of Atherosclerotic Lesions (Reproduced from [46]).

Histology classification	**Description**	**Macroscopic Terminology**
Type I lesion	Initial lesion	Early lesions
Type IIa lesion	Progression-prone type II lesion	Fatty dot or streak
Type IIb lesion	Progression-resistant type II	–
Type III lesion	Intermediate lesion (preatheroma)	–
Type IV lesion	Atheroma	Atheromatous plaque
Type Va lesion	Fibroatheroma (type V lesion)	Fibrolipid plaque
Type Vb lesion	Calcific lesion (type VII lesion)	Calcified plaque
Type Vc lesion	Fibrotic lesion (type VIII lesion)	Fibrous plaque
Type VI lesion	Lesion with surface defect, hematoma-hemorrhage, or thrombotic deposit	Complicated lesion, complicated plaque

Virmani et al. proposed some further modifications of the AHA classifications to include plaque rupture phenomenon and erosion [47]. Figure 2.11 below presents the proposed updated and universally used classification:

	Description	Thrombosis
Nonatherosclerotic intimal lesions		
Intimal thickening	The normal accumulation of smooth muscle cells (SMCs) in the intima in the absence of lipid or macrophage foam cells	Absent
Intimal xanthoma, or "fatty streak"	Luminal accumulation of foam cells without a necrotic core or fibrous cap. Based on animal and human data, such lesions usually regress.	Absent
Progressive atherosclerotic lesions		
Pathological intimal thickening	SMCs in a proteoglycan-rich matrix with areas of extracellular lipid accumulation without necrosis	Absent
Erosion	Luminal thrombosis; plaque same as above	Thrombus mostly mural and infrequently occlusive
Fibrous cap atheroma	Well-formed necrotic core with an overlying fibrous cap	Absent
Erosion	Luminal thrombosis; plaque same as above; no communication of thrombus with necrotic core	Thrombus mostly mural and infrequently occlusive
Thin fibrous cap atheroma	A thin fibrous cap infiltrated by macrophages and lymphocytes with rare SMCs and an underlying necrotic core	Absent; may contain intraplaque hemorrhage/fibrin
Plaque rupture	Fibroatheroma with cap disruption; luminal thrombus communicates with the underlying necrotic core	Thrombus usually occlusive
Calcified nodule	Eruptive nodular calcification with underlying fibrocalcific plaque	Thrombus usually nonocclusive
Fibrocalcific plaque	Collagen-rich plaque with significant stenosis usually contains large areas of calcification with few inflammatory cells; a necrotic core may be present.	Absent

Figure 2.11: Updated AHA lesions classification from [47].

2.3.3 Measurement methods

Stenosis quantification methods were established from two significant clinical studies namely the North American Symptomatic Carotid Endarterectomy Trial (NASCET) [48] and the European Symptomatic Carotid Surgery Trial (ECST) [49]. As depicted in Figure 2.12 below from Ota et al., the stenosis percentage can be measured based on different reference sites (either NASCET or ECST method) [50]. It is thus of utmost importance to detail which has been used.

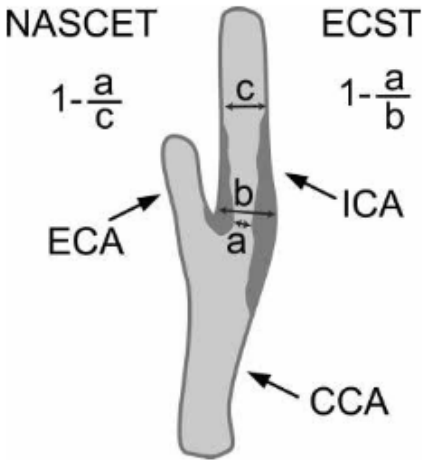

Figure 2.12: Schematic illustrating the different method for stenosis calculation based on either the NASCET (1-a/c) or the ESCT (1-a/b) taken from [50].

US imaging is a routine non-invasive technique used to quantify the degree of stenosis. Doppler US enables the measurement of blood flow velocity by taking advantage of the Doppler shift in reflected sound waves, see Figure 2.13 . The peak systolic velocity (PSV) can then be determined and velocity related parameters can be derived such as the PSV ratio. The latter is calculated by dividing the PSV anterior to the stenosis by the PSV posterior to the stenosis [50]. A high PSV ratio suggests a high stenosis.

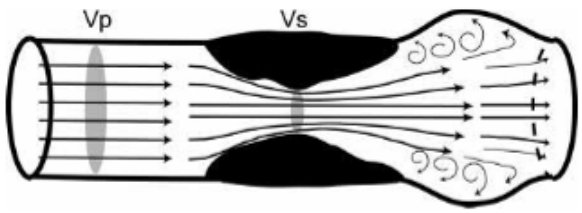

Figure 2.13: Schematic of blood flow change caused by the presence of stenosis from [50].

Other imaging techniques such as MRI or computed tomography angiography (CTA) can be used to evaluate the severity of stenosis of a patient. These techniques will further be detailed in Section 2.4.

2.3.4 Vulnerable plaque features

Plaques at a higher risk of rupture are called "vulnerable" plaques. They have been characterised by the presence of a thin cap fibroatheroma. Virmani et al. gave a criterion of plaque cap thickness of 65 μm under which the plaque is considered highly vulnerable [51]. The 2017 ESVS guidelines issued refined characteristics that might be linked with late ipsilateral stroke, for instance, intraplaque haemorrhage (IPH), lipid-rich necrotic core or a thin/ruptured fibrous cap on carotid MRI and large plaque area on US (>40 mm squared) [52]. Moreover, high-risk plaques were found to be associated with the following prevalent features: neovascularisation, echolucency and lipid-rich necrotic core [53]. Additionnaly, Carr et al. found that plaque rupture occurred in 74% of symptomatic patients and 32% of asymptomatic patients, despite similar mean stenosis percentages (74% in symptomatic vs. 77% in asymptomatic patients) [54]. This suggests that factors beyond the degree of stenosis contribute to plaque instability and rupture.

It has also been shown that plaque exhibiting calcified regions show a more stable structural environment with less inflammation [55]. Overall, these studies show that the vulnerability of carotid atherosclerotic plaques cannot be totally described by lumen stenosis and the management of such disease lies beyond the sole use of such a parameter. Thus effective disease management requires a deeper understanding of the behaviours and characteristics of different plaques depending on their microstructure. This need for comprehensive risk stratification has led to the development of the Carotid Plaque-RADS classification system, which introduces a standardised approach to carotid plaque evaluation by integrating plaque morphology with multimodal imaging parameters beyond stenosis alone [23]. Ranging from Plaque-RADS 1 (absence of plaque) to Plaque-RADS 4 (high-risk plaque features, such as IPH, fibrous cap rupture, or intraluminal thrombus), this scoring system further accounts for ancillary features—such as inflammation, neovascularisation, remodelling, and plaque burden—to provide a more nuanced risk assessment. By facilitating clear communication and consistent reporting across imaging modalities, Plaque-RADS enhances clinical reliability, aiming to guide personalised treatment strategies that could capture the full complexity of plaque vulnerability [23].

Intraplaque neovascularisation

The vasa vasorum are small microvessels that supply oxygen and nutrients to the outer layers of large arteries, particularly in regions where diffusion from the lumen is insufficient. In vessels exceeding 0.5 mm in diameter or containing more than 29 medial lamellar units, the presence of vasa vasorum becomes essential for maintaining vascular homeostasis [56], [57]. Although the exact number of lamellar units in the human

carotid artery is not routinely documented, it is a large elastic artery directly branching from the aortic arch and located proximally to the heart. As such, its structural and functional characteristics closely resemble those of the thoracic aorta, which has been shown to contain between 35 and 56 medial lamellar units throughout development [58], [59]. These features strongly support the presence of a well-developed vasa vasorum network in the carotid artery. In the context of atherosclerosis, these microvessels proliferate abnormally from the adventitia and extend into the media and intima, facilitating inflammation and contributing to plaque progression. Neovascularisation is thus the formation of these new microvessels within tissues, typically in response to stimuli such as hypoxia or inflammation [60]. Specifically, neovascularisation within atherosclerotic plaques represents a multifaceted response to the increased metabolic needs of the progressing plaque, primarily driven by hypoxia [61]. In healthy arteries, oxygen and nutrients are delivered to the intima and media from the luminal side, while the adventitia is supplied by microvessels originating from the primary artery or neighbouring vessels [62]. Simultaneously, a decrease in arterial elasticity due to ageing or metabolic conditions reduces the natural flow driven by arterial pulsations. This flow aids nutrient transport across the vessel wall; however, its reduction further limits oxygenation, aggravating the hypoxic environment [62]. In atherosclerotic lesions, this situation intensifies, as expanding plaques not only restrict diffusion but also elevate local oxygen demand due to inflammation. The resulting hypoxia, particularly within the plaque core and adjacent media, promotes the release of pro-angiogenic factors like vascular endothelial growth factor (VEGF), which drive the formation of fragile and permeable neovessels from the adventitia.

As plaques develop and thicken the vessel wall, diffusion from the lumen is insufficient to reach deeper regions. This requires the vasa vasorum to proliferate from the adventitia and extending into the outer media to eventually penetrating the plaque. Moulton's review explores the role of plaque angiogenesis in atherosclerosis, emphasising that neovascularisation in atherosclerotic plaques predominantly originates from the adventitial vasa vasorum and extends into the intima [63], [64]. Unlike stable arterial microvessels, these newly formed neovessels lack structural support, presenting incomplete endothelial junctions, leaving them vulnerable to rupture and IPH [24], [65]–[67]. Neovascularisation also facilitates inflammatory cell recruitment. This is mediated by the overexpression of VCAM-1 in intraplaque microvessels, which binds monocytes and T-cells, promoting their infiltration into the plaque [68]. The resulting inflammatory activity further weakens the fibrous cap, exacerbating plaque instability and increasing the risk of rupture.

Neovascularisation has been shown to influence the mechanical properties of atherosclerotic plaques. Several studies have reported that plaques with a higher density of neovessels exhibit distinct mechanical characteristics. Wang et al. found that plaques

with increased neovascularisation tended to be more compliant, whereas Zhang et al. observed a negative correlation between neovascularisation and tissue elasticity [69], [70]. The power of combining both plaque elasticity and intraplaque neovascularisation in stroke is also demonstrated [71]. These findings highlight the potential for neovascularisation to alter plaque integrity, making it an important factor to consider in biomechanical and clinical assessments of plaque stability. Moreover, the distribution of neovascularisation within plaques is not uniform, with evidence suggesting that microvessel-rich regions often overlap with structurally vulnerable areas [72]. Using finite element modelling, Teng et al. demonstrated that regions containing dense neovessel networks experience elevated stress and strain during the cardiac cycle, particularly in areas subject to mechanical loading [72].

Table 2.3 summarises recent studies that examined how intraplaque neovascularisation relates to mechanical characteristics and vulnerability of atherosclerotic plaques.

Table 2.3: Summary of studies linking neovascularisation with mechanical properties or plaque vulnerability.

Study	**Method**	**Neovascularisation Assessment**	**Findings**
Zhang et al. [69]	SWE and CEUS	CEUS-derived neovessel density	Increased neovascularisation correlated with reduced elasticity
Wang et al. [70]	SWE and echogenicity analysis	CEUS scoring	Softer plaques (lower Young's modulus and echogenicity) had increased neovascularisation
Zhang et al. [71]	SWE + CEUS	Combined SWE and CEUS metrics	Combination of low stiffness and high neovascularisation improved stroke risk prediction
Teng et al. [72]	Finite Element Modelling	Histology-confirmed neovessels	Neovessel-rich regions showed elevated stress and strain during the cardiac cycle
Tian et al. [73]	CEUS	Quantitative CEUS scoring	Soft, non-calcified plaques exhibited higher neovascularisation

Understanding these relationships is essential for developing more comprehensive risk stratification approaches, particularly when integrating mechanical and imaging-based assessments in clinical practice.

Marsch et al. showed that hypoxia within plaques contributes to necrotic core expansion by impairing the process of where macrophages clear apoptotic cells [74]. Their findings suggest that hypoxia drives plaque vulnerability highlighting neovascularisation as a potential marker of this process.

Studies also found that IPH is prevalent in symptomatic carotid plaques, even in cases of mild stenosis, suggesting that factors beyond lumen narrowing can influence plaque vulnerability [75]. Neovascularisation plays a crucial role in this context, as the fragile microvessels formed within the plaque are prone to rupture, leading to IPH. As stated earlier, the hypoxic environment stimulates neovascularisation which in turn

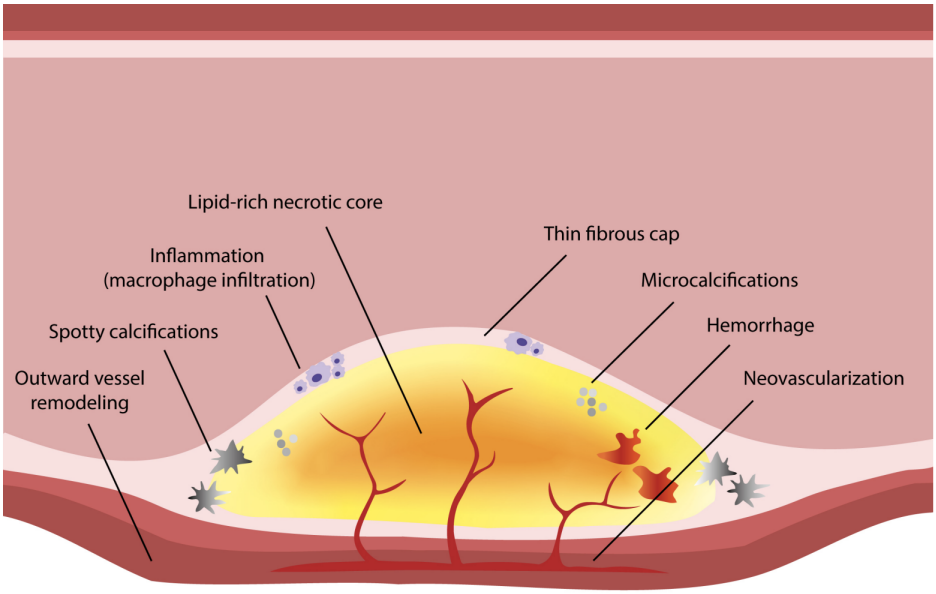

Figure 2.14: Schematic representation of a vulnerable plaque. The lipid-rich necrotic core is centred in the plaque and separated from the lumen by a thin fibrous cap (<65 µm), which is infiltrated by inflammatory cell types such as macrophages. Spotty calcifications and microcalcifications are present, and neovascularisation from the vasa vasorum leads to intraplaque haemorrhage. To prevent lumen compromise, outward vessel remodelling is present. Adapted from [64].

can create a cycle that drives plaque vulnerability. The study by Herrmann et al. investigates the early development of neovascularisation in the coronary vasa vasorum in a hypercholesterolaemia model [76]. It demonstrates that neovascularisation occurs within the first few weeks of cholesterol exposure, prior to the onset of endothelial dysfunction—a common early marker of atherosclerosis. This finding supports the idea that neovascularisation is an early feature of plaque instability. Together, these findings support the use of neovascularisation assessment in imaging protocols, as its presence not only correlates with inflammation and IPH but also enhances the accuracy of risk stratification in atherosclerotic disease management [23], [66], [77]. Therefore, imaging of plaque neovascularisation may provide additional information about the presence of vulnerable plaques in patients. This is further detailed in Section 2.4.5 where contrast-enhanced ultrasound (CEUS) is introduced and described.

2.4 Imaging Techniques

2.4.1 Histology

As described previously, plaque composition can be accurately assessed through histology. Different staining techniques allow the detection of plaque components, as seen in the colour-coded image and histology panel, see Figure 2.15 [78]. Histological staining remains the gold standard for assessing atherosclerotic plaque composition,

providing direct visualisation of structural components with high specificity. Cross-sectional images of a carotid plaque are presented, illustrating how different staining techniques highlight key plaque features, see Figure 2.15. Haematoxylin and Eosin (H&E) staining provides an overview of plaque morphology, distinguishing cellular structures, necrotic cores, and fibrous regions, see Figure 2.15.F. Masson's Trichrome stain is particularly valuable for identifying fibrotic areas, with collagen fibres stained blue, see Figure 2.15.G. Oil Red O staining selectively marks lipid deposits in red, facilitating the identification of lipid pools and foam cell accumulation within the necrotic core, see Figure 2.15.H. Prussian Blue staining detects iron deposits, indicating prior intraplaque haemorrhage, which further contributes to plaque destabilisation, see Figure 2.15.I. Von Kossa staining identifies calcified regions, which appear dark brown or black, signifying advanced plaque progression, see Figure 2.15.J.

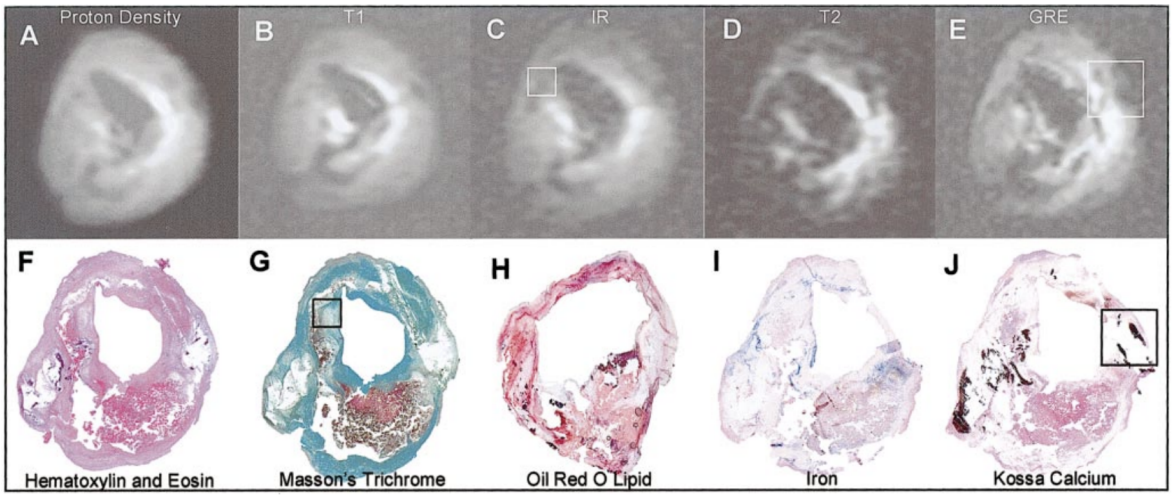

Figure 2.15: (A–E) Intravascular MRI sequences: (A) Proton density, (B) T1-weighted, (C) Inversion recovery, (D) T2-weighted, and (E) Gradient echo. (F–J) Histological staining: (F) H&E for general morphology, (G) Masson's Trichrome for fibrous content, (H) Oil Red O for lipids, (I) Prussian Blue for iron deposits, and (J) von Kossa for calcification. Adapted from [78].

Figure 2.16 illustrates different plaque types across varying degrees of stenosis, with Movat pentachrome and H&E staining providing detailed insights. Movat staining highlights extracellular matrix components, allowing clear differentiation of thrombi, necrotic cores, and fibrous tissue, see Figures 2.16.A–2.16.C. Thin-cap fibroatheromas, where a thin fibrous cap overlays a necrotic core, increasing rupture risk, are effectively delineated, see Figures 2.16.D–2.16.F. Stable plaques exhibit calcifications, which are better visualised with von Kossa staining, see Figures 2.16.G–2.16.I. Movat pentachrome remains one of the most powerful stains for comprehensive plaque assessment, as it simultaneously differentiates fibrotic, lipid-rich, thrombotic, and calcified regions, reinforcing histology as the gold standard in plaque characterisation. However, this technique is destructive because the plaque samples must be sliced to be imaged.

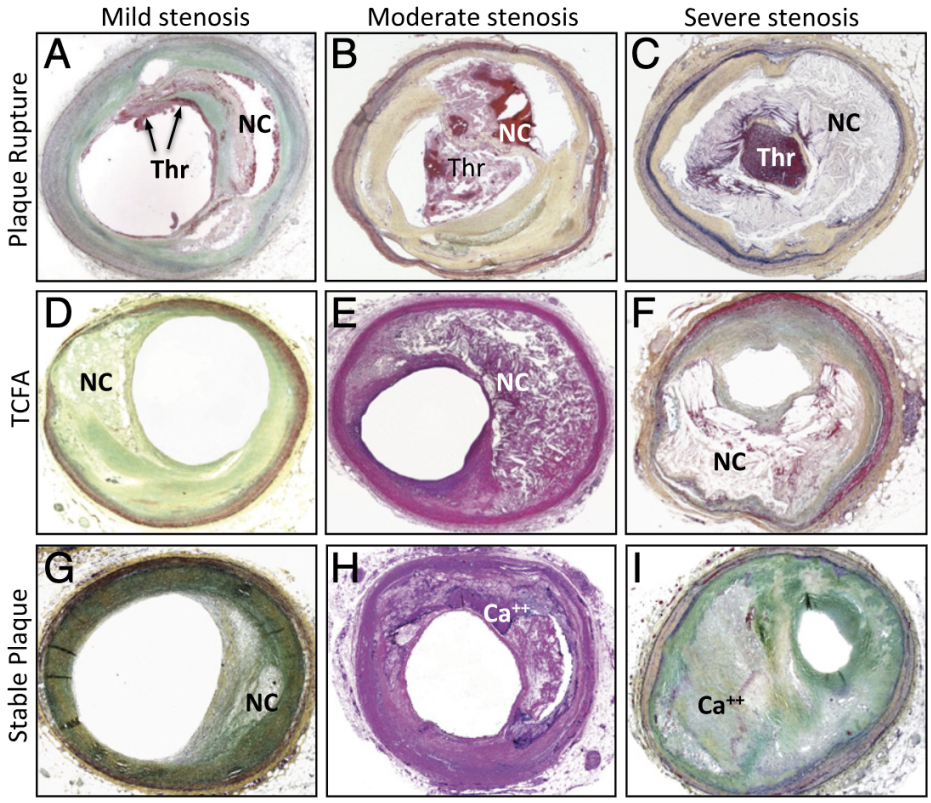

Figure 2.16: Photomicrographic cross-sections of human coronary plaques with varying degrees of stenosis. (A–C) Plaque rupture with mild, moderate, and severe luminal stenosis. Nonocclusive thrombi are visible in (A), whereas occlusive thrombi occupy the lumen in (B) and (C). (D–F) Thin-cap fibroatheromas at different stenosis levels, with a necrotic core covered by a thin fibrous cap. (G–I) Stable plaques frequently exhibit calcifications, with necrotic cores appearing relatively small when calcification is present. Adapted from [79].

2.4.2 Intravascular imaging

Intravascular imaging enables high-resolution visualisation of the artery's inner lumen, providing detailed assessment of plaque features critical to cardiovascular risk stratification. Two primary techniques used in clinical practice are optical coherence tomography (OCT) and intravascular ultrasound (IVUS).

OCT, an advanced imaging method, uses near-infrared light delivered through a fibre optic catheter to capture high-resolution (10–20 μm) images of the artery's inner wall. This technique excels at detecting fine details such as TFC, making it ideal for identifying complex plaques [80]. However, OCT's limited tissue penetration (1–2 mm) restricts its application to superficial plaque assessment.

In contrast, IVUS utilises a high-frequency US probe that provides deeper penetration (up to 8 mm) into the vessel wall, allowing for a broader view of plaque burden and composition, including calcified regions. Although IVUS has lower spatial resolution than OCT, it remains valuable for assessing overall plaque volume and morphology. Additionally, IVUS images can be processed through virtual histology to further char-

acterise plaque features, such as lipid cores and fibrous caps, based on their US signal properties [81] [82]. Despite its advantages, IVUS, like OCT, is an invasive technique, which limits its use to specific clinical settings [83].

2.4.3 Computed tomography

Diverse non-invasive imaging techniques have emerged to visualise atherosclerotic plaques in carotid arteries, offering critical insights into plaque composition and stability. Computed tomography (CT) imaging uses X-rays that rotate around the patient. As the X-ray source rotates, it emits beams that penetrate different tissues, which are detected on the opposite side. The degree of attenuation of the X-ray signal varies depending on tissue density, allowing differentiation between various structures and producing high-resolution greyscale images. CTA, a specialised form of CT, involves injecting an iodine-rich contrast agent to enhance vessel visualisation, improving the visibility of blood flow and arterial structures.

Josephson et al. investigated CTA's accuracy in assessing carotid artery stenosis, finding it 100 % sensitive and 63% specific for detecting stenosis over 70%, see Figure 2.17 [84]. However, while CT provides excellent spatial resolution, it is limited in differentiating specific plaque components, such as fibro-atheroma from thrombotic material [83]. Additionally, as CT involves ionising radiation, use is limited in clinical contexts.

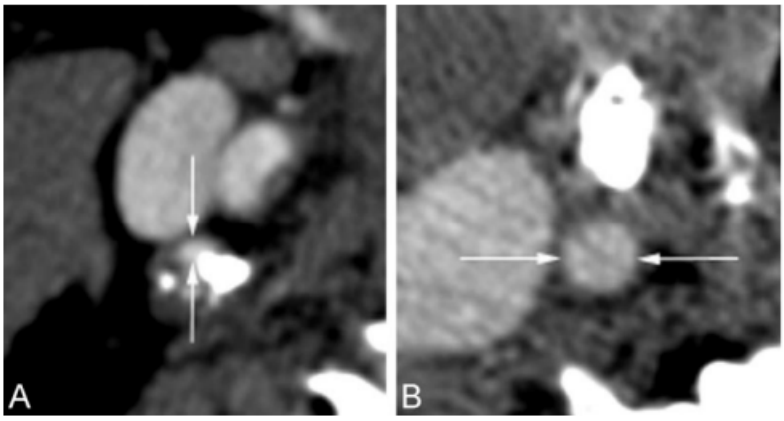

Figure 2.17: CT scans showing showing (A) cross-section at maximum stenosis of the ICA in axial view and (B) distal cervical artery cross section used as reference diameter taken from [84].

2.4.4 Magnetic resonance imaging

MRI is regarded as the clinical "gold standard" for characterising atherosclerotic plaque, due to its ability to distinguish plaque components with high accuracy [14]. Multi-contrast MRI sequences, such as fast spin echo, allow differentiation of plaque struc-

tures by varying the tissue contrast. MRI can reliably identify critical plaque features—such as calcification, lipid-rich necrotic cores, fibrous caps, and intraplaque haemorrhage—with good agreement to histology [85]. MRI also allows for "bright blood" contrast, which enhances blood flow signals, or "black blood" sequences, like T1-weighted imaging, where blood flow is suppressed to highlight vessel walls.

This imaging modality shows good to excellent intra- and inter-reader reproducibility, reinforcing its reliability in clinical assessments [86]. However, MRI is time-intensive, costly, and unsuitable for patients with metal implants, limiting its accessibility and clinical utility in certain scenarios.

2.4.5 Ultrasound imaging

US imaging is widely recognised for being fast, cost-effective, and non-ionising. The fundamental principle behind ultrasound imaging lies in the emission of sound waves at frequencies higher than 20 kHz (typically between 1 MHz and 20 MHz) [87]. Piezoelectric arrays emit sound waves that interact with different tissue types, a phenomenon referred to as tissue echogenicity. The most basic form of US, A-mode, represents signal amplitude in the tissue with respect to time or depth, though it is rarely used in clinical practice. B-mode (brightness mode), the most commonly used imaging modality, creates a 2D grayscale image of the tissue by stacking multiple A-mode scans. M-mode visualises tissue movement as a series of B-mode images taken along a single A-scan, and duplex B-mode combined with Doppler US can calculate peak systolic velocities to assess the degree of stenosis [50].

Echogenicty, a phenomenon where different tissues reflect sound waves at varying intensities based on their density and composition, can be used to determine plaque types from uniformly echolucent or translucent tissue to completely echogenic or heavily calcified tissue [88]. In fact, tissue regions appear as hyperechoic (bright), hypoechoic (gray), or anechoic (dark) areas, depending on their properties [89]. For instance, Grønholdt et al. highlighted that echolucent carotid plaques causing a 50% diameter stenosis or more, are associated with a higher likelihood of future strokes [90]. Sztajzel's review reinforces the significance of echogenicity in risk assessment, noting that anechogenic or heterogeneous plaques are more frequently associated with cerebrovascular events and may serve as markers of plaque instability due to features like thin fibrous caps and superficial necrotic cores [91].

While US imaging is highly versatile, it does have several limitations due to artifacts [92]–[94]:

- Shadowing artifacts are characterized by a significant reduction in signal intensity, often caused by structures such as bone that attenuate sound waves.
- Reverberation artifacts occur when imaging hyperechoic thin objects, leading to

multiple reflections between tissue interfaces.

- Edge artifacts arise when the ultrasound beam interacts with round structures, causing image distortion.

- Side or grating lobe artifacts are caused by imperfect focusing, where the ultrasound beam does not perfectly isolate the region of interest.

Recent advances in US imaging have introduced several techniques to improve image quality. Dynamic focusing involves emitting or receiving sound waves with a delay to create a dynamic lens effect, enhancing the focus on a desired area. Kern et al. demonstrated the use of compound ultrasound imaging which enhances intra- and inter-observer reproducibility in assessing plaque morphology compared to conventional B-mode, with higher reproducibility in characterising plaque echogenicity and surface features [95]. Tissue harmonic imaging achieves better resolution for deep tissue imaging by utilizing harmonic frequencies that are multiples of the fundamental wavelength [96]. Additionally, Yen et al. explored the combination of tissue harmonic imaging (THI), real-time spatial compound sonography, and adaptive image processing, which together reduce artifacts like speckling and clutter, enhancing the visualisation of carotid plaques and intima-medial thickness beyond what is achievable with traditional methods. This combination method improves clarity and image resolution by highlighting plaque borders and textures, offering a clearer assessment of plaque vulnerability [97].

Elastography

With these advancements, US imaging now offers enhanced clarity and depth, expanding its applications in diagnostic and therapeutic settings. US imaging also features advanced modalities such as elastography, which quantifies tissue stiffness non-invasively. Specifically, shear wave elastography (SWE) measures shear wave speed to estimate tissue elasticity, represented by Young's modulus [98]:

$$\mu = \rho \times c^2$$

$$E \approx 3 \times \mu = 3 \times \rho \times c^2$$

where E is the elastic modulus of the medium, c the speed of the sound in the medium and ρ the medium density. Ramnarine et al., [99] demonstrated the clinical potential of SWE with results showing good reproducibility. The inter-frame coefficient of variation was 22 % within the vessel wall and 19% within the carotid plaque. Figure 2.18 illustrates an elastogram of a plaque located at the origin of the internal carotid

artery.

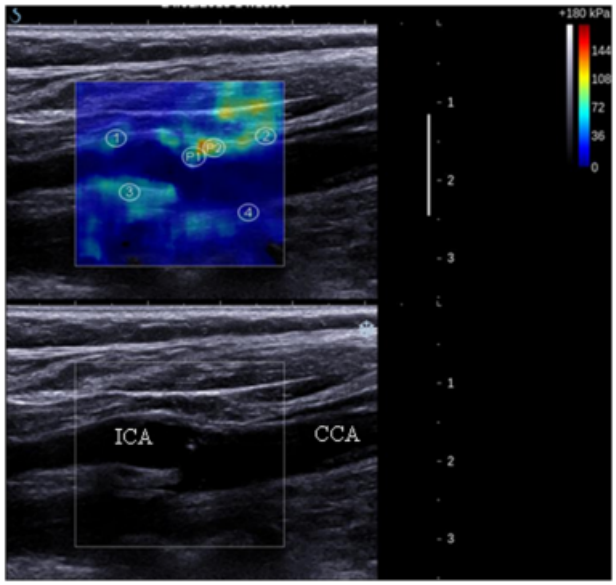

Figure 2.18: Image of a grade 1, 30-40 % stenosis at the origin of the internal carotid artery (above: elastogram; below: B-mode image) taken from [99].

Moreover, Widman et al. performed uniaxial tensile testing as well as SWE of soft and hard plaque surrogates [100]. Their results showed good agreements between the two methods with 5.8 ± 0.3 kPa and 106.2 ± 17.2 kPa versus 3.3 ± 0.5 kPa and 98.3 ± 3.4 kPa for mechanical testing and SWE respectively. Mellucci et al. discussed the technical principles of SWE and its clinical application for assessing carotid artery plaques. The study emphasised the importance of SWE's reliability for evaluating plaque stiffness and its role in improving therapeutic decision-making for patients with carotid artery disease [101]. Marlevi et al. demonstrated that combining spatiotemporal and frequency-dependent SWE allowed for the detection of vulnerable plaques - based on the modified AHA classification [102] - by assessing variations in group and phase velocities. This refined approach enabled more accurate predictions of atherosclerotic risk compared to standard SWE techniques [103]. SWE also shows promise in detecting soft, lipid-rich regions within vessel mimicking phantoms and plaques. Hansen et al. [104] demonstrated SWE's ability to detect lipid content in transverse arterial cross-sections, emphasizing the technique's utility in identifying vulnerable plaques based on morphology. Ramnarine et al. have demonstrated SWE's clinical potential, showing reproducibility in assessing vascular and plaque stiffness [99]. Further supporting SWE's role in clinical settings, Tjan et al. explored the correlation between carotid artery stiffness and stroke risk [105]. Their study showed that stiffer carotid arteries, as measured by SWE, were associated with a higher risk of stroke, underscoring the clinical relevance of stiffness measurements for stroke prediction. Recent advances in SWE technology have further improved its accuracy. Davidhi et al. highlighted SWE's utility in differentiating between hyperechoic and hypoechoic plaques, which are commonly

linked to plaque vulnerability. This method showed excellent reproducibility, supporting its clinical utility for routine assessments [106]. In summary, SWE is a powerful tool for non-invasively assessing plaque stiffness and, offering significant potential for improving risk stratification and guiding treatment decisions in patients with carotid artery disease. Although SWE has demonstrated reliability and accuracy, larger clinical trials are needed to standardise its application in clinical practice. In fact, SWE is subject to limitations, including variability between operators, which can impact consistency in measurements. Larger clinical trials are therefore needed to standardise SWE application in clinical practice and address these limitations to ensure uniformity across different clinical settings [107]–[109].

Strain imaging

Building on the principles of elastography, strain imaging focuses on quantifying the deformation, or strain, of tissues under applied forces. While elastography assesses tissue stiffness, strain imaging provides detailed insights into how much and where a tissue segment deforms. By measuring the amount and pattern of tissue deformation, strain imaging provides insights into tissue elasticity or stiffness, which can be critical in diagnosing and characterising certain diseases, particularly in cardiovascular imaging. These measurements are derived from the analysis of radiofrequency (RF) signals received during imaging. RF signals are typically filtered to demodulate the echo peaks, producing what are known as envelope signals, which are visualised in B-mode images. The speckle patterns observed in these images arise from the constructive and destructive interferences of the emitted echoes as they interact with the tissue. By manipulating the RF data, it is possible to calculate both axial and lateral displacements of tissues with high precision. This method, first introduced by using a cross-correlation approach to compare RF signals pre- and post-compression, laid the foundation for elastography [110]. Lopata et al. later provided an extensive review of techniques to obtain 2D and 3D strain imaging from RF signals [111]. Recent advancements in RF data analysis have led to significant improvements in strain imaging. For instance, Khavari et al. introduced a non-local coherent denoising technique for RF data in elastography, which significantly enhances the strain results by reducing noise while preserving key information [112]. Similarly, Omidyeganeh et al. proposed a method that utilizes both the displacement field and RF frames to obtain accurate strain estimates, further improving strain elastography accuracy [113]. In addition, deep learning techniques are being integrated into RF data analysis to optimise results. Delaunay et al. [114] developed a convolutional neural network for time-delay estimation between RF data, enhancing the precision of strain imaging. These recent advances in RF data analysis are pushing the boundaries of non-invasive ultrasound imaging, allowing for deeper insights into tissue mechanics and improving the detection

of vulnerable atherosclerotic plaques.

Contrast enhanced ultrasound (CEUS)

While elastography and strain imaging provide valuable insights into tissue stiffness and deformation, recent advancements in ultrasonography have introduced CEUS, expanding the diagnostic toolkit for assessing plaque vulnerability. Unlike elastography, which evaluates tissue elasticity, CEUS enables detailed visualisation of intraplaque neovascularisation, offering a new dimension in characterising plaque composition and associated risks. The principle is based on micro-bubble contrast agents injected intravenously which enhance US signals by increasing blood backscatter [115], [116]. As mentioned in Section 2.3.4, Virmani et al. observed that angiogenesis can be the cause of intraplaque haemorrhage due to neovessel leakage and neovascularisation is also associated with plaque enlargement [24]. It also serves as a complementary modality alongside techniques like SWE and has the potential of being integrated in clinical risk assessments to help guide interventions aimed at preventing cerebrovascular events [117], [118]. Furthermore, research has demonstrated a strong correlation between neovascularisation identified through histological analysis and CEUS findings [119], [120].

Zhang et al. explored the correlation between intraplaque neovascularisation (IPN) and plaque stiffness using both CEUS and elastography [69]. Their findings suggested that plaques with extensive neovascularisation tend to have lower elasticity. Studies have attempted to grade the degree of contrast-enhancement [119], [121]. Coli et al. characterised IPN as either absent/peripheral (grade 1) or extensive/internal (grade 2) [119]. Figure 2.19 below shows a hypoechoic carotid plaque grade 2 contrast enhancement [119]. Similarly, in Shah et al.'s study, neovascularisation was categorised as follows: grade 0 for no appearance of neovascularisation, grade 1 limited neovascularisation, grade 2 for moderate and grade 3 for arterial vessel within the plaque [121].

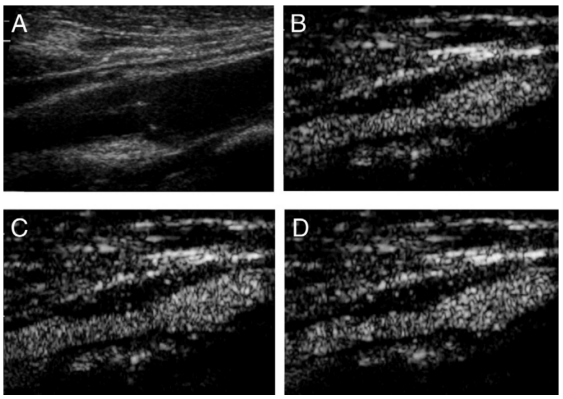

Figure 2.19: Panel A shows a hypoechoic plaque at the origin of the internal carotid artery. After the injection of Optison, as seen in Panels B to D, an extensive contrast-agent enhancement is observed, represented by several bright spots within the plaque itself from [119].

However, one limitation of this visual grading system is its reliance on the examiner's experience, which introduces potential variability in assessment. In Zhang et al.'s study, CEUS results were evaluated both semi-quantitatively and quantitatively using time-intensity curves, as seen in Figure 2.20, providing a more objective approach to analysing neovascularisation [122].

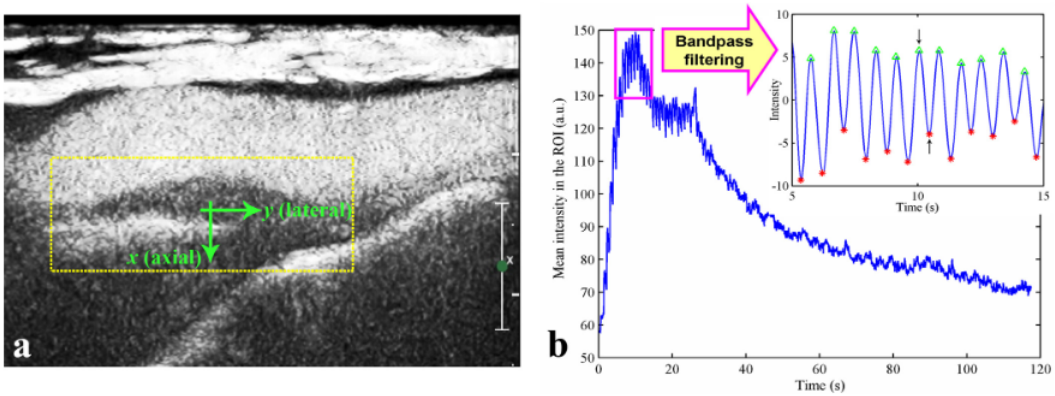

Figure 2.20: (a) CEUS scan of carotid plaque delineated with ROI and (b) associated time intensity curve from [122].

Joo et al. showed that high densities of vasa vasorum correlate with carotid plaque vulnerability, where active microvessels and delayed microbubble influx can be markers of instability [123]. Alonso et al. also highlighted CEUS as an effective tool in identifying intraplaque neovascularisation, emphasising its role in predicting symptomatic disease by visualising delayed microbubble influx, indicative of plaque vulnerability [124]. IPN has been identified as a key feature of vulnerable plaques, particularly at the fibrous cap and plaque shoulders, where neovessel formation is often most pronounced [125]. Joining this, Che et al. demonstrated that carotid IPH, closely linked with neovascularisation, significantly predicts recurrent ischemic strokes in patients with carotid atherosclerosis [126]. The density of neovascularisation is also strongly

associated with symptomatic presentations of carotid atherosclerosis, indicating that it could serve as a useful metric for predicting stroke risk [127]. In a recent study, Tian et al. further demonstrated that soft plaques, characterised on US as having low echogenicity and lacking acoustic shadowing, exhibit significantly higher contrast enhancement and neovascularisation density using CEUS, further validating its role in plaque characterisation and risk stratification [73].

Ultrasound localisation microscopy

Ultrasound localisation microscopy (ULM) is a cutting-edge imaging technology that combines ultrafast ultrasound and micro bubble tracking to achieve super-resolution visualisation of microvascular structures, including neovascularisation in arterial plaques. It offers a high spatial resolution far beyond the the limit of conventional US, making it an essential tool for non-invasive evaluation of vascular conditions. Recent studies underscore ULM's effectiveness in identifying and quantifying neovascularisation within atherosclerotic plaques. Goudot et al. highlighted ULM's utility in imaging vasa vasorum and differentiating active from quiescent inflammation in Takayasu arteritis, showcasing its versatility for broader applications, including plaque assessment [128]. More recently, Leroy et al. demonstrated ULM's ability to accurately assess microvascular flow parameters in human carotid plaques, providing significant insights into plaque vulnerability and linking findings to histological validation [129]. These studies reinforce ULM's role as a transformative, non-invasive modality for evaluating microvascular health and disease progression.

Superb microvascular imaging

Superb microvascular imaging (SMI) represents a significant advancement in vascular US imaging by enabling the non-invasive and contrast-free evaluation of plaque neovascularisation, making it a safer and more accessible alternative to CEUS. SMI uses advanced filtering algorithms to extract real blood flow signals while eliminating tissue motion artifacts, allowing for high-resolution visualisation of microvascular flow. Studies have demonstrated strong concordance between SMI and CEUS, with SMI successfully detecting neovascularisation even in hypoechoic plaques and across varying plaque thicknesses [130]. Research by Chen et al. highlighted that SMI correlates strongly with histologically validated microvessel density [127]. Zamani et al. showed SMI's diagnostic reliability as comparable to CEUS [131]. Additionally, Meng et al; confirmed SMI's reliability in characterising neovessels, correlating its findings with histology and CEUS [132]. Oura et al. emphasised SMI's role in clinical settings where contrast agents are not feasible [133]. Although promising, SMI has limitations, including its operator dependency, and requires further large-scale validation to estab-

lish its clinical utility. Nevertheless, its potential to assess plaque vulnerability and guide clinical decision-making makes it an invaluable tool in cerebrovascular disease management.

In summary, while traditional US imaging continues to be a cornerstone of non-invasive assessment, advanced modalities like CEUS, SMI, and ULM offer enhanced insights into plaque vulnerability. CEUS captures the dynamic processes of neovascularisation, improving the identification of plaques that may be prone to rupture. SMI further advances non-invasive imaging by enabling high-resolution visualisation of microvascular flow without the need for contrast agents, making it safer and more accessible. Similarly, ULM combines ultrafast US and micro-bubble tracking to achieve super-resolution imaging, providing unprecedented detail of microvascular structures, including neovascularisation, far beyond the limits of conventional US. Additionally, advances like 3D ultrasound, which provides a volumetric view of plaques for detailed assessment of structure and heterogeneity, and photoacoustic imaging, which combines optical and US techniques to visualise plaque composition and neovascularisation with exceptional contrast, show great promise in advancing the understanding of plaque vulnerability [134], [135]. A recent review underscores the transformative potential of these US techniques in redefining the identification and characterisation of vulnerable atherosclerotic plaques [136]. While these emerging technologies show significant promise, particularly in identifying and quantifying plaque neovascularisation, there remains a need for further research to establish stronger links between neovascularisation, mechanical vulnerability, and plaque rupture. Such efforts are crucial for refining clinical decision-making and improving risk assessment in carotid artery disease.

2.5 Insights from mechanical testing

2.5.1 PVA arterial surrogates

Vessel-mimicking phantoms have been developed as controlled, reproducible alternatives for studying human plaque tissue which is challenging to obtain. Among these, PVA-based surrogates have gained significant interest due to their tunable mechanical properties and acoustic similarity to arterial tissue, making them well-suited for both mechanical testing and US imaging applications [137]. Additionally, their material properties and heterogeneity can be precisely controlled, enabling systematic investigation of rupture mechanisms [138]. Furthermore, phantoms play a crucial role in validating computational modelling approaches, bridging the gap between experimental and simulated data. Among the various materials used for vessel phantoms, PVA is of particular interest due to its ability to polymerise and stiffen through freeze-thaw cycles (FTCs) [139]–[141]. Numerous studies have investigated the potential of PVA

for replicating atherosclerotic plaque characteristics [142]–[146]. In a recent study, Crielaard et al. replicated soft inclusions in plaque caps analogues using fibrin [147]. Le Floc'h et al. developed phantoms with a necrotic core or soft inclusion, using PVA treated with a single FTC. This advancement allowed for the simulation of more realistic plaque morphologies [148]. Chayer et al. extended this work by designing phantoms mimicking the carotid bifurcation, enabling the study of more anatomically accurate geometries for evaluating flow and stiffness [145]. Pazos et al. demonstrated the feasibility of imaging mock carotid arteries composed of a double-layered PVA wall and lipid inclusions using IVUS [149]. Widman et al. characterised PVA-based surrogate models of hard and soft carotid plaques through SWE and mechanical testing [100]. Nafo and Al-Mayah explored the mechanical response of PVA phantoms subjected to two FTCs through both uniaxial and cavity expansion tests, providing valuable insights into their multi-axial behaviour [150]. Hansen et al. developed a two-layered vessel-mimicking phantom consisting of a stiff outer layer and a softer inner layer to simulate vessels with soft plaques, lipid pools, fibrous cap regions, and cap shoulders. They used US-based strain imaging to evaluate mechanical properties under pulsatile pressure [151]. While testing PVA phantoms as surrogates for modelling diseased vessels enables valuable insights on plaque mechanics, transitioning to real tissue testing enables a deeper understanding of the complex microstructural and mechanical behaviours inherent in atherosclerotic plaques.

2.5.2 Mechanical testing of carotid atherosclerotic plaques

Mechanical testing of soft tissues provides insights into their mechanical behaviour. These methods are particularly helpful to better characterise atherosclerotic tissue behaviour. An extensive study led by Teng et al. [152] performed uniaxial tensile testing of media, fibrous cap, lipid and IPH of carotid plaques from 21 patients. Overall, 65 media samples, 59 fibrous cap samples, 31 lipid samples and 21 IPH samples were tested in the circumferential direction. Results showed the nonlinear behaviour of carotid plaques components. The stress-stretch curves extracted highlighted the high variability of plaque components' behaviour, see Figure 2.21.

The average stress-stretch curve of each plaque component was then plotted and fitted using an energy-based approach, see Figure 2.22.

This study [152] showed that media and fibrous cap have comparable stiffness and were stiffer than lipid and intraplaque haemorrhage. The latter two components also have comparable stiffness.

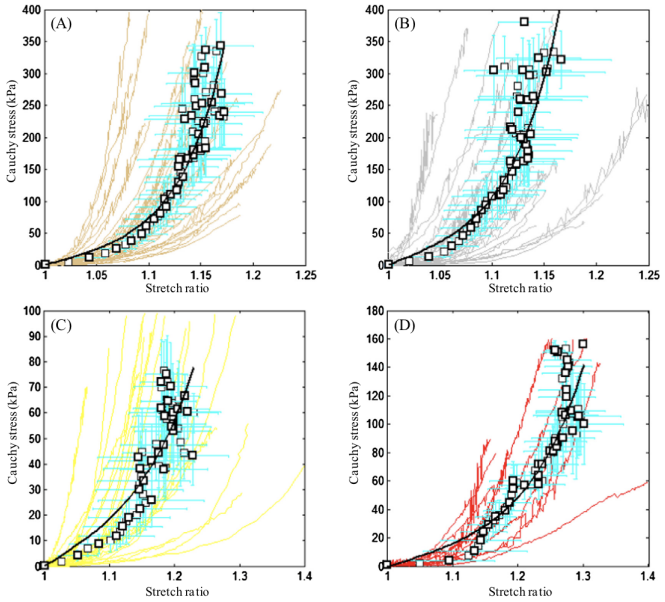

Figure 2.21: Stress-Stretch curve of tested samples (A) media, (B) FC, (C) lipid and (D) intraplaque haemorrhage taken from [152].

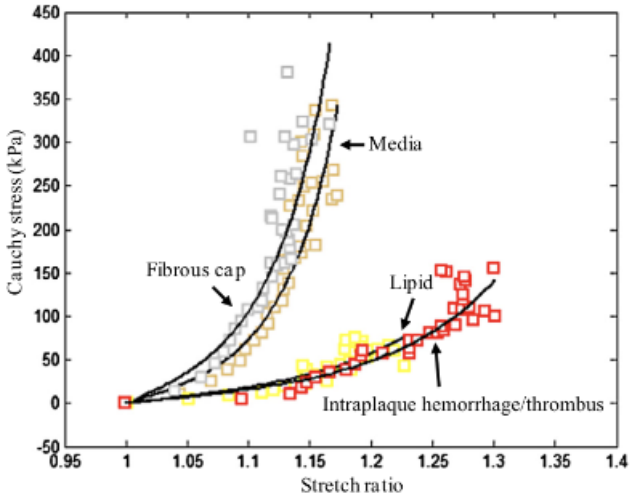

Figure 2.22: Stress-Stretch curve of average data points and fitted curves taken from [152].

The material parameters of the fitted Mooney-Rivlin from this study are presented in Table 2.4 [152].

Table 2.4: Material parameters of the fitted Mooney-Rivlin model for different plaque components.

Tissue Component	$\mathbf{C_1}$ (kPa)	$\mathbf{D_1}$ (kPa)	$\mathbf{D_2}$ (kPa)
Media	0.138	3.833	18.803
Fibrous cap	0.186	5.769	18.219
Lipid tissue	0.046	4.885	5.426
Intraplaque Haemorrhage	0.212	4.260	5.312

Barrett et al. [153] performed indentation tests on carotid fibrous plaque caps.

Shear modulus values between 7-100 kPa were obtained. In addition, indentation tests combined with confocal microscopy were performed on eight human carotid arteries by Chai et al. [154]. The schematic below depicts the testing set-up:

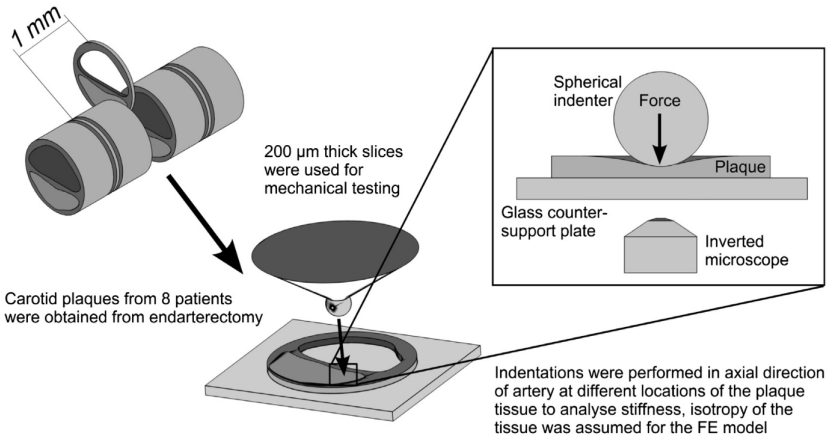

Figure 2.23: Indentation testing set up taken from [154].

The tests were performed in the axial direction and a least square function was used to fit a Neo-Hookean model to force-indentation curves. Compressive Young's moduli values ranged from 6 kPa to 891 kPa. This study found that collagen regions to be stiffer than poor collagen regions. An extensive study by Holzapfel et al. [155] investigated the anisotropy of iliac atherosclerotic plaque components. Uniaxial tensile testing was performed in the axial and circumferential directions. The conclusions drawn were the following:

- The diseased media is stiffer than non-diseased media. Similarly for the intima.
- The lowest ultimate stresses were found for the fibrous cap in the circumferential direction.
- Samples tested in the circumferential direction have a larger hysteresis area.

Mulvihill et al. [156] combined scanning electron microscopy (SEM), Fourier Transformed Infrared (FTIR) and uniaxial tensile testing to analyse the mechanical properties of 25 carotid plaques samples in the circumferential direction. FTIR was used to evaluate the plaques' components. The stress-stretch curves plotted were classified based on the calcification to lipid ratio,see Figure 2.24. Figure 2.24 below shows the variability of plaque samples' mechanical properties and that more calcified samples are stiffer.

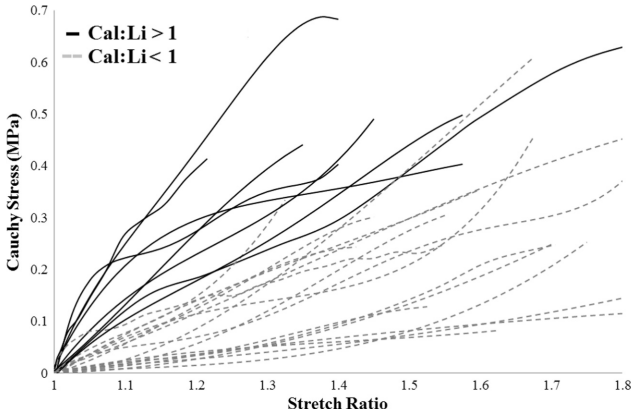

Figure 2.24: Stress-Stretch classified based on the calcification to lipid ratio from [156].

SEM images revealed that nodule-like calcified regions can increase the vulnerability of plaques by creating voids. Combining tissue microstructure with mechanical testing provides valuable insights into plaque behaviour. Johnston et al. demonstrated that collagen alignment significantly influences plaque cap structural stability [19]. Tornifoglio et al. utilised tractography-based grouping to analyse plaque strips and demonstrated that plaques with misaligned collagen fibre microstructures failed at lower strains, highlighting the structural influence on mechanical integrity [20]. On the other hand, Guvenir et al. used this technique to assess fibre dispersion in plaque specimens subjected to uniaxial tensile testing, finding that while collagen orientation was predominantly circumferential, no significant differences in fibre direction or dispersion were observed between rupture-prone regions and other areas of the samples [21]. However, uniaxial tensile testing possesses inherent limitations for it does not replicate the multiaxial physiological loadings applied on the arterial wall.

To answer this limitation, bi-axial tensile tests or inflation testing can be carried out. Boekhoven et al. [157] conducted inflation testing of nine human carotid atherosclerotic plaques to assess their strain environment using US imaging, see Figure 2.25. The radiofrequency data extracted from US scans between pressure steps are cross-correlated to obtain displacement maps.

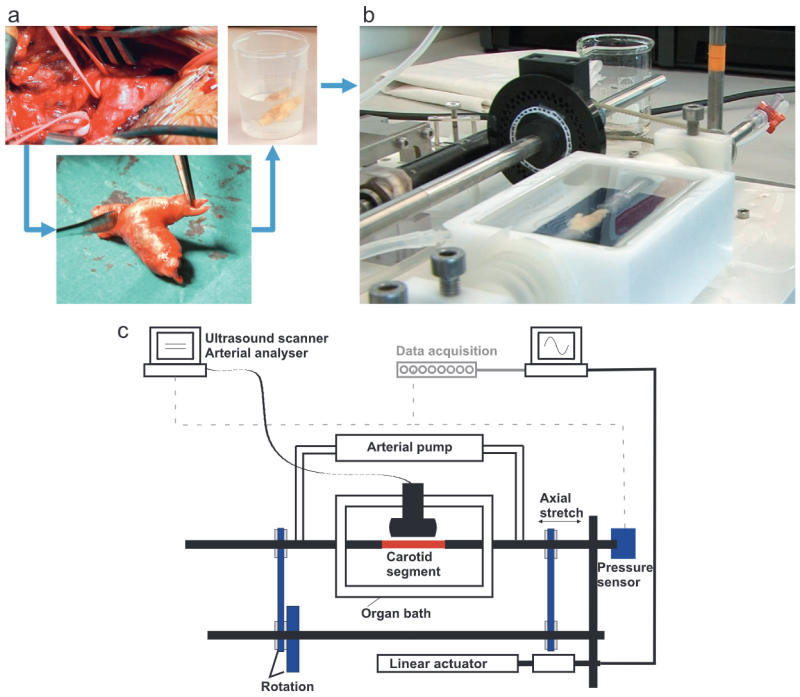

Figure 2.25: Inflation testing set up taken from [157].

Similarly, Sanders et al. [158] inflated four healthy porcine carotid arteries combining ultrasound imaging as depicted in Figure 2.26.

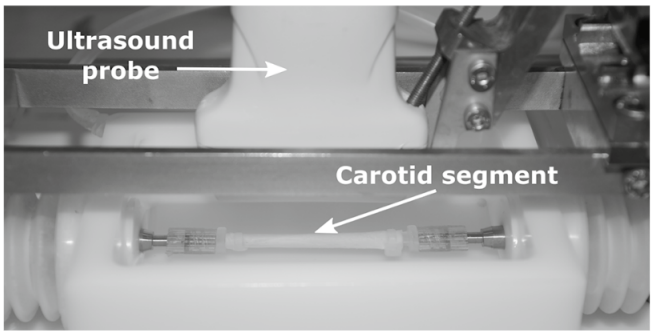

Figure 2.26: Inflation testing set up taken from [158].

Pressure-diameter curves allowed the estimation of the material parameters of the Holzapfel-Gasser-Ogden model, see Figure 2.27.

Pressurisation of plaques renders it possible to mimic *in vivo* physiological loadings; however, this technique remains challenging due to the delicate nature of plaque specimens and the complexity of test setup and execution. Overall, mechanical testing allows the characterisation of soft tissues, and when combined with computational models, it offers a powerful approach to gain valuable insights into plaque mechanical behaviour. In this regard, computational models have seen a considerable expansion in order to characterise the mechanical environment of plaques.

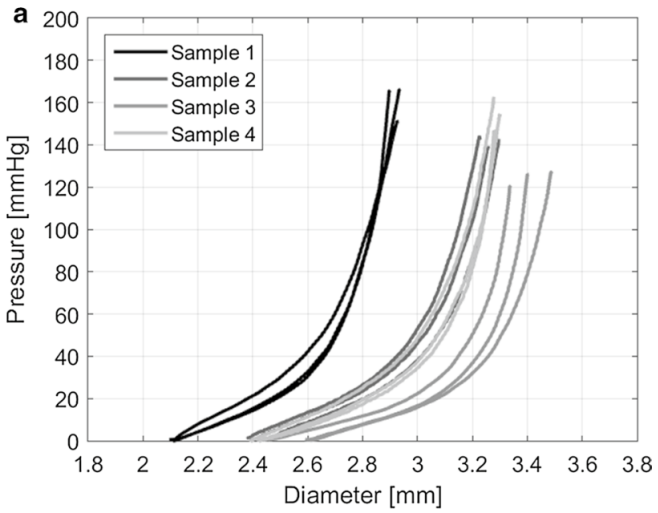

	Vessel-inflation		
Sample	c_1 (kPa)	k_1 (kPa)	k_2 (–)
1	18.4 ± 5.7	12.1 ± 0.9	19.1 ± 0.6
2	23.2 ± 0.9	12.5 ± 0.8	20.9 ± 2.2
3	17.5 ± 3.0	10.4 ± 2.5	26.6 ± 6.1
4	19.7 ± 2.5	14.4 ± 1.1	19.5 ± 1.8

Figure 2.27: Pressure-diameter curves (top) and parameter estimation of the HGO model (bottom) from [158].

2.6 Computational methods

The combination of experimental and computational work allows us to deepen our understanding on the mechanical behaviour of atherosclerotic plaques. The refinement of finite element models to mimic *in vivo* loading and boundary conditions can help find better mechanical indicators of vulnerable plaques. Accurate computational models are required to reproduce the complex and heterogeneous microstructure of plaques. From a mechanical perspective, a plaque is likely to rupture when the stresses exerted are greater than its ultimate strength. The schematic in Figure 2.28 from Sadat et al. illustrates the different stresses in an idealised atherosclerotic plaque geometry [159]. The principal stresses in a cylindrical coordinate system are represented in Figure 2.28.B :

2.6.1 Constitutive modelling

Computational models of healthy and diseased arteries require their material models to be defined. The equation relating stress and strain is the constitutive equation. To account for the non-linear hyperelastic behaviour of arterial vessels, numerous strain-energy density functions usually denoted ψ have been developed. The latter were initially created to characterise the mechanical behaviour of rubber-like materials. It

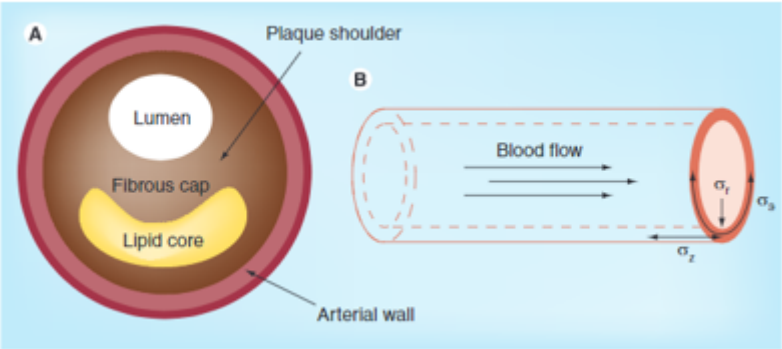

Figure 2.28: Mechanical stresses in an idealised heterogeneous plaque from [159].

is common to consider the arterial wall as incompressible. Strain-energy density functions can be more or less complex depending on if the tissue is considered isotropic or anisotropic.

Under the assumption that a material is isotropic, the strain-energy density functions is expressed in terms of the strain invariants of the right or the left Cauchy-Green deformation tensor [160]:

$$\psi_{iso} = \psi(I_1, I_2, I_3)$$

with :

$$I_1 = \sum_{i=1}^{3} {\lambda_i}^2$$

$$I_2 = \sum_{i=i,j}^{3} \lambda_i^2 {\lambda_j}^2, i \neq j$$

$$I_3 = \prod_{i=1}^{3} \lambda_i^2$$

and λ_1,λ_2,λ_3 the principal stretches.

Hooke's law linearly relate stress and strain and is characterized by two parameters namely, the Young's modulus and the Poisson's ratio. This model is used for linear elastic, isotropic materials and accurate only for small strains. The Neo-Hookean model, proposed by Ronald Rivlin in 1948, is a one term material model used for an isotropic, linear elastic material and valid for large deformations [161]. The Mooney-Rivlin model extends the Neo-Hookean model for hyperelastic materials. It is defined by a linear combination of the two invariants of the left Cauchy-Green deformation tensor B and is expressed as followed for an incompressible material:

$$\psi = \frac{\mu_1}{2}(I_1 - 3) - \frac{\mu_2}{2}(I_2 - 3)$$

with μ_1 and μ_2 material parameters.

The Ogden material model proposed is expressed in terms of principal stretches [162] :

$$\psi = \sum_{i=1}^{N} \frac{\mu_i}{\alpha_i}(\lambda_1^{\alpha_i} + \lambda_2^{\alpha_i} + \lambda_3^{\alpha_i} - 3)$$

with $N \times 2$ pairs of material constants α and μ to be determined.

Delfino et al. proposed an exponential model for isotropic, hyperelastic and homogeneous material where a and b are material constants [163]:

$$\psi = \frac{a}{b}[exp(\frac{b}{2}(I_1 - 3)) - 1]$$

The aforementioned models do not incorporate the microstructure of the arterial wall. The Holzapfel Gasser Ogden model combined the Neo-Hookean and exponential constitutive laws to include anisotropy of collagen fibres [31].

The strain energy density function can then be written as follows to integrate anisotropy [164]:

$$\psi = \psi_{isotropic} + \psi_{anisotropic}$$

$$\psi = \frac{c}{2}(I_1 - 3) + \frac{k_1}{k_2}[exp[k_2(I_4 - 1)^2] - 1]$$

where c > 0, $k_1 > 0$ are stress-like material parameters and $k_2 > 0$ is a dimensionless parameter [164].

Concerning the modelling of atherosclerotic plaques, their inherent heterogeneity and patient specificity makes applying a general constitutive model challenging. As presented previously, mechanical testing allows the behaviour of diseased tissues to be described by fitting constitutive laws to mechanical results [152]. The combination of finite element modelling and mechanical testing allows suitable models to be found to describe the behaviour of atherosclerotic plaque at a component-wise level.

2.6.2 2D finite element models

The inclusion of material properties in finite element models renders it a powerful tool to investigate the complex phenomena involved in plaque rupture. One of the first studies in this field was led by Richardson et al. [165]. This finite element analysis (FEA) study showed how regions of high circumferential stresses were related to plaque

vulnerability in 2D models of coronary atherosclerotic plaques. This study also demonstrates how the presence and geometry of lipid pool increases circumferential stresses. Another commonly used metric to highlight the mechanical behaviour of plaques or arteries is the von Mises stress. Sadat et al. showed that for 2D models, the von Mises stress and maximum principal stress do not differ significantly, see Figure 2.29 [159].

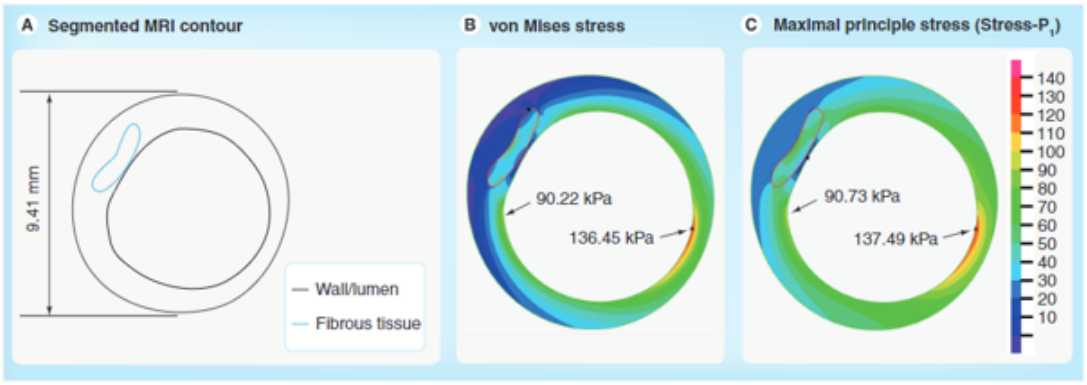

Figure 2.29: Comparison of von Mises stress (b) and Maximum principal stress (c) (Stress-P1) in 2D plaque model from in vivo MRI contour (a) taken from [159].

Williamson et al. studied the influence of material properties on 2D finite element models of a post-mortem diseased coronary arteries [166]. Figure 2.30 below illustrates the computational mesh obtained from histology segmentation:

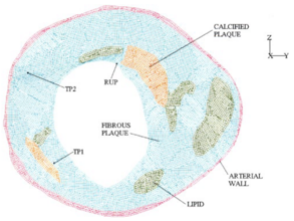

Figure 2.30: 2D FE mesh of diseased coronary artery incorporating arterial wall, lipid pool, calcification and fibrous plaque taken from [166].

This study showed that predicted stresses had small sensitivity when varying properties of nonlinear or orthotropic materials. Loree et al. showed that plaque geometrical features such as thickness of the fibrous cap are pivotal parameters of stress distribution in idealized 2D models of atherosclerotic plaque [167]. Finet et al. further investigated the influence of fibrous cap thickness and different material properties of the atheromatous core [168] . The 2D FE models were obtained from *in vivo* IVUS. This study showed that circumferential stresses exceeding 300 kPa were indicators of plaque instability. This stress threshold was obtained with plaque cap thicknesses inferior to 60 μm. They also demonstrated how the fibrous cap thickness was exponentially correlated with the peak circumferential stresses as shown in Figure 2.31 below:

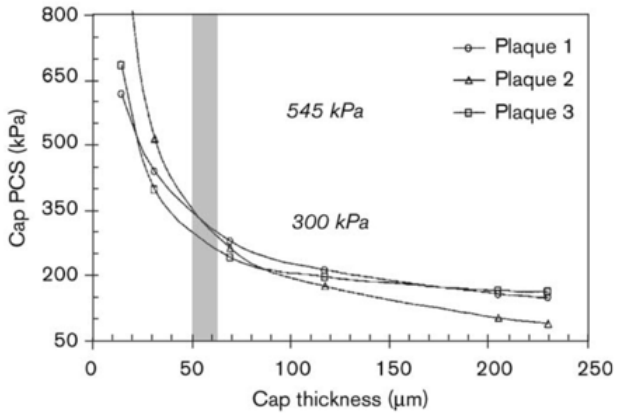

Figure 2.31: Cap peak circumferential stress (kPa) with respect to cap thickness (micrometre) for a blood pressure of 110 mmHg. The gray area being the cap thickness threshold of plaque instability lying between 50 and 62 μm. Image taken from [168].

Additionally, Li et al. generated 2D FE models of five atherosclerotic carotid plaques from *in vivo* high resolution MRI data [169]. Plaque components were thus delineated and registered to histology images. From the five plaques studied, three were deemed as type IV plaques while the two remaining plaques were ruptured. This study showed that the stresses experienced in the ruptured plaques are greater than in non-ruptured plaques as seen in Figure 2.32 below :

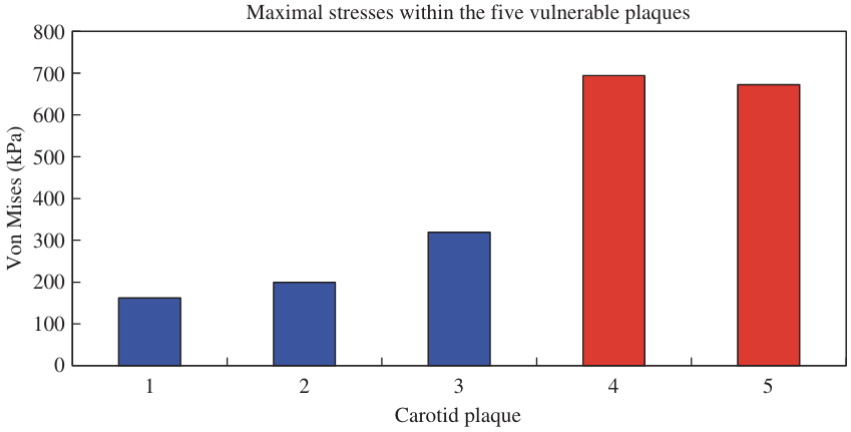

Figure 2.32: Maximum von Mises stresses (kPa) within the five plaques studied. Blue being the non-ruptured plaques while red refers the ruptured ones. Figure taken from [169].

The study by Ohayon et al. compared the stresses in 2D and 3D models study obtained from *in vivo* IVUS images of a 50 year old male patient [170]. This showed that 2D models overestimated the values of the peak cap stresses. The 2D model also failed to predict the concentration of peak cap stresses when compared to the postoperative reconstructed model. It is important to note that in 2D finite element models, plane-strain is assumed, and such assumptions can lead to inaccurate results when modelling such complex heterogeneous tissues.

2.6.3 3D finite element models

The accurate representation of atherosclerotic plaques allows to have a more when evaluating the structural stresses. As discussed in the previous paragraph, 2D models might result in inaccurate predicted stresses. The development of 3D FE approaches has thus been extensively studied. Carotid artery atherosclerosis mainly occurs at vulnerable sites namely the bifurcation. The development of 3D models allows to visualise structural stresses in such complex geometries. It has been shown that flow velocity is disturbed at this location suggesting that shear stress has an impact on plaque formation [171]. However, the study led by Teng et al., highlights that the structural stresses endured by the plaque cause it to fail [172]. *In-vivo* MRI data from 18 atherosclerotic plaques were obtained whereby 6 plaques ruptured. 3D fluid structure interaction models were reconstructed from MRI data. The critical plaque wall stress and critical flow shear stress were identified. Figure 2.33 shows how the critical plaque wall stress was a better predictor of rupture compared to critical flow shear stress from [172].

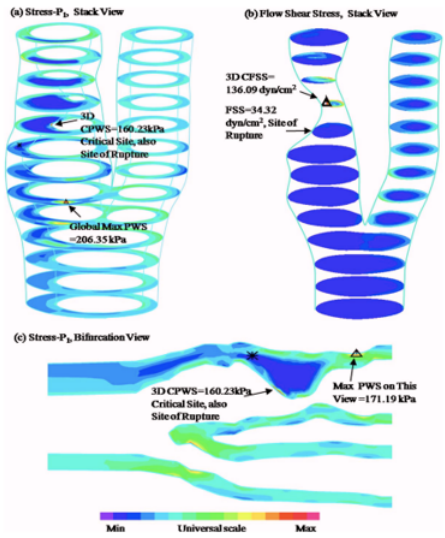

Figure 2.33: Band plot of plaque wall stress (stress-P1) and flow shear stress showing that plaque wall stress was able to predict the rupture site taken from from [172].

Teng et al. assumed that the material properties of the vessel and the fibrous cap followed a Mooney-Rivlin model [172]. Material parameters were obtained for each stiffness category of each plaque component by fitting a Mooney-Rivlin model to the stress-stretch curves. The value and distribution of stresses in a 3D idealised plaque model was highly impacted by the material properties. Cardoso et al. investigated the influence of the presence of micro-calcifications on the circumferential stress in the cap of the fibroatheroma as well as how the stress concentration factor is altered [173]. An idealised multi-scale FEA model was used as seen in Figure 2.34 below:

This study showed that the micro calcifications lead to higher circumferential stresses

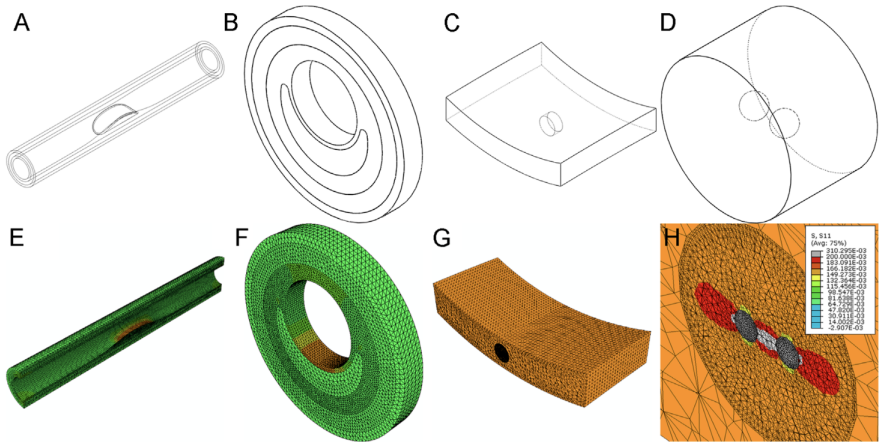

Figure 2.34: (A) Macroscopic (global) model, (B) annular section of the atheroma, (C) microscopic model of the atheroma cap with micro calcifications in the centre of the cap, and (D) magnified view of the cylindrical ROI containing two micro calcifications aligned with the tensile axis of the tensile axis of the cap. (E-H) Map of circumferential stresses under the loaded condition for all three scales of modelling from [173].

in the plaque cap. In addition, it was found that several parameters impact on the stress concentration factor created by the micro calcifications, namely the material properties of the arterial wall, the size and shape of the micro calcifications, their proximity and orientation. One limitation in most of these studies lies in the fact that the geometries analysed were not-patient specific. This can lead to discrepancies in the predicted stresses. To overcome this constraint, robust frameworks of parameters estimation have widely been developed namely inverse finite element analyses.

2.6.4 Material parameter estimation - inverse finite element modelling

Combining experimental and computational modelling can be a powerful tool to accurately estimate the stress/strain fields of the arterial wall. By matching finite element models to experimental measurements obtained from *in vivo* or *ex vivo* data, material properties can be inferred. This material parameter methodology is named inverse finite element analysis (iFEA). In this regard, Karimi et al. used a genetic algorithm approach to estimate material parameters of atherosclerotic coronary arteries [174]. 2D FE models from OCT sections were generated as well as an idealised 3D model. A Mooney-Rivlin model was employed for the vessel wall, fibrous plaque, and lipid pool. Elastography measurements were performed from OCT images and compared to the FE computed strain maps to infer intraplaque mechanical properties.

This workflow is depicted in Figure 2.35 below:

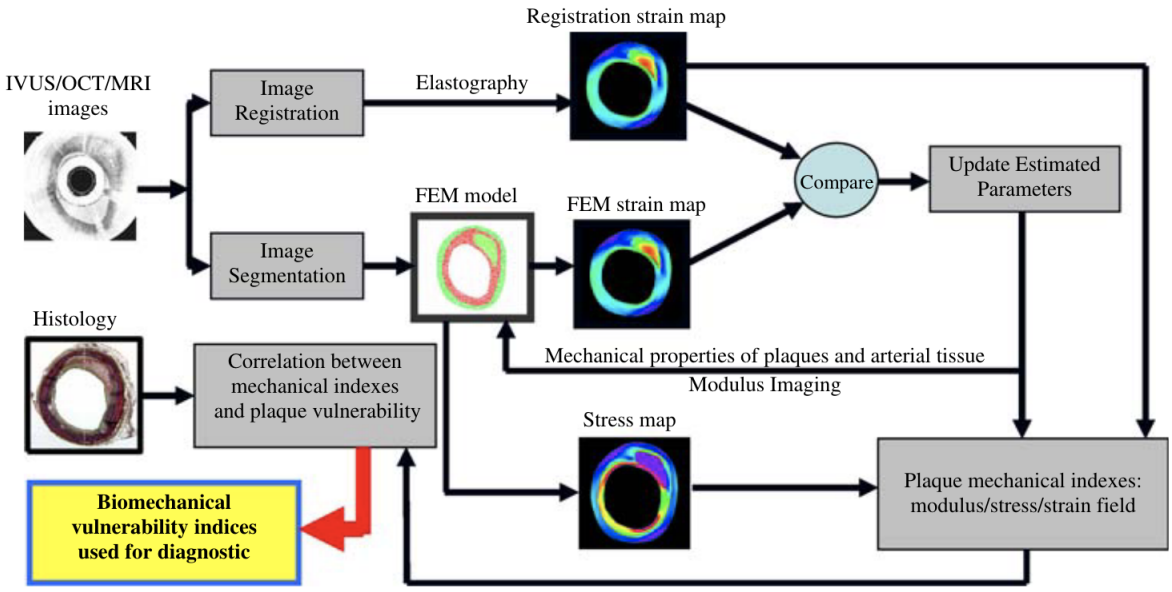

Figure 2.35: Framework of inverse FE from elastography measurements for parameter estimation. Figure taken from [174].

Nieuwstadt et al. combined *in vivo* MRI and simulated US elastography of carotid plaques [175]. Both imaging modalities balance out each other's limitations. US elastography from RF data has a higher resolution than MRI while the latter allows a better delineation of plaque components. Figure 2.36 below details the parameter estimation process:

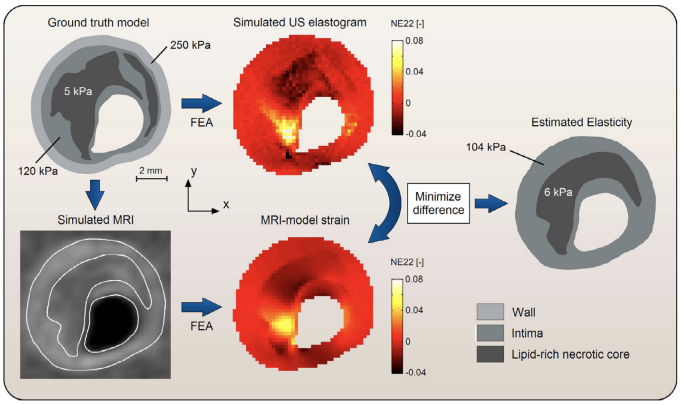

Figure 2.36: Hybrid MR-US inverse FE parameter estimation workflow.

The difference between FEM strains and US strains was minimised using a grid search method. The tissue was modelled using an isotropic, nonlinear, incompressible Neo-Hookean model. Only two parameters were to be found namely C_1 for the intima and the lipid rich necrotic core. In this study, a non-invasive hybrid-numerical local parameter estimation approach was validated. This also showed the pivotal role of accurate plaque delineation from MR images but also in this case, MR-US registration for it greatly influences the estimated parameters. Akyildiz et al. have developed an

iFEA method to determine local material properties of atherosclerotic plaques from US images [16]. Harvested iliac atherosclerotic plaques from six pigs were inflated *ex vivo* to obtain ground truth displacement maps. The latter were calculated from raw frequency data obtained using a high frequency linear array transducer. The coarse-to-fine cross-correlation algorithm utilised is explained in detail in Lopata et al. [176]. 2D FE models with plaque components were generated by registering histology slices to B-mode cross sections using a software named elastix. An incompressible Neo-Hookean material model was assigned to the intima and arterial wall (adventitia and media). Material parameters were finally inferred by matching the computational displacement with the experimental ones following a grid search method. The framework is illustrated in Figure 2.37:

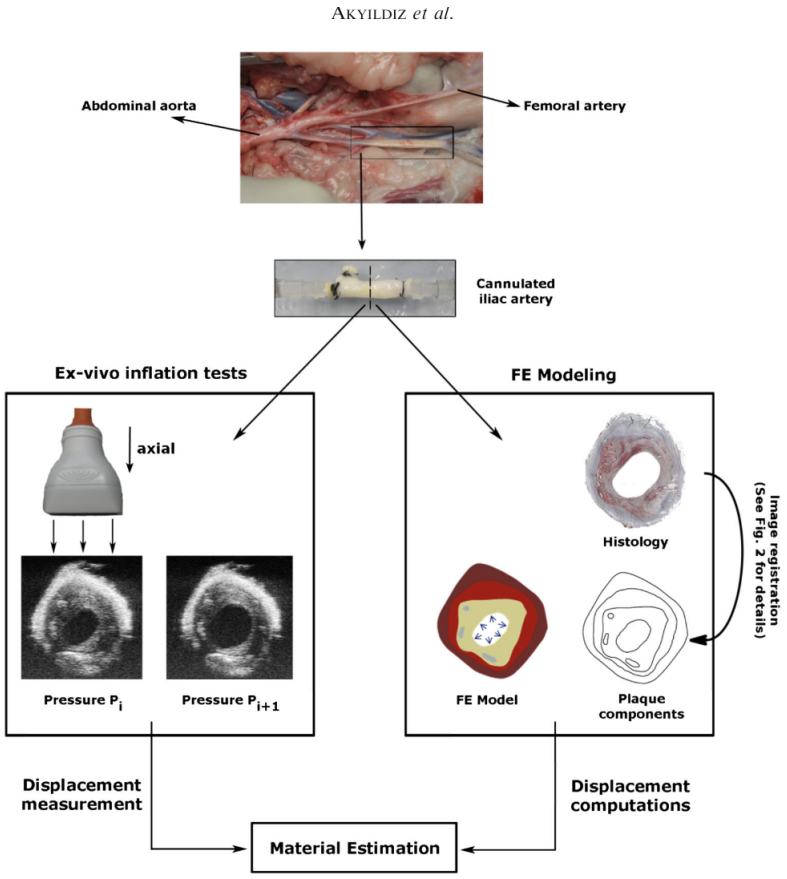

Figure 2.37: US iFEM workflow.

This hybrid study by Akyildiz et al. accurately determined local mechanical properties of atherosclerotic plaques from iliac arteries using US imaging [16]. This framework was further refined by Guvenir et al., see Figure 2.38 [17]. *Ex vivo* inflation of cadaveric atherosclerotic carotid arteries was performed combined with high resolution US imaging.

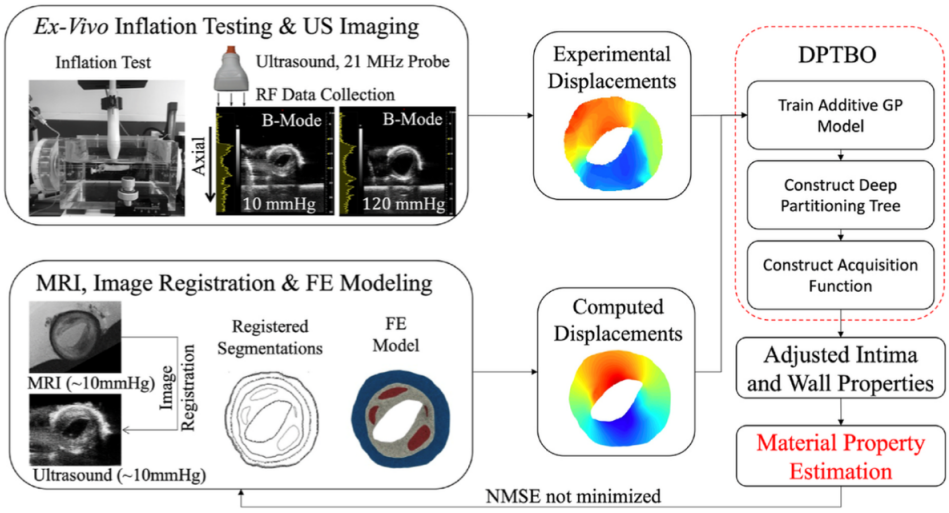

Figure 2.38: iFEM pipeline from [17].

Axial stretch of 15% was kept throughout the whole inflation testing [177]. RF data was used to obtain displacement maps using a coarse-to-fine method [151]. T1 and T2- weighted MR images were used to segment out the lipid pool, media, fibrous intima, and calcification. The MR images were registered to the US scans to create heterogeneous 2D FE models. The process is pictured in Figure 2.39.

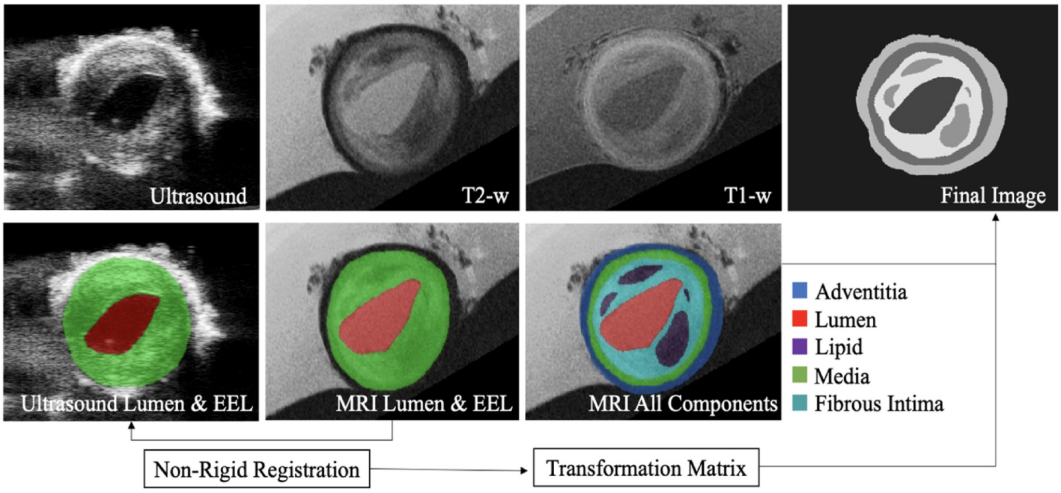

Figure 2.39: Non-rigid and rigid registration to obtain final heterogeneous 2D FE model of atherosclerotic carotid plaque taken from .

The fibrous intima and adventitia were modelled with an incompressible, nonlinear, hyperelastic Yeoh model. Lipid pool and calcification were considered using a Neo-Hookean model with C_1= 1 kPa and C_1= 1 GPa respectively. A grid search method was employed to minimise the normalised mean square error between the experimental and computed displacements. A Bayesian optimisation machine learning approach was used to verify the uniqueness of the solution obtained from the iFEM pipeline. This study is a major step forward in determining component wise mechanical properties of

atherosclerotic carotid plaques and provides a high capability in being transferred clinically. Nonetheless, plane strain assumptions were made which can limit the accuracy of predicted displacements in such complex tissues. Noble et al. utilised virtual histology from IVUS scans to create 3D FE models of human diseased cadaveric femoral arteries [81]. An inverse FE method was then used to minimise the difference between minimum and maximum diameters. This pipeline can be transferred clinically to obtain patient-specific data. More recently, Narayanan et al. developed a robust iFEM to obtain multiple patient specific parameters from 3D reconstructed atherosclerotic geometry [17]. An interface matching method was developed to capture the micro morphology of the plaque. A 3D FE model was generated using a smooth fit surface contour method whereby the plaque components were delineated using a deep learning method algorithm of OCT images. The error function was defined by the Euclidean distance between the node sets of the deformed and target geometries, see Figure 2.40. A multi-objective optimisation algorithm was then defined by implementing the error functions of each component interface and a multi-step optimisation process was used in order to limit the existence of multiple local minima. This inverse method proved to be efficient and robust.

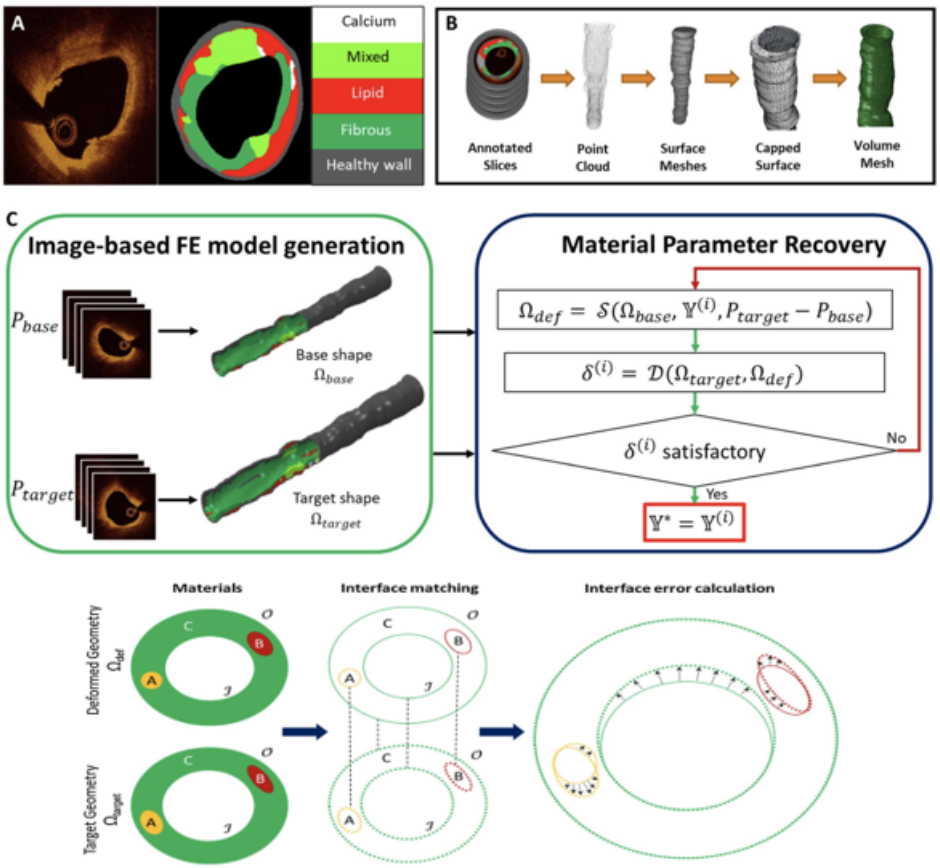

Figure 2.40: iFEM approach and simplified interface matching method schematic taken from [178].

Overall, iFEM allow the recovery of material properties of tested tissue with the

possibility to be used clinically.

2.7 Literature review summary

As highlighted in this review, numerous studies have examined the behaviour of atherosclerotic tissue to better understand its rupture potential. Mechanical testing is often performed to extract mechanical properties through different methods: indentation tests [153], [154], uniaxial tensile testing [156] and inflation testing which allows for the multi axial analysis of mechanical properties of vessels [16], [157], [158]. The advances in computational methods have permitted geometrical parameters to be determined for better risk assessment of plaques. Hence, Finet et al. demonstrated, by means of 2D finite element models, that plaque cap thicknesses less than 60 μm were indicators of plaque instability. Additionally, 3D models have been developed to account for out of plane stresses and strains [172], [173]. Inverse finite element methods consist in the direct comparison of experimental and computational results to infer mechanical properties of tissue [16], [17], [178]. Many studies have taken advantage of US imaging to assess plaque mechanical properties [16], [17] and to demonstrate the efficacy of combining US parameters to identify vulnerable plaques [18]. Depending on the imaging technique, plaque characteristics can be inferred with more or less accuracy with MRI being the gold standard to accurately delineate plaque components [14]. US, however, is the commonly used imaging protocol during clinical routine assessment of patients with carotid artery disease. Novel US modalities such as elastography and CEUS enable tissue stiffness and angiogenesis to be determined respectively. However, the integration of neovascularisation imaging into plaque risk assessment remains limited. Studies have demonstrated the efficacy of US-based mechanical characterisation in identifying vulnerable plaques, but few have investigated the role of neovessels in altering plaque mechanical integrity. There thus remains a clear need for a non-invasive imaging technique which can characterise vascular tissue, both in disease diagnosis and treatment monitoring.

Chapter 3

Simulating Atherosclerotic Plaque Mechanics using Polyvinyl Alcohol (PVA) Cryogel Artery Phantoms, Ultrasound Imaging and Inverse Finite Element Analysis

---

3.1 Introduction

Several studies have carried out uniaxial and bi-axial tensile testing to understand the mechanical properties of intact plaques and components of the plaque [19], [20], [179]–[182]. However, these techniques fail to adequately reproduce *in vivo* loading conditions. To avoid these limitations, accurately replicate these conditions and allow for valuable insights into plaques' mechanical behaviour, inflation testing can be carried out [16], [17], [81], [157]. Boekhoven et al. carried out inflation testing on intact carotid endarterectomy samples collected from surgeries [157]. The challenge lies in the fact that carotid plaque specimens obtained from CEA procedures are often fragmented or cut longitudinally depending on the surgical approach, rendering pressurisation highly challenging if not impossible [157]. To this extent, the use of phantoms as vessel surrogates have many advantages: i) circumventing limited plaque tissue accessibility or availability, ii) enabling the testing of rupture mechanisms by offering complete control over material properties and heterogeneity [138], and iii) allowing for validation of computational modelling approaches. One material of particular interest is PVA. PVA has been widely used as a tissue mimicking material due to its ability to polymerise

and stiffen when subjected to subsequent FTCs [140]. Additionally, it possesses similar acoustic properties to arterial tissue which is of great benefit for studies involving US imaging [137]. Many studies have sought to investigate the use of PVA to mimic atherosclerotic plaque features [142]–[144], [146]. Pazos et al. used IVUS to image mock carotid arteries made with a double layered PVA wall and lipid inclusions [149]. Widman et al. characterised hard and soft carotid plaque PVA-based surrogate models through SWE and mechanical testing [100]. Additionally, Hansen et al. developed a two-layered vessel-mimicking phantom with a stiff outer layer and a softer inner layer to simulate vessels with soft plaques and the presence of lipid pool, shoulders of cap and centre of fibrous cap, using US-based strain imaging to assess mechanical properties under pulsatile pressure [151]. However, few studies have combined inflation testing of diseased vessel surrogates with non-invasive US imaging and computational modelling.

The importance of using iFEM in our research lies in its ability for accurate material property estimations via physiologically relevant simulations, essential for comprehending the mechanical behaviour of diseased tissue surrogates. While experimental methods such as ring tensile testing and inflation testing provide valuable data on global deformation, they do not allow for the estimation of internal stress and strain distributions within complex geometries. FE and iFEM address this limitation by integrating experimental data with computational modelling, enabling the recovery of material parameters and the simulation of internal mechanical fields under physiologically relevant conditions. This combined approach enhances the understanding of how different plaque features, such as lipid pools or varying degrees of stenosis, influence local stress concentrations, and ultimately, plaque vulnerability. Thus, in this study, we explore the pipeline presented by Narayanan et al., where an iFEM was used to obtain multiple patient specific parameters from OCT reconstructed atherosclerotic geometries based on an interface matching method [183]. While they established the foundational framework, our study advances this by adapting the iFEM to artery-mimicking phantoms with lipid inclusion. We integrate this methodology into an automated iFEM using iSight, enabling efficient iterative parameter estimation. The purpose of our study is to investigate the potential of PVA phantoms as diseased vessel substitutes using a combination of mechanical characterisation from ring tensile testing and under pressure loading conditions, US imaging, and computational modelling. Through this study, both experimental and computational approaches can provide invaluable insights into the mechanical behaviour of diseased vessels with the help of vessel surrogates and in turn can help better determine rupture risk from non-invasive US imaging.

This study is innovative as it combines the following key areas:

1. Creation of complex arterial phantoms: design and fabrication of phantoms with two layers and a lipid inclusion to more accurately mimic stenosed arteries.

2. Controlled inflation with US imaging: implementation of a controlled inflation pro-

cess to simulate physiological conditions, acquiring realistic deformation captured by non-invasive US imaging.

3. Inverse finite element analysis with iSIGHT: application of a boundary-matching-based iFEM adapted for complex phantoms and lipid inclusions using iSIGHT to streamline iterative parameter estimation.

The study workflow is presented in Figure 3.1

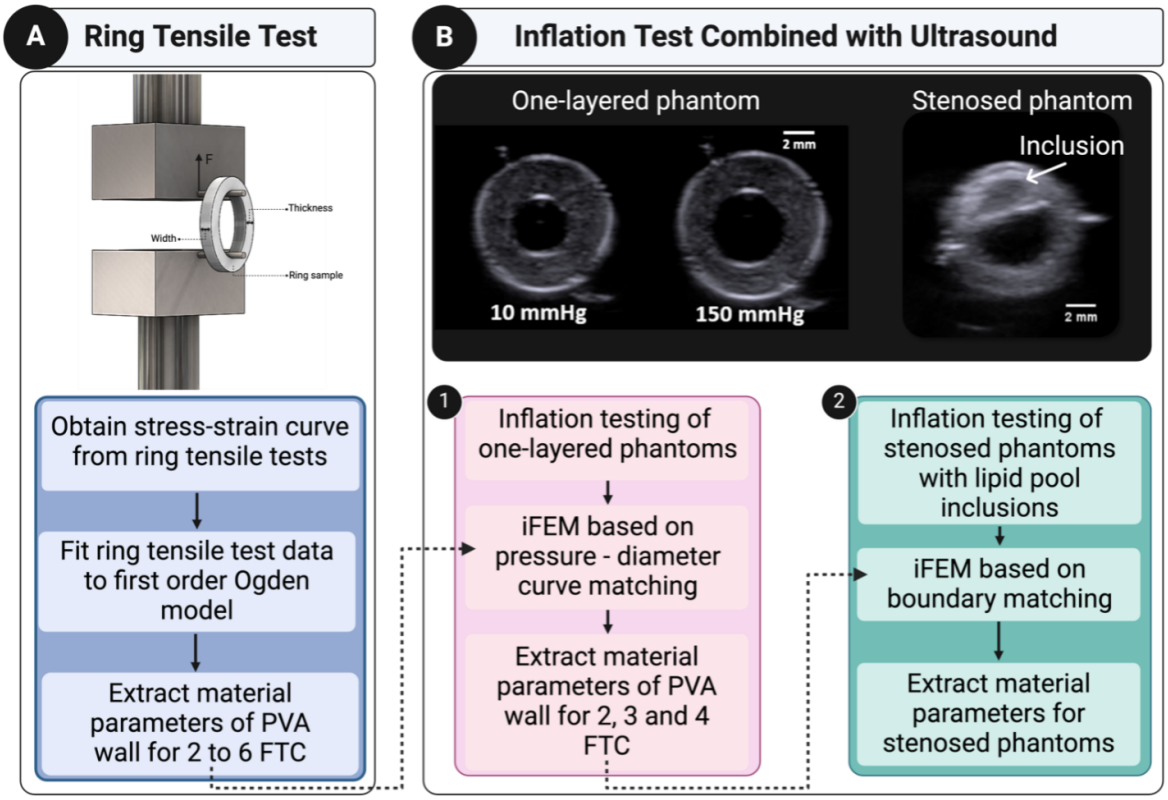

Figure 3.1: Study Workflow. Dashed arrows indicate parameters used as initial guesses for the iFEM. (A) Schematic of the ring tensile test setup and steps to extract PVA material parameters for 2 to 6 FTC. (B) Inflation test combined with US: workflow includes inflation testing, iFEM analysis for pressure-diameter curve matching (one-layered phantoms), and boundary matching (stenosed phantoms) to extract relevant material parameters.

A secondary aim of this study is to develop a comprehensive workflow for the inflation and non-invasive US imaging of fresh human atherosclerotic plaques. This pipeline allows for precise control of inflation conditions while simultaneously capturing US data.

3.2 Materials and methods

It is important to note that the design of the phantoms and the inflation testing of stenosed phantoms were initially developed as part of an MSc thesis project. Under my supervision, the MSc student designed and fabricated the phantom geometries and carried out inflation experiments on stenosed models.

3.2.1 PVA phantom creation

An adaptation of a protocol described in the literature was used where a 10% weight/volume (w/v) PVA solution was created with aluminum oxide (<50 nm particle size) as a scatterer [184]. Briefly, PVA powder, aluminium oxide powder, glycerol, and deionised water were mixed and heated to 80-85°C for an hour until a homogeneous solution was obtained. The mixture was then cooled down to 10°C to limit sedimentation of the aluminium oxide particles during the first thermal cycle. Finally, the solution was injected into 3D printed moulds made from polylactic acid. The geometric design of these moulds is described in the next section, see Figure 3.2. The moulds were maintained at room temperature for an hour to let any air bubbles rise to the surface as any air stuck within the phantom creates artefacts under US imaging. The phantoms then underwent between two and six FTCs. One FTC consists of a controlled freezing phase at -1°C/minute to -15ºC for 14 hours and controlled thawing phase at room temperature for 10 hours. See Appendix A, Figure A.1 for detailed process of the phantom creation.

3.2.2 Geometric designs

The phantoms' moulds were designed using SOLIDWORKS® 3D mechanical CAD software (version 2018, Dassault Systems, S.A., Suresnes, France), see Figure 3.2. One-layered phantoms were created using a two-piece hollow cylinder (outer diameter = 9 mm) and a tubular insert (outer diameter = 3.6 mm). One-layer phantoms were designed with a thickness of approximately 2.7 mm, which is greater than the typical healthy carotid vessel thickness of around 1 mm. The increased thickness was selected to meet several experimental requirements. This design choice enhances the structural integrity of the phantoms, ensuring they can withstand the intraluminal pressure applied during testing without breaking. Additionally, thicker phantoms provide a more robust sample for imaging and experimental techniques, reducing the risk of damage during handling and testing. To create bi-layer phantoms, moulds were designed using a two-piece hollow cylinder (final outer diameter = 9 mm) and an inserted tube (outer diameter = 6 mm). The empty space was filled with the 10 % w/v PVA solution and

sealed. A second mould with an inner diameter of 7.5 mm was then placed in the larger diameter mould and another layer injected resulting in two layers each having a wall thickness of 0.75 mm. The bilayer design was chosen to mimic the arterial wall's structural properties, representing the intimal thickening-media complex. The inner layer underwent six FTCs to simulate increased stiffness with intimal thickening associated with atherosclerosis [23], [185]. The outer layer represents the media layer. The bi-layered models underwent physical cross-linking (via FTCs) so that the inner layer would be stiffer (six FTCs) than the outer layer (four FTCs). Figure 3.2 shows the core mould design, see Figure 3.2(A) alongside different stenosis percentages on the inserted cylinders, see Figure 3.2(B). Mock vessels with different percent stenoses were created with concave inserted tubes allowing for lumens featuring protrusions of different sizes, 0%, 25%, 50%, 75% stenosis.

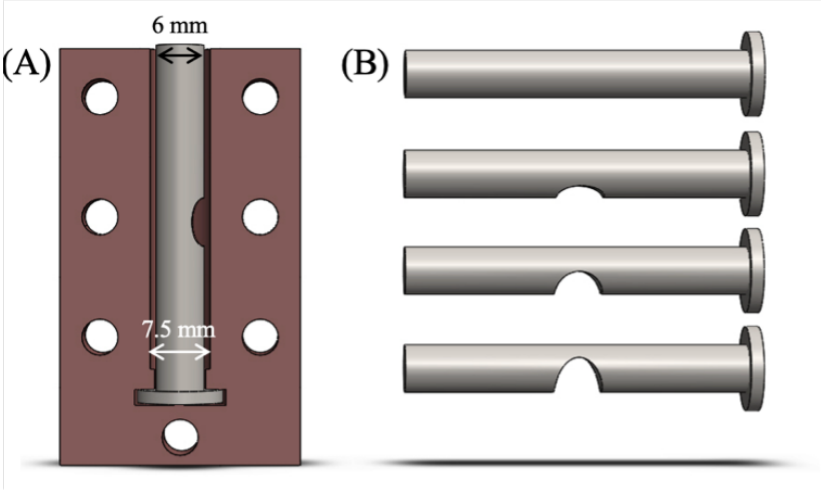

Figure 3.2: (A) Design of the first mould for bi-layered phantom and (B) inner lumen with 0%, 25%, 50%, 75% stenosis (from top to bottom).

3.2.3 Creation of lipid-pool like inclusions

To include a lipid pool-like component (mayonnaise) within the stenoses, an empty space was created within the wall of the phantom. The empty space was created by placing dissolvable 0.4 mm thick PVA fragments - initially used as support to print complex geometries and printed using an Ultimaker 3 (Ultimaker BV, the Netherlands) - in the first layer of the bi-layered phantoms. This layer was placed in water until complete dissolution of the PVA fragments prior to a lipid pool-like substance being injected into the designated space [186]. The addition of the second layer then covered the first layer as well as the lipid pool inclusion. Lipid regions were included in the phantoms to replicate the heterogeneous nature of atherosclerotic plaques, which often present with lipid-rich necrotic cores in a more advanced stage. The carotid plaque-RADS system by Saba et al. highlights that these cores indicate a higher RADS score.

By incorporating lipid pools, our phantoms aim to emulate these high-risk plaques [23].

3.2.4 Ring tensile test

Ring tensile tests of PVA vessel phantoms were performed for each FTC going from two to six FTCs. The phantoms were made with a nominal mould thickness of 1.0 mm (outer diameter is 7 mm) to have an adequate ratio of the ring thickness to pin radius [187]. Mechanical testing was performed at room temperature for each FTC (i.e., two to six FTC with 10% PVA solution). Each tubular PVA was cut into 2-mm rings using a custom 3D-printed microtome blade cutter. The samples were then measured for their thickness and length using a Vernier caliper. Three random points of the sample were measured to obtain a mean thickness and length. The samples were submerged in 10% glycerol solution using a transfer pipette before loading on the pins to avoid dehydration. Samples were stretched with a Zwick Roell Z2.5 machine (Zwick Roell Group, Ulm, Germany) with a 20N load cell. The rings were placed in the middle of a custom-made test gauge with a pin radius of 0.5 mm. Samples were set to pre-load of 0.05 N at a speed of 5.0 mm/min. The samples were then pre-conditioned for 5 cycles to 10% strain at a speed of 60% Lo/min with Lo the initial gauge length. The ring samples were stretched until failure with the same speed of the pre-conditioning cycles [188]. The stress-strain curves obtained from the ring tensile test [189] were used as input to calibrate the material model described in Section 3.2.6 using the Hyperfit software (`http://www.hyperfit.wz.cz/`). The fitting was performed on a representative sample for each FTC. Additionally, we used MATLAB's polyfit function to perform linear regression on the initial stress-strain data (up to a strain of 0.2) to calculate the tangent elastic modulus by fitting it to a straight line. The mean elastic modulus of each FTC was thus obtained. The ring tensile test offers essential foundational insights into mechanical behaviour, providing a strong basis for initial parameter estimation and setup in the iFEM framework. Although exact parameter matches between ring and inflation tests are not expected - owing to differences in boundary conditions, coupling effects, and deformation modes - the approach remains clinically relevant. This is especially significant in cases where initial parameters are unknown *in vivo*, supporting its utility as a translational tool for clinical applications.

3.2.5 Combined inflation testing and ultrasound imaging

Figure 3.3 illustrates the inflation testing rig developed to incorporate US imaging. Drawings of the inflation rig are outlined in Appendix A, Figure A.2. US scans were acquired using the SIEMENS ACUSON S2000™ ultrasound system. A 9L4 linear array probe was used with a frequency at 9 MHz to acquire scans. The probe was positioned above the water bath and can be rotated to either obtain cross-sectional or

longitudinal views of the phantom. Pressure inflation tests were carried out using a PID controlled PHD Ultra 703007 Syringe Pump (Harvard Apparatus, Holliston, MA, USA) and pressure was monitored with a fibre optic pressure sensor FOP-M260 pressure probe (FISO, Quebec, QC, Canada). The PVA phantoms were axially stretched (10%) and pressurised from 0 to 150 mmHg, in 10 mmHg increments. US B-mode scans were acquired at each pressure step (see Appendix A, Table A.1 for acquisition parameters). During pressurisation, no buckling was observed in the phantoms. Overall, three one-layered phantoms (n=1 for each FTC (two to four FTC)) and 12 bi-layered stenosed phantoms (n=3 for each stenosis percentage, 0-75%) were successfully tested and imaged.

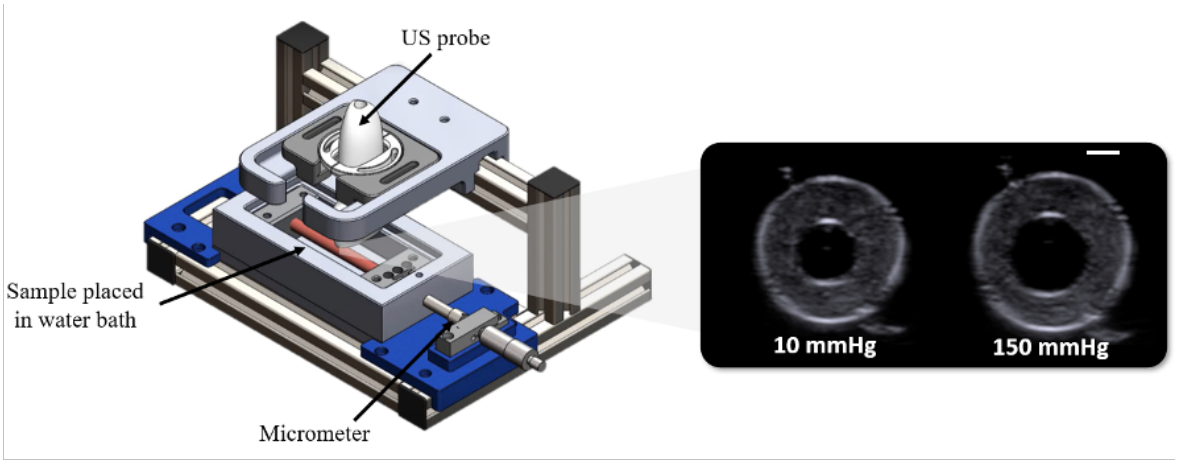

Figure 3.3: Inflation testing rig setup for US imaging of phantoms: the left part of the figure shows the experimental setup, where a sample is placed in a water bath. A micrometer is used for axial stretching of the sample. An US probe is positioned above the sample to capture B-mode scans. The right part of the figure displays US images of the sample at two different pressures, 10 mmHg and 150 mmHg, demonstrating how the sample expands under intraluminal pressure. Scale bar: 2 mm.

3.2.6 Constitutive modelling

PVA is a hydrogel capable of undergoing large deformations and exhibiting non-linear stress-strain behaviour [150]. Several studies have investigated different material models to characterise the mechanical behaviour of PVA [150], [190]. In this study, we used a first order Ogden model (stretch-based). The Ogden model is expressed as followed:

$$U_{\text{Ogden}} = \sum_{i=1}^{N} \frac{2\mu_i}{\alpha_i^2} \left(\lambda_1^{\alpha_i} + \lambda_2^{\alpha_i} + \lambda_3^{\alpha_i} - 3\right) \tag{3.1}$$

where μ_i (shear modulus) and α_i (dimensionless) are material parameters and λ_1, λ_2 and λ_3 are the principal stretches. The principal stretches λ_1, λ_2 and λ_3 define the material deformation in different directions, while the parameters μ_i and α_i are specific to the material's mechanical properties. For N=1, we thus have the following

parameters: μ_1, the shear modulus, represents the initial stiffness of the material and dictates how resistant the material is to shear deformations at small strains. The parameter α_1 is a dimensionless parameter and governs the nonlinearity of the material response. A higher value of α_1 indicates a more pronounced nonlinearity in the stress-strain relationship.

3.2.7 Inverse finite element framework

Diameter matching for one-layered phantoms

FE models of the phantoms were created to model the inflation of the one-layered phantoms (n=3) in ABAQUS (Dassault Systemes, 2017) for the 2, 3 and 4 FTC. The models were set to simulate the setup of the experiments and to represent the 3D geometry of the PVA sample. Fixed boundaries were applied in the U1 (radial) and U2 (circumferential) directions and U3 (axial) on both ends of the sample to replicate the physical constraints of the experimental setup. An intraluminal pressure load was applied on the inner surface of the model for each pressure step. The model used a mesh with 17500 elements to ensure accurate results without excessively high computational costs. The simulations were conducted using ABAQUS/STANDARD, ensuring convergence and stability of the solutions. See Appendix A Figure A.3 for convergence studies for mesh choices. Hybrid 8-node brick elements with reduced integration (C3D8HR), chosen due to the assumption of material incompressibility, were used to mesh the geometries. The goal of this inverse FE methodology is to determine the optimal material parameters, namely μ_1 and α_1, by matching the experimental and computational pressure diameter curves. Initial guesses were obtained from the corresponding FTC ring test parameters. The objective function ϕ minimised the sum of squared difference (SSD) between the experimental and computational diameters, where the shear modulus μ_1 and α_1 were the optimised parameters, as follows:

$$\phi = \text{Minimise} \sum_{i=1}^{n} (x_i - \hat{x}) \tag{3.2}$$

where n is the number of data points, x_i are the observed experimental diameter values and $\hat{x}$ the observed computational diameter values. The optimisation technique followed a Hookes-Jeeves direct search method, and the optimal solution was reached after 50 iterations. This inverse FE methodology was implemented in iSIGHT 5.9 (Dassault Systèmes Simulia corporations, Vèlizy-Villacoublay, France). Briefly, the output coordinates from a created node set on the inner lumen of the phantom model are retrieved from ABAQUS. Experimental and computational pressure-diameter curves can then be plotted in the "Data Matching" component in which the comparison metric, the sum of squared difference (SSD) is defined and used in our optimisation procedure.

Boundary matching for stenosed phantoms

After data acquisition, an open-source toolbox, namely Ultrasound Research Interface Offline Processing Tools (URI-OPT), was used to read in the beamformed RF data as a matrix for each frame acquired [191]. The outer, inner lumen and lipid pool were segmented in a two-step process using an in-house MATLAB (The Mathworks Inc., Natick, MA) code. Firstly, a freehand tool was used to define the initial region of interest for each delineation. The latter was then used as an input for an active contour segmentation algorithm. Due to the inherent scattered nature of the US images, the outlines output from the active contour function were irregular. A smoothing step was thus needed and was performed by importing the boundary coordinates in SOLIDWORKS® (version 2018, Dassault Systems, S.A., Suresnes, France). Using the curve wizard tool, the contours were smoothed and exported as an .igs file. A sketch was then created in ABAQUS (Dassault Systemes, 2017) to define a 2D cross-section of the PVA phantom. The nodal coordinates of the boundaries of interest (i.e., inner, outer lumen and lipid pool) were exported in an Excel file and read into a MATLAB (The Mathworks Inc., Natick, MA) code to obtain the final smoothed region of interest. For more complex cross-sectional geometries, a boundary matching inverse approach was proposed following the framework presented in [183]. Briefly, if we name the target geometry g_{target}, at intraluminal pressure P_{final} and the optimised geometry g_{Opt} with an intraluminal pressure $\Delta P = P_{\text{final}} - P_{\text{initial}}$, the objective was to determine optimised parameters that will allow for the boundaries of g_{Opt} to match the ones of the target geometry g_{target}. As shown in Figure 3.4, the aim was to match boundaries of the optimised pressurised geometry to the target geometry contours. We modelled the 2D cross sections of the phantom's wall as first order Ogden models where $\mu_{1\text{wall}}$, $\alpha_{1\text{wall}}$ are the parameters to be optimised. Initial material parameters of the wall were taken from the one layered 4 FTC phantom optimised parameters. Additionally, the lipid pool was defined with a Neo-Hookean model with an initial guess of C_{10} of 1 kPa [192]. See Appendix Table A.2 for boundary matching iFEM initial parameters. Plane strain hybrid elements (CPE4H) were used for the finite element simulations. A coupling constraint was applied between a reference point selected in the inner lumen of the phantom cross section and the inner lumen contour. A boundary condition on the reference point was then applied, constraining U1, U2, and UR3. A pressure load was applied on the inner contour surface. The model used a mesh with 1500 elements. The simulations were also conducted using ABAQUS/STANDARD. An inverse FE algorithm was implemented to adjust the parameters to the inflation testing data using ISIGHT 5.9 (Dassault Systèmes Simulia corporations, Vèlizy-Villacoublay, France). A Python code was developed to calculate the sum of the minimal Euclidean distance between the nodal coordinates of the respective boundaries of the optimised $x_{\text{opt}_k}, y_{\text{opt}_k}$ and target

geometry $x_{\text{target}_k}, y_{\text{target}_k}$. The final error ϵ to be minimised was defined as follows:

$$\epsilon = \sum_{i=1}^{N_{\text{boundaries}}} \frac{1}{N_{\text{target}_i}} \sum_{j=1}^{N_{\text{target}_i}} \min_{k \in \{1,\ldots,N_{\text{optimised}_i}\}} \sqrt{(x_{\text{target}_k} - x_{\text{opt}_k})^2 + (y_{\text{target}_k} - y_{\text{opt}_k})^2} \tag{3.3}$$

Where $N_{\text{boundaries}}$ is the number of boundaries to be matched, N_{target_i} is the number of nodes in the target geometry of the interface i, and $N_{\text{optimised}_i}$ is the number of nodes on the optimised geometry of the interface i. Figure 3.4 shows the iSight workflow. Briefly, an input file is read into the "Abaqus component" where the material parameters to be optimised are selected. Material parameters from the inflation test calibration were used as initial guesses. The in-house Python script was run in Abaqus where the .odb file was taken as the input to calculate the error and write it to a text file. This text file was then read in the "Data Exchanger" component to create the error variable. Finally, the error minimisation was carried out in the "Optimisation" component where a Hookes-Jeeves algorithm was used to identify optimal parameters. We estimated parameter uncertainty by identifying regions with minimal gradients in error values within the optimisation procedure and selecting parameter sets within 5% of the minimum error for each sample. This approach allowed us to focus on stable regions around the optimal solution. For each stenosis level, we then computed the mean and standard deviation (SD) of the key parameters to quantify the expected spread.

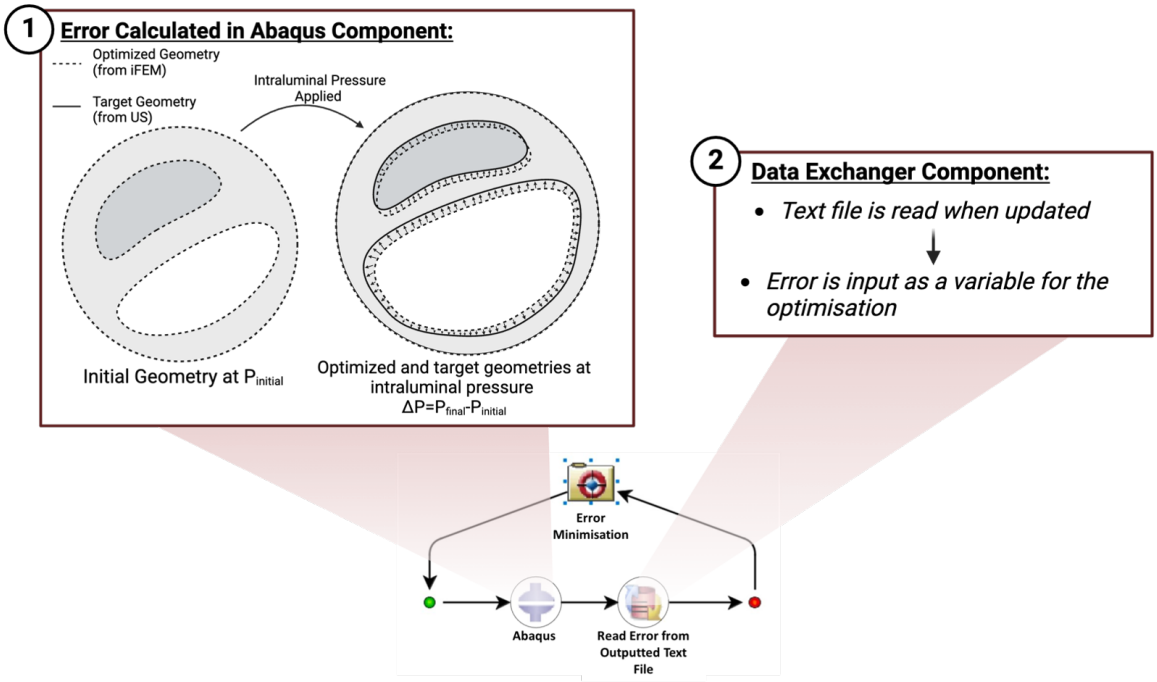

Figure 3.4: iSight iFEM framework: this involves simulations using Abaqus, reading error from output files, and refining parameters to achieve the best fit. 1. Error calculation in Abaqus: cross-sectional schematics of optimised geometry (from iFEM) and target geometry (from US). 2. Error reading used as input for the optimisation.

3.2.8 Statistical analysis

Statistical analysis was performed with Prism 6 statistical software (GraphPad Software Inc., San Diego, California). All data were tested for normality using Shapiro-Wilk normality tests and equality of group variances using Brown-Forsythe ANOVAs. All data in this study passed normality tests. In the case of unequal group variances, Brown-Forsythe and Welch ANOVAs with Dunnet's T3 multiple comparison tests were used, otherwise ordinary one-way ANOVAs with Tukey's multiple comparison were used. For the pressure-diameter experimental data, a one-way ANOVA was performed to investigate statistical significance (i.e., $p < 0.05$) between each of the tested stenosed phantom groups (0%, 25%, 50%, 75%).

3.3 Results

A comprehensive summary of the mechanical testing and iFEM analyses results is provided in Appendix Table A.4 and Table A.5.

3.3.1 Ring tensile test

Stress-strain curves from the ring tensile tests of each FTC group show strain stiffening behaviour typical of arterial tissue, specifically when the number of FTC increases, see

Figure 3.5(A). Looking at the mechanical data of all 35 rings tested between 2 and 6 FTC, stiffening and strengthening is observed with increased numbers of FTCs. This is further shown in Figure 3.5(B) where the ultimate tensile (UT) stress of the 2 FTC group (0.14 ± 0.03 MPa) is significantly lower than the 3 FTC (0.33 ± 0.03 MPa) and 6 FTC (0.86 ± 0.27 MPa) groups. Groups 4 FTC (0.49 ± 0.32 MPa) and 5 FTC (0.49 ± 0.32 MPa) did not show any significant difference compared to the other groups. Figure 3.5(C) shows a similar trend where an increase in the number of FTCs leads to higher UT strain values. The 2 FTC group had a significantly lower UT strain (0.44 ± 0.09) compared to the 3 FTC (0.68 ± 0.09), 5 FTC (0.77 ± 0.22), and 6 FTC (0.93 ± 0.18) groups. No statistically significant difference between the 4 FTC (0.76 ± 0.34) group and the other sample groupings was observed.

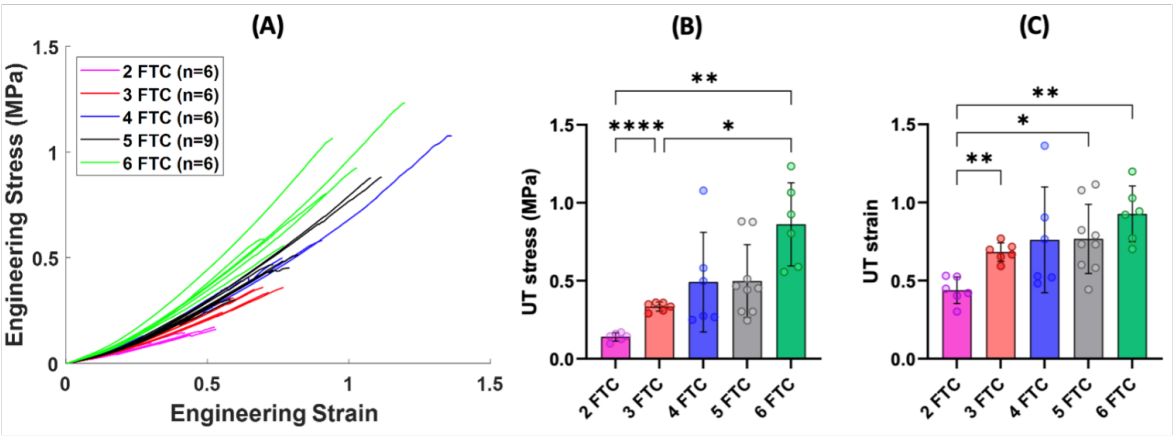

Figure 3.5: Stress-strain curves for n=35 rings, colour coded by their respective groupings. (B) UT stress: significance determined by Brown-Forsythe and Welch ANOVA with Dunnett's T3 post hoc multiple comparisons, 2 FTC and 3 FTC ****p<0.0001, 2 FTC and 6 FTC **p=0.0083, 3 FTC and 6 FTC *p=0.0317. (C) UT strain: significance determined by Brown-Forsythe and Welch ANOVA with Dunnett's T3 post hoc multiple comparisons, 2 FTC and 3 FTC **p=0.0001, 2 FTC and 5 FTC *p=0.0177, 2 FTC and 6 FTC **p=0.0042.

Table 3.1 shows the average elastic modulus of the 2, 3, 4, 5, and 6 FTCs to be equal to 331 ± 21, 510 ± 43, 630 ± 110, 662 ± 110, and 957 ± 147 kPa, respectively. Fig. 3.6 illustrates the fitted 1-term Ogden model to the experimental data of a representative sample for 4 FTCs with high goodness of fit.

Mean elastic modulus					
	2 FTC	3 FTC	4 FTC	5 FTC	6 FTC
E (kPa) ± SD	331 ± 21	510 ± 43	630 ± 110	662 ± 110	957 ± 147

Table 3.1: Elastic modulus of ring test (Mean ± SD) of each FTC.

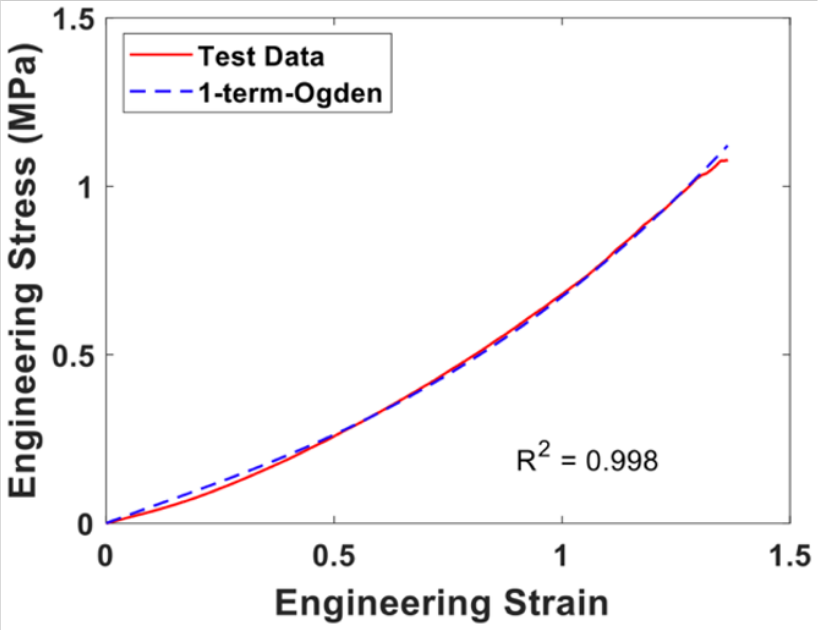

Figure 3.6: First order Ogden model fitted to the stress-strain curve of a 4 FTC ring sample.

The results of the fitted models for each FTC are depicted in more detail in Table 3.2, with a shear modulus μ_1 ranging from 90 kPa to 235 kPa for 2 to 6 FTCs. The α_1 value did not vary much between FTCs, ranging from 4.0 to 4.8.

First-order Ogden constitutive parameters					
	2 FTC	3 FTC	4 FTC	5 FTC	6 FTC
μ_1 (kPa)	90	122	171	188	235
α_1	4.8	4.8	4.0	4.1	4.1
r^2	0.998	0.995	0.998	0.995	0.997

Table 3.2: Estimated material parameters of the PVA ring tests for the first order Ogden constitutive models with the coefficient of determination (r^2) for each sample.

3.3.2 Inflation of bi-layered phantoms

Bi-layered stenosed phantoms featuring lipid-pool-like inclusions were successfully inflated and imaged using US from 0 to 150 mmHg, see Figure 3.7. The hypoechoic (dark grey areas indicated by the white arrows in Figure 3.7) reveal the presence of the lipid-like content in the occluded regions. The red dashed circles indicate regions known as the plaque "shoulders." It is interesting to qualitatively note that a higher displacement was observed at the shoulders compared to the rest of the phantom wall, further quantified in Figure 3.11. Additionally, the sagittal cut-plane of the 50% stenosis phantom in Figure 3.7 shows a longitudinal view of the phantom, highlighting the internal structure of the stenosis with the lipid inclusion.

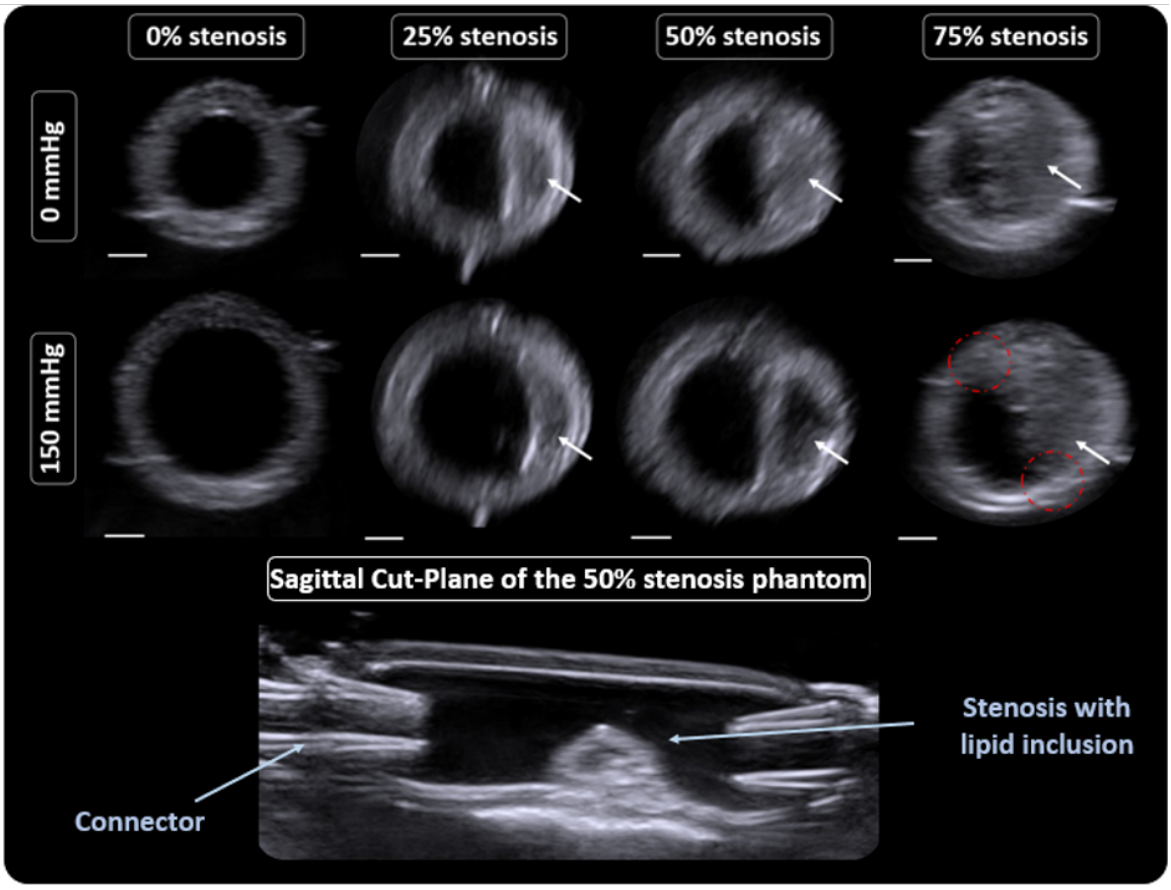

Figure 3.7: B-mode US images of PVA phantoms with varying degrees of stenosis (0%, 25%, 50%, and 75%), captured with a depth of 3 cm and a frequency of 9.0 MHz. A rubber mat was placed under the samples for sound absorption to minimise extraneous noise. White arrows indicate the lipid pool inclusions in the cross-sectional views, while red dotted circles highlight the shoulder regions in the 75% stenosis phantom. The bottom image shows a sagittal cut-plane of the 50% stenosis phantom at 120 mmHg, indicating the position of the stenosis with lipid inclusion and the connector to secure the phantom during inflation. Scale bars: 2 mm.

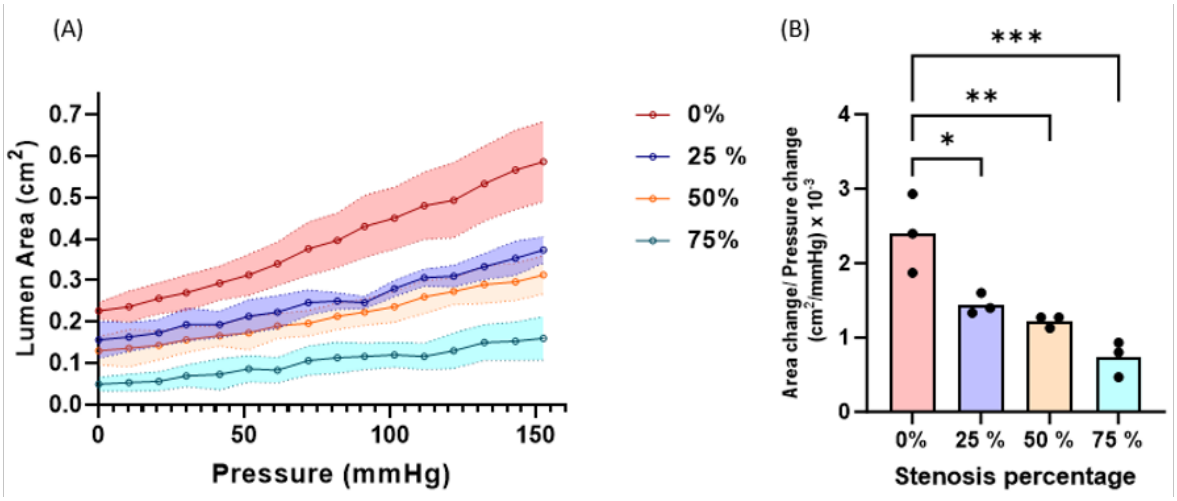

Figure 3.8: (A) Lumen area against pressure curves for 0%, 25%, 50%, and 75% groups, and (B) bar plot of the slope of the curves in (A) for each specimen group. Significance was determined by multiple comparisons one-way ANOVA with Tukey's multiple comparisons test; $^*p < 0.05$, $^{**}p < 0.01$, and $^{***}p < 0.001$.

Lumen area is plotted as a function of pressure in Figure 3.8 (A) as it provides a better representation of the lumen's elliptical shape compared to a single diameter measurement. The solid lines in Figure 3.8(A) represent the mean from $n = 3$ samples at each stenosis level, while the shaded areas represent the standard deviation. Additionally, the slope of the lumen area versus pressure curve (across the total pressure range of 150 mmHg) is given in Figure 3.8(B). The latter shows that the area expansion of the 0% (2.4 ± 0.53 cm^2/mmHg $\times 10^{-3}$) stenosis samples is significantly higher than that of the 25% (1.4 ± 0.14 cm^2/mmHg $\times 10^{-3}$), 50% (1.2 ± 0.08 cm^2/mmHg $\times 10^{-3}$), and 75% (0.73 ± 0.24 cm^2/mmHg $\times 10^{-3}$) groups.

3.3.3 Inverse FE

Diameter matching for one-layered phantoms

Experimental pressure-diameter curves did not exhibit strain stiffening behaviour but rather a near-linear relationship. Optimised material properties of homogeneous PVA phantoms were recovered by matching the experimental and computational pressure-diameter curves of 2, 3, and 4 FTC one-layered phantoms, as illustrated in Figure 3.9. The figure shows good matching of the computational results with the experimental pressure-diameter curves, most notably as the sample gets stiffer—i.e., with increasing numbers of FTCs.

For the 2, 3, and 4 FTCs, the recovered shear moduli μ_1 and α_1 values were: $\mu_1 = 40$ kPa and $\alpha_1 = 6.7$, $\mu_1 = 82$ kPa and $\alpha_1 = 9.7$, $\mu_1 = 191$ kPa and $\alpha_1 = 9.2$, respectively, see Fig. 3.9.

Boundary matching for bi-layered phantoms

The proposed boundary matching framework, based on the approach by Narayanan et al., was used to estimate $\mu_{1\text{wall}}$ and $\alpha_{1\text{wall}}$ for the PVA wall, and the C_{10} parameter for the lipid pool, from the inflation testing data between 80 and 120 mmHg for stenosed phantoms with lipid-pool-like inclusions [183]. The final recovered shear moduli for the PVA ranged between 27 and 53 kPa. In the cases where the lipid was included (i.e., 25% and 50%), the recovered C_{10} values were 0.1 kPa and 0.38 kPa, respectively. The final error ϵ, defined in Section 3.2.7, was minimised for $n = 1$ sample of each stenosis percentage group, i.e., 0%, 25%, 50%, and 75%. It is important to note that the lipid pool could not be delineated for the 75% sample; hence, only two boundaries were matched, namely the inner and outer lumen boundaries. Figure 3.10 illustrates the final minimised error and recovered material parameters of the presented inverse FE methodology for each percent stenosis group.

The 0% stenosis sample, with two boundaries to match, had the lowest final error with a value of 0.28 mm and a percentage of area difference of 1.4%. On the other hand,

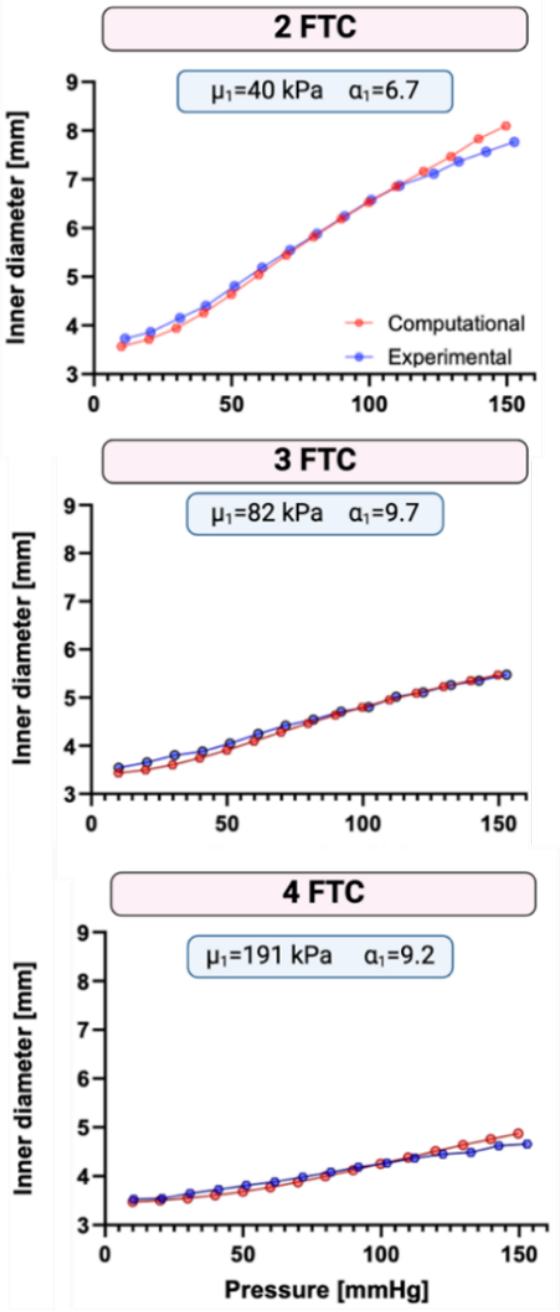

Figure 3.9: Comparison of experimental and computational pressure-diameter curves for homogeneous PVA phantoms with 2, 3, and 4 FTCs. The curves illustrate the increasing stiffness with more FTCs).

the highest error, 0.5 mm (5.7% percentage of area difference), was reached for the 50% stenosis sample with three boundaries matched, including the lipid pool. The 25% and 75% stenosis phantoms, respectively, reached errors of 0.48 mm (2.5% percentage of area difference) and 0.45 mm (2.7% percentage of area difference).

Maximum principal Green Lagrange strain Figure 3.11(A), maximum principal engineering strain Figure 3.11(B) and von Mises stress Figure 3.11(C) contour plots are shown in Figure 3.11 for each stenosis percentage. The presence of the lipid core yields

Percent Stenosis	0%	25%	50%	75%
Optimized geometry boundaries (from iFEM) Target geometry boundaries (from US)	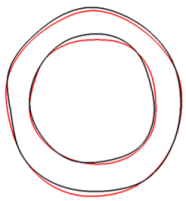	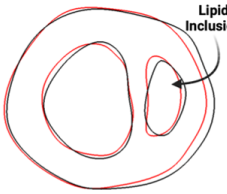	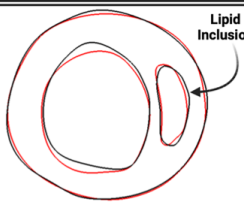	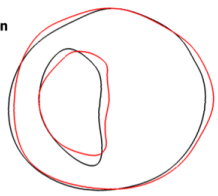
Final Optimization Error	0.28 mm	0.48 mm	0.5 mm	0.45 mm
Percentage of Area Difference	1.4%	2.5%	5.7%	2.7%
PVA wall: Ogden material parameters	μ_{1wall} = 41 kPa α_{1wall} = 1.86	μ_{1wall} = 29 kPa α_{1wall} = 1.39	μ_{1wall} = 53 kPa α_{1wall} = 1.76	μ_{1wall} = 27 kPa α_{1wall} = 3.89
Lipid pool: Neo-Hookean material parameter	NA	C_{10} = 0.1 kPa	C_{10} = 0.38 kPa	NA

Figure 3.10: From top to bottom, contours visualisation of the target (red) and deformed (black) geometries, final errors of the optimisation process, percentage of area differences, PVA wall Ogden optimised material parameters and lipid pool optimised parameters for the 25% and 50% stenosis.

higher strains, as seen in Figure 3.11. This is specifically notable for the 75% stenosis phantom, where a maximum principal in-plane engineering strain of 0.33 is present at the shoulder regions. A maximum von Mises stress was also observed for the 75% stenosis, at the shoulder region, with a peak value of 34 kPa. Panel D shows the evolution of the strain map of the 25% stenosis phantom over increasing pressure levels (from 90 to 120 mmHg), providing a stepwise representation of strain accumulation in physiologically relevant increments.

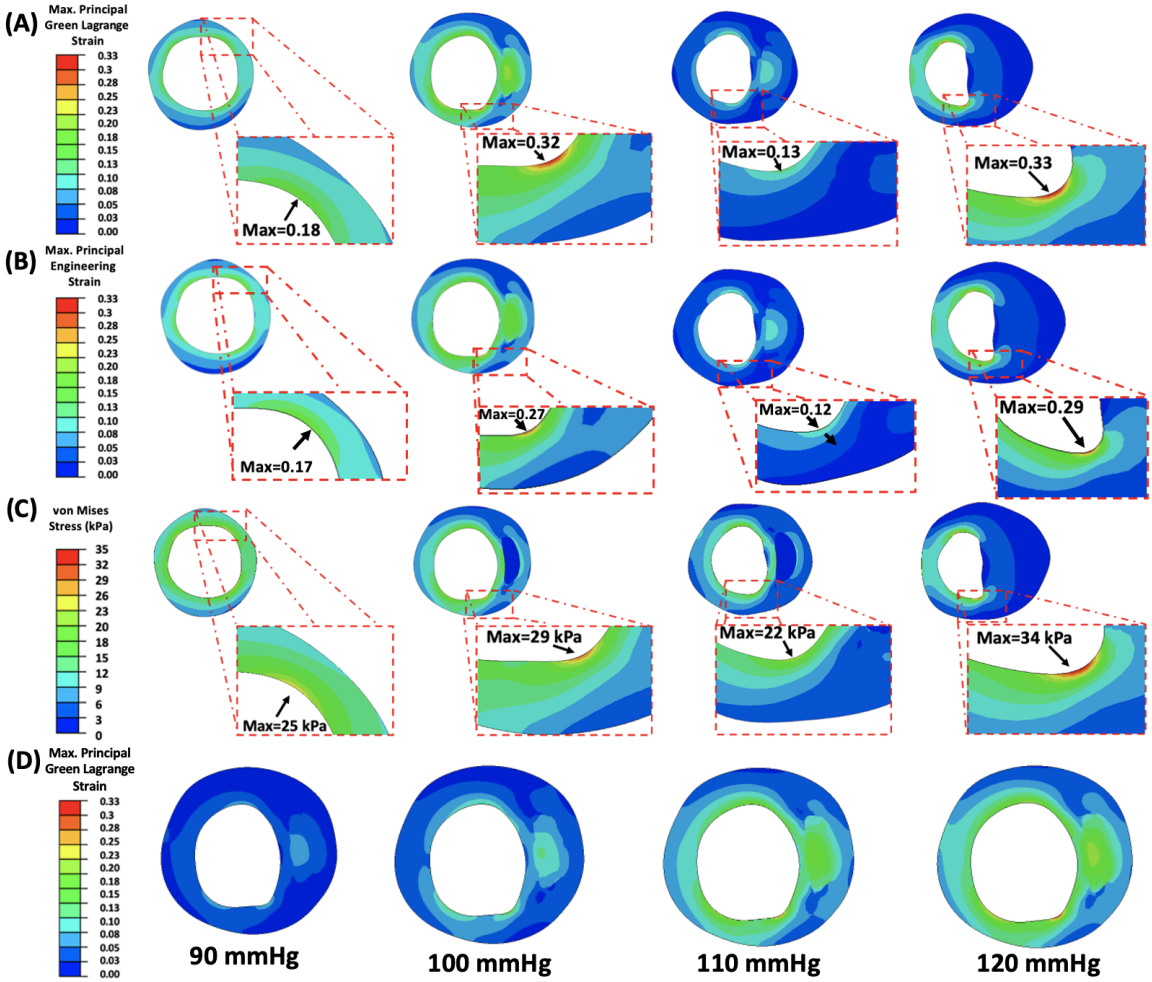

Figure 3.11: Maximum principal Green-Lagrange strain (A), maximum principal engineering strain (B), and von Mises stress (C) contour plots for 0%, 25%, 50%, and 75% stenosis (left to right). Insets highlight regions of peak strain or stress. Panel (D) illustrates the evolution of the maximum principal Green-Lagrange strain with increasing pressure (90–120 mmHg), for the 25% stenosis phantom.

3.4 Discussion

Through a combination of experimental and computational methodologies, this study highlights the potential of PVA phantoms to offer key insights into diseased vessel mechanical behaviours. As illustrated through the results from the ring tensile testing, PVA has tunable material properties; specifically, it stiffens with an increasing number of FTCs with shear moduli ranging between 90 and 235 kPa. In fact, this behaviour has been previously shown in several studies illustrating the cross-linking phenomenon induced by the freeze-thaw process [137], [139], [141]. King et al. performed uniaxial tensile testing and found that the stiffness of 10% wt PVA specimens reaches a plateau after five FTCs with Young's modulus values between 19 and 165 kPa [141]. Comparatively, the averaged values of elastic modulus from the ring test ranged between 331 $\pm$ 21 kPa and 957 $\pm$ 147 kPa, exceeding the higher range documented in the study by

King et al. [141].

A similar levelling trend starting from 4 FTCs was found in Malone et al. who carried out uniaxial tensile tests on dog-bone and vessel-shaped tubular samples [137]. The stress-strain curves from the ring tensile test exhibit a hyperelastic behaviour especially for higher FTCs. Khamdaeng et al. assessed carotid stiffness *in vivo* using an US-based technique in seven healthy volunteers [193]. The reported average moduli before and after the transition point (slope change in stress-strain curve) were equal to 160 ± 40 kPa and 900 ± 250 kPa. Franquet et al. evaluated the elastic modulus of the common carotid *in vivo* using MRI and found a 38% increase between the 'Young healthy subjects' and 'Old diseased patients', with respective values of 315 ± 29 kPa and 509 ± 65 kPa [194]. These values overlap with the elastic moduli found in our study, highlighting the potential for PVA to mimic arterial tissue properties.

A comprehensive study by Fegan et al. reported first-order Ogden and Yeoh constitutive material coefficients for 10% wt PVA/gelatin samples fitted to compression tests [190]. The results in Fegan et al. agree with our findings, revealing that the first Ogden model provided a good fit for the PVA phantoms' stress-strain curves. Moreover, the shear moduli gathered from the ring tensile testing and inflation testing in our study are on a higher range compared to those found in Fegan et al., with values ranging between 22 to 44 kPa. It should be noted that this discrepancy might be due to the fact that values we compare are extracted from different types of mechanical tests [190].

Additionally, the shear moduli extracted from the inflation testing of one-layered phantoms in our study sit well within the range of porcine native tissue. In fact, studies on porcine carotid arteries, using both inflation testing and bi-axial tensile testing, have estimated the shear modulus of porcine carotid arteries to range between 48 – 65 kPa [195], [196], highlighting that PVA subjected to two and three FTCs is a mechanically suitable healthy vessel surrogate.

PVA also holds significant promise when it comes to replicating diseased and atherosclerotic geometries [137]. Tornifoglio et al. uniaxially tested human atherosclerotic plaques yielding a mean elastic modulus of 1260 ± 600 kPa [20]. Plaque caps tested uniaxially by Johnston et al. exhibited a mean stiffness of 50 ± 30 kPa in the axial direction versus 190 ± 70 kPa in the circumferential direction [19]. Davis et al. performed tensile testing on fibrous caps and determined a high strain modulus of 1029.8 ± 795.4 kPa [197]. The elastic modulus values identified in this study align with those reported in existing literature for plaque tissue. However, it is important to note the considerable mechanical variability inherent in such tissue. Therefore, PVA emerges as an optimal material choice for replicating this broad mechanical range via varied concentrations and FTCs [137]. Even if a plateau in stiffness is reached with the number of freeze-thaw cycles (FTCs), increasing the PVA concentration, such as using 15% wt

PVA, can achieve greater stiffnesses [137].

Previous studies have investigated the creation of PVA phantoms with varying degrees of stenosis [144], [146], lipid pool inclusions [142], [143], and hard inclusions [143]. Le Floc'h et al. were the first to create a vessel with a necrotic core or soft inclusion, made from PVA subjected to one FTC [148]. The versatility of PVA also permits the creation of complex geometries to better imitate specific anatomies such as the carotid bifurcation [145]. Many of these studies have looked into the use of those phantoms for flow evaluation and stiffness measurements; however, few focus on their mechanical behaviour [150], [157]. While uniaxial tests have been performed to provide understanding of the mechanical properties of PVA [140], [150], these do not accurately reproduce the multi-axial nature of physiological loadings. Nafo and Al-Mayah carried out uniaxial tests and cavity expansion (pressure with equi-biaxial tension) tests of PVA hydrogel specimens that underwent two FTCs [150]. Three models were used to predict the PVA shear moduli, namely, the Ogden, Yeoh, and Arruda-Boyce models. Nafo and Al-Mayah reported shear moduli ranging between 20 and 26 kPa, values that are below what we obtained for 2 FTC from ring tensile test (90 kPa) and inflation testing (40 kPa).

This work expands on these previous studies by investigating bi-layered phantoms featuring different stenoses and lipid pool inclusions. Fig. 3.7 illustrates the characteristic speckle pattern of arterial tissue successfully reproduced by the PVA phantoms. While differentiating the two layers was not possible, we were able to delineate the lipid inclusion—hypoechoic regions—for the 25% and 50% stenosis samples. Moreover, Figure 3.7 highlights the uniform wall expansion of a 0% stenosis bi-layered phantom, a result very characteristic of a healthy artery. On the other hand, the 75% stenosed sample in Fig. 3.7 shows an inhomogeneous expansion of the vessel wall—with a higher displacement in the "shoulder" regions circled in red. This is further displayed in Figure 3.11, with a peak maximum principal engineering strain of 0.33 in the 75% stenosis sample.

This aligns with findings from [142], who used inflation testing of PVA phantoms mimicking fatty plaques and observed higher strains collocated with the fatty pool, which we can visualise as well for the 25%, 50%, and 75% stenosis samples in Figure 3.7. These observations show great promise and warrant further investigations into the development of surrogates to decipher the mechanical behavior of diseased tissue.

Additionally, pressure-lumen area curves in Figure 3.8 (A) showed that higher stenosis percentage yields decreased area expansion. This was further revealed in Figure 3.8 (B), where the slope of the curve for the 0% stenosed specimen (2.4 ± 0.53 $cm^2/mmHg \times 10^{-3}$) was significantly higher than for all other stenosed groups across the same pressure range. This corroborates with findings in Loizou et al., who found a linear relationship between the percent stenosis in the internal carotid artery and

the percent of carotid distensibility, with a decrease of distensibility when the stenosis percentage increases [198].

To further characterise the stenosed vessel surrogates, this study presents a boundary matching based inverse FE framework. For the 25% and 50% stenosis phantoms - where the lipid was included - the recovered C_{10} values were respectively equal to 0.1 kPa and 0.38 kPa. The latter values are within the range of lipid pool material properties chosen in the literature for inverse FE modelling [192]. This approach demonstrates very good agreement between the boundaries delineated from the inflation test (between 80 and 120 mmHg) and the FE simulations with the highest percentage of area difference of 5.7% for the 50% stenosis phantom, see Fig. 3.10. Through the combined use of inflation testing and US imaging, insightful information on the behavior of these bi-layered stenosed models was thus revealed. It was seen that the highest stenosis percentage leads to the highest strain and stresses at the shoulder regions, Figure 3.11. This aligns with findings in the literature [159], [169], [199]. The stress ranges found in Li et at al. [169], were however on a higher scale than in this study ranging from 161.1 kPa to 694.1 kPa. Soleimani et al. also found that the mean effective, circumferential and first principal stress values increased when the stenosis increased from mild to significant in carotid arteries [200].

Some limitations need to be acknowledged in this study. Firstly, the phantoms have a wall thickness of 2.7 mm, which is thicker than typical human carotid arteries (around 1 mm). This increased thickness was chosen to ensure structural integrity during inflation testing and to facilitate imaging. While this difference was necessary for the experimental setup, future work could aim to reduce the wall thickness of the phantoms to match physiological conditions more closely. While our study primarily focused on straight vessels, replicating the complex geometries of pathological arteries, such as bifurcations, would provide a more relevant model. Although the creation of complex geometries like the carotid bifurcation can be achieved [145], fabricating phantoms with these features is intricate. Despite these complexities, our study provides a foundation for developing more realistic and physiologically relevant arterial models.

Besides, in comparing PVA material parameters from ring testing and the diameter-matching method, notable differences arise. In fact, the ring tensile test, was conducted at a higher strain rate of 5 mm/min compared to the inflation tests which were operated quasi-statically. This is consistent with findings by Sarkar et al., who highlight the impact of testing choices and emphasised by Laterreur et al., who used similar strain rates to compare ring test and burst test results [201], [202]. Additionally, Boekhoven et al, demonstrated that bi-axial and inflation testing resulted in comparable behaviour [196]. This suggest that future material characterisation of PVA could be leaning towards the use of bi-axial tensile testing.

The use of non-invasive US imaging to delineate material boundaries can prove to be

non-trivial. In fact, for the 75% stenosis phantom, manual delineation of the lipid inclusions and wall layers was not possible. The PVA wall was thus considered as a whole for the inverse FE framework with only one shear modulus and α value to be optimised. In Narayanan et al., a deep learning method for OCT images was used to classify the microstructural components in five classes: calcium, mixed, lipid, fibrous and healthy wall [183]. This limitation can however be overcome using US-based imaging techniques such as elastography for instance. Hence, Le Floc'h et al. developed an IVUS based elastography map to accurately detect soft inclusions within PVA phantoms and were able to characterise their Young's moduli [148]. Furthermore, US machines such as the Aixplorer were specifically designed to quantify tissue elasticity of soft and hard regions using shear wave elastography. Widman et al. constructed n=6 PVA based carotid phantoms with soft and hard inclusions [100]. An Aixplorer US machine was used to acquire SWE measurements of the phantoms. The shear moduli yielded from SWE for the soft and hard plaques were respectively 5.8 $\pm$ 0.3 kPa and 106.2 $\pm$ 17.2 kPa. Strain based methods have also proven to be efficient to delineate components. More recently, Latorre et al. introduced a strain gradient-based plaque segmentation framework [203]. This approach was able to delineate the fibrous cap thickness and lipid pool from simulated data with a segmentation index related to the segmentation performance, above 90%. An expanding field, namely photoacoustic imaging, has also shown promising results concerning the discrimination of plaque components. In this regard, Cano et al. used multispectral photoacoustic imaging on plaque PVA phantoms and plaque tissue to accurately decipher plaque components [134].

In this study, we modelled the 1-layer phantoms in 3D to capture their uniform structure effectively. However, for the stenosed 2-layer phantoms, we opted for a 2D approach due to the slice-based nature of the US imaging technique. As demonstrated by Narayanan et al., a full 3D approach could be achieved by reconstructing from multiple 2D slices along the vessel [183]. This approach proves the feasibility of translating our method to more complex models.

Additionally, we did not incorporate anisotropy in our study. A non-linear stress-strain curve would be expected in inflation testing of arteries due to their anisotropy whereas PVA is more homogenous and shows a near linear behaviour in our inflation testing [196]. In fact, melt electrowriting can be used to design fiber arranged patterns to mimic native tissue architecture [204]. Inducing anisotropy in PVA could also be achieved by stretching the PVA hydrogel while it is being cross-linked [205]. Bernal et al. developed anisotropic aortic models and evaluated their shear modulus using a custom-made US probe [206]. They observed an increase in the shear modulus as a function of pressure from 61 kPa to 263 kPa, between 20 mmHg and 150 mmHg for their models. Viscoelastic properties were neglected in this study due to the quasi-static nature of the inflation testing performed.

Another limitation of the iFEM approach is its reliance on pressure data, which may not be directly measurable *in vivo*. However, alternative approaches, such as pressure wires for direct measurements or non-invasive US-based estimation techniques, could allow for the adaptation of the iFEM method to clinical settings [207].

Overall, this study presented a combined mechanical, US imaging, and computational framework. The results indicate the promising potential of PVA as a diseased artery surrogate to yield insights into the mechanical behaviour of vessels with atherosclerosis. Such experimental and computational work combined with non-invasive US imaging can provide a means to better understand why plaques are more prone to rupture and ultimately help improve the clinical management of carotid atherosclerosis.

Chapter 4

A Methodological Framework to Inflate Human Endarterectomy Samples

4.1 Introduction

This chapter builds upon the groundwork laid in Chapter 3, advancing it to the inflation testing of human endarterectomy samples to provide clinically relevant insights into plaque vulnerability. The study introduces a comprehensive inflation testing protocol for fresh human endarterectomy samples, employing in-house made compliant balloons. An intermediate step was performed using native porcine carotid arteries (NPCaAs), enabling validation of the inflation setup on intact, healthy vessels before applying it to complex, diseased tissue. NPCaAs served to evaluate the influence of the balloon-inflation technique proposed, ensuring that the balloon does not alter vessel mechanical behaviour.

While uniaxial and bi-axial tensile testing have provided valuable mechanical insights [19], [20], [197], fewer studies have focused on the inflation of endarterectomy samples under conditions mimicking physiological pressures [157]. Additionally, prior inflation testing has primarily been conducted on plaques within arterial walls of cadaveric specimens [16], [192], a method limited by the availability of samples.

Through inflation testing and US imaging, this study emulates *in vivo* conditions to evaluate carotid plaque behaviour under physiological pressures. This work ultimately paves the way for a more detailed exploration of plaque mechanics and neovascularisation in Chapter 5.

4.2 Material and methods

The presented approach is divided in two parts:

- Sample acquisition and preparation.
- US imaging and inflation testing: this describes a methodology to inflate fresh human atherosclerotic plaques using compliant balloons, the impact of these balloons was assessed on NPCaAs. Each part is described below.

4.2.1 Sample preparation and acquisition

Porcine carotid arteries

NPCaAs (n=6) from 6-month-old healthy white pigs were obtained from a local abattoir. Excess loose connective tissue was removed prior cryopreservation within 3 hours of sacrifice. Samples were then placed in room temperature tissue freezing medium and immediately frozen down at a controlled rate of 1°C/min to -80°C using a Mr. Frosty (Merck). Samples remained at -80°C until *ex vivo* testing. Cryopreservation was used to maintain microstructural integrity of the samples between collection and mechanical testing. On testing day, samples were thawed at 37°C and rinsed with phosphate buffer saline solution (PBS) to remove excess of cryoprotectant.

Endarterectomy samples

Carotid atherosclerotic plaques (n=6) were obtained from symptomatic carotid endarterectomy patients at the Galway Clinic, see Figure 4.1. All patients had a percent stenosis greater than 50%. Ethical approval was obtained from Galway Clinic ethical committee in compliance with the declaration of Helsinki (2016-12 List 47 (4)). Carotid plaques were rinsed in PBS to remove residual blood and cryopreserved as previously reported [20]. After the PBS wash, samples were placed in room temperature tissue freezing medium and immediately frozen down at a controlled rate of 1°C/min to -80°C using a Mr. Frosty™ (Merck).

4.2.2 Ultrasound imaging and inflation testing

A SIEMENS ACUSON S2000™ US machine was used during testing to capture arterial and plaque wall displacement under intraluminal pressure. Either a 9L4 linear array probe (frequency: 9 MHz) or 12L4 linear array probe (frequency: 12 MHz) probe was transversely placed above the tested sample. Pressure inflation testing was carried out using a PID controlled PHD Ultra 703007 Syringe Pump (Harvard Apparatus, Holliston, MA, USA). Pressure levels were monitored using a fibre optic pressure sensor

Figure 4.1: Fresh human carotid endarterectomy samples prepared for inflation testing. Scale bars: 1 cm.

FOP-M260 pressure probe (FISO, Quebec, QC, Canada). For both the plaques and NPCaAs samples, quasi-static pressurisation was carried out in 10 mmHg pressure steps. For each pressure step, a B-mode scan was acquired to obtain cross-sectional views of the samples.

4.2.3 Balloon influence on NPCaA wall expansion

Excised plaques can present with large incisions due to the surgical technique. Thus, plaque samples with lacerations were first sutured closed to facilitate the pressurisation procedure. To measure reproducibility of the balloons creation, the thicknesses of n=4 balloons were assessed using a Mitutoyo Litematic VL-50B high accuracy measuring unit, with n=5 measurements taken for each balloon. To then allow for a watertight inflation, highly deformable balloons were created using a liquid latex:water solution (3:2) that was dip moulded on stainless steel rods as presented in Figure 4.2.

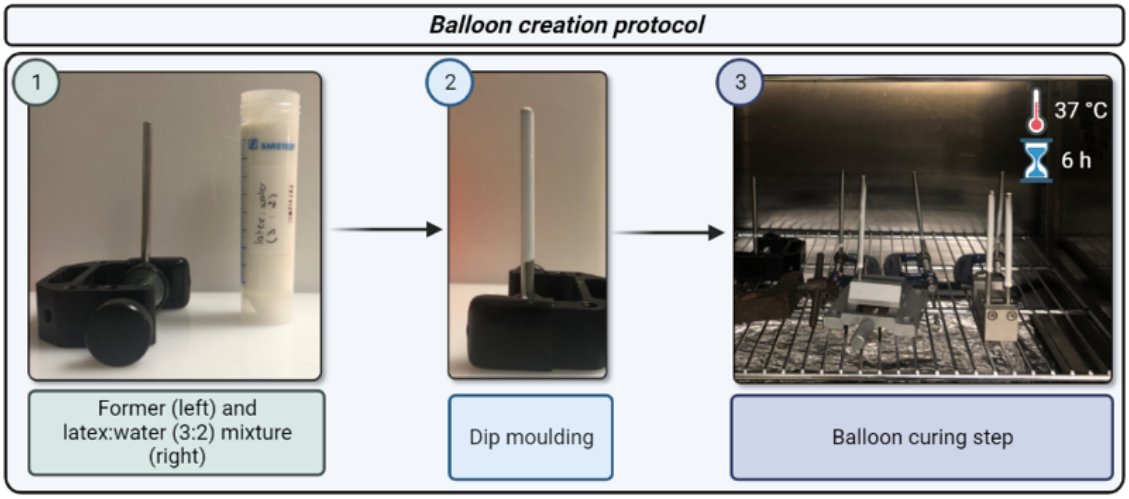

Figure 4.2: Methodology steps for balloon creation protocol.

To first evaluate the mechanical influence of balloons during inflation, vessel compliance was evaluated on NPCaA with (Balloon group) and without balloon inserted (No Balloon group). Briefly, each NPCaA (n=6) was inflated three consecutive times to 120 mmHg with and without a balloon inserted in the lumen. An axial stretch of 10% was applied to the NPCaA during inflation to replicate *in vivo* pre-stretch. The framework is depicted in Figure 4.3:

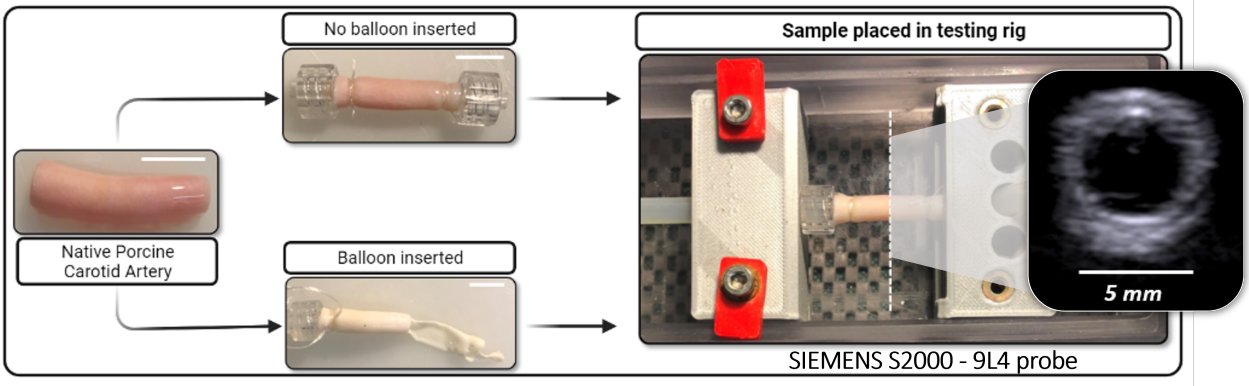

Figure 4.3: Framework to evaluate balloon influence on porcine carotid wall expansion.

Outer diameters were measured using ImageJ [208]. Three measurements were taken for each B-mode scan and static compliance was calculated for each inflation. The slope of the pressure-diameter curves gives the static compliance using the following equation [209]:

$$C_D^{STAT} = \frac{d(\ln D)}{dP} \tag{4.1}$$

4.2.4 Atherosclerotic plaque inflation

As explained in Section 4.2.3, any lacerations or holes on the plaques were sutured closed using 6-0 polypropylene sutures to facilitate the pressurisation procedure. A compliant balloon is then inserted within the plaque lumen, see Figure 4.4(B). Samples were then attached to connectors via the common branch and either the external or internal branch, see Figure 4.4(C). The remained unattached branch was sutured closed to avoid leakage. Connectors were then secured in the testing rig, see Chapter 3, Figure 3.3. Lumen area was measured using the ImageJ interface to generate lumen area versus pressure curves [208]. The slope of these curves provided a measurement of compliance.

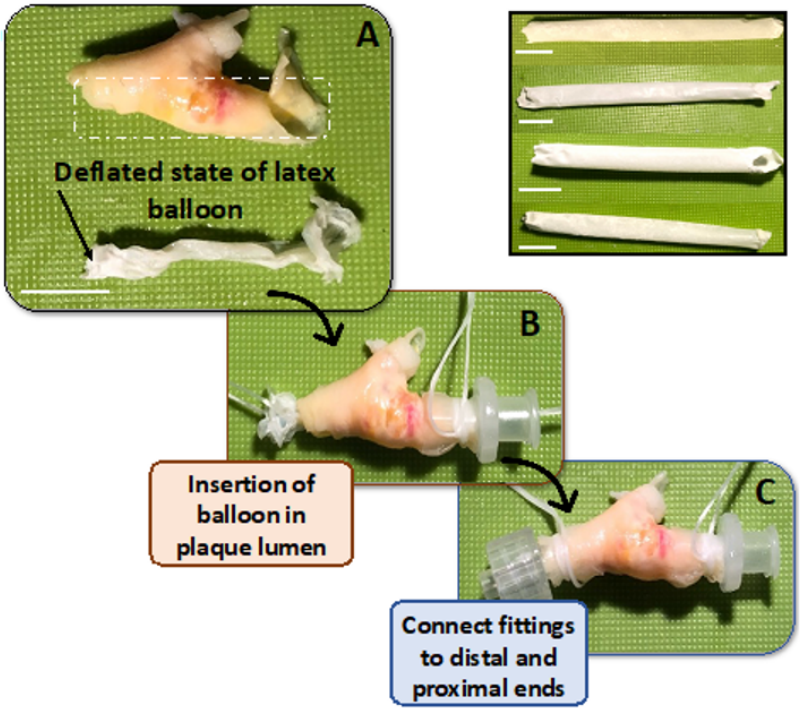

Figure 4.4: Proposed workflow to inflate endarterectomy samples. (A) Plaque sample with balloon in its deflated state, white dotted rectangle indicates the lumen in which the balloon is inserted. (B) Insertion of balloon within plaque lumen. (C) Connection of fittings to the plaque and balloon at the distal and proximal ends. Scale bars: 1 cm.

4.2.5 Statistical analysis

Statistical analyses were performed using GraphPad Prism (Version 10). Non-parametric Mann-Whitney tests were conducted to compare the NPCaA groups (No Balloon & Balloon) for each sample, as the data did not follow a normal distribution. Significance was considered when $p < 0.05$.

4.3 Results

4.3.1 Balloon thickness

The thicknesses of n=4 compliant balloons, with n=5 measurements taken for each balloon is depicted in Figure 4.5. As shown in Figure 4.5, the mean thicknesses for each balloon were as follows:

- Balloon 1: $124.6 \pm 15.5\,\mu$m (range: 103–146 μm),
- Balloon 2: $111.0 \pm 16\,\mu$m (range: 93–131 μm),
- Balloon 3: $104.4 \pm 8\,\mu$m (range: 91–111 μm),
- Balloon 4: $130.2 \pm 8.6\,\mu$m (range: 120–141 μm).

The mean thickness across all measurements was $117.6 \pm 15.7\,\mu$m.

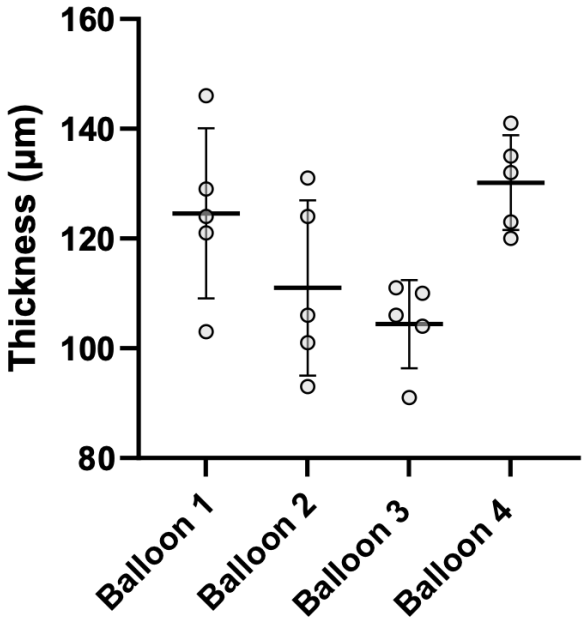

Figure 4.5: Thickness measurements for n=4 individual balloons. Each dot represents a single measurement, with horizontal bars indicating the mean and error bars represent the SD for each balloon.

4.3.2 Balloon influence on NPCaA wall expansion

US cross-sectional images of a NPCaA sample inflated to 120 mmHg, both with and without balloon insertion, are presented in Figure 4.6. Qualitatively, no significant difference in arterial wall expansion is observed between the two conditions, indicating that the presence of the balloon does not appear to affect the overall expansion behaviour of the artery at this pressure level.

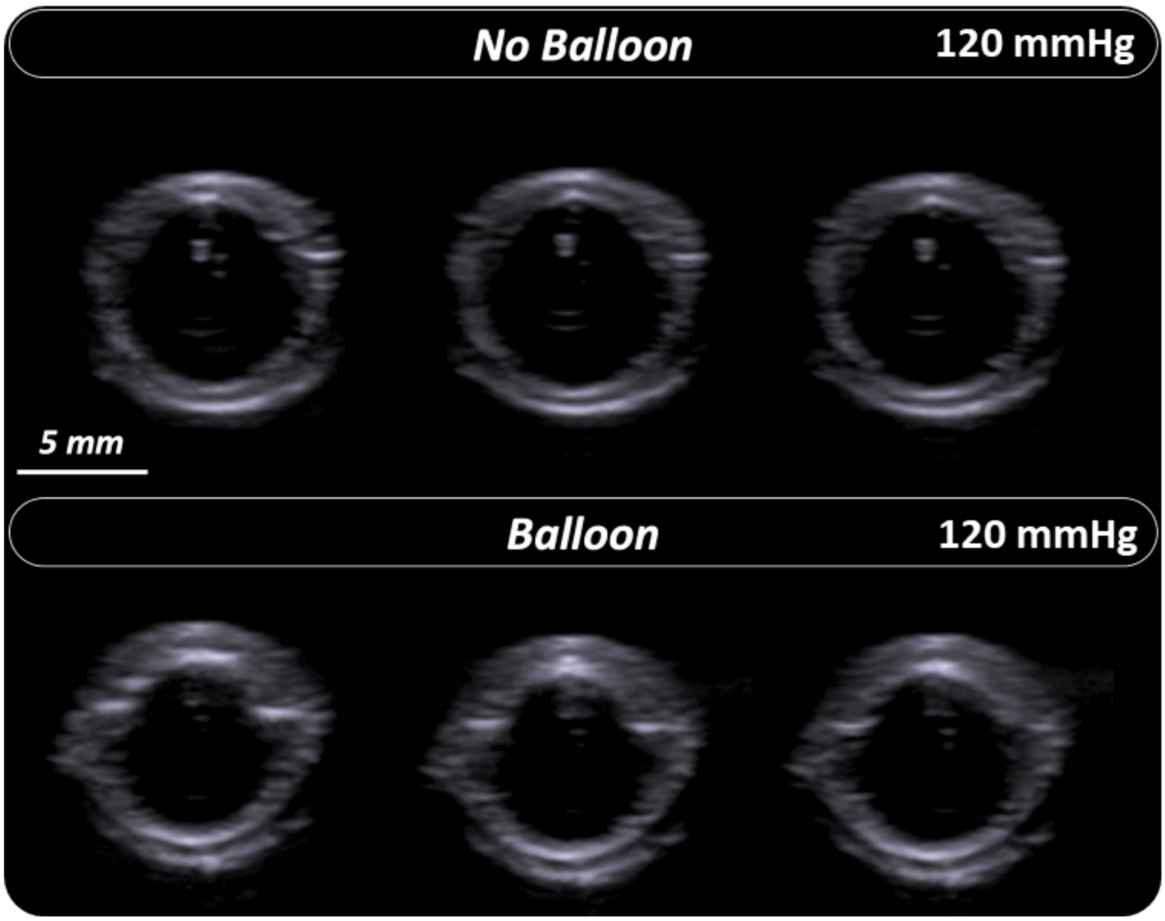

Figure 4.6: B-mode scans of cross-sections of inflated NPCaA (n=1) without (top row) and with balloon (bottom row).

While the qualitative assessment of the US images, see Figure 4.6, shows no discernible difference in arterial wall expansion between the balloon and no-balloon conditions, these observations are further supported by the quantitative analysis of static compliance. As shown in Figure 4.7, the static compliance of NPCaA inflated three times, both with and without a balloon, is presented. Each bar represents the compliance values for individual samples, with solid bars indicating the no-balloon condition and chequered bars representing the balloon-inserted condition. Across all samples, there is no significant difference in compliance between the balloon and no-balloon conditions. This shows that the presence of a balloon does not significantly alter the static compliance of the samples under these testing conditions.

To further assess whether the presence of the compliant balloon affected compliance measurements, a Bland–Altman analysis was performed. The plot confirmed that the differences between balloon and no-balloon conditions were small and consistently fell within the 95% limits of agreement, see Figure 4.8. This result supports the conclusion that the balloon had no significant effect on the measurement of static compliance and validates the use of this method for testing excised human plaques.

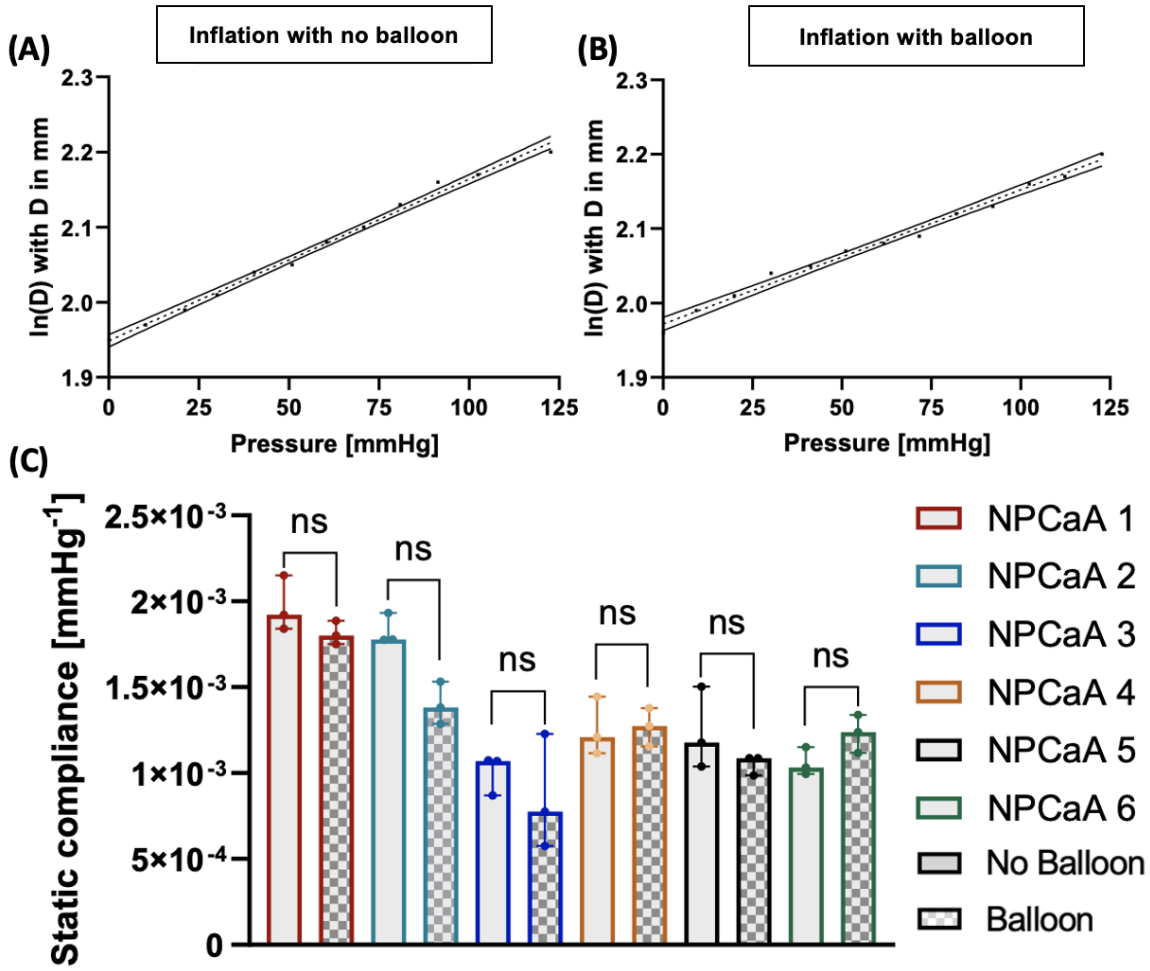

Figure 4.7: (A) Inflation iteration 1 of NPCaA 1 without a balloon: $(\ln(D))$ with D in mm plotted against pressure (mmHg). The data is fitted with a linear regression model to determine static compliance and 95% confidence interval are shown in solid lines. (B) Inflation iteration 1 of NPCaA 1 with a balloon: $\ln(D)$ plotted against pressure (mmHg). The data is fitted with a linear regression model to determine static compliance. (C) Median static compliances in mmHg^{-1} of NPCaA (n=6) each inflated three consecutive times with and without balloon.

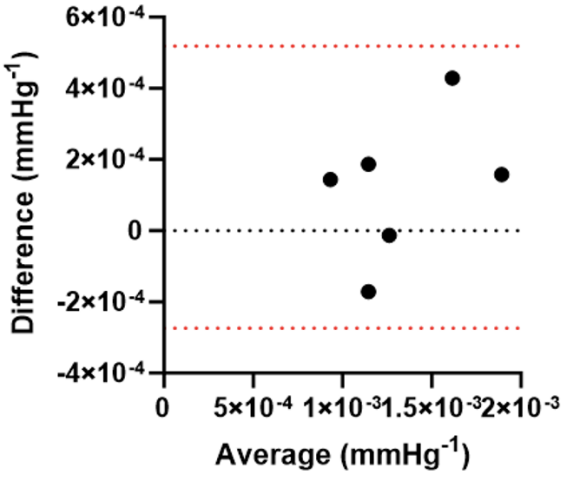

Figure 4.8: (Bland–Altman plot comparing mean static compliances measured in n=6 NPCaAs with and without the compliant balloon. Each point represents one sample. The x-axis shows the average compliance between the two conditions, while the y-axis displays the difference (No Balloon – Balloon). The dashed red lines indicate the 95% limits of agreement.

4.3.3 Atherosclerotic plaque inflation

Plaques were inflated using the method outlined, with balloons inserted, and subjected to various pressure levels while imaged using different US probes. Across all pressure conditions, the arterial wall expansion were successfully visualised with both probes (9L4 and 12L4). Plaques were successfully inflated using the described methodology, with balloons inserted and subjected to varying pressure levels. In fact, not all plaques were inflated to 120 mmHg due to structural limitations such as leakage or early mechanical failure, including rupture at suture sites or through existing fissures. These issues prevented reaching the maximum pressure without compromising sample integrity. The method allowed for clear visualisation of the plaques across different pressure conditions, and successful inflation was achieved at each pressure level until rupture or evident leakage. This demonstrates that the approach is effective for inflating plaques under a range of pressures and with different US probes.

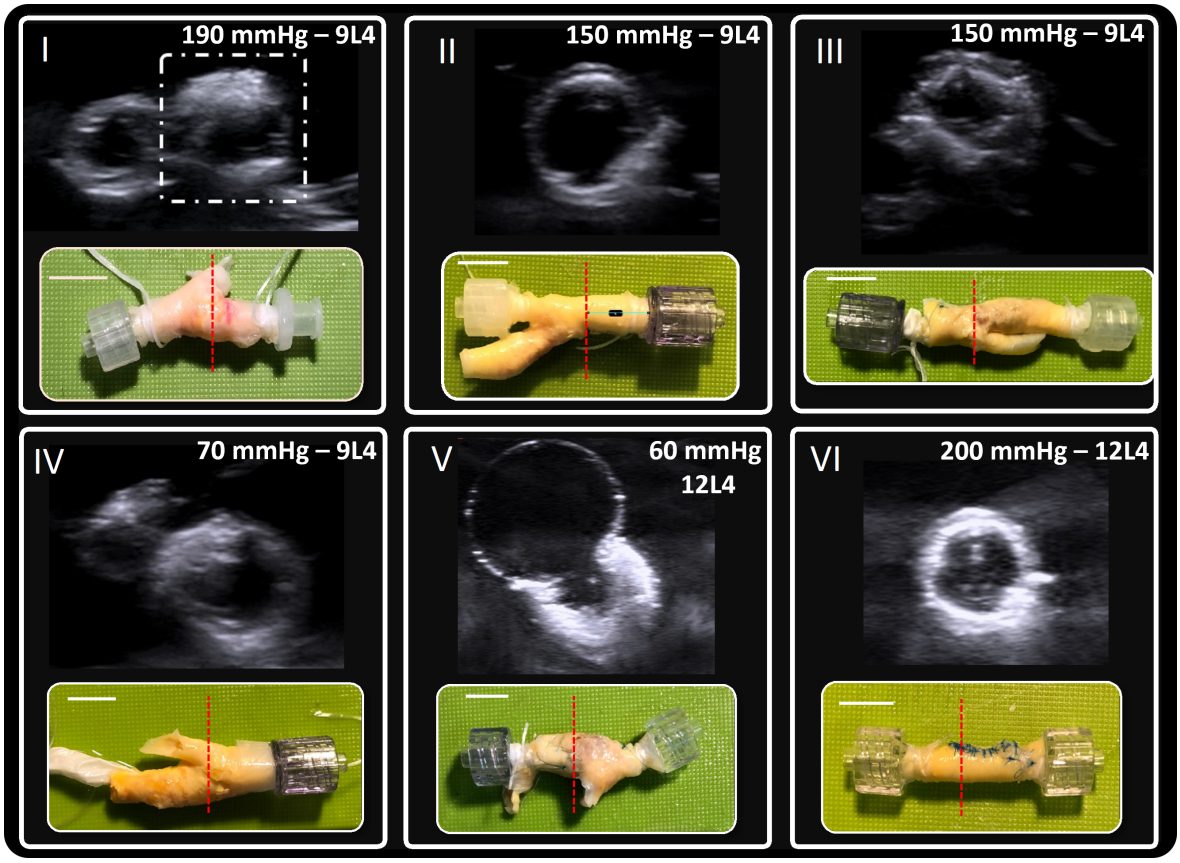

Figure 4.9: Photographs and B-mode US images of plaque cross-sections captured at varying pressures. Red dashed lines show probe position during testing. Scale bars: 1 cm.

The graph in Figure 4.10 illustrates the relationship between applied pressure and the mean inner lumen area for various plaques, which were pressurised at different pressures to simulate physiological loading. The error bars reflect variability across three manual measurements at each pressure level, demonstrating minimal variation and thus reliability in the measurement process. Each curve represents an individual

cross-section, revealing variability in their response to increasing pressure. Across all samples, the mean inner lumen area generally expands with rising pressure. However, plaques differ in their extent of distension. For example, plaques 2 and 4 show a pronounced increase in lumen area, reaching values exceeding 30 mm^2 at higher pressures. This response is synonym of greater compliance in contrast to stiffer plaques like plaque 1 and plaque 3, which exhibit a plateau in area expansion indicating limited compliance.

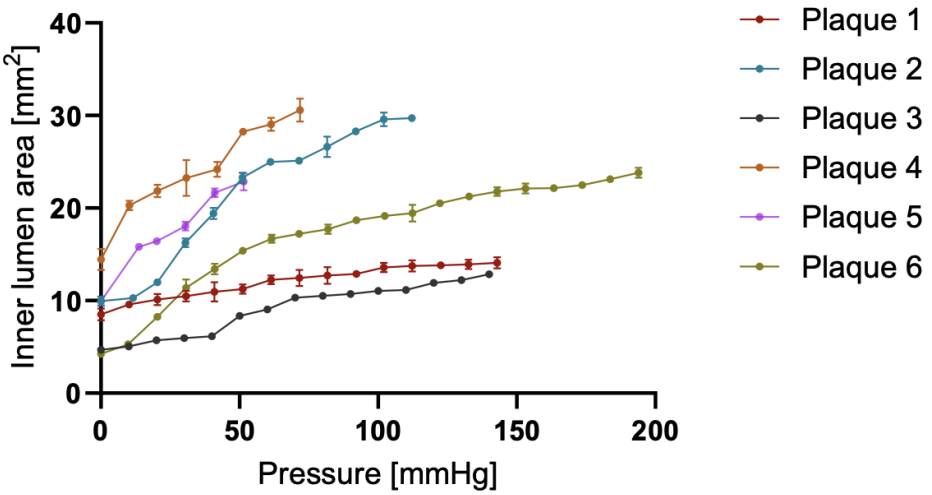

Figure 4.10: Inner lumen area (mm^2) plotted against pressure (mmHg) for various plaques.

Building on the pressure against mean inner lumen area analysis, we extracted the slope of each pressure curve to calculate vessel compliance. This approach provides a quantitative measure of the plaques' stiffness, offering further insight into their mechanical properties under simulated physiological conditions.

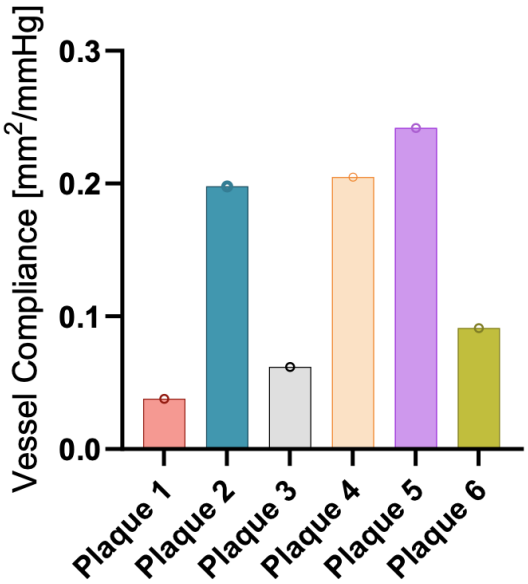

Figure 4.11: Vessel compliance (mm^2/mmHg) of plaques inflated, calculated from the slopes of their pressure-area curves.

Figure 4.11 presents the vessel compliance (mm^2/mmHg) calculated from the slope of the pressure curves for each plaque. Each bar represents a unique plaque or cross-section, highlighting the range of compliance among samples. Plaques 2, 4, and 5 show higher compliance, reaching respectively 0.198 mm^2/mmHg, 0.205 mm^2/mmHg and 0.242 mm^2/mmHg indicating a more distensible response under pressure. In contrast, plaques 1 and 3 exhibit lower compliances, with values respectively equal to 0.038 mm^2/mmHg, 0.062 mm^2/mmHg indicating a stiffer behaviour under pressure. Plaque 6 displays an intermediate level of compliance (0.091 mm^2/mmHg), positioning it between the more compliant and stiffer plaques.

4.4 Discussion

This study presents a novel, watertight methodology for pressurising excised human plaque samples, allowing for controlled inflation that simulates physiological conditions. By ensuring robust sealing, this setup enables mechanical assessment and US imaging of plaques under pressure, bridging a gap left by traditional uniaxial and biaxial tensile tests on tissue strips. Inflation testing on NPCaAs showed no statistically significant differences in compliance values between the balloon and no-balloon groups, indicating that balloon insertion does not interfere with arterial wall expansion, thereby validating its use for inflation testing, see Figure 4.7(C).

In addition, the mean static compliance values obtained in this study for the n=6 NPCaAs inflated without balloon ($1.4 \pm 0.4 \times 10^{-3}\,\mathrm{mmHg}^{-1}$) and with balloon ($1.3 \pm 0.3 \times 10^{-3}\,\mathrm{mmHg}^{-1}$) compare well within the range reported for pressurised canine carotid arteries [209]. Specifically, at $P = 140\,\mathrm{mmHg}$, they found a mean static compliance of $1.0 \pm 0.5 \times 10^{-3}\,\mathrm{mmHg}^{-1}$ which closely aligns with the mean compliance observed in NPCaAs.

Applying this method to atherosclerotic plaques provided valuable insights into their stiffness under pressurisation. The compliance measurements obtained from pressure-area curves revealed variability across plaques. More compliant plaques, such as plaques 2 and 4, exhibited greater expansion under pressure. In contrast, stiffer plaques, such as plaques 1 and 3, showed limited distensibility. Quantitative compliance values further highlight this range, with some plaques displaying compliance as high as 0.242 mm^2/mmHg, while others showed values as low as 0.038 mm^2/mmHg. These values partially overlap with those reported by Williams et al. in patients with coronary artery disease, where compliance ranged from 0.010 to 0.052 mm^2/mmHg at a pressure of 100 mmHg, as measured *in vivo* using IVUS [210]. The higher values observed in our study could be due to differences in pressure ranges, vessel size and the quasi-static nature of our measurements. Williams et al. highlight the importance of compliance as a marker for arterial stiffness and atherosclerotic disease progression [210]. Syeda et

al. further underscored this by demonstrating the utility of the small arterial elasticity index, derived from pulse wave contour analysis and the Windkessel model, as a specific compliance measure. Their findings revealed a strong link between this reduced index and diffuse coronary artery disease [211]. Additionally, as Haluska et al. demonstrated, compliance metrics such as total arterial compliance and the distensibility coefficient offer additional prognostic value, enhancing risk stratification for patients with intermediate cardiovascular risk beyond the Framingham score—a widely used tool that estimates 10-year cardiovascular disease risk based on factors such as age, cholesterol levels, blood pressure, and smoking status [212] Interestingly, van Popele et al. found that common carotid artery stiffness was strongly associated with atherosclerosis [213]. Boesen et al. further emphasise the consistent finding in the literature: reduced carotid elasticity is closely linked to the presence of atherosclerotic plaques and an elevated risk of stroke [214]. Nevertheless, the variability in measurement methods and the lack of standardised reporting for carotid compliance indices present challenges in comparing findings across studies and translating them into clinical practice [214].

The inclusion of US imaging in this experimental setup not only provides a non-destructive means of observing plaque deformation in real time but also opens up potential for clinical translation. The use of both high- and low-frequency probes allowed for flexibility in visualising plaques at different resolutions, reinforcing the robustness of this method across various imaging conditions.

While this study provides valuable insights into the mechanical behaviour of atherosclerotic plaques under controlled pressurisation, several limitations should be acknowledged. One key limitation is the reliance on single cross-sectional images, which, while useful, may not capture the full three-dimensional complexity of plaques. A 3D US imaging approach, as demonstrated by Boekhoven et al. using echo-computed tomography, could offer a more comprehensive view across the plaque's geometry [215], [216]. Spence and Parraga emphasise that 3D US not only improves visualisation of plaque volume but also captures critical morphological features like ulceration and surface irregularities, which are often missed in 2D imaging [135]. Additionally, plaques were not always subjected to the same pressure ranges due to the challenges of this type of testing [157]. The effectiveness of the inflation technique which included a suturing procedure also relies heavily on the quality of the collected sample. In cases where branches are calcified, securing an airtight seal for clamping can be particularly challenging. Calcified branches not only complicate the pressurisation process but may also lead to issues in maintaining sample integrity during testing. To minimise compliance mismatch at the suture line and enable watertight closure, we employed intermittent sutures. This decision is supported by Hasson et al., who demonstrated that interrupted sutures result in reduced compliance mismatch and lower risk of para-anastomotic hyperplasia compared to continuous sutures [217]. Nonetheless, future work could incorporate cut-

and-sutured porcine arteries to more systematically investigate the mechanical effects of suturing on vessel compliance.

Moreover, this study does not replicate the dynamic, pulsatile environment *in vivo* conditions due to the quasi-static nature of the inflation testing. Future work should aim to take viscoelastic properties into account.

Despite these limitations, this study establishes a robust methodology for assessing plaque mechanics under pressurised conditions. The next chapter will use this approach combining US imaging and immunohistochemistry to investigate the relationship between neovessel presence and plaque mechanical behaviour. Understanding this correlation could offer critical insights into plaque vulnerability, aiding in the prediction of stability and improving clinical management of carotid artery disease.

Chapter 5

Assessing Plaque Mechanics and Neovascularisation Through Inflation Testing: Towards a Clinically Translatable Approach

5.1 Introduction

Atherosclerosis remains one of the leading causes of cardiovascular morbidity and mortality worldwide [1]. Characterised by the build-up of plaques within the arterial walls, this progressive disease can lead to life-threatening complications such as strokes. Despite advances in cardiovascular care, predicting plaque rupture remains challenging, emphasising the need for better risk indicators beyond traditional metrics [9].

Current clinical practice primarily assesses plaque vulnerability based on the degree of stenosis—the narrowing of the artery. However, research has shown that stenosis alone is insufficient to capture the complex behaviour of plaques and their rupture potential [9], [53]. This underscores the need for a a more comprehensive risk assessment of plaque rupture [23].

US imaging, particularly CEUS, has gained traction in clinical settings for visualising plaque neovascularisation [73], [119]. Although CEUS holds promise as a non-invasive method for assessing neovascularisation, robust evidence linking neovascularisation to plaque rupture risk remains limited [121], [122]. This gap highlights the need for further research to support or enhance US-based risk assessment.

Building on the methodological groundwork established in the previous chapter, we now examine the relationship between plaque neovascularisation and mechanical prop-

erties, as assessed through inflation testing and immunohistochemistry. By integrating the iFEM boundary matching approach applied in Chapter 3, this study combines experimental and computational findings to enhance our understanding of carotid plaque properties.

5.2 Material and methods

5.2.1 Sample acquisition

Carotid atherosclerotic plaques (n=5) were obtained from symptomatic carotid endarterectomy patients at the Galway Clinic. All patients had a percent stenosis greater than 50%. Ethical approval was obtained from Galway Clinic ethical committee in compliance with the declaration of Helsinki (2016-12 List 47 (4)). Carotid plaques were rinsed in PBS to remove residual blood and cryopreserved as previously reported [20]. After the PBS wash, samples were placed in a room temperature tissue freezing medium and immediately frozen down at a controlled rate of 1°C/min to -80°C using a Mr. Frosty™ (Merck). Samples remained at -80°C until *ex vivo* imaging. Cryopreservation was used to maintain microstructural integrity of the samples between collection and mechanical testing.

5.2.2 Ultrasound imaging and inflation testing

A SIEMENS ACUSON S2000™ US machine was utilised to scan the plaque samples under intraluminal pressure. A 12L4 linear array probe (frequency: 12 MHz, THI ON) probe was transversely placed above the tested samples. Pressure inflation testing was carried out using a PID-controlled PHD Ultra 703007 Syringe Pump (Harvard Apparatus, Holliston, MA, USA). Pressure levels were monitored using a fibre-optic pressure sensor FOP-M260 pressure probe (FISO, Quebec, QC, Canada). Quasi-static pressurisation was carried out in 10 mmHg pressure steps until leakage appeared or rupture occurred. The methodology to inflate fresh atherosclerotic plaques is described in further detail in Chapter 4. For each pressure step, a B-mode scan and beamformed RF data sampled at 40 MHz were acquired to obtain cross-sectional views of the samples, see Figure 5.1. Lumen area was measured using ImageJ to obtain lumen area versus pressure curves [208]. The slope of these curves provided a measurement of compliance.

5.2.3 Displacement maps

This work was conducted in collaboration with Erasmus MC in Rotterdam and the MUSIC lab at Radboud University.

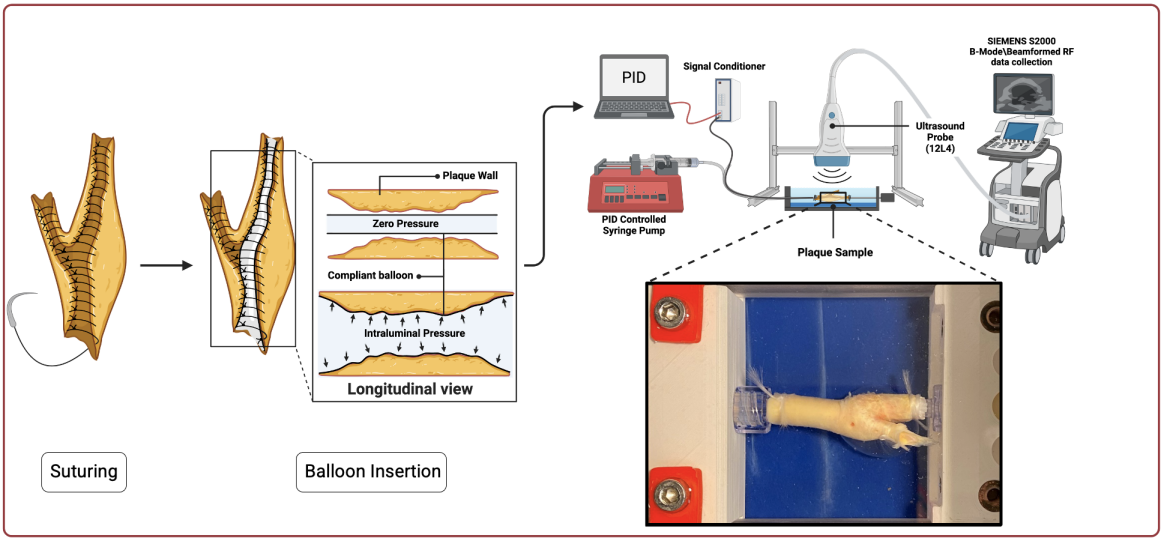

Figure 5.1: Experimental setup for inflation testing and US imaging of plaque samples.

The in-built AXIUS software on the SIEMENS ACUSON S2000™ US system allows for the acquisition and transfer of beamformed RF data. The RF data was subsequently processed using an open-source MATLAB-based toolbox, namely Ultrasound Research Interface Offline Processing Tools [191].

Axial displacements (Y-direction) were estimated using a coarse-to-fine cross correlation algorithm with two iterations [176]. In this study, we refer to "Y-direction displacement" as the displacement along the axial direction of the ultrasound beam, and these terms are used interchangeably throughout the chapter. Positive displacement values indicate speckles moving towards the probe along the US beam, while negative values indicate motion in the opposite direction. The first iteration was applied to the enveloped data with a kernel size of [0.8, 0.8] mm (axial, lateral) and a search margin of [0.4, 0.4] mm. The second iteration was applied to the RF data, using a [0.4, 0.4] mm kernel size and a search margin of [0.3, 0.3] mm. After each iteration, the estimated displacements were filtered using a rigid median filter with a [0.4, 0.4] mm window size.

The cross-correlation analysis was performed on the plaque cross-section only, defined by a region of interest mask of the inner lumen at the first pressure step and the outer lumen at the final pressure step. In this study, only Y-direction displacements were used, due to the lower accuracy of lateral (X-direction) displacements [16], [17].

5.2.4 Constitutive modelling

As mentioned in Chapter 3, the Ogden model has been widely used to characterise the non-linear mechanical behaviour of soft tissues, including atherosclerotic plaque tissue [152]. In this study, the first-order Ogden model was employed:

$$U_{\text{Ogden}} = \frac{2\mu_1}{\alpha_1^2}\left(\lambda_1^{\alpha_1} + \lambda_2^{\alpha_1} + \lambda_3^{\alpha_1} - 3\right) \tag{5.1}$$

where μ_1 (shear modulus) and α_1 (dimensionless) are material parameters and λ_1, λ_2 and λ_3 are the principal stretches.

5.2.5 Inverse finite element framework

Boundary matching of plaque samples

As outlined in Chapter 3, the same approach was used for data acquisition and processing. US RF data were imported using the Ultrasound Research Interface Offline Processing Tools (URI-OPT) [191]. Segmentation of the outer and inner lumen was performed in MATLAB, followed by smoothing in SolidWorks®. The final boundaries were imported into Abaqus to define the 2D cross-sectional geometry, with nodal coordinates used for region of interest delineation.

As explained in Chapter 3, a boundary-matching inverse approach was employed. The material behaviour of the plaque wall was modelled using a first-order Ogden model, with initial parameters derived from Teng et al., see Table 5.1 [152]. The parameters optimised were $\mu_{1\text{wall}}$ and $\alpha_{1\text{wall}}$. As described in Chapter 3, finite element simulations were performed in Abaqus/Standard. An iFEM algorithm, implemented using iSight 5.9 (Dassault Systèmes), calculated the sum of minimal Euclidean distances between the nodes of the optimised and target geometries—denoted as ϵ—which was minimised through parameter optimisation using the Hooke-Jeeves algorithm. The iSight workflow integrates simulations, error calculation, and optimisation, see Figure 3.4.

Parameter	Initial Guess	Source	Upper Bound	Lower Bound
μ_{1wall}	6.8 kPa	Teng et al. [152]	10 MPa	0.0
α_{1wall}	24.5	Teng et al. [152]	50	0.0

Table 5.1: Boundary matching initial parameters for plaque wall

5.2.6 Histological analysis

Histological processing

After testing, all samples were cut into 2 mm thick rings using a 3D-printed blade holder and fixed in 10% formalin for histological processing for no more than 48 hours. After fixation, strips were stepwise dehydrated (Leica TP1020, semi-enclosed bench-top tissue processor, Germany) and embedded in paraffin wax blocks. Strips were embedded to obtain the same view as acquired on the B-mode scans. Samples were sectioned

at 5 µm using FEATHER C35 microtome blades and stained with haematoxylin & eosin (H&E). Intraplaque neovascularisation was evaluated using CD31 markers with immunohistochemistry. Deparaffinised sections were processed for antigen retrieval using a pressure cooker. The sections were incubated with the primary antibody against CD31 (mouse monoclonal, 1:50 dilution, Anti-CD31 antibody [JC/70A]; Abcam) overnight at 4°C. Sections were subsequently treated with the secondary antibody for 1 hour at room temperature (EnVision+/HRP, Mouse, HRP, K4001, Agilent). Finally, the liquid DAB chromogen (Liquid DAB+, 2-component system, K3468, Agilent) was applied for 6–8 minutes. Brightfield imaging was performed on an APERIO CS2 microscope using IMAGESCOPE software V12.3 (LEICA BIOSYSTEMS IMAGING, INC., Vista, California) was then performed on the stained sections.

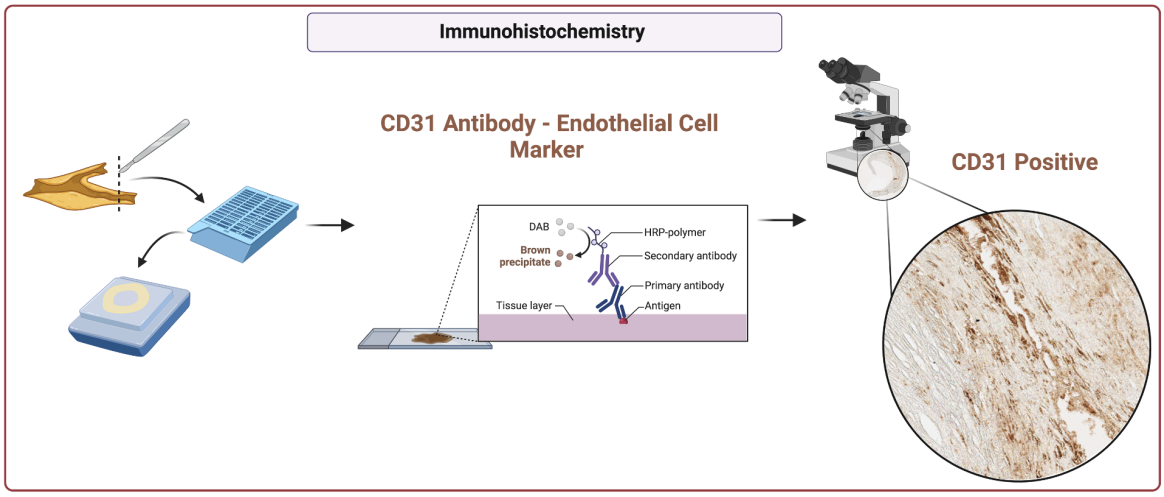

Figure 5.2: Immunohistochemistry workflow for detecting neovessels in plaque tissue.

Neovascularisation quantification

Histology quantification was performed using QUPATH (v 0.5.1) [218]. Digital whole immunohistochemistry slides were opened in QUPATH, where the following procedure was followed to quantify the neovessel percentage per stained area. An automated thresholding approach was used to analyse positively stained plaque sections. This analysis employed an automated thresholding tool developed on GitHub, using the triangle method to identify neovessels. For each of the n=5 plaques, two sections were analysed, and the mean neovascularisation percentage was calculated. Consistent tissue regions were delineated using the Wand tool in QUPATH, avoiding any folded areas or regions with background staining. The features of the thresholding algorithm were as follows: moderate resolution (3.96 µm/px) with DAB channel selected. Neovessel percentages were calculated based on area for each tissue section, providing a measure of neovascularisation.

Plaque classification

Plaque samples were classified using the histological information gathered through H&E-based morphological features, following the classification system defined by Stary et al. [46]. The H&E staining enabled a precise examination of plaque morphology to identify features such lipid core presence, and cellular regions and calcifications. This morphological assessment provided the foundation for categorising each plaque sample within Stary's classification framework.

5.2.7 Statistical analysis

Statistical analyses were performed using GraphPad Prism (Version 10). Pearson's correlation coefficient (r) was used to assess the relationship between shear modulus $\mu_{1\text{wall}}$ from the iFEM framework and neovascularisation, with correlation strengths defined as follows: weak ($r < 0.3$), moderate ($0.3 < r < 0.7$), and strong ($r > 0.7$).

5.3 Results

5.3.1 Ultrasound imaging and inflation testing

US cross-sections of human atherosclerotic plaques were successfully obtained at their maximum inflated pressure levels. B-mode images are shown in Figure 5.3, illustrating the distinct mechanical responses of the plaques samples under pressure, with different changes in lumen geometry.

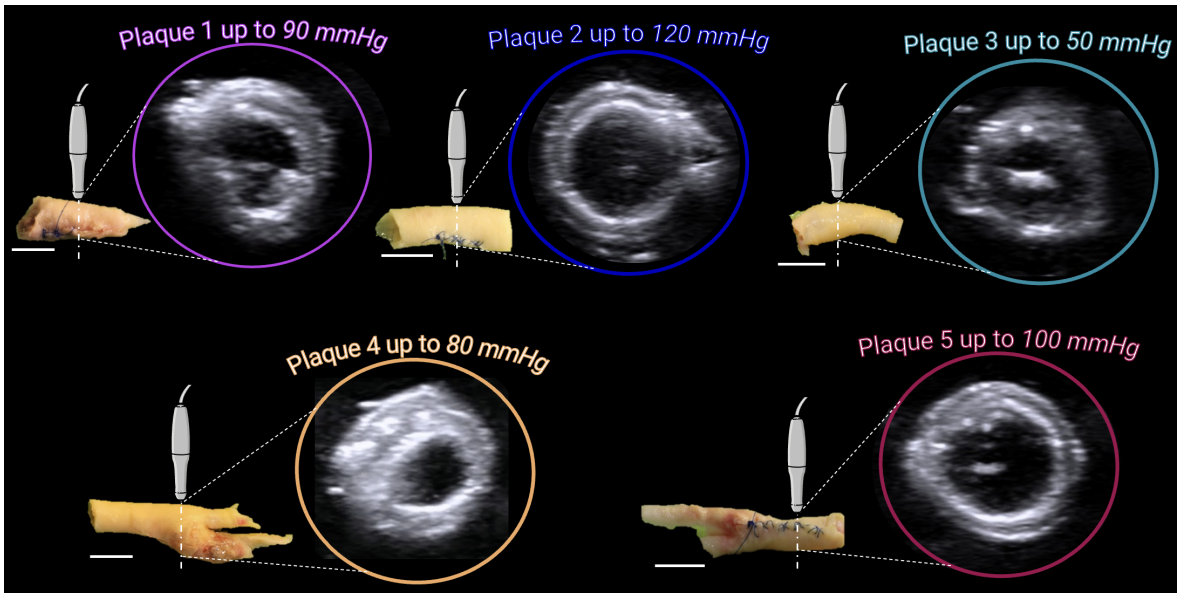

Figure 5.3: B-mode scan of cross-sections of five atherosclerotic plaques inflated to different pressure levels. Scale bars: 1 cm.

Plaque 2 and plaque 5 exhibited a relatively uniform expansion under inflation.

These plaques maintained homogeneous expansion and showed gradual, consistent wall thinning with increasing pressure levels, reflecting greater compliance. On the other hand, plaque 3 demonstrated limited deformation under inflation, showing stiffer mechanical properties. Plaque 1 and plaque 4 exhibited inhomogeneous inflation patterns, with localised expansion observed specifically in the upper right region of the plaques. This uneven deformation was distinct compared to the more uniform behaviour seen in other plaques.

To quantify these differences, the inner lumen area was plotted against pressure for each plaque, with vessel compliance defined as the slope of each curve, see Figure 5.4.

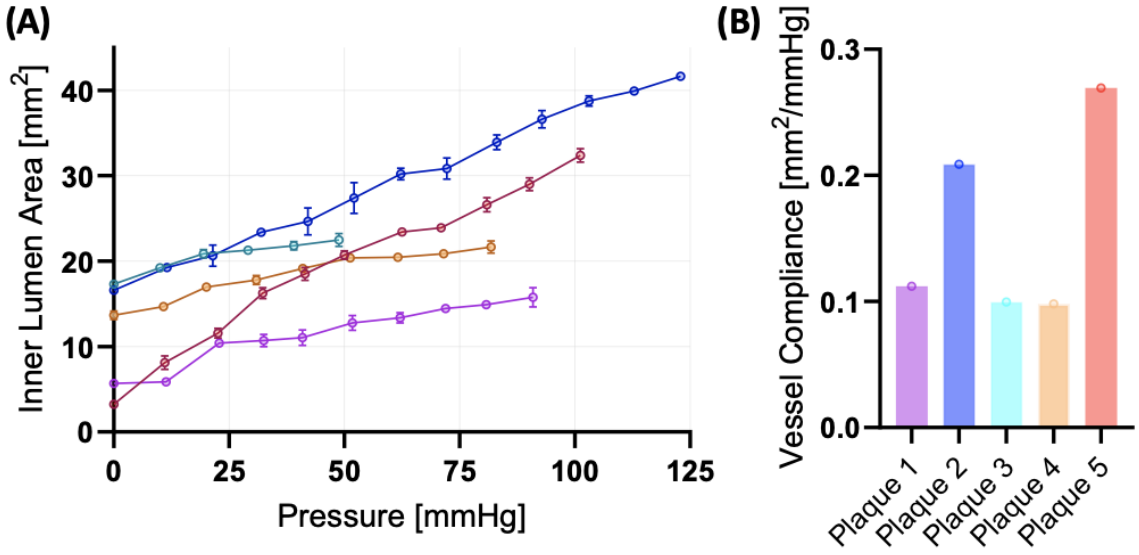

Figure 5.4: (A) Quantification of inflation testing for the n=5 plaque samples with the pressure-lumen area relationship, highlighting variability in lumen expansion across plaques, with different maximum pressures achieved. (B) Vessel compliance, calculated as the slope of the pressure-lumen area curve.

The results of the inflation testing are summarised in Figure 5.4. Notably, plaques did not inflate to the same maximum pressure. The pressure-lumen area curves reveal distinct mechanical behaviours among the five plaques, with varying degrees of lumen expansion under inflation. For example, plaque 5 exhibited the largest increase in lumen area, reaching 32.4 mm^2 at 100 mmHg, while plaque 3 reached 22.5 mm^2 at 50 mmHg. To allow comparison across plaques with differing inflation limits, vessel compliance was calculated as the slope of the pressure-lumen area curve. Plaque 5 demonstrated the highest compliance (0.27 mm^2/mmHg), followed by plaque 2 (0.21 mm^2/mmHg), indicating greater compliance to pressure changes. In contrast, plaque 3, plaque 1, and plaque 4 exhibited similar compliance values, measured at 0.1 mm^2/mmHg, 0.11 mm^2/mmHg, and 0.1 mm^2/mmHg, respectively, indicating limited expansion across these samples.

5.3.2 Displacement maps

Displacement maps in the Y direction, as shown in Figure 5.5, were obtained using cross-correlation algorithms and revealed different deformation patterns, providing spatial information into the samples' mechanical properties. While plaque samples did not go to the same maximal pressure during inflation, displacement maps provide a means to compare deformation patterns within the plaques cross-sections. Plaque 1, subjected to a pressure of up to 90 mmHg, exhibits minimal displacement throughout its cross-section, with a slightly higher displacement visible in the right corner. For plaques 2 (120 mmHg) and 5 (100 mmHg), a pattern of positive (red) displacement at the top and negative (blue) at the bottom was observed, indicative of homogeneous wall expansion under higher pressures. In contrast, plaques 3 (50 mmHg) and 4 (80 mmHg) displayed lower displacement magnitudes. Plaque 4 exhibited a higher displacement region on the top right side, while plaque 3 demonstrated stiffer behaviour.

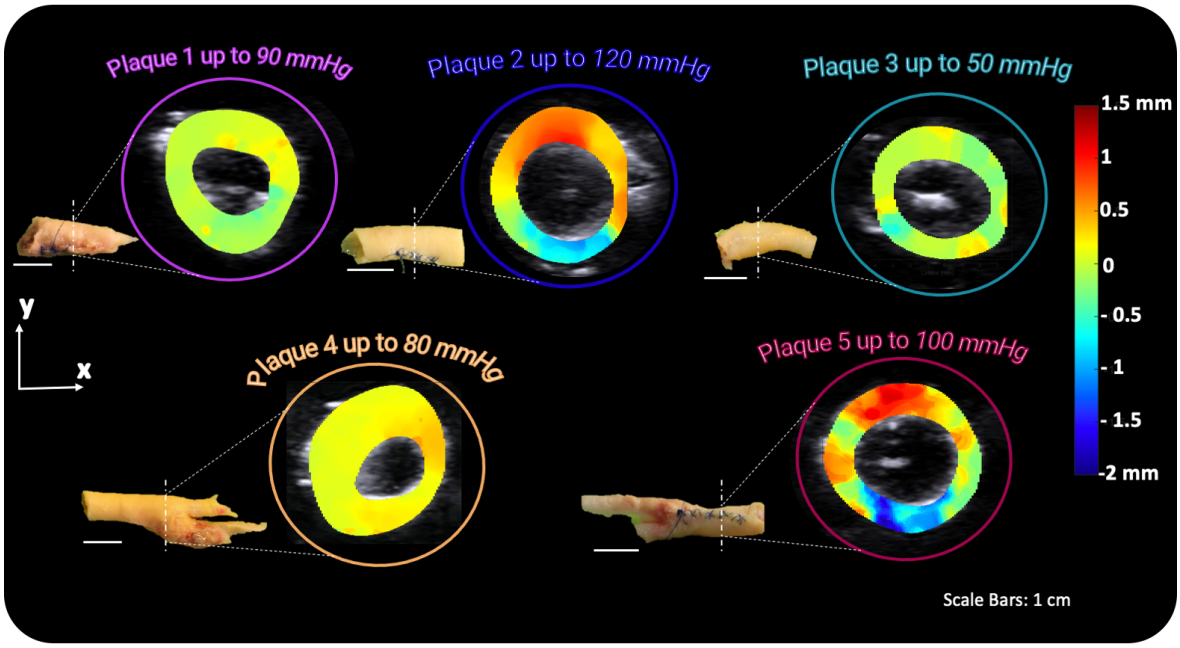

Figure 5.5: Y-displacement maps of five carotid plaques subjected to inflation testing at varying peak pressures (50–120 mmHg). Scale bars: 1 cm.

5.3.3 Boundary matching iFEM

The boundary-matching framework introduced in Chapter 3 was applied to estimate the Ogden material parameters ($\mu_{1\text{wall}}$, $\alpha_{1\text{wall}}$) across the five different plaque samples. The results are presented in Figure 5.6. The final optimisation error (ϵ) ranged from 0.3 mm to 0.72 mm, with plaque 3 exhibiting the lowest error ($\epsilon = 0.3$ mm) and an absolute percentage area difference of 4.7%, indicating a strong agreement between simulation and US-derived boundaries. In contrast, plaque 4 showed the highest error ($\epsilon = 0.72$ mm) with an absolute percentage area difference of 6.8%. Plaque 1 reached

$\epsilon = 0.51$ mm, with an absolute percentage area difference of 7.43%, while plaque 2 exhibited an error of $\epsilon = 0.46$ mm with an area difference of 1.5%. Plaque 5 yielded an error of $\epsilon = 0.66$ mm and an absolute percentage area difference of 10%. The recovered Ogden material parameters revealed variability in plaque stiffness, with $\mu_{1\text{wall}}$ ranging from 1.5 kPa to 22.9 kPa.

Plaque Sample	Optimised geometry boundaries (from iFEM) / Target geometry boundaries (from US)	Final Optimisation Error	Percentage of Area Difference (Absolute Value)	*Plaque wall:* Ogden material parameters
Plaque 1 (between 10 and 90 mmHg)	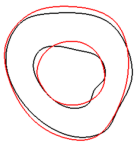	0.51 mm	7.43%	μ_{1wall} = 1.5 kPa α_{1wall} = 19
Plaque 2 (between 10 and 120 mmHg)	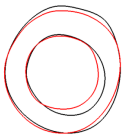	0.46 mm	1.5%	μ_{1wall} = 6.8 kPa α_{1wall}= 16
Plaque 3 (between 10 and 50 mmHg)	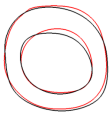	0.3 mm	4.7%	μ_{1wall} =19 kPa α_{1wall} = 32
Plaque 4 (between 10 and 80 mmHg)	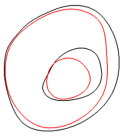	0.72 mm	6.8%	μ_{1wall} = 22.9 kPa α_{1wall} = 6
Plaque 5 (between 10 and 100 mmHg)	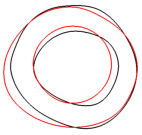	0.66 mm	10%	μ_{1wall} = 5 kPa α_{1wall} = 8.7

Figure 5.6: From left to right, plaque sample name with pressure used for iFEM, contours visualisation of the target and deformed geometries, final errors of the optimisation process, percentage of area differences, plaque wall Ogden optimised material parameters.

Figure 5.7 presents the Y-displacement maps obtained from the iFEM and US cross-correlation for the five different plaques. The iFEM contour plots exhibit smoother displacement fields, whereas the US-derived maps display greater spatial variability. Despite these differences, the overall displacement patterns remain consistent between both methods.

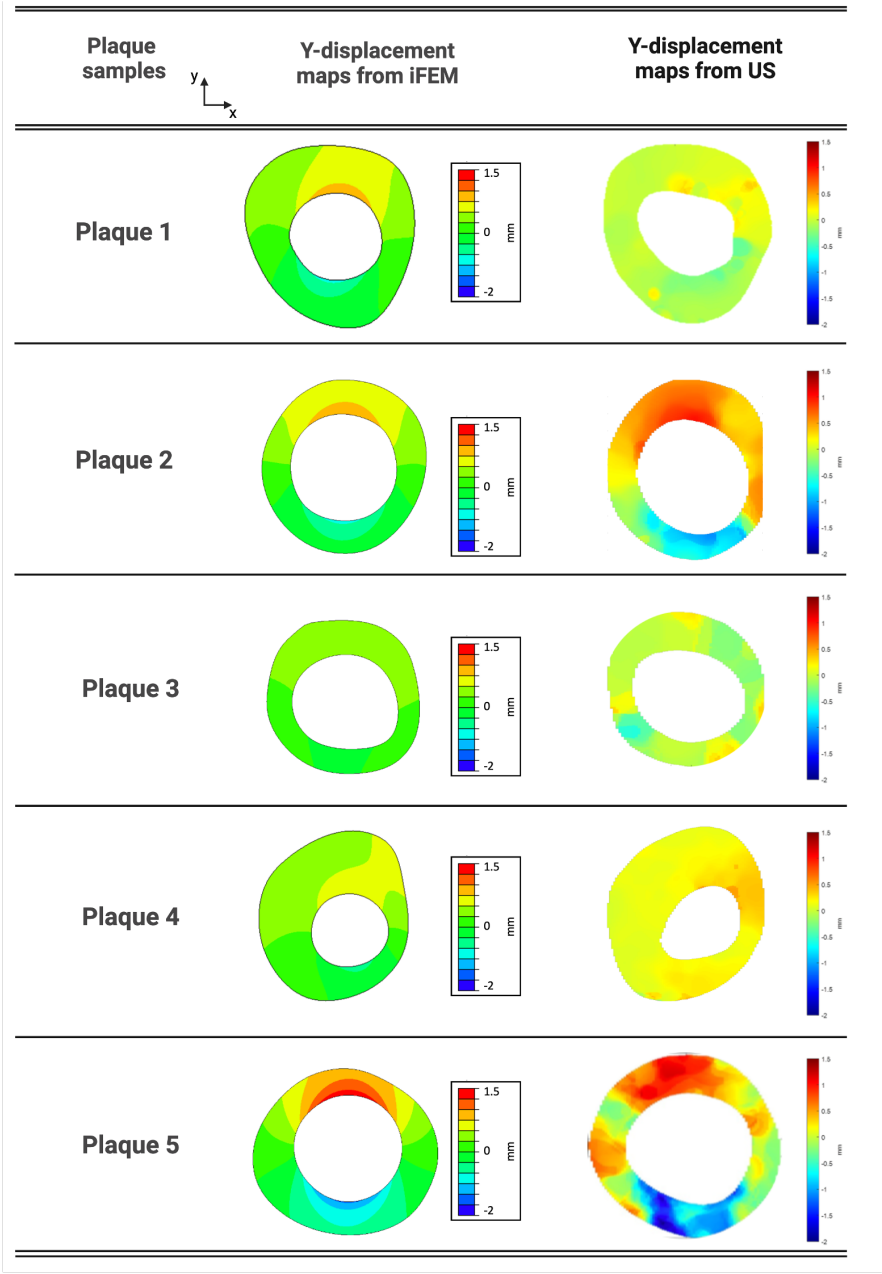

Figure 5.7: Y-displacement maps obtained from US and boundary-matching iFEM for the n=5 plaque samples. Both contour legends range from -2 to 1.5 mm.

A quantitative comparison of maximum and minimum displacements extracted from both methods is presented in Table 5.2. The absolute errors between US and iFEM displacement values vary across the plaques. Plaque 3 exhibits the best agreement overall, with absolute errors of 0.01 mm for maximum displacement and 0.18 mm for minimum displacement. In contrast, plaque 1 shows the largest discrepancies, with an absolute error of 0.56 mm for maximum displacement and 0.55 mm for minimum displacement, indicating that iFEM overestimates displacement compared to US. Plaque 2 demonstrates strong agreement, with absolute errors of 0.07 mm (maximum displacement) and 0.15 mm (minimum displacement). Plaque 4 has an intermediate discrepancy, with absolute errors of 0.07 mm (maximum displacement) and 0.51 mm (minimum

displacement). Plaque 5 also shows notable differences, with absolute errors of 0.36 mm (maximum displacement) and 0.52 mm (minimum displacement), making it one of the plaques with the highest deviation between the two methods.

Table 5.2: Comparison of maximum and minimum displacement values (respectively named Max Disp and Min Disp) obtained from US and iFEM for the $n = 5$ plaque samples. Absolute errors highlight the differences between both methods. All values are in mm.

Sample	Max Disp (US)	Max Disp (iFEM)	Abs Error Max	Min Disp (US)	Min Disp (iFEM)	Abs Error Min
Plaque 1	0.34	0.9	0.56	-0.38	-0.93	0.55
Plaque 2	1.00	0.93	0.07	-1.08	-0.93	0.15
Plaque 3	0.33	0.32	0.01	-0.57	-0.39	0.18
Plaque 4	0.64	0.57	0.07	-0.15	-0.64	0.51
Plaque 5	1.18	1.54	0.36	-2.00	-1.48	0.52

5.3.4 Plaque neovascularisation

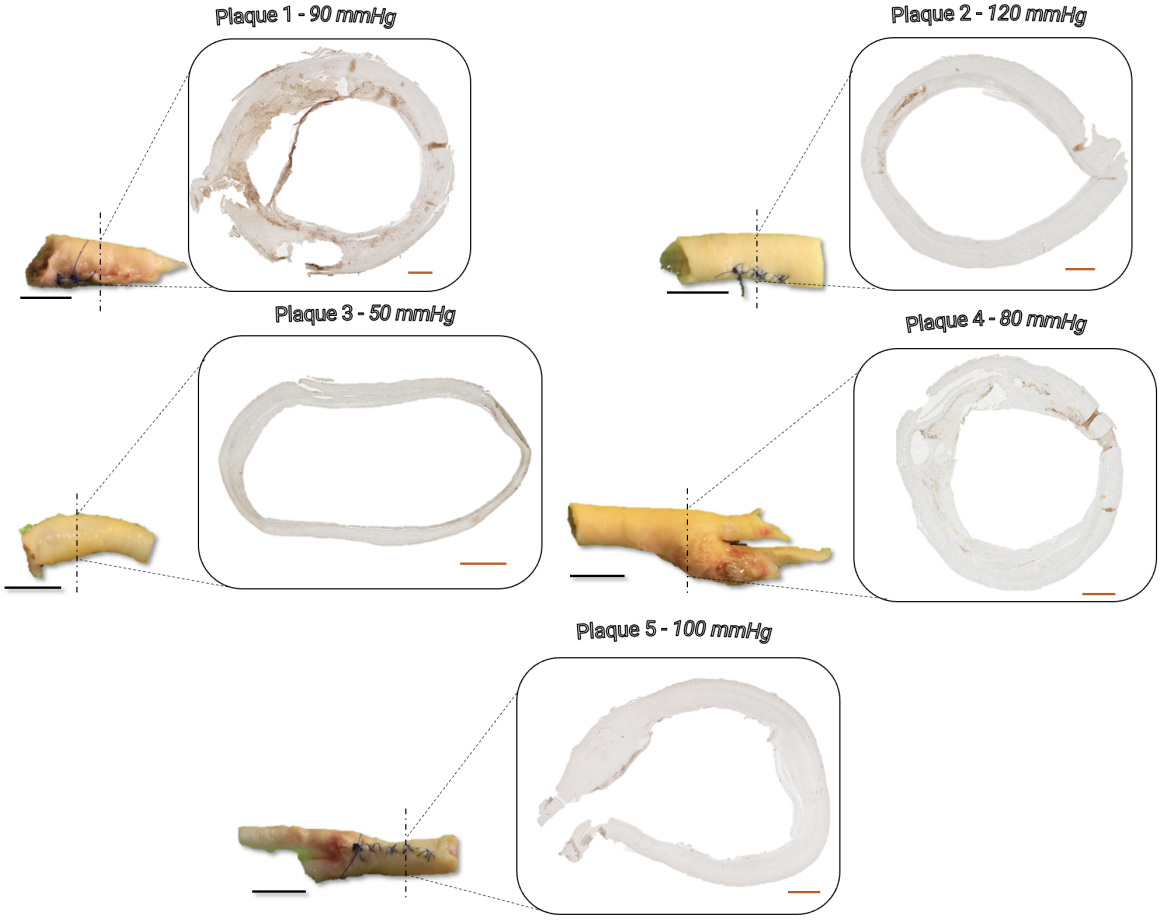

Figure 5.8: Representative histological sections of five atherosclerotic plaques stained with CD31, a marker for endothelial cells, to assess neovascularisation. Black scale bars: 1 cm. Brown scale bars: 1 mm.

The histological analysis of the five plaques, stained with CD31 to identify neovascularisation, revealed distinct patterns, see Figure 5.8. Plaque 1 exhibited the most extensive neovascularisation, with CD31-positive staining observed throughout the tissue,

while plaque 2 showed sparse and scattered staining, indicating less neovascularisation. In contrast, plaque 3 displayed negligible staining, reflecting an absence of significant neovascularisation. Plaque 4 demonstrated concentrated CD31-positive staining along the outer regions, with distinct clusters suggesting localised areas of neovascularisation. Plaque 5 exhibited localised CD31-positive staining primarily along the inner circumference. These results highlight the heterogeneous nature of neovascularisation among the tested plaques, with varying degrees of vascular network presence across the samples.

A notable observation emerged in plaque 4, where region of higher displacement appeared to co-localise with areas of neovascularisation. As observed in the US cross-section, a localised region of increased displacement became evident at 80 mmHg compared to 10 mmHg, circled in red in Figure 5.9(A) and further demonstrated in the Y-displacement map in Figure 5.9(B). Histological examination of the corresponding area, stained with CD31, confirmed the presence of neovessels, with CD31-positive staining localised in the same region, indicated by red arrows in Figure 5.9(C). In addition to this observation, plaque 3 demonstrated a high stiffness both through vessel compliance measurement (0.1 mm^2/mmHg) and shear modulus ($\mu_{1\text{wall}} = 19kPa$), with negligible neovascularisation presence (0.44%).

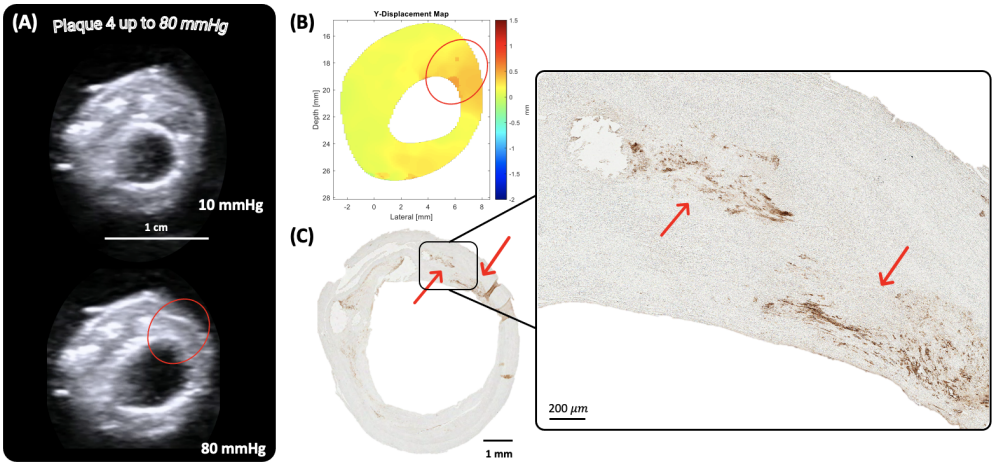

Figure 5.9: Multimodal analysis of plaque 4 under inflation. (A) Ultrasound B-mode images of the plaque at 10 mmHg (top) and 80 mmHg (bottom), showing deformation and localised displacement, with a red circle highlighting a region of greater displacement. (B) Corresponding Y-displacement map obtained from US, indicating regions of increased displacement (red) that spatially correspond to the circled area in (A). (C) Immunohistochemical staining of the same plaque, showing neovascularisation (brown-stained regions) in the highlighted region. The zoomed-in view confirms the presence of neovessels in the area exhibiting significant displacement. Scale bars: 1 cm (A), 1 mm (C), 200 µm (zoomed inset).

This prompted a closer examination of the corresponding histological and US data to explore this potential relationship further. The quantification of neovascularisation (shown in pink) and vessel compliance (shown in blue) for the plaque samples is

presented in Figure 5.10. Neovascularisation levels ranged from negligible (0.44% for plaque 3) to the highest levels (3.31% for plaque 1), with intermediate values observed for plaques 2, 4 and 5. Similarly, vessel compliance varied across plaques, with values ranging from 0.1 mm^2/mmHg for plaque 3 to 0.27 mm^2/mmHg for plaque 5.

When visualising the two metrics displayed together, no clear relationship is apparent between neovascularisation and vessel compliance across the samples. Plaques with high compliance do not consistently correspond to those with higher neovascularisation, and intermediate plaques exhibit variability in both metrics.

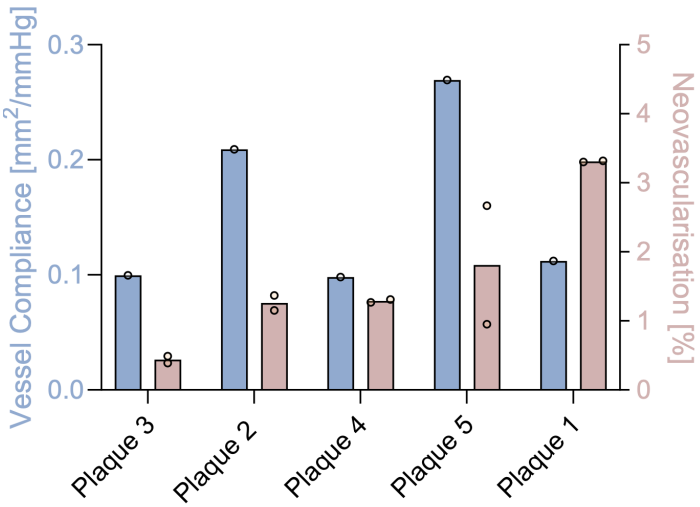

Figure 5.10: Quantification of vessel compliance (blue) and neovascularisation (pink) for the five plaque samples inflated.

In addition, as shown in Figure 5.11(A), plaque 1 demonstrates both the lowest shear modulus ($\mu_{1\text{wall}} = 1.5\,\text{kPa}$) and the highest neovascularisation (3.31%). On the other hand, plaque 3 has the lowest neovascularisation (0.44%) but a higher shear modulus ($\mu_{1\text{wall}} = 19\,\text{kPa}$). Plaque 4, which exhibits the highest shear modulus ($\mu_{1\text{wall}} = 22.9\,\text{kPa}$), shows moderate neovascularisation (1.29%). While Figure 5.11(B) suggests a strong inverse relationship ($r = -0.7307$) between $\mu_{1\text{wall}}$ and neovascularisation, this relationship does not reach statistical significance ($p = 0.1608$).

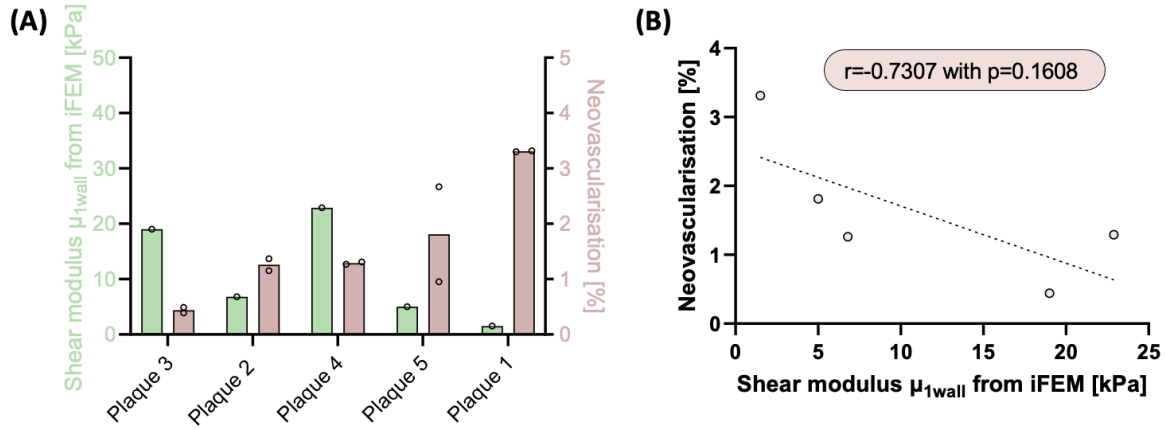

Figure 5.11: (A) Bar plot showing the shear modulus ($\mu_{1\text{wall}}$) derived from iFEM in green and neovascularisation percentages in pink for the n=5 plaque samples. (B) Scatter plot showing a negative correlation ($r = -0.7307$) between neovascularisation and $\mu_{1\text{wall}}$. The p-value (0.1608) indicates that this correlation is, however, not statistically significant.

5.3.5 Plaque classification

The plaques were classified according to the Stary et al. framework, which categorises atherosclerotic lesions into progressive stages based on their structural and compositional features [46]. Figure 5.12 presents the histological sections of the plaques, stained with CD31 for neovascularisation (top row) and H&E for plaque morphology (bottom row).

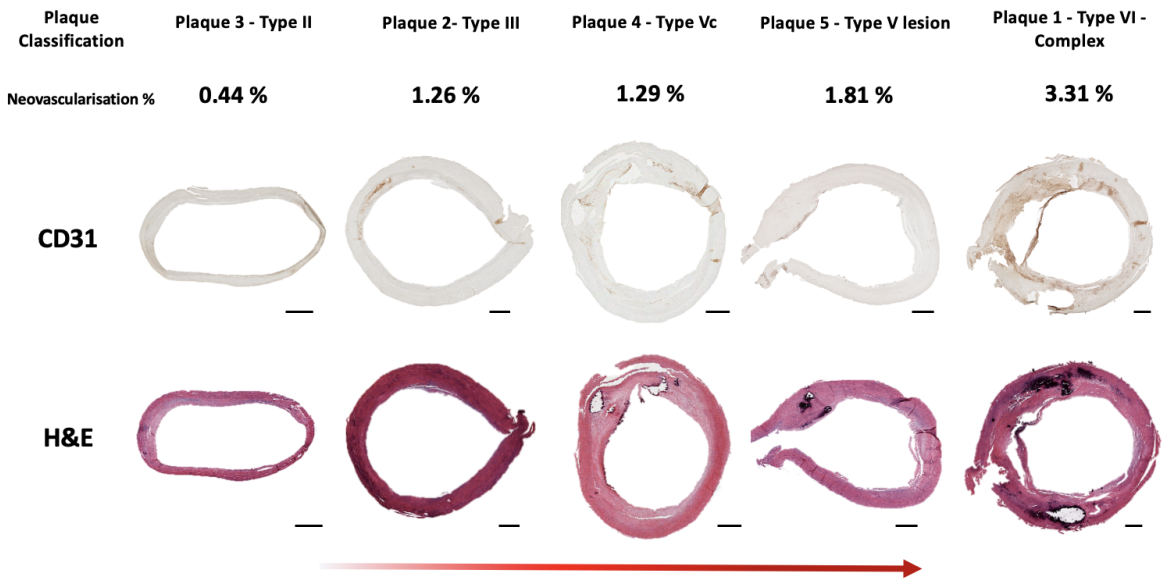

Figure 5.12: Histological sections of atherosclerotic plaques classified using the Stary framework [46]. The top row displays CD31-stained sections highlighting neovascularisation. The bottom row shows H&E-stained. Scale bars: 1 mm.

Plaque 3, classified as Type II, exhibited minimal structural complexity and sparse CD31-positive staining, indicating limited neovascularisation (0.44%). Plaque 2, identified as Type III, displayed slightly increased vascularisation (1.26%). Plaque 4, cat-

egorised as Type Vc, demonstrated the presence of distinct lipid cores, thick fibrous cap and calcifications with localised neovascularisation (1.29%). Plaque 5, classified as a Type V lesion, showed the presence of fibrous structures, necrotic core and calcification with localised neovascularisation in the inner lumen of the plaque (1.81%). Finally, plaque 1, identified as a Type VI (complicated lesion), exhibited the most advanced structure, with extensive CD31-positive staining and the highest neovascularisation percentage (3.31%). This classification highlights a trend of increasing neovascularisation with plaque complexity. More advanced plaques, such as Type V and Type VI, displayed greater neovascularisation compared to less developed plaques, such as Types II and III.

5.4 Discussion

This study used US imaging, inflation testing, iFEM, and immunohistochemistry to investigate the relationship between neovascularisation and mechanical behaviour in excised human carotid atherosclerotic plaques.

Inflation testing demonstrated significant variability in deformation and compliance across the samples. Plaques with higher compliance, such as plaque 2 and 5, exhibited uniform lumen expansion. In contrast, plaque 3, showed limited deformation, demonstrating stiffer behaviour. Localised deformation patterns observed in plaques 1 and 4 further emphasise the importance of regional mechanical behaviour. Interestingly, Robertson et al. found differences in compliance measurements extracted from OCT wall motion analysis between calcified plaques and lipid-rich plaques in the femoral arteries. Lipid-rich plaques were significantly softer than the surrounding tissue, with a compliance of 117±20% relative to the surrounding tissue ($p < 0.01$), while calcified plaques were stiffer, with a compliance of 81±16% relative to the surrounding tissue ($p < 0.01$) [219].

Investigating the mechanical behaviour of different plaque components has been crucial in understanding their structural variability. Teng et al. conducted uniaxial tensile tests on strip samples from the media, fibrous cap, lipid core, and intraplaque haemorrhage/thrombus, demonstrating a highly variable mechanical response across these components [181]. Their findings revealed that the fibrous cap and media are consistently stiffer than lipid-rich or thrombotic regions, reinforcing the role of structural composition in plaque mechanics. Similarly, Davis et al. focused on uniaxial tensile testing of the fibrous cap, specifically characterising its behaviour. Their study provided valuable insights into the material properties critical for assessing plaque vulnerability, particularly in evaluating fibrous cap rupture risk [197]. Walsh et al. highlight the need for standardised methodologies in uniaxial testing to improve comparability between studies [220]. However, they also advocate for methods that enable

in vivo characterisation of diseased tissue, highlighting the necessity of techniques that capture mechanical behaviour under physiological conditions that are also translatable clinically.

While these studies provide a strong foundation for understanding the mechanical properties of key plaque components, they do not account for the role of neovascularisation, which has been increasingly recognised as potential marker of plaque progression and instability [24].

This work integrates neovascularisation, investigating its relationship with plaque deformation during inflation testing. While compliance measures provided insight into global plaque stiffness, Y-displacement maps revealed areas of inhomogeneous deformation in plaque samples such as plaque 1 and 4. The integration of mechanical and microstructural information, with a focus on clinical translatability, is crucial for advancing the management of atherosclerotic disease. For example, Schaar et al. demonstrated the potential of US-based palpography as a tool for assessing vulnerable plaques. They defined vulnerable plaques as atheromas covered by thin caps less than 250 μm thick and found that high-strain regions adjacent to low-strain areas strongly correlated with histologically defined vulnerable plaques [221]. Their study underscores the predictive value of IVUS techniques in discriminating vulnerable plaques and highlights the importance of combining imaging and mechanical analysis for clinical applications [221].

US-derived displacement maps provided spatial information into plaque deformation and revealed heterogeneous mechanical responses within our dataset. Plaques 2 and 5 showed high displacement magnitudes and more homogeneous wall expansion, while plaque 3 displayed limited displacement, indicating greater stiffness. In contrast, plaques 1 and 4 showed localised regions of increased displacements, particularly in the upper-right sections, suggesting asymmetrical deformation. The displacement patterns observed generally align with compliance measurements (Figure 5.4 and Figure 5.5). Plaque 5, which had the highest compliance (0.27 mm^2/mmHg), exhibited the largest displacement magnitudes. Similarly, plaque 3, which had the lowest compliance (0.1 mm^2/mmHg), exhibited the least displacement, showing its stiffer mechanical properties. However, in plaques 1 and 4, displacement maps revealed localised regions of increased deformation despite their intermediate compliance values (0.11 mm^2/mmHg and 0.1 mm^2/mmHg, respectively). This highlights the added value of displacement maps in identifying heterogeneous mechanical responses through spatial information within the plaque cross-section. By identifying areas of high and low displacement within the same plaque, this approach complements compliance measures. However, since the plaque samples did not experience the same pressure ranges, iFEM was employed for further characterisation, enabling a more comprehensive evaluation of the plaque's material properties.

The boundary matching framework introduced in Chapter 3 for PVA phantoms was thus further expanded to excised human atherosclerotic plaques. This approach provided a computational perspective on plaque deformation, complementing the experimental displacement maps derived from US. A direct comparison between these two methods offers valuable insights, particularly in capturing spatial variations in deformation and stiffness across different plaques. However, noticeable differences emerged in the magnitude and spatial distribution of displacements. The absolute errors between US and iFEM displacement values varied across plaques, with the best agreement observed for plaque 3 (0.3 mm) and the largest discrepancies for plaque 1 (0.56 mm).

In the iFEA, plaques with higher compliance yielded lower stiffness parameters ($\mu_{1\text{wall}}$), while stiffer plaques had higher $\mu_{1\text{wall}}$ values. For instance, plaque 5, which had the highest compliance (0.27 mm^2/mmHg), exhibited a relatively low $\mu_{1\text{wall}}$ value (5 kPa), consistent with its higher compliance. Conversely, plaque 4, which demonstrated one of the lowest compliance values (0.1 mm^2/mmHg), exhibited the highest $\mu_{1\text{wall}}$ value (22.9 kPa), confirming its stiffer mechanical nature. Plaque 3 exhibited a relatively high $\mu_{1\text{wall}}$ value (19 kPa) and a compliance of 0.1 mm^2/mmHg. In contrast, plaque 1 exhibited the lowest $\mu_{1\text{wall}}$ value (1.4 kPa) despite having a compliance (0.11 mm^2/mmHg) that was only slightly higher than plaque 3 with, however, the final optimised error was also relatively high ($\epsilon = 0.51$ mm).

The $\mu_{1\text{wall}}$ values derived in this study ranged from 1.5 kPa to 22.9 kPa, reflecting variability in plaque stiffness. These values show concordance with those reported by Teng et al., who found μ_1 values of 13.92 kPa for the fibrous cap, 6.83 kPa for the media, 4.75 kPa for lipid-rich regions, and 1.43 kPa for intraplaque haemorrhage [152]. Particularly, the lower $\mu_{1\text{wall}}$ values in this study for softer plaques closely correspond to Teng et al.'s findings for lipid-rich and haemorrhagic regions. In contrast, the higher $\mu_{1\text{wall}}$ values from this study for stiffer plaques are substantially lower than those reported for hypocellular (93.73 kPa) and calcified plaques (84 kPa) [222], [223].

Interestingly, the iFEM performed well for plaques with relatively homogeneous wall expansion, such as plaque 2 and plaque 5, where displacement patterns were more uniform. In these cases, iFEM successfully captured the mechanical response of the plaque with reasonable accuracy. However, for plaques exhibiting more complex deformation patterns such as plaque 1 and plaque 4, which had localised regions of increased displacement iFEM struggled to reproduce these heterogeneities.

In this study, we present a clinically translatable framework based on non-invasive US imaging-derived mechanical characterisation of plaques to explore neovascularisation as a potential microstructural marker that could be assessed *in vivo* through CEUS [73], [119]. We employed immunohistochemistry using CD31 immunostaining to evaluate neovascularisation levels after *ex vivo* inflation testing.

Of note, no clear correlation was observed between neovascularisation and vessel

compliance. For instance, while plaque 1 exhibited the highest level of neovascularisation, it did not correspond to the highest or lowest compliance. Similarly, plaque 5, with the greatest compliance, displayed similar levels of neovascularisation. The shear modulus ($\mu_{1\text{wall}}$) exhibited a negative correlation with neovascularisation, as shown in Figure 5.11(B); however, this relationship was not statistically significant ($p = 0.1608$). While a larger sample size might reinforce this trend, it is worth noting that our dataset encompasses plaques across different grades, from less vulnerable to highly complex plaques, as shown in Figure 5.12, allowing to capture the plaque progression spectrum.

When considering plaque complexity, we observed an increasing degree of neovascularisation with advancing plaque stages, as categorised by the Stary classification [46]. This trend highlights the potential role of neovascularisation as a marker of plaque progression, warranting further investigation into its clinical implications. Advanced plaques, such as Type V and Type VI, demonstrated greater CD31-positive staining compared to less complex plaques, such as Types II and III. These findings are consistent with studies highlighting neovascularisation as a hallmark of plaque progression and its association with rupture risk [24], [61].

An interesting observation emerged in the study: in plaque 4, regions of high displacement during inflation co localised with areas of dense neovascularisation, as identified through CD31 staining. On the other hand, plaque 3 exhibited low neovascularisation and showed the stiffest behaviour. Li et al. investigated the role of neovessels in plaque vulnerability using two-dimensional plaque models derived from CEUS imaging [224]. They implemented a one-way fluid-structure interaction model to simulate the effects of pulsatile blood flow on the plaque structure, including the embedded neovessels. Their findings demonstrated that the pulsatile flow caused significant deformation of the neovessels, particularly in regions of high stress and strain. This deformation was hypothesised to increase the likelihood of IPH. Additionally, Ma et al., combined CEUS with 2D strain imaging to assess carotid plaque vulnerability [225]. Strain parameters were significantly higher in unstable plaques (defined based on histological features), with peak strain and strain rate correlating positively with CEUS-derived peak intensity, microvascular density, and VEGF expression [225]. These findings emphasise the importance in combining mechanical features and microstructural ones to gain a better understanding of plaque stability assessment.

This study underscores the clinical relevance of combining US-based mechanical testing with neovascularisation assessment. Such an approach provides a comprehensive understanding of plaque behaviour and could contribute to improved risk stratification in cardiovascular disease. However, translating these findings into clinical practice requires further validation and this study holds several shortcomings.

Firstly, the displacement maps were derived solely from Y-direction displacements, without incorporating lateral (X-direction) information. While a complete 2D dis-

placement field would provide a more detailed representation of plaque deformation, US-based displacement estimation in the lateral direction is known to have a lower signal-to-noise ratio (SNR) than in the axial direction [16], [17]. Even though peak pressures differed between samples, these displacement maps provided additional insight into plaque deformation patterns.

In addition, while the iFEM based on boundary matching provides a powerful tool for estimating material properties from US data, several limitations must be acknowledged. One major limitation is the assumption of isotropic material behaviour in 2D finite element models. Atherosclerotic plaques exhibit complex anisotropic properties due to collagen fibres, yet the inverse modelling approach in this study assumes isotropic behaviour. This assumption simplifies the parameter estimation process but may introduce inaccuracies in capturing the true mechanical response of the tissue [155], [226].

In this study, the iFEM assumes a single-material model for the plaque wall, which may not adequately capture spatial variations in mechanical properties. To address this, previous studies have integrated multimodal imaging for plaque composition mapping. Akyildiz et al. utilised histology-based co-registration to spatially map plaque components, while Guvenir et al. employed MRI co-registration for component tracking [16], [17]. Hegner et al. computed *in vivo* strains from 4D US and used histology and FEA based registration in murine aortic aneurysms [227]. This framework allowed to correlate deformations within segmented tissue regions. However, co-registration techniques remain limited by resolution mismatches and registration errors. Narayanan et al. proposed a boundary-matching method incorporating IVUS for plaque component delineation. While this approach enables the inclusion of additional boundaries for matching, IVUS remains an invasive imaging modality. An alternative approach explored in a recent study by Latorre et al. involved gradient strain-based methods to infer plaque composition [203]. This technique offers a non-invasive means of detecting material heterogeneity, potentially improving the accuracy of biomechanical modelling. Nevertheless, our framework presents a clinically translatable approach, as it implements inflation testing, displacement maps and iFEM solely based on non-invasive US imaging, offering a promising step towards *in vivo* plaque characterisation. As mentioned in Chapter 4, this study does not replicate the dynamic, pulsatile environment *in vivo* conditions due to the quasi-static nature of the inflation testing.

Neovascularisation quantification was based on the mean of two histological slices, providing a representative but limited assessment of neovascularisation within the plaque. This approach may not fully capture the three-dimensional heterogeneity of neovascularisation throughout the sample. Nevertheless, these findings offer valuable initial insights, and expanding the analysis to include additional slices along the plaque's length could improve the characterisation of neovascularisation patterns and

their potential role in plaque behaviour.

Overall, this study presents an innovative framework integrating US-based mechanical testing with neovascularisation analysis, highlighting its potential to enhance the identification and risk stratification of vulnerable plaques. Despite its promise, this type of testing remains highly challenging and does not allow for a systematic assessment of rupture, as rupture dynamics cannot be fully captured in a single cross-section.

To address this, the next chapter will incorporate uniaxial tensile testing of carotid plaque strips in the circumferential direction. This approach aims to achieve greater specificity in linking mechanical rupture metrics with neovascularisation, contributing to the establishment of neovascularisation as a clinically significant marker for plaque vulnerability.

Chapter 6

Low Ultimate Tensile Strain in Atherosclerotic Plaques is Linked to Presence of Neovascularisation: Insights from *Ex Vivo* Uniaxial Tensile Testing

6.1 Introduction

Several studies in the literature have focused on exploring plaque microstructure and their link to mechanical behaviour using advanced imaging techniques. Johnston et al. have used small angle light scattering to evaluate the dominant fibre orientation in plaque caps [19]. Findings in the literature highlight the need for further investigation into the local microstructure of the tissue to better understand its mechanical behaviour [20], [21], [179]. However, the use of non-invasive imaging or microstructural information directly linked with mechanics and translatable to the clinic is still scarce. Maher et al. used clinical US imaging to classify plaques as either calcified, mixed or echolucent revealing that calcified plaques exhibited the stiffest behaviour while echolucent plaques were the least stiff [179]. Tornifoglio et al. used a specific MRI sequence, namely diffusion tensor imaging to non-invasively obtain collagen fibre orientation. Although this technique is promising, translation from the lab to the clinic still requires considerable advancements, particularly in reducing the sequence acquisition time [20].

Despite extensive efforts in the literature, a direct link between composition and plaque vulnerability remains lacking. As no current clinical imaging technique directly

correlates composition with mechanical rupture of plaque, it is crucial to investigate the *ex vivo* mechanical characterisation of plaque incorporating microstructural information that could be translated into clinical practice.

This study aims to bridge this gap by investigating the relationship between neovascularisation and plaque vulnerability. By employing uniaxial tensile testing, this study directly assesses plaque mechanical failure while incorporating histological quantification of neovascularisation. This combined approach seeks to establish whether the presence and extent of neovascularisation can serve as an indicator of mechanical instability, ultimately aiming to surpass the limitations of percent stenosis as a sole predictor of plaque rupture risk.

6.2 Material and methods

An overview of the methods used in this study are shown in Figure 6.1.

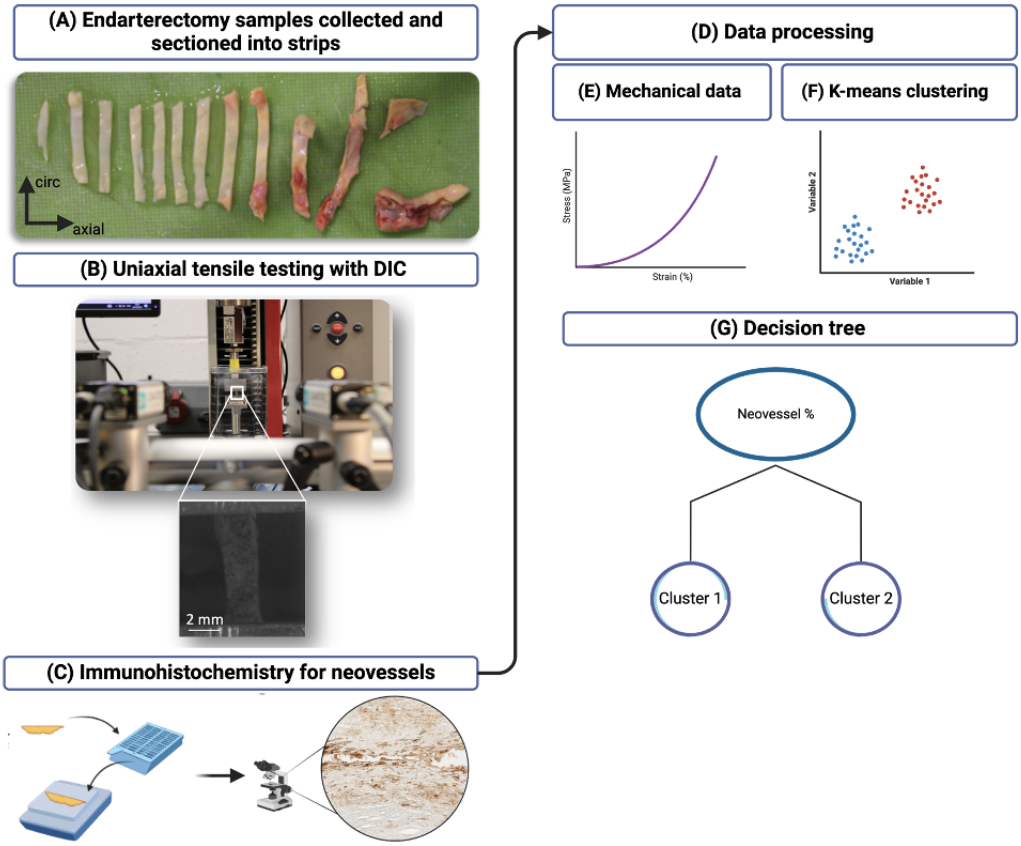

Figure 6.1: Brief overview of methods. A) Excised endarterectomy carotid sample cut into strips. B) Photograph of strip mounted for uniaxial tensile testing. C) Schematic of immunohistochemistry workflow. D) Data processing flow. E) Representative stress-strain extracted from mechanical testing. F) K-means clustering. G) Decision tree classifier implemented to investigate neovascularisation as a classifier between the clusters.

6.2.1 Sample acquisition

Carotid atherosclerotic plaques (n=7) were obtained from symptomatic carotid endarterectomy patients at the Galway Clinic, see Figure 6.2. Ethical approval was granted in accordance with the Declaration of Helsinki (2016-12 List 47 (4)). Plaques were rinsed in PBS, cryopreserved, and stored at -80°C until *ex vivo* testing, as detailed in previous chapters.

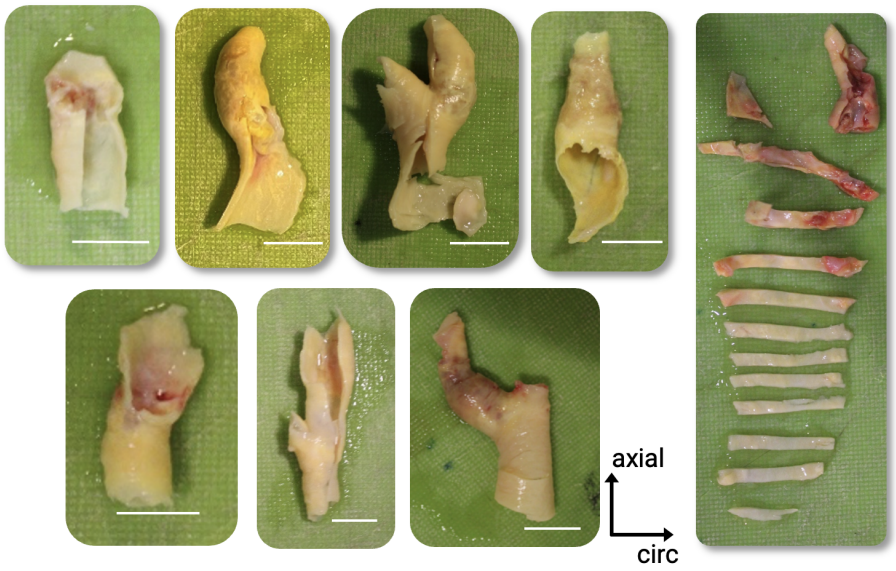

Figure 6.2: Photographs of atherosclerotic carotid plaques cut into strips for testing. Scale bars: 1 cm.

6.2.2 Mechanical testing

Circumferential strips

Samples were thawed at 37°C and rinsed in PBS. Circumferential strips (n=38) were sectioned from the plaques, see Figure 6.3(1). Due to plaque tissue heterogeneity, dog-bone shapes - which are designed to minimise edge stress concentrations and ensure failure occurs at the centre of the gauge length - were not feasible. Plaque samples were cut into rectangular strips 2 mm in width, Figure 6.3(2). The mean thickness for each strip was determined from three measurements taken with the Mitutoyo Litematic VL-50B for accuracy, allowing cross-sectional areas to be calculated. Of the 38 strips tested, 13 were excluded due to failure near the grips, issues with digital image correlation (DIC) analysis, or due to histological processing. To enable DIC analysis, the strips were sprayed with a tissue marking dye (Epredia™, Fisher Scientific) using an airbrush (Kkmoon Airbrush) connected to a single-cylinder piston compressor (ABEST). The workflow is illustrated in Figure 6.3.

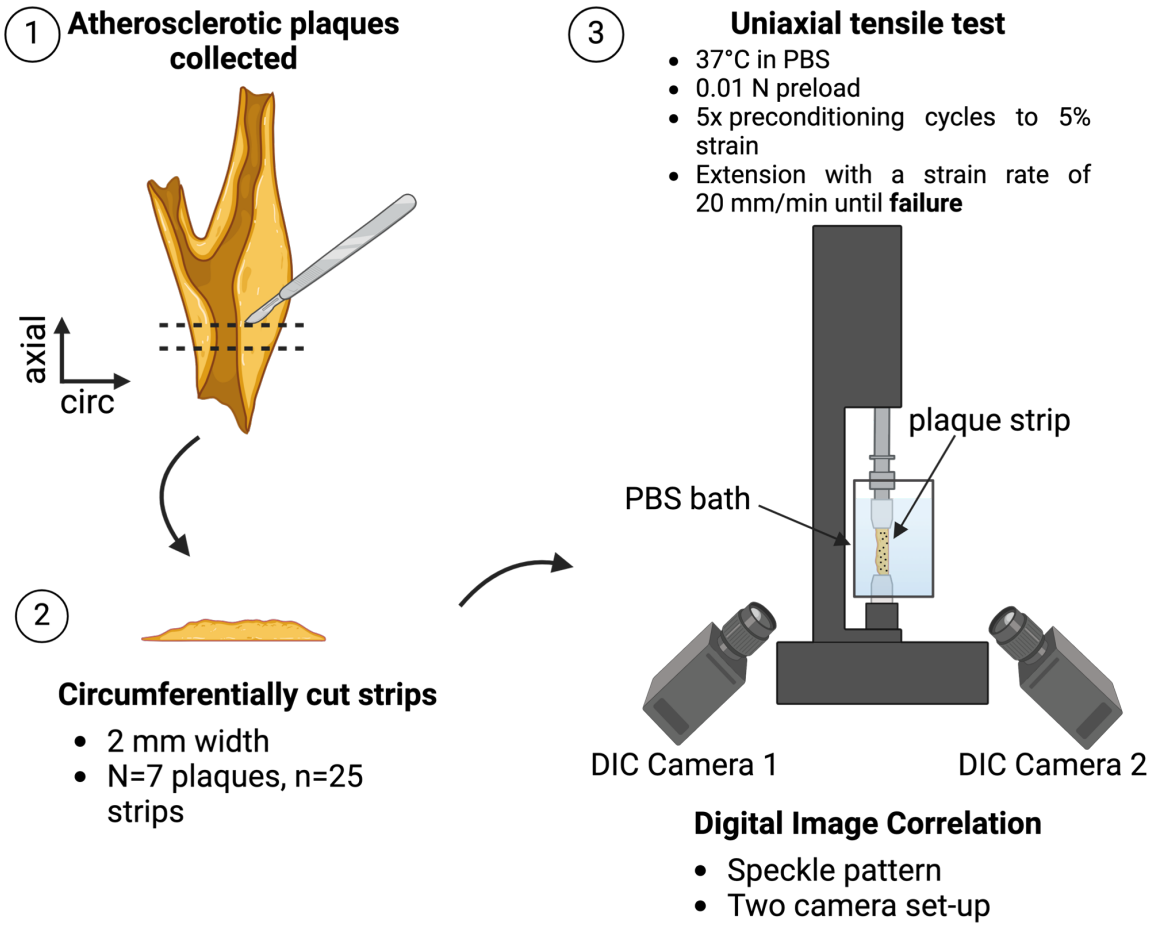

Figure 6.3: Framework for plaque testing.

Uniaxial tensile tests and DIC

Strips were subjected to uniaxial extension until failure using a uniaxial testing machine (Zwick Z005, Zwick GmbH & Co., Ulm, Germany). Strips were loaded in the circumferential direction to provide insights into the mechanical behaviour in the primary load-bearing orientation Figure 6.3(1,2). All tests were conducted in a PBS bath maintained at 37°C. The protocol started with a preload of 0.01 N, after which the force was zeroed, followed by five preconditioning cycles to 5% strain, and extension to failure, see Figure 6.3(3). Each step was performed at a strain rate of 20 mm/min. DIC was employed to track local strain deformations, using a two-camera system (Dantec Dynamics GmbH, Denmark) with prior calibration, see Figure 6.4. Images were captured at 5 Hz. After failure, all samples were fixed in 10% formalin for subsequent histological processing for no more than 48 hours.

6.2.3 Histological analysis

After fixation, strips were processed for histology as described in Chapter 5. Samples were embedded to obtain axial cross-sections, sectioned at 5 μm thickness, and

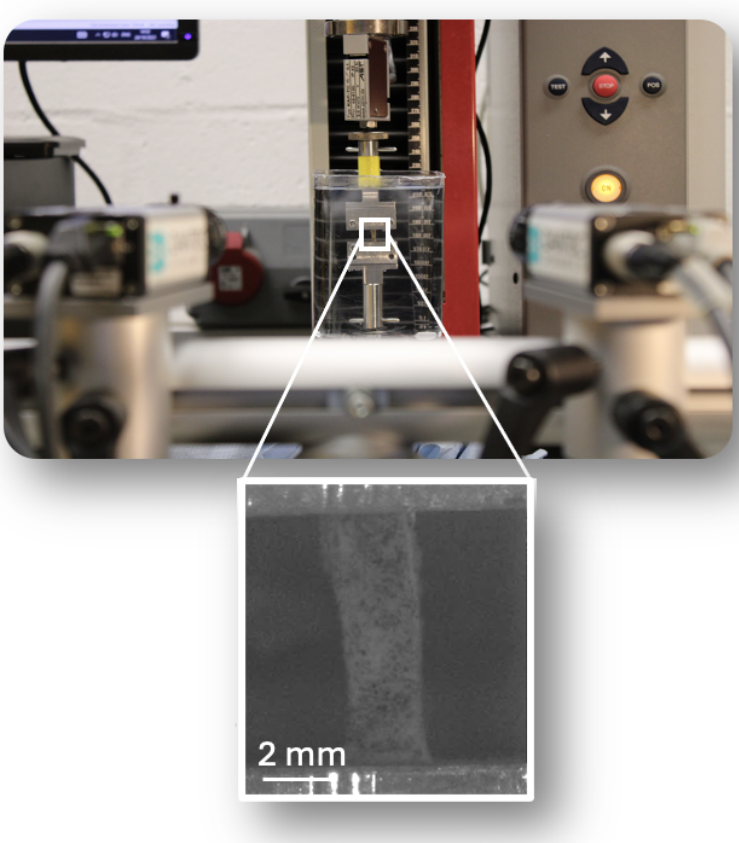

Figure 6.4: Experimental setup for uniaxial tensile testing with DIC. Close-up view shows spray-painted plaque strip for adequate speckle pattern tracking.

stained with H&E and CD31 for neovascularisation assessment. Immunohistochemistry followed the same protocol outlined previously, including antigen retrieval, primary antibody incubation, and DAB staining. Brightfield imaging was performed to visualise neovessels, see Figure 6.5.

Neovascularisation quantification

Neovascularisation quantification was performed using QuPath (v 0.5.1) [218], as previously described in Chapter 5. Two sections per strip were analysed, with tissue regions delineated to exclude folds. Neovessel percentage based on stained area was averaged across both slices to provide a measure of neovascularisation.

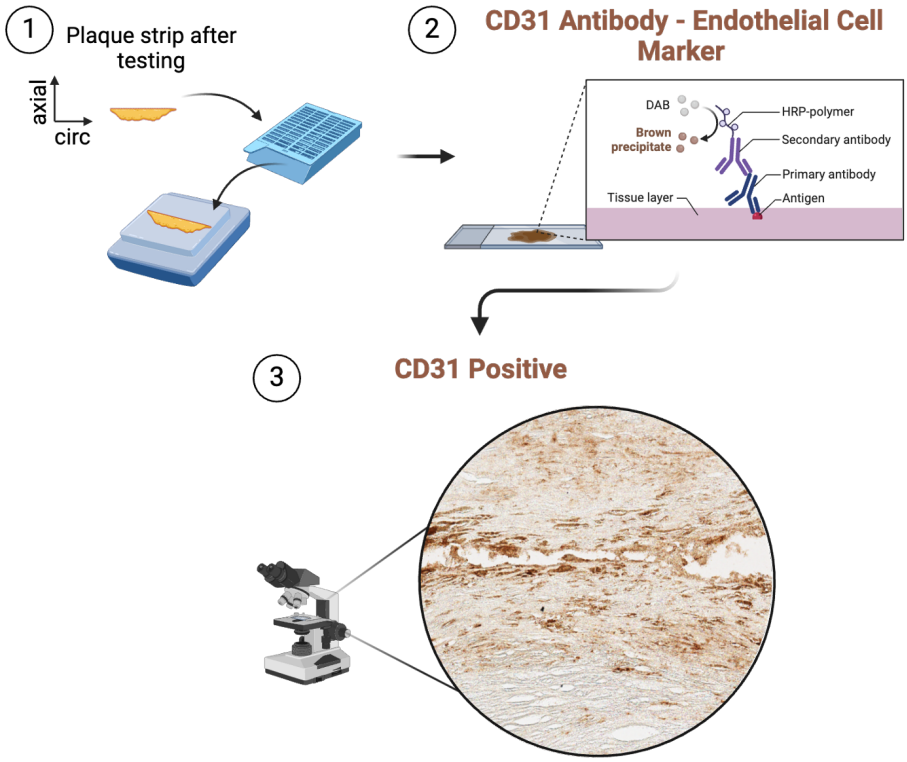

Figure 6.5: Immunohistochemistry workflow to visualise neovessels in strips.

6.2.4 Mechanical data

Engineering stress was calculated using the cross-sectional area of each specimen. The force-displacement curves obtained after preconditioning, were analysed to determine the stress-strain behaviour of the samples. Failure was defined as the point at which a 5% decrease in stress between two consecutive points was first observed [180]. At this point, ultimate tensile (UT) stress and UT strain values were recorded. The final elastic modulus was calculated by fitting a line between the UT stress and 70% of the UT stress, while the initial elastic modulus was defined as the slope of the curve between zero and 5% strain [228]. DIC analysis was conducted using Istra4D software (x64 V4.4.6.534) with the following parameters: facet size of 69, 3D residuum of 10, grid spacing of 15 pixels, and a low outlier tolerance. The reference frame for all analyses was the final frame of the preconditioning cycles, just before extension to failure began. Engineering strain was assessed using DIC in two ways: (1) the average strain across the gauge length on the tissue surface, referred to as DIC strain named DIC-G, and (2) the average strain locally at the failure site, referred to as DIC local failure strain or DIC-L.

6.2.5 K-means clustering and decision tree classifier

A k-means clustering algorithm was implemented to classify strips based on UT stress and UT strain. These parameters were chosen due to their direct relevance to mechanical failure and clear interpretability from stress-strain curves. Additionally, preliminary analyses were conducted to evaluate the impact of adding other mechanical features to UT stress and UT strain for k-means clustering. These are detailed in the supplementary data; however, UT stress and UT strain alone provided the best clustering performance, see Appendix C Figure C.2. As a result, these two features were solely used in the final k-means clustering approach. The optimal number of clusters (k) was determined by evaluating multiple clustering validity indices, including the elbow method, silhouette analysis, Davies-Bouldin index, gap statistic, and Calinski-Harabasz index. These metrics were computed for k values ranging from 2 to 4 to assess clustering robustness. Based on these analyses, $k = 2$ was selected as the most appropriate cluster number, balancing intra-cluster compactness and inter-cluster separation. A detailed evaluation of the different clustering metrics is presented in Appendix C, Figure C.3.

Neovascularisation percentages, quantified from histological analysis, were then extracted for each identified cluster. To validate neovascularisation as a discriminative feature between the two clusters, a decision tree classifier was trained using neovascularisation percentages as the predictor variable and the k-means cluster labels as the response. The classification accuracy was calculated as:

$$\text{Accuracy} = \frac{TP + TN}{TP + TN + FP + FN} \tag{6.1}$$

where TP refers to true positives, TN to true negatives, FP to false positives, and FN to false negatives. True positives and true negatives indicate correctly classified samples within their respective clusters, while false positives and false negatives represent misclassified samples. A receiver operating curve (ROC) curve was plotted, and the area under the curve (AUC) was calculated to quantify the discriminative ability of the classifier.

6.2.6 Statistical analysis

Statistical analyses were performed using GraphPad Prism (Version 10). All data were tested for normality using the D'Agostino-Pearson test and for equality of variances using Brown-Forsythe ANOVA. If normality was not met, non-parametric tests were applied. Pearson's correlation coefficients (r) were used to assess relationships between mechanical properties and neovascularisation, with correlation strengths defined as follows: weak ($r < 0.3$), moderate ($0.3 < r < 0.7$), and strong ($r > 0.7$). Outliers were identified using the ROUT method (maximum false discovery rate =

1%, $Q = 1\%$). Any identified outliers were excluded from statistical analysis but are displayed in supplementary data. Results are presented as mean ± standard deviation (SD) for t-tests, median with interquartile range (IQR) for Mann-Whitney tests, and median with 95% confidence intervals (CI) in figures where applicable.

6.3 Results

Across the 25 strips, a significant variability in mechanical properties was observed, as illustrated in Figure 6.6(A-D). This variability is further evidenced by the different responses to load observed in the stress-strain curves, as shown in Figure 6.6(E). The average uniaxial tensile (UT) stress and strain for the samples were 0.47 ± 0.46 MPa and 32.6 ± 18.5% strain, respectively. The mean initial modulus was 0.54 ± 0.63 MPa. The overall mean final elastic modulus across all samples was calculated as 2.30 ± 2.28 MPa.

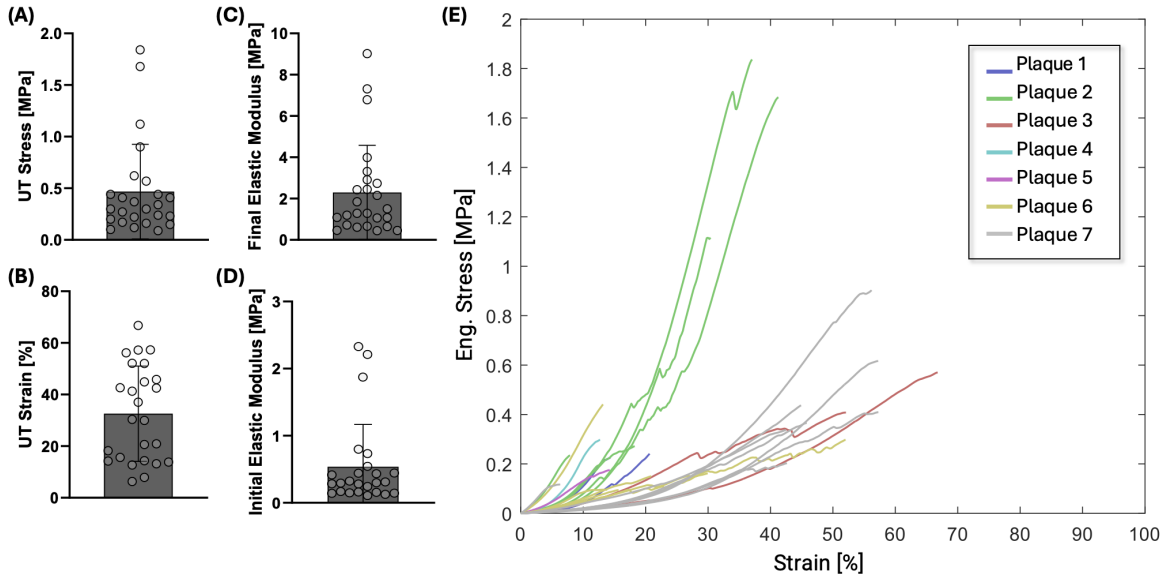

Figure 6.6: Mechanical properties of carotid atherosclerotic plaque strips (n=25). (A) UT Stress [MPa], (B) UT Strain [%], (C) Final elastic modulus [MPa], (D) Initial elastic modulus [MPa] and (E) Engineering stress-strain curves for n=25 strips, colour coded by their respective plaque provenance. Note that SD exceeds the lower limit for the initial elastic modulus, resulting in clipped error bars at zero.

DIC allowed for visualisation of the progression of strain from the initial state to the point of rupture, with localised strain significantly higher at failure sites compared to the mean strain across the tissue surface, see Figure 6.7. This is also shown quantitatively by comparing localised strains at failure points, DIC-L, to DIC-G strain, where DIC-L was significantly higher than DIC-G. Additionally, the grip-to-grip strain substantially overestimated the DIC-G strain on the tissue surface.

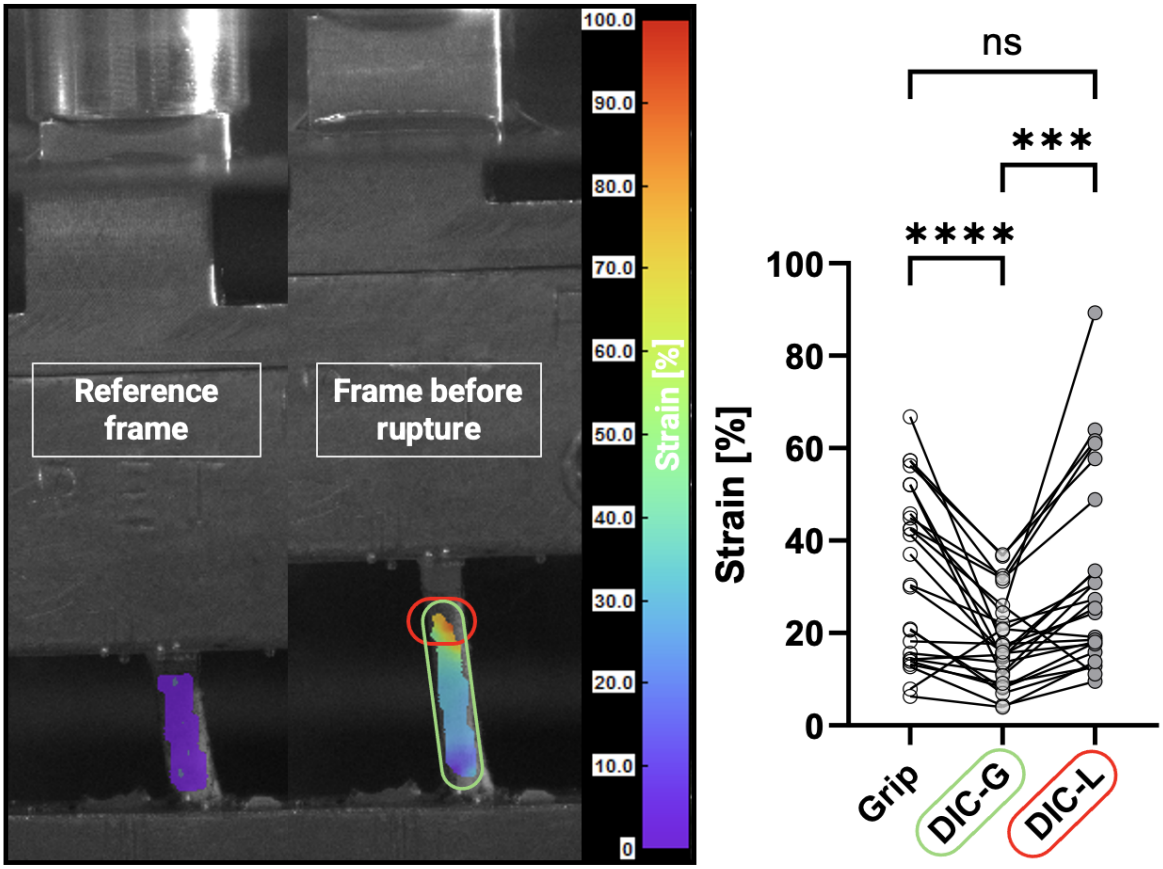

Figure 6.7: Strain maps at the reference frame and the frame before rupture, with DIC highlighting localised strain concentrations at failure (circled in red) and strain distribution across the surface (circled in green). Grip-to-grip strain (Grip), mean DIC strain across the tissue surface (DIC-G), and localised DIC strain at failure (DIC-L) are compared, demonstrating significant differences between these measurements. Statistical significance was assessed using repeated measures one-way ANOVA with Tukey's post hoc multiple comparisons; ns = not significant, ***p < 0.001, ****p < 0.0001.

Notably, strain maps revealed that rupture locations coincided with regions of maximum localised strain in $n = 20$ out of the total $n = 25$ tested strips, emphasising the role of localised strain concentration in mechanical failure. This is shown in Figure 6.8, which groups all tested plaque strips by parent plaque. Strain maps and rupture locations are presented for each strip. Moreover, the relationship between UT stress and localised DIC-L strain at failure is illustrated in Appendix Figure C.1. Each plaque strip is represented as an individual data point, with the corresponding strain maps visually confirming the location of rupture (circled in red).

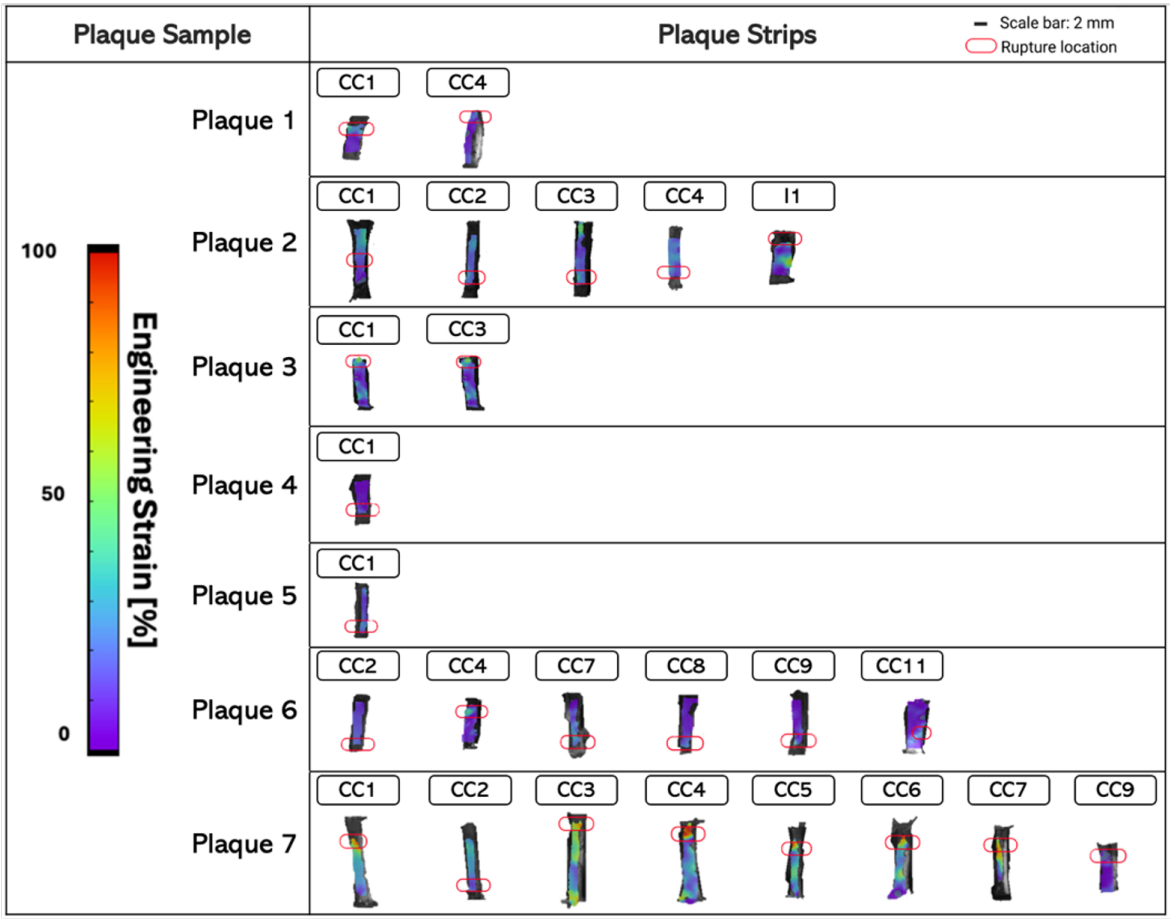

Figure 6.8: Summary of strain distribution and rupture locations across all tested plaque strips. Digital image correlation (DIC) maps for each strip are shown, grouped by plaque. The colour bar represents localised engineering strain (%). Rupture locations are indicated with red ellipses. In 20 of the 25 tested strips, rupture occurred at or near the region of highest strain, supporting the relationship between local deformation and failure. Scale bar: 2 mm.

Neovascularisation was quantified for each plaque, and after performing outlier analysis, one data point was excluded. Additionally, due to histological processing, some sections were not analysable and therefore excluded from the analysis, leaving a final sample size of $n = 23$. Figure 6.9 shows the correlations between neovascularisation percentages and mechanical properties extracted from strip testing, including UT stress, UT strain, and initial and final elastic moduli. A weak negative correlation was observed between UT stress and neovascularisation ($r = -0.2412$). In contrast, UT strain showed a statistically significant moderate negative correlation ($r = -0.4585$, $^*p = 0.0278$), indicating that strips with higher neovascularisation tend to fail at lower strains. The final elastic modulus exhibited no meaningful correlation with neovascularisation ($r = -0.0376$), while the initial elastic modulus displayed a negligible positive correlation ($r = 0.0468$), suggesting no significant interaction in either case. Among all mechanical properties analysed, UT strain demonstrated the strongest relationship with neovascularisation. Additionally, to enhance interpretation, the area correspond-

ing to UT strain values below 20% has been shaded in red, representing a threshold for typical physiological circumferential strain in human carotid arteries. This visual aid highlights that many plaque strips with higher neovascularisation percentages failed below this physiological strain level. These findings suggest that plaques rich in neovessels may rupture under normal or even sub-physiological loading conditions, reinforcing their mechanical vulnerability and supporting the role of neovascularisation as a clinically relevant marker of plaque instability.

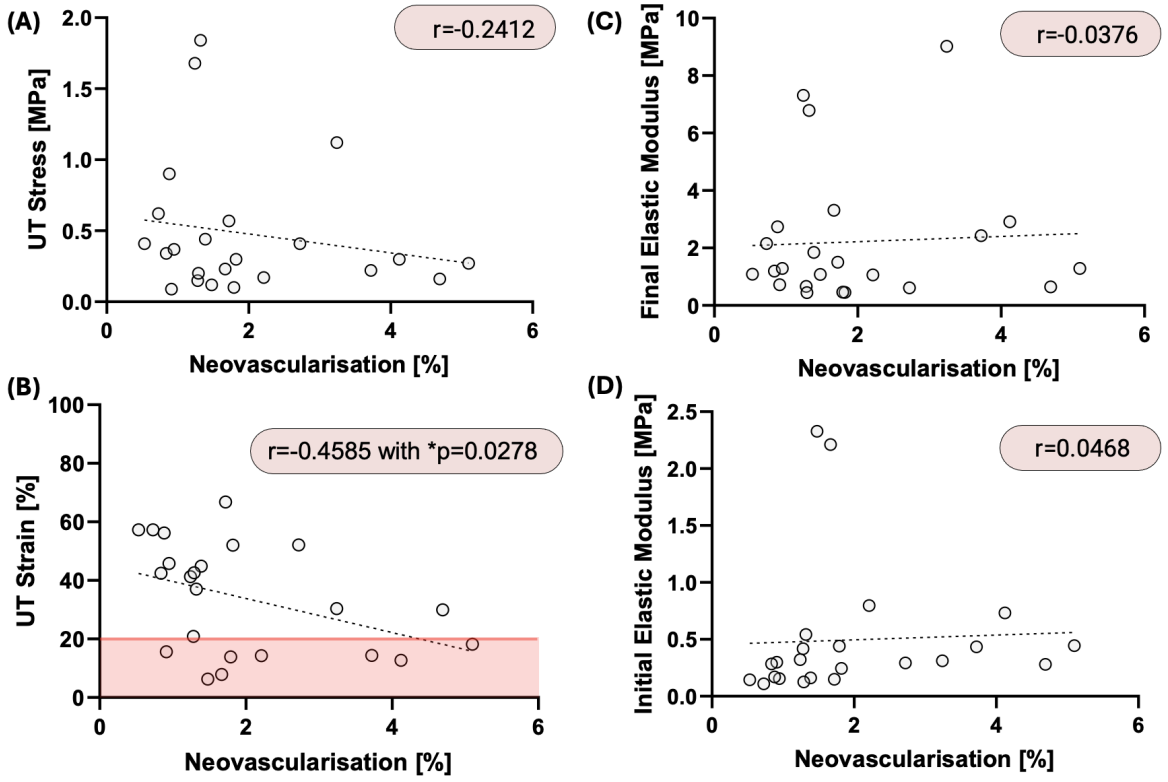

Figure 6.9: Scatter plots showing correlations between neovascularisation percentage and (A) UT stress, (B) UT strain, (C) final elastic modulus, and (D) initial elastic modulus for n=23 strips. Dashed lines represent linear regression fits. Shaded red region highlights the area below 20% UT strain, corresponding to the average physiological circumferential strain range typically experienced in human carotid arteries. Correlation coefficients (r) are provided, with significant correlations denoted by an asterisk ($^*p < 0.05$).

Additionally, a strong negative correlation ($r = -0.6420$, $^{***}p < 0.001$) was found between UT strain and the initial elastic modulus, see Figure 6.10. This trend suggests that strips with higher initial elastic modulus tend to fail at lower strains.

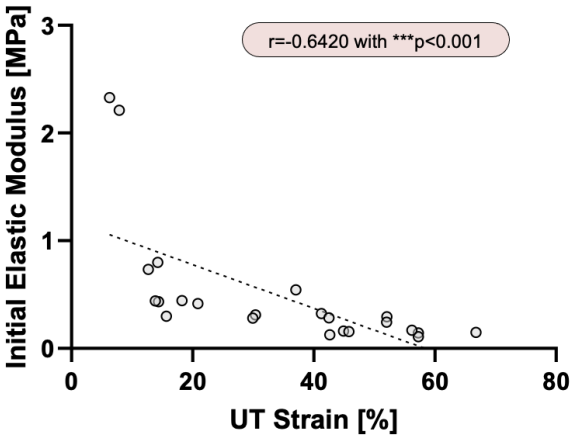

Figure 6.10: Scatter plot showing correlation between UT strain and initial elastic modulus of n=23 strips.

Figure 6.11 illustrates the relationship between UT strain and UT stress, with bubble sizes representing the percentage of neovascularisation. The plot highlights a distribution pattern where plaque strips exhibiting lower UT strain tend to have higher neovascularisation percentages, as shown by the cluster of larger bubbles within the red ellipse. This observation suggests that increased neovascularisation is associated with reduced strain at failure corroborating with findings seen in Figure 6.9(B).

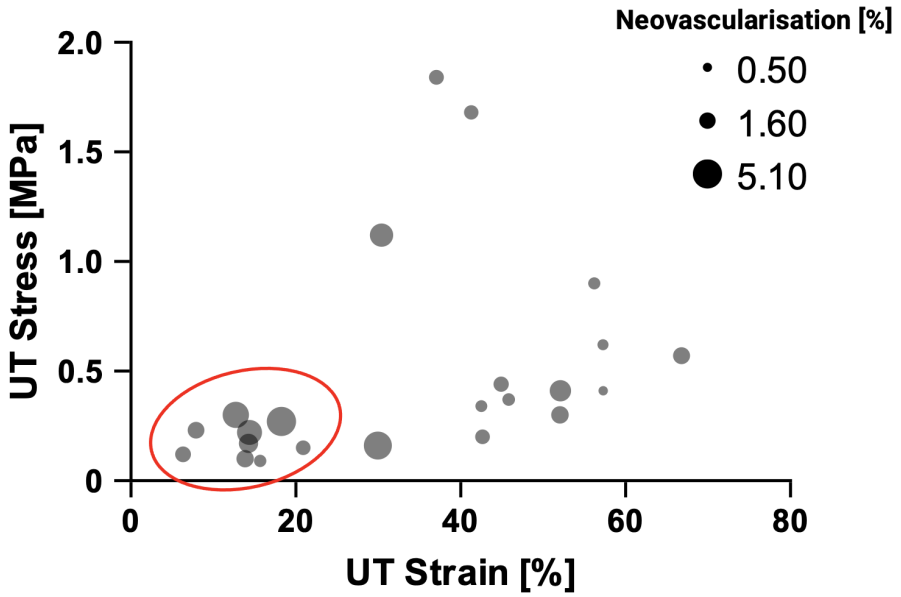

Figure 6.11: Bubble plot showing the relationship between UT strain and UT stress, with bubble sizes representing the quantification of neovascularisation percentages. The red ellipse highlights a cluster of plaques with low UT strain where larger bubbles indicate higher neovascularisation percentages.

The observed pattern between neovascularisation and mechanical behaviour highlighted in Figure 6.11 prompted further investigation. To gain deeper insights, k-means clustering was applied, dividing it into two clusters based on UT stress and UT strain.

Figure 6.12 provides an overview of the clustering results. Panel (A) shows the stress-strain curves for each sample, with data points coloured by cluster (cluster 1: red, cluster 2: blue), and cluster centroids marked with black crosses. Panel (B) further visualises the separation of the two clusters where each point represents a specific strip specimen, colour-coded by plaque. The clustering revealed two distinct behaviours within the dataset. Cluster 1 primarily consists of samples with lower UT strain values, suggesting a group of plaques that fail earlier under tensile loading. In contrast, cluster 2 includes samples capable of withstanding higher strains before failure. Interestingly, some strips from individual plaques predominantly belonged to a single cluster. Notably, strips from plaque 6 predominantly belonged to cluster 1, reflecting its distinct mechanical properties characterised by lower UT strain. In contrast, strips from plaque 7 were largely grouped in cluster 2, indicative of higher ability to strain before failing. However, overlap was observed for strips from plaques 2 and 6, with some strips appearing in both clusters, suggesting that these plaques exhibit mixed mechanical characteristics.

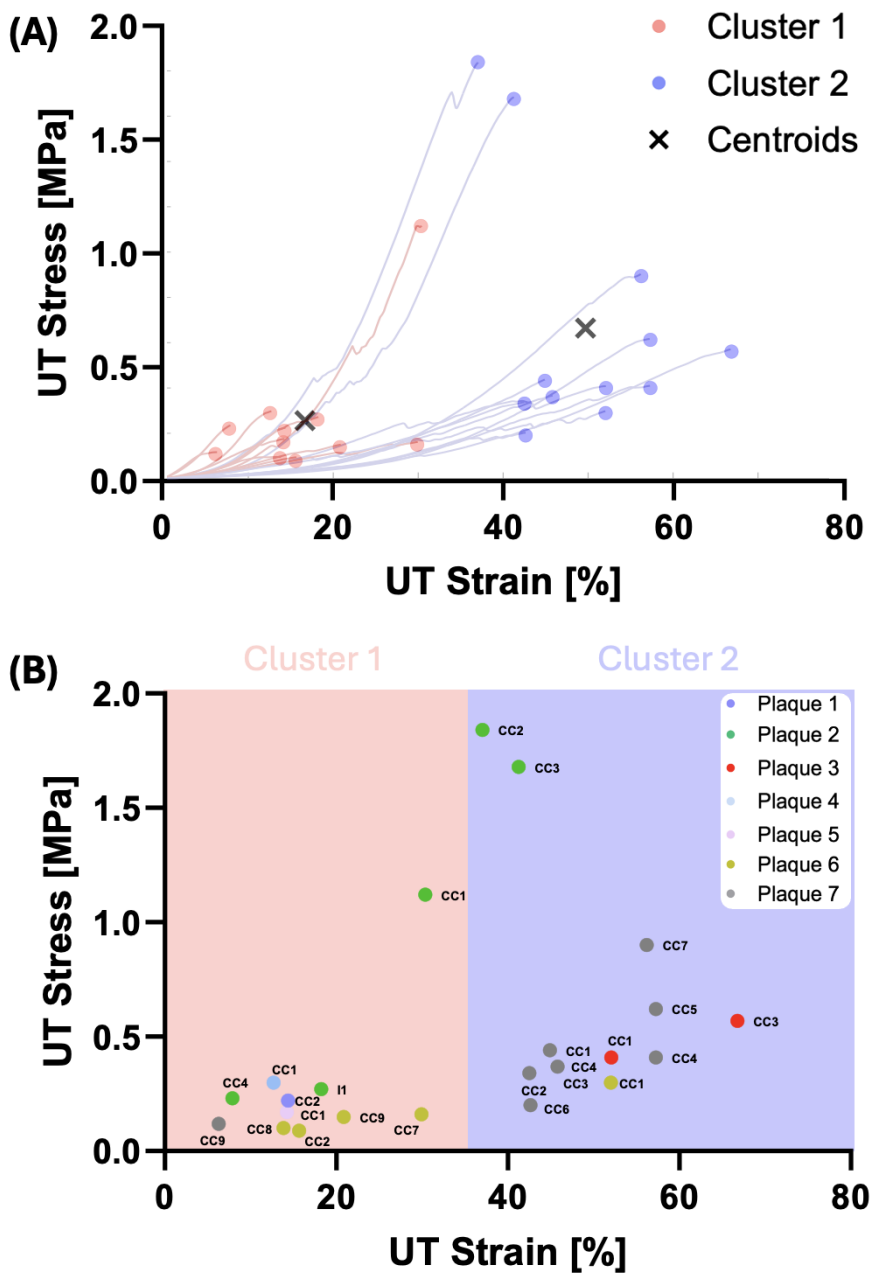

Figure 6.12: (A) Stress-strain curves for strips clustered into two groups using k-means clustering (cluster 1: red, cluster 2: blue). Cluster centroids are marked with black crosses. (B) Scatter plot of UT strain versus UT stress, showing the distribution of samples across the two clusters. Each point is colour-coded by plaque identifier, highlighting the distinct mechanical behaviours of the two groups. CC: common carotid, I: internal.

To further characterise the strips within each cluster, Figure 6.13 integrates the k-means clustering results with histological observations. Representative histological sections, including H&E and CD31 staining, are shown for strips closest to each cluster centroid. The H&E staining highlights areas of heterogeneity within one strip from cluster 1, specifically at the rupture region. CD31 staining reveals increased neovascularisation, particularly in this thickened, disorganised zone. In contrast, a

representative strip in cluster 2, displays less complex and more homogeneous tissue structures. The H&E staining reveals more organised tissue layers and CD31 staining further demonstrates reduced neovascularisation. Red rectangles in the figure highlight magnified zones for a closer examination of tissue organisation where rupture occurred showing no presence of neovascularisation for the strip in cluster 2. These observations are further shown in supplementary data, see Appendix C, Figure C.5 and Figure C.6.

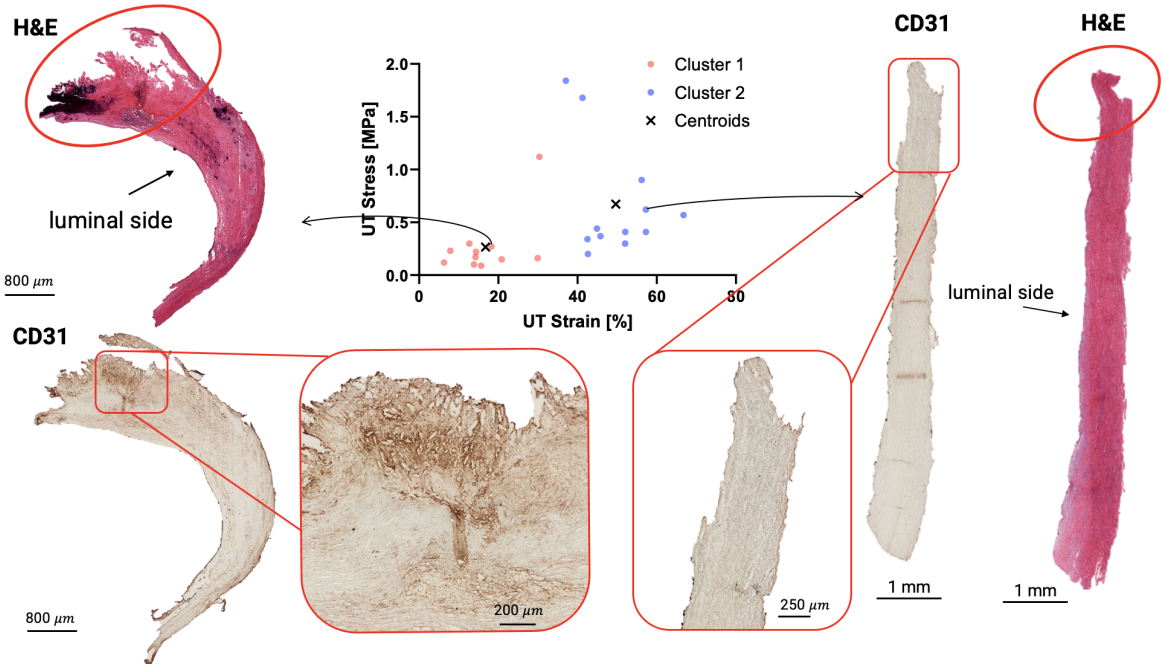

Figure 6.13: Combined k-means clustering of UT stress versus UT strain with representative histological sections (H&E and CD31 staining) for strips closest to each cluster centroids. Scatter plot shows the two clusters (cluster 1: red, cluster 2: blue) with centroids marked as black crosses. Red rectangles indicate magnified zones for detailed visualisation of tissue organisation and neovascularisation.

Figure 6.14 compares neovascularisation, DIC-L, final elastic modulus, and initial elastic modulus between cluster 1 and cluster 2. Neovascularisation percentages were significantly higher in cluster 1 (Median = 2.21%, IQR = 2.64) compared to cluster 2 (Median = 1.27%, IQR = 0.79) ($^{**}p < 0.01$, Mann-Whitney test), see Figure 6.14.(A). For DIC-L, a significant difference was found, with cluster 2 (43.92% ± 23.34) exhibiting significantly higher values than cluster 1 (20.60% ± 7.62) ($^{**}p < 0.01$, t-test), see Figure 6.14.(B). This indicates that strips in cluster 2 experience greater strain at rupture compared to those in cluster 1. The final elastic modulus showed no significant difference between clusters (cluster 1: 1.46 ± 1.04 MPa, cluster 2: 1.31 ± 1.31 MPa) ($p = 0.74$, *ns*, t-test), see Figure 6.14.(C). The initial elastic modulus was significantly higher in cluster 1 (Median = 0.43 MPa, IQR = 0.28) compared to cluster 2 (Median = 0.17 MPa, IQR = 0.15) ($^{**}p < 0.01$, Mann-Whitney test), see Figure 6.14.(D). This suggests that strips in cluster 1 exhibit greater initial stiffness but fail at lower strains compared to cluster 2. Outliers were observed in initial and final elastic modulus

measurements for cluster 1. These outliers were not included in the statistical analysis but are presented in the supplementary data for completeness, see Appendix C, Figure C.4.

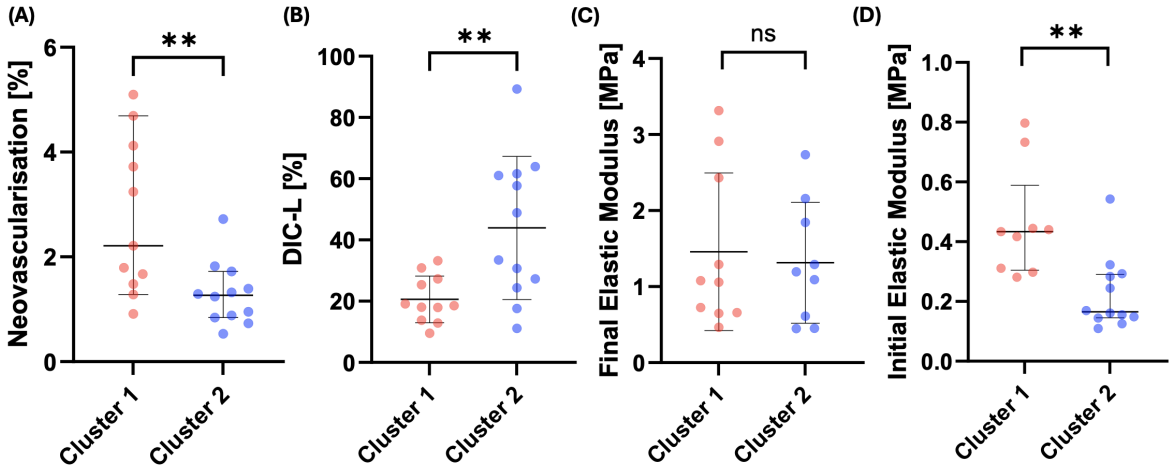

Figure 6.14: Comparison of mechanical and structural properties between cluster 1 (red) and cluster 2 (blue). (A) Neovascularisation percentages, analysed using the Mann-Whitney test (**$p < 0.01$), reported as median with 95% CI. (B) DIC-L, analysed using a t-test (**$p < 0.01$), reported as mean ± SD. (C) Final elastic modulus, analysed using a t-test ($p = 0.74$, ns), reported as mean ± SD. (D) Initial elastic modulus, analysed using the Mann-Whitney test (**$p < 0.01$), reported as median with 95% CI. Black horizontal lines indicate either median or mean values, depending on the statistical test used.

The decision tree classifier identified a neovascularisation threshold of 1.44% as the optimal cut-off for classifying the two clusters. This threshold yielded a classification accuracy of 78.26%, suggesting that neovascularisation alone provides a reasonable, though not perfect, discriminant metric for mechanical clustering. To further assess the classification performance of neovascularisation as a discriminant metric between clusters, a ROC curve was generated (Figure 6.15). The ROC curve illustrates the trade-off between sensitivity (true positive rate) and specificity (false positive rate) in classifying plaques into the two clusters. The AUC was found to be 0.784, indicating that the decision tree model performed significantly better than random guessing.

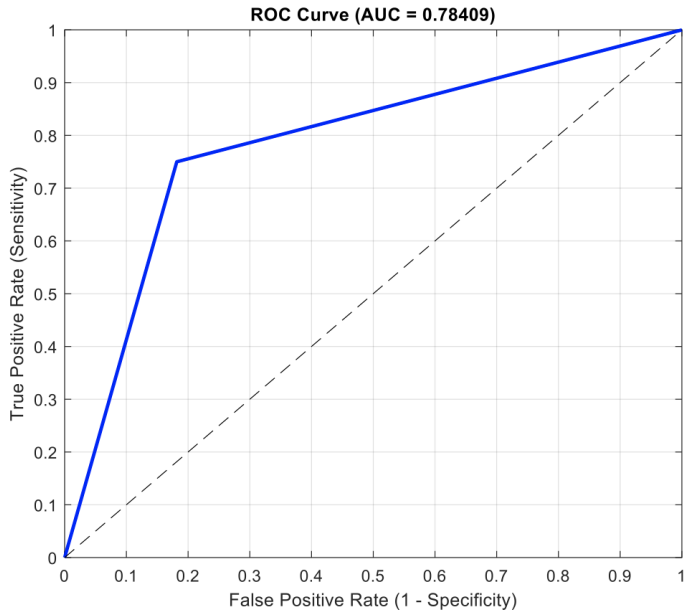

Figure 6.15: Decision tree classification of plaques based on neovascularisation percentage. The optimal threshold of 1.44% yielded a classification accuracy of 78.26%.

6.4 Discussion

This study provides significant insights into the relationship between neovascularisation and the mechanical properties of carotid atherosclerotic plaques. Neovascularisation has long been recognised as a key feature of atherosclerotic plaque instability. Virmani et al. emphasised neovascularisation's critical role in advancing plaque vulnerability by facilitating microvessel formation and intraplaque haemorrhage [24], [61], [121]. These studies highlight how neovascularisation has remained a focal point in understanding plaque instability, emphasising its critical potential in identifying and addressing vulnerable plaques. Multimodal US techniques have significantly advanced the assessment of carotid atherosclerotic plaques. Among these techniques, CEUS has emerged as a powerful tool for visualising intraplaque neovascularisation [116]. The ability of CEUS to capture and quantify IPN highlights its utility in both research and clinical settings, where it can complement other imaging modalities like SWE [117]. Feinstein et al. highlighted the critical role of neovascularisation within carotid atherosclerotic plaques as a marker of vulnerability with the use of CEUS for visualising the vasa vasorum and assessing plaque pathology as well as guiding clinical management to prevent cerebrovascular events [118]. Huang et al. found that neovascularisation originates predominantly from the adventitial vasa vasorum linking vascular remodelling to plaque instability [229]. This joins Moulton's review which examines the role of plaque angiogenesis in atherosclerosis, highlighting that neovascularisation within atherosclerotic plaques primarily arises from the adventitial vasa vasorum and extends into the intima [63]. Additionally, studies have shown the high correlation between histology-based

neovascularisation and CEUS [119], [120]. Many studies in the literature have tackled the question inquiring the role that neovascularisation plays in atherosclerosis. Shah et al. emphasised the critical association between IPN and plaque instability, with a particular focus on the impact of radiotherapy (RT) [230]. Their findings demonstrated that plaques in patients with prior RT exhibited significantly increased IPN compared to non-RT plaques. Interestingly, RT is strongly associated with a heightened risk of ischaemic stroke, potentially due to the presence of neovascularisation and its contribution to plaque instability.

However, few studies have explored the connection between plaque mechanical behaviour and neovascularisation, leaving this area of research still relatively scarce [69]–[71], [73]. Tian et al. used CEUS and found increased neovascularisation in soft plaques [73]. Wang et al. found that plaques with lower echogenicity and lower Young's modulus showed increased neovascularisation [70]. Zhang also showed the predictive power of SWE and CEUS for stroke [71]. On the other hand, Zhang et al. found a negative correlation between neovascularisation and elasticy, where increased neovascularisation was synonym of lower elasticity [69]. This aligns with our findings, where strips with higher neovascularisation were associated with greater initial elastic modulus, see Figure 6.14.(D).

The variability in the mechanical response of carotid plaques observed in this study is consistent with previously reported findings [19]–[21], [156], [197], [220], [231]. Loree et al. measured the tangential moduli of atherosclerotic plaques under a tensile stress of 0.025 MPa and reported values of 0.927 ± 0.468 MPa for cellular samples, 2.312 ± 2.180 MPa for hypocellular samples, and 1.466 ± 1.284 MPa for calcified samples [231]. These values overlap with the range of final elastic modulus observed in our study, which was 2.30 ± 2.28 MPa. Similarly, Tornifoglio et al. reported a mean final elastic modulus of 1.26 ± 0.6 MPa, further supporting the consistency of our findings with existing literature.

Additionally, the UT stresses observed in this study are comparable to those reported in prior studies. Lawlor et al. found Cauchy stresses ranging from 0.131 to 0.779 MPa, while Johnston et al. recorded UT stresses of 0.31 ± 0.18 MPa and 0.87 ± 0.63 MPa for axially and circumferentially aligned plaque cap samples, respectively [19], [232]. Guvenir et al. reported UT stresses ranging from 0.12 to 0.36 MPa, which align well with the mean UT stress of 0.47 ± 0.46 MPa found in this study [21]. Similarly, Tornifoglio et al. reported mean UT stress values of 0.293 ± 0.2 MPa, which also overlap with our results [20].

For UT strains, Lawlor et al. reported Green strains between 0.299 and 0.588, while Johnston et al. observed values of 0.13 ± 0.04 and 0.09 ± 0.04 for axially and circumferentially aligned plaque cap samples, respectively [19], [232]. Guvenir et al. noted stretch ratios between 1.16 and 1.64, showing some overlap with our findings,

where the mean UT strain was 32.6 ± 18.5% [21]. Additionally, Tornifoglio found UT strains of 38.3 ± 19% which are similar to our findings [20]. These comparisons further underscore the alignment of our findings within the literature while highlighting the variability in mechanical behaviour of atherosclerotic tissue.

Another interesting observation relates to the rupture initiation regions reported by Guvenir et al. which exhibited significantly higher stretch ratios (1.26 [1.15–1.40]) compared to the tissue's average stretch ratio (1.11 [1.10–1.16]) [21]. This aligns with our findings that strain at rupture (DIC-L) was significantly higher than strain across the tissue surface (DIC-G). A similar observation was made in the study by Tornifoglio et al., further supporting the idea that strain could serve as an indicator of plaque vulnerability [106], [233], [234].

In a recent study, Crielaard et al. performed uniaxial tensile testing on tissue-engineered fibrous cap analogues and demonstrated that rupture initiates and propagates through regions of high strain, mirroring patterns observed in human plaques [147]. This observation is further supported by our findings, where DIC revealed that rupture locations consistently coincided with regions of maximum localised strain in $n = 20$ out of the total $n = 25$ tested strips. The coincidence of rupture location and high strain concentration highlights the importance of incorporating localised strain metrics when assessing plaque vulnerability, as these regions may represent focal points for mechanical instability and potential rupture.

Adding to this, correlation analysis in this study, revealed that UT strain demonstrated the strongest association with neovascularisation with statistically significant moderate negative correlation ($r = -0.4585$, $^{*}p = 0.0278$). This moderate correlation between UT strain and neovascularisation underscores its role on plaque mechanical vulnerability highlighting the critical importance of integrating mechanical metrics with microstructural information. UT strain was also found to be significantly correlated to the initial elastic modulus ($r = -0.6420$, $^{***}p < 0.001$) where lower UT strain are associated with higher initial elastic modulus.

Furthermore, the scatter plot reveals a notable pattern where larger bubbles, representing higher neovascularisation percentages, seem predominantly associated with lower UT strain values, see Figure 6.11. This observation suggests that plaques with greater neovascularisation may rupture at lower strain, further reinforcing the interplay between microstructural features and mechanical properties in plaque vulnerability. A closer examination of the scatter plot through that k-means clustering further highlights this behaviour within the dataset. Cluster 1, characterised by lower UT strain, was associated with higher neovascularisation percentages and demonstrated significantly higher initial elastic modulus, see Figure 6.14.(A,D). In contrast, strips in cluster 2 displayed higher UT strain, as well as lower initial elastic modulus, see Figure 6.14.(A,D).

Such observations support the hypothesis that neovascularisation, through its association with immature and leaky microvessels contributes to overall plaque instability [24], [61]. Teng et al. investigated the mechanical environment surrounding neovessels and found that neovessels experienced the highest levels of stress and stretch during the cardiac cycle through finite element analysis and histological analyses [72]. These mechanical conditions around neovessels are potentially driving the progression of IPH. This highlights the critical role of neovascularisation in understanding and managing plaque vulnerability. Supporting this, Saba et al. emphasised the importance of neovascularisation as a factor in the RADS scoring system, further linking it to an increased risk of plaque rupture [23]. Li et al. used numerical simulations based on CEUS images to evaluate stress and strain distribution within carotid atherosclerotic plaques [224]. Their findings indicate that neovessels within plaques are particularly prone to deformation, which can lead to rupture. Altogether, these findings highlight the power in integrating both plaque mechanical as well as microstructural characteristics to enhance risk assessment.

In this study specifically, combining neovascularisation with mechanical properties highlighted the potential to provide deeper insights into plaque vulnerability. The findings in this study suggest that neovascularisation may contribute to mechanical instability as neovascularisation was moderately negatively correlated with UT strain reinforced by the k-means clustering revealing that strips with lower strain at failure exhibited significantly higher neovascularisation and greater initial elastic modulus. To further assess the discriminative power of neovascularisation in classifying mechanical behaviour, a decision tree classifier was implemented using neovascularisation percentage as the sole predictor variable. The classification results revealed an optimal threshold of 1.44% neovascularisation for distinguishing between the two k-means clusters, achieving an overall classification accuracy of 78.26%. This suggests that neovascularisation alone provides a reasonable, though not absolute, metric for stratifying plaques based on their mechanical properties. Additionally, the ROC curve analysis demonstrated an AUC of 0.784, further supporting the ability of neovascularisation to differentiate between plaques with lower and higher UT strain at failure. Together, these findings demonstrate that neovascularisation may contribute to mechanical instability, supporting its role as a potential marker for plaque mechanical integrity.

This study is, however, subject to some limitations that warrant consideration. First, uniaxial tensile testing which was conducted on *ex vivo* samples, does not fully replicate the physiological *in vivo* conditions. However, the strips were tested axially to replicate physiological loading in the circumferential direction, making the findings still relevant to understanding plaque behaviour under loading.

Furthermore, while uniaxial tensile testing offers valuable insight into rupture mechanics, it does not replicate the repetitive, cyclic loading environment experienced *in*

vivo. Arterial tissues are subjected to continuous pulsatile pressure and cyclic mechanical stresses, which can induce fatigue-related damage over time. As such, future investigations incorporating fatigue loading protocols would be essential to better mimic physiological conditions and assess time-dependent plaque weakening mechanisms.

Secondly, the quantification of neovascularisation relied on histological analysis, which provides only a partial measurement of its spatial variability through the whole plaque. Specifically, the analysis was based on two histological slices per plaque, with neovascularisation averaged across these sections. This approach may not fully capture the heterogeneous distribution of neovascularisation throughout the entire plaque. Nonetheless, the moderate but significant correlation observed between UT strain and neovascularisation from immunohistochemistry offers promising insights into the relationship between neovascularisation and plaque instability.

Future studies should prioritise *in vivo* evaluation of neovascularisation using readily available techniques like CEUS, which can provide a more comprehensive view of neovascularisation distribution and its association with mechanical properties. Such imaging methods could enhance our understanding of plaque vulnerability and improve clinical risk stratification. Additionally, ongoing advancements in US imaging, such as SMI, could enable non-contrast quantification of neovascularisation, making these techniques more accessible for routine clinical use [130]–[133].

While this study focused on individual strips, the overlap of plaques between clusters suggests that strip-level analysis may not fully capture the mechanical behaviour of entire plaques. Some plaques predominantly contributed to one cluster, while others exhibited characteristics spanning the two clusters. This variability highlights the importance of whole-plaque studies that integrate mechanical testing with imaging to better understand the spatial heterogeneity of plaque properties.

As mentioned, the relationship between plaque neovascularisation, progression, and symptoms remains complex and unresolved. For example, while inflammation has been shown to be more pronounced in symptomatic patients, neovascularisation does not consistently correlate with symptoms [235]. On the other hand, Nardi et al. found that symptomatic plaques were associated with IPH, which is closely linked with neovascularisation [75].

To our knowledge, this is the first study to establish a link between neovascularisation and rupture mechanical metric, specifically UT strain, showing that plaques with higher neovascularisation have lower UT strain, indicating greater vulnerability. By integrating imaging-derived metrics with mechanical properties, clinicians could better stratify patients and optimise surgical interventions. This approach moves beyond the traditional reliance on stenosis as a primary risk metric, advocating for a multimodal assessment of plaque vulnerability. Given that neovascularisation is already measurable using clinical tools like CEUS, its incorporation into clinical workflows could facilitate

improved risk assessment with minimal barriers to bridge the gap between the lab and the clinic.

Chapter 7

Final discussion

Cardiovascular diseases remain the leading cause of death worldwide, with carotid artery disease contributing to 10–20% of all strokes [3]. High-risk plaques, often referred to as 'vulnerable plaques', exhibit specific features, including a lipid-rich necrotic core and a thin fibrous cap [5].

Current clinical guidelines for determining whether a patient should undergo carotid endarterectomy rely predominantly on the degree of stenosis, a metric that quantifies lumen narrowing [6]. However, evidence suggests that stenosis alone is insufficient to fully assess rupture risk, as it fails to capture critical structural and compositional features of plaques associated with vulnerability [7], [8].

Non-invasive imaging modalities offer a promising avenue for refining risk assessment, enabling early detection of high-risk plaques and potentially reducing the burden of cardiovascular diseases. MRI is widely regarded as the gold standard for detailed plaque characterisation, offering the ability to distinguish features such as lipid cores, calcifications, and intraplaque haemorrhage with high accuracy [14]. However, its high cost, lengthy scanning times, and limited accessibility restrict its routine use in clinical settings. In contrast, US offers a faster, more cost-effective alternative that is highly adaptable to existing clinical workflows [15]. Advances in US techniques have further enhanced its utility by enabling the assessment of features such as plaque neovascularisation and stiffness. This has led to increasing interest in ancillary features that provide a more comprehensive understanding of plaque vulnerability. The recently introduced plaque RADS-score emphasises the need for multimodal imaging to assess additional characteristics such as intraplaque haemorrhage, lipid content, as well as neovascularisation [23]. Particularly, neovascularisation has gained increasing interest in the field. While it is being increasingly recognised as a factor to consider in clinical management, research investigating its direct impact on plaque mechanical behaviour remains limited [69]–[71]. Despite efforts to explore this relationship, the connection between

neovascularisation and plaque mechanics is still not fully understood, underscoring the need for further investigation.

This thesis aims to bridge the gap in understanding the relationship between plaque mechanics and neovascularisation by combining *ex vivo* mechanical testing of phantoms and diseased human tissue, US imaging, and microstructural analysis. A key focus is to investigate how neovascularisation influences plaque mechanical integrity, recognising its potential as a critical biomarker of rupture risk. By integrating these methodologies, this work seeks to refine risk assessment beyond stenosis as a sole predictor, providing a more comprehensive framework for evaluating plaque vulnerability.

Chapter 3 focused on PVA cryogel-based artery phantoms to simulate atherosclerotic plaques under physiological conditions. By fabricating phantoms with tunable mechanical properties through controlled FTCs, along with varying stenosis levels and lipid pool inclusions, this study provided key insights into the mechanical responses of diseased vessels [142]–[144], [146]. Chapter 3 also outlined a comprehensive characterisation framework integrating inflation testing and non-invasive US imaging. This framework enabled the evaluation of lumen expansion, strain distributions, and mechanical heterogeneity across different phantom designs. The results highlighted that higher strains were observed in the plaque shoulder regions, particularly in phantoms with higher degrees of stenosis. Additionally, higher stenosis levels resulted in reduced lumen expansion under increasing pressure, reinforcing the role of stenosis severity in arterial compliance [198]. To enhance material characterisation, this study introduced a boundary-matching-based iFEM framework to accurately estimate mechanical properties from inflation testing data. This methodology, adapted from Narayanan et al., was adapted to non-invasive US imaging allowing for parameter estimation [183]. The integration of iSight automation streamlined the iterative optimisation process, offering an efficient approach to characterising plaque-mimicking materials. By combining mechanical testing, US imaging, and computational modelling, this chapter provides a foundation for inflation testing of human atherosclerotic carotid plaques, explored in Chapters 4 and 4. The findings from this initial study lay the groundwork for subsequent investigations, where the relationship between plaque stiffness and neovascularisation is explored in more clinically relevant applications.

While Chapter 3 established a robust framework for studying atherosclerotic plaque mechanics using PVA phantoms mocking diseased vessels, it remained a surrogate approach. To move closer to clinical relevance, Chapter 4 extends this work to fresh human carotid endarterectomy samples. Building on the inflation testing framework developed in Chapter 3, this chapter adapts the methodology to address the challenges of testing human diseased tissue, such as maintaining sample integrity and replicating physiological conditions. This transition is critical for clinically meaningful insights into plaque tissue. A novel, watertight inflation setup was designed to simulate physio-

logical pressures while enabling US imaging. To ensure the feasibility of this approach, compliant balloons were introduced to facilitate plaque inflation. Their mechanical influence was first validated using NPCaAs, demonstrating that balloon insertion did not significantly alter arterial vessel compliance. Applying this framework to human plaques enabled the assessment of their mechanical behaviour under physiological loading conditions, revealing substantial variability in compliance across samples. This study provided a foundation for exploring the relationship between plaque deformation and neovascularisation.

Building on the framework established in Chapters 3 and 4, Chapter 5 integrated mechanical testing, US imaging, and histological analysis to investigate the role of neovascularisation in plaque mechanical behaviour through compliance assessment, displacement maps and iFEA. By combining these approaches, this study provided new insights into the interplay between these metrics. The results revealed substantial variability in compliance and deformation patterns among plaques. Displacement maps generated from US cross-correlation further highlighted these localised variations, revealing spatial differences in deformation across plaques. For further characterisation, the iFEM framework introduced in Chapter 3 was applied to estimate material properties of plaques, revealing a shear moduli values $\mu_{1\text{wall}}$ ranging from 1.4 kPa to 22.9 kPa. Analysis using CD31 staining provided additional insights. While no direct correlation was observed between neovascularisation and compliance, a strong negative, however not significant, trend was found between $\mu_{1\text{wall}}$ values and neovascularisation.

An interesting observation was the co-localisation of high-displacement regions with areas of dense neovascularisation in plaque 4. Additionally, plaque 3 showed the stiffest behaviour among plaque samples with the lowest neovascularisation presence. Altogether, these findings suggests a potential interplay between plaque stiffness and neovascularisation.

The plaque samples tested, spanning from less vulnerable to highly complex, allowed us to observe that neovascularisation levels increased with plaque complexity. This supports existing literature identifying neovascularisation as a hallmark of plaque progression and its association with rupture risk reinforcing its potential role in linking mechanical properties to plaque instability [24], [61].

To further explore the potential of neovascularisation as a marker of vulnerability in atherosclerotic plaques and assess its clinical relevance, Chapter 6 expands on previous findings by analysing failure behaviour in strips in the circumferential direction, the most physiologically relevant orientation. This chapter represents a significant advancement in the field, as it is the first study to directly correlate neovascularisation with failure properties of plaque strips tested under uniaxial tension. This controlled testing framework provides a more precise characterisation of plaque rupture mechanics, enabling failure metrics to be directly linked to neovascularisation. A moderate

but statistically significant negative correlation was identified between UT strain and neovascularisation (r = -0.4585, $^{*}p = 0.0278$), demonstrating that plaques with higher neovascularisation fail at lower strains, indicating increased vulnerability. This finding suggests that strips with higher neovascularisation may be structurally weaker and more prone to rupture. The role of neovascularisation in strips instability aligns with prior findings indicating that intraplaque neovessels may contribute to potential intraplaque haemorrhage [23], [72], [230].

To further characterise strips mechanical behaviour, k-means clustering of UT strain and UT stress identified two distinct plaque phenotypes:

1. Cluster 1: high neovascularisation, lower strain capacity, and increased initial stiffness suggesting greater mechanical instability.

2. Cluster 2: lower neovascularisation, higher strain capacity suggesting greater resilience to loading.

Notably, significant differences were observed between these clusters, with cluster 1 exhibiting higher neovascularisation (2.21% vs. 1.27%,$^{**}p < 0.01$) and significantly lower UT strain compared to cluster 2. Additionally, cluster 1 displayed a significantly higher initial elastic modulus, indicating stiffer behaviour in strips with early failure under mechanical loading. A decision tree classifier using neovascularisation percentage as the sole predictor identified a 1.44% threshold, achieving 78.26% accuracy (AUC = 0.78), highlighting neovascularisation as a reasonable metric for distinguishing strips failing at lower strains. These results reinforce the potential of neovascularisation as a biomarker for plaque vulnerability. By directly linking UT strain with neovascularisation, this study bridges the gap between microstructural information and mechanical integrity, providing a new paradigm for assessing plaque vulnerability. Given that CEUS is already widely used in clinical practice to assess neovascularisation, these findings hold strong potential for translation into clinical workflows to improve risk stratification and rupture prediction [23], [45], [136].

This thesis demonstrates the power of integrating mechanical testing, US imaging, and histological analysis to uncover the intricate relationships between neovascularisation and mechanical properties in atherosclerotic plaques. Chapter 3 laid the groundwork by using PVA cryogel phantoms to investigate plaque mechanics under inflation, incorporating vulnerable features such as lipid-pool inclusions to mimic plaque features. This work also highlighted the feasibility of integrating US imaging, inflation testing, and iFEA into a unified framework, setting the stage for more clinically relevant studies. The findings from Chapter 4 established a robust methodological foundation for plaque testing, introducing a novel inflation testing framework tailored for excised human plaque tissue. Chapter 5 expanded upon this by incorporating US imaging and histological quantification of neovascularisation, providing a multimodal perspective on

plaque stiffness and neovessel presence under simulated physiological conditions. Chapter further deepened this investigation, leveraging uniaxial tensile testing to establish a link between UT strain and neovascularisation. This groundbreaking finding bridges the gap between plaque neovascularisation and mechanical vulnerability, advancing our understanding of plaque rupture risk.

Together, these chapters outline a comprehensive and innovative approach to studying atherosclerotic plaques, emphasising the potential of neovascularisation as a biomarker for vulnerability and moving beyond traditional metrics like stenosis. This work lays the groundwork for improved diagnostic strategies and highlights the importance of a multifaceted approach to assessing cardiovascular disease risk.

7.1 Limitations and future perspectives

It is worth noting that, while promising, the findings of this thesis come with certain limitations. This section explores these challenges and proposes avenues for future research to expand upon this work.

While Chapter 3 focused on the development and mechanical characterisation of PVA phantoms to mimic healthy and diseased arteries, several limitations highlight opportunities for future refinement and application. The tunable properties of PVA align well with the mechanical range of arterial tissues reported in the literature, making it an excellent surrogate material [137], [141]. However, the simplified geometry and lack of anisotropy in the phantoms limit their ability to fully replicate the complex microstructures and physiological loading conditions of native vessels [20], [196]. To address these limitations, the integration of fibres printed through melt electro-writing could be investigated to better emulate plaque tissue [204]. Additionally, developing more physiologically accurate geometries, such as bifurcations, could improve the clinical relevance of these phantoms [143], [148]. More advanced PVA phantoms could also incorporate different grades of neovascularisation while mimicking different stages of atherosclerotic disease. Such advancements could offer a deeper understanding of the mechanisms underlying plaque mechanical behaviour and neovascularisation. This study also opens avenues for investigating various pathologies. For instance, by leveraging the developed inflation testing rig, one could mimic aneurysmal tissue using phantoms with a low number of FTCs. By improving the realism and complexity of PVA phantoms, this work sets the stage for deeper investigations into the mechanical behaviours of plaques but also other pathologies where tissue access can be limited.

Chapter 4 presented a novel methodology for pressurising excised human atherosclerotic plaques, offering valuable insights into their compliance under simulated physiological conditions. However, the study's reliance on single cross-sectional 2D imaging limited the ability to capture the full 3D complexity of plaques. Additionally, the

quasi-static nature of the inflation testing lacked the dynamic and pulsatile environment of *in vivo* conditions, neglecting viscoelastic properties. While this setup allows for a controlled evaluation of vessel expansion and compliance, it does not replicate the dynamic, cyclic stresses that arteries are subject to *in vivo*. As a result, fatigue-related mechanical failure mechanisms could not be assessed. Future studies should consider integrating cyclic or pulsatile inflation to better mimic physiological conditions and gain insight into the long-term mechanical durability of both healthy and diseased vessels.

Chapter 5 focused on exploring the interplay between plaque mechanics and neovascularisation, using a combination of inflation testing, US imaging, and histological analysis. While the potential trend between $\mu_{1\text{wall}}$ values and neovascularisation is promising, this study is limited by the low n numbers. The dataset in this study, however, spans plaques ranging from less vulnerable to highly complex, allowing a visualisation of progression across different stages of plaque vulnerability. When increasing n numbers, future work should also include clinical data such as *in vivo* CEUS of patients before endarterectomy. It is worth noting that all plaques analysed in this study were obtained from patients with 50–70% stenosis. This introduces a degree of selection bias, as plaques with minimal or severe narrowing were not represented. To assess whether the findings are applicable across the broader spectrum of atherosclerotic disease, future work should incorporate samples spanning a wider range of stenosis severity. One can envision a future study where neovascularisation is quantified *in vivo* by following patients until endarterectomy procedure, after which the framework developed in Chapter 3 could be used for subsequent mechanical characterisation. Additionally, not all plaques could be inflated to the full 120 mmHg target due to leakage or early rupture during sealing. These issues made it difficult to apply the same pressure range across all samples. The iFEM implemented in this study provided a computational approach to estimate plaque material properties from non-invasive US imaging. However, the framework assumes one pair of material parameters to be determined for the whole plaque cross-section. While registration-based methods have inherent limitations, non-invasive techniques such as photoacoustic imaging or SWE could enable plaque composition delineation to further refine the iFEM framework [134], [236]. Additionally, future studies could enhance clinical translatability by leveraging the developed inflation framework with advanced US techniques, such as tomographic 3D US, to generate volumetric plaque geometry at each pressure step [237]. Integrating this with a slice-based iFEM boundary-matching approach and *in vivo* CEUS analysis could provide invaluable insights. This would also address a key limitation of this study, where neovascularisation was assessed using only two histological slices per plaque. Incorporating *in vivo* CEUS would not only refine neovascularisation assessment but also take this research a step closer to clinical application. The versatility of

the framework developed in Chapter 5 holds high potential to further explore the role of neovascularisation in a multitude of scenarios with high clinical translatability.

Chapter 6 presented a groundbreaking investigation linking the mechanical failure properties of atherosclerotic plaque strips to neovascularisation, revealing a correlation between UT strain and neovascularisation establishing that strips with higher neovascularisation fail at lower strains. However, several limitations and areas for future exploration should be considered. One key limitation of the study is the reliance on uniaxial tensile testing. While this method provides a controlled environment to study mechanical failure in circumferentially oriented strips, it does not replicate the complex multi-axial loading states experienced by plaques *in vivo*. This limitation was indirectly addressed in the previous chapter through inflation testing, which simulated more physiologically relevant conditions. Additionally, the use of uniaxial tensile testing under monotonic loading presents a limitation. Although this method effectively captures failure behaviour in a controlled environment, it does not replicate the pulsatile stresses experienced by plaques in vivo. Integrating cyclic loading protocols in future studies could help assess the resistance of plaques more accurately. While Chapter 5 suggested a potential trend where high stiffness was associated with low neovascularisation, this contrasts with the findings of this chapter. However, the differing loading conditions make direct comparisons less evident. The integration of both studies could bridge this gap and provide valuable insights into mechanical characterisation under both loading conditions. One could envision a study where *in vivo* CEUS is performed prior to the surgical excision of plaque samples. As mentioned earlier, the framework developed in Chapter 5 would allow for physiological loading of plaque samples and volumetric reconstruction using systems such as PIUR tUS [237]. The samples could then be tested until failure, offering further insights into the role of individual plaque samples within a cluster of strips, as observed in Chapter 6. This combination could offer a more comprehensive understanding of how neovascularisation and mechanical metrics interplay to determine plaque vulnerability. While this study showed a statistically significant correlation between neovascularisation and lower UT strain, this does not imply a causal relationship. The data suggest that plaques with more neovessels tend to rupture at lower strains, pointing to a possible link with mechanical fragility. However, this does not mean that neovascularisation directly causes plaques to become weaker. Future studies could investigate this further, for example by using animal models where neovessel density is manipulated, such as through VEGF administration, and then testing how this affects mechanical failure. Longitudinal studies combining *in vivo* imaging with clinical outcomes could also help clarify whether neovascularisation actively contributes to plaque vulnerability or simply coexists with other features of vulnerability.

7.2 Clinical translation

The findings presented in this thesis emphasise the potential of neovascularisation as a biomarker for assessing atherosclerotic plaque vulnerability. While neovascularisation is already recognised as a hallmark of advanced plaques, its integration into clinical workflows has the power to revolutionise cardiovascular diagnostics [23], [24]. Existing imaging modalities, such as CEUS, provide a robust and non-invasive means to visualise and quantify neovascularisation. CEUS is already available in many clinical settings and has demonstrated exceptional utility in visualising intraplaque neovascularisation *in vivo*. Despite its promise, its adoption remains inconsistent, limiting its impact on routine clinical practice. Studies have demonstrated its effectiveness, with strong correlations to histology-derived neovascularisation measurements [116], [119], [120]. Expanding the adoption of CEUS could have an immediate impact on improving risk stratification and treatment planning for patients with atherosclerosis. Additionally, the field of US imaging continues to evolve, with emerging technologies such as SMI and ULM offering new opportunities to assess neovascularisation. ULM can offer unprecedented detail of IPN making it a transformative modality for evaluating plaque neovascularisation *in vivo* [128], [129]. SMI provides high-resolution visualisation of neovascularisation and has the potential to be seamlessly integrated into routine clinical workflows without the need of contrast agents [127], [131]–[133].

Neovascularisation holds significant promise as a tool for stratifying cardiovascular risk. Beyond its association with advanced plaque stages, neovascularisation correlates with key indicators of vulnerability. This thesis has demonstrated that UT strain correlates with neovascularisation, providing further evidence of its role in governing plaque behaviour. By leveraging these insights, clinicians could better stratify patients based on rupture risk, moving beyond the traditional reliance on stenosis as the primary metric.

While this thesis highlights the potential of neovascularisation, there remains a critical need for studies that delve deeper into its clinical implications. Large-scale *in vivo* investigations are essential to validate the findings from *ex vivo* studies and to establish robust associations between neovascularisation, mechanical properties, and rupture risk. As mentioned previously, longitudinal studies that track changes in neovascularisation in patients over time could also provide insights into disease progression, helping to identify patients at critical risk of adverse events.

As stated earlier, a promising direction for future work should involve linking *in vivo* CEUS imaging with *ex vivo* testing of plaques. This approach would provide critical insights into the interplay between imaging-derived neovascularisation metrics and plaque mechanical behaviour, bridging the gap between diagnostic imaging and mechanical risk assessment. Moreover, the inclusion of neovascularisation in risk as-

sessment frameworks, such as the plaque RADS-score, could enhance clinical decision-making by providing a multifactorial evaluation of vulnerability [23].

This thesis underscores the transformative potential of neovascularisation in revolutionising the clinical management of atherosclerosis. CEUS, already established in many settings, offers a ready pathway for adoption, while emerging technologies like SMI and ULM provide exciting prospects for expanding accessibility. By prioritising neovascularisation in future studies and integrating advanced imaging techniques into routine workflows, clinicians can move beyond stenosis-focused metrics.

Chapter 8

Concluding remarks

The overarching goal of this thesis was to explore the relationship between plaque mechanical properties and neovascularisation and determine its clinical potential as an additional biomarker of vulnerability. The major contributions of this thesis to the biomedical field are summarised below:

- By combining inflation testing with iFEM and US imaging, Chapter 3 established a physiologically relevant approach for estimating material properties and characterising plaque surrogates deformation under controlled loading conditions. Of note, higher strain and von Mises stress values were observed at the shoulder regions of phantoms with 75% stenosis, aligning with clinical findings on regions prone to rupture.

- Translating this clinically relevant framework, excised human atherosclerotic plaques were pressurised to enable exploration of plaque mechanical behaviour and neovascularisation. Neovascularisation analysis revealed higher levels in more complex plaques.

- Key mechanical insights were gained into excised human atherosclerotic plaques when assessing neovascularisation and rupture metrics. Particularly, UT strain demonstrated a statistically significant moderate negative correlation ($r = -0.4585$, $^*p = 0.0278$). K-means clustering of UT stress and UT strain further identified two distinct mechanical behaviour clusters: cluster 1 with lower strain at failure and higher initial stiffness, and cluster 2 with higher strain at failure and lower initial stiffness. These insights ultimately identified vulnerable strips that failed at lower strains presenting with higher neovascularisation levels.

- Clinical relevance of neovascularisation for risk stratification: cumulatively, these findings reinforce neovascularisation as a potential marker of plaque mechanical instability, supporting its integration into clinical workflows through imaging modalities like CEUS.

Together, these findings represent a significant step forward in understanding the complex interplay between plaque mechanics and microstructure. By establishing neovascularisation as a critical marker of vulnerability and advocating for its integration into clinical practice, this thesis lays a strong foundation for future research and clinical translation, with the ultimate goal of improving the prevention and treatment of atherosclerotic disease.

Bibliography

[1] G. A. Roth, G. A. Mensah, C. O. Johnson, *et al.*, "Global burden of cardiovascular diseases and risk factors, 1990–2019: Update from the gbd 2019 study," *Journal of the American college of cardiology*, vol. 76, no. 25, pp. 2982–3021, 2020.

[2] W. Herrington, B. Lacey, P. Sherliker, J. Armitage, and S. Lewington, "Epidemiology of atherosclerosis and the potential to reduce the global burden of atherothrombotic disease," *Circulation research*, vol. 118, no. 4, pp. 535–546, 2016.

[3] L. Saba, P. L. Antignani, A. Gupta, *et al.*, "International union of angiology (iua) consensus paper on imaging strategies in atherosclerotic carotid artery imaging: From basic strategies to advanced approaches," *Atherosclerosis*, vol. 354, pp. 23–40, 2022.

[4] C. Yuan, S.-x. Zhang, N. L. Polissar, *et al.*, "Identification of fibrous cap rupture with magnetic resonance imaging is highly associated with recent transient ischemic attack or stroke," *Circulation*, vol. 105, no. 2, pp. 181–185, 2002.

[5] W. Insull Jr and S. J. Lewis, "Clinical management of atherosclerosis: A checklist," *The American journal of medicine*, vol. 122, no. 1, S60–S62, 2009.

[6] L. H. Bonati, S. Kakkos, J. Berkefeld, *et al.*, "European stroke organisation guideline on endarterectomy and stenting for carotid artery stenosis," *European stroke journal*, vol. 6, no. 2, pp. I–XLVII, 2021.

[7] D. Tang, Z. Teng, G. Canton, *et al.*, "Sites of rupture in human atherosclerotic carotid plaques are associated with high structural stresses: An in vivo mri-based 3d fluid-structure interaction study," *Stroke*, vol. 40, no. 10, pp. 3258–3263, 2009.

[8] X. Huang, Z. Teng, G. Canton, M. Ferguson, C. Yuan, and D. Tang, "Intraplaque hemorrhage is associated with higher structural stresses in human atherosclerotic plaques: An in vivo mri-based 3d fluid-structure interaction study," *Biomedical engineering online*, vol. 9, no. 1, pp. 1–12, 2010.

[9] P. Cyréus, K. Wadén, S. Hellberg, *et al.*, "Atherosclerotic plaque instability in symptomatic non-significant carotid stenoses," *JVS-Vascular Science*, p. 100 280, 2025.

[10] D. Camasão and D. Mantovani, "The mechanical characterization of blood vessels and their substitutes in the continuous quest for physiological-relevant performances. a critical review," *Materials Today Bio*, vol. 10, p. 100 106, 2021.

[11] C. Costopoulos, Y. Huang, A. J. Brown, *et al.*, "Plaque rupture in coronary atherosclerosis is associated with increased plaque structural stress," *JACC: Cardiovascular Imaging*, vol. 10, no. 12, pp. 1472–1483, 2017.

[12] M. J. Daemen, M. S. Ferguson, F. J. Gijsen, *et al.*, "Carotid plaque fissure: An underestimated source of intraplaque hemorrhage," *Atherosclerosis*, vol. 254, pp. 102–108, 2016.

[13] T. Wissing, K. Van der Heiden, S. Serra, A. Smits, C. Bouten, and F. Gijsen, "Tissue-engineered collagenous fibrous cap models to systematically elucidate atherosclerotic plaque rupture," *Scientific Reports*, vol. 12, no. 1, p. 5434, 2022.

[14] W. Brinjikji, J. Huston, A. A. Rabinstein, G.-M. Kim, A. Lerman, and G. Lanzino, "Contemporary carotid imaging: From degree of stenosis to plaque vulnerability," *Journal of neurosurgery*, vol. 124, no. 1, pp. 27–42, 2016.

[15] M. J. Gough, "Preprocedural imaging strategies in symptomatic carotid artery stenosis," *Journal of vascular surgery*, vol. 54, no. 4, pp. 1215–1218, 2011.

[16] A. C. Akyildiz, H. H. Hansen, H. A. Nieuwstadt, *et al.*, "A framework for local mechanical characterization of atherosclerotic plaques: Combination of ultrasound displacement imaging and inverse finite element analysis," *Annals of biomedical engineering*, vol. 44, no. 4, pp. 968–979, 2016.

[17] S. G. Torun, H. M. Torun, H. H. Hansen, *et al.*, "Multicomponent material property characterization of atherosclerotic human carotid arteries through a bayesian optimization based inverse finite element approach," *journal of the mechanical behavior of biomedical materials*, vol. 126, p. 104 996, 2022.

[18] M.-H. Roy-Cardinal, F. Destrempes, G. Soulez, and G. Cloutier, "Assessment of carotid artery plaque components with machine learning classification using homodyned-k parametric maps and elastograms," *IEEE transactions on ultrasonics, ferroelectrics, and frequency control*, vol. 66, no. 3, pp. 493–504, 2018.

[19] R. D. Johnston, R. T. Gaul, and C. Lally, "An investigation into the critical role of fibre orientation in the ultimate tensile strength and stiffness of human carotid plaque caps," *Acta Biomaterialia*, vol. 124, pp. 291–300, 2021.

[20] B. Tornifoglio, R. Johnston, A. Stone, C. Kerskens, and C. Lally, "Microstructural and mechanical insight into atherosclerotic plaques: An ex vivo dti study to better assess plaque vulnerability," *Biomechanics and Modeling in Mechanobiology*, vol. 22, no. 5, pp. 1515–1530, 2023.

[21] S. G. Torun, P. de Miguel Munoz, H. Crielaard, *et al.*, "Local characterization of collagen architecture and mechanical failure properties of fibrous plaque tissue of atherosclerotic human carotid arteries," *Acta Biomaterialia*, vol. 164, pp. 293–302, 2023.

[22] A. Corti, A. De Paolis, P. Grossman, *et al.*, "The effect of plaque morphology, material composition and microcalcifications on the risk of cap rupture: A structural analysis of vulnerable atherosclerotic plaques," *Frontiers in Cardiovascular Medicine*, vol. 9, p. 1 019 917, 2022.

[23] L. Saba, R. Cau, A. Murgia, *et al.*, "Carotid plaque-rads: A novel stroke risk classification system," *Cardiovascular Imaging*, vol. 17, no. 1, pp. 62–75, 2024.

[24] R. Virmani, F. D. Kolodgie, A. P. Burke, *et al.*, "Atherosclerotic plaque progression and vulnerability to rupture: Angiogenesis as a source of intraplaque hemorrhage," *Arteriosclerosis, thrombosis, and vascular biology*, vol. 25, no. 10, pp. 2054–2061, 2005.

[25] P. A. Iaizzo, *Handbook of cardiac anatomy, physiology, and devices*. Springer Science & Business Media, 2009.

[26] E. Witzleb, "Functions of the vascular system," in *Human physiology*, Springer, 1989, pp. 480–542.

[27] M. H. Johnson, H. M. Thorisson, and M. L. DiLuna, "Vascular anatomy: The head, neck, and skull base," *Neurosurgery Clinics*, vol. 20, no. 3, pp. 239–258, 2009.

[28] J. Krejza, M. Arkuszewski, S. E. Kasner, *et al.*, "Carotid artery diameter in men and women and the relation to body and neck size," *Stroke*, vol. 37, no. 4, pp. 1103–1105, 2006.

[29] W. Lee, "General principles of carotid doppler ultrasonography," *Ultrasonography*, vol. 33, no. 1, p. 11, 2014.

[30] J. D. Humphrey, "Mechanics of the arterial wall: Review and directions," *Critical Reviews™ in Biomedical Engineering*, vol. 23, no. 1-2, 1995.

[31] G. A. Holzapfel, T. C. Gasser, and R. W. Ogden, "A new constitutive framework for arterial wall mechanics and a comparative study of material models," *Journal of elasticity and the physical science of solids*, vol. 61, no. 1, pp. 1–48, 2000.

[32] G. A. Holzapfel *et al.*, "Biomechanics of soft tissue," *The handbook of materials behavior models*, vol. 3, no. 1, pp. 1049–1063, 2001.

[33] M. R. Roach and A. C. Burton, "The reason for the shape of the distensibility curves of arteries," *Canadian journal of biochemistry and physiology*, vol. 35, no. 8, pp. 681–690, 1957.

[34] G. Holzapfel, "Sommer g, and regitnig p," *Anisotropic mechanical properties of tissue components in human atherosclerotic plaques. J Biomech Eng*, vol. 126, pp. 657–665, 2004.

[35] N. A. S. C. E. T. Collaborators*, "Beneficial effect of carotid endarterectomy in symptomatic patients with high-grade carotid stenosis," *New England journal of medicine*, vol. 325, no. 7, pp. 445–453, 1991.

[36] T. Reiff, H.-H. Eckstein, U. Mansmann, *et al.*, "Carotid endarterectomy or stenting or best medical treatment alone for moderate-to-severe asymptomatic carotid artery stenosis: 5-year results of a multicentre, randomised controlled trial," *The Lancet Neurology*, vol. 21, no. 10, pp. 877–888, 2022.

[37] J. C. Ritter and M. R. Tyrrell, "The current management of carotid atherosclerotic disease: Who, when and how?" *Interactive cardiovascular and thoracic surgery*, vol. 16, no. 3, pp. 339–346, 2013.

[38] M. Clinic, *Carotid endarterectomy - mayo clinic*, `https://www.mayoclinic.org/tests-procedures/carotid-endarterectomy/about/pac-20393379`, Accessed: 2025-01-23, 2017.

[39] G. W. van Lammeren, B. L. Reichmann, F. L. Moll, *et al.*, "Atherosclerotic plaque vulnerability as an explanation for the increased risk of stroke in elderly undergoing carotid artery stenting," *Stroke*, vol. 42, no. 9, pp. 2550–2555, 2011.

[40] M. Clinic, *Carotid angioplasty - mayo clinic*, `https://www.mayoclinic.org/diseases-conditions/carotid-artery-disease/multimedia/img-20360716`, Accessed: 2025-01-23, 2017.

[41] M. Clinic, *Carotid stenting - mayo clinic*, `https://www.mayoclinic.org/diseases-conditions/carotid-artery-disease/multimedia/img-20360718`, Accessed: 2025-01-23, 2017.

[42] F. D. Kolodgie, K. Yahagi, H. Mori, *et al.*, "High-risk carotid plaque: Lessons learned from histopathology," in *Seminars in vascular surgery*, Elsevier, vol. 30, 2017, pp. 31–43.

[43] H. C. Stary, A. B. Chandler, S. Glagov, *et al.*, "A definition of initial, fatty streak, and intermediate lesions of atherosclerosis. a report from the committee on vascular lesions of the council on arteriosclerosis, american heart association.," *Circulation*, vol. 89, no. 5, pp. 2462–2478, 1994.

[44] H. C. Stary, "Natural history and histological classification of atherosclerotic lesions: An update," *Arteriosclerosis, thrombosis, and vascular biology*, vol. 20, no. 5, pp. 1177–1178, 2000.

[45] L. Saba, W. Brinjikji, J. Spence, *et al.*, "Roadmap consensus on carotid artery plaque imaging and impact on therapy strategies and guidelines: An international, multispecialty, expert review and position statement," *American Journal of Neuroradiology*, vol. 42, no. 9, pp. 1566–1575, 2021.

[46] H. C. Stary, A. B. Chandler, R. E. Dinsmore, *et al.*, "A definition of advanced types of atherosclerotic lesions and a histological classification of atherosclerosis: A report from the committee on vascular lesions of the council on arteriosclerosis, american heart association," *Circulation*, vol. 92, no. 5, pp. 1355–1374, 1995.

[47] R. Virmani, F. D. Kolodgie, A. P. Burke, A. Farb, and S. M. Schwartz, "Lessons from sudden coronary death: A comprehensive morphological classification scheme for atherosclerotic lesions," *Arteriosclerosis, thrombosis, and vascular biology*, vol. 20, no. 5, pp. 1262–1275, 2000.

[48] G. G. Ferguson, M. Eliasziw, H. W. Barr, *et al.*, "The north american symptomatic carotid endarterectomy trial: Surgical results in 1415 patients," *Stroke*, vol. 30, no. 9, pp. 1751–1758, 1999.

[49] C. Warlow, "Mrc european carotid surgery trial: Interim results for symptomatic patients with severe (70-99%) or with mild (0-29%) carotid stenosis," *The Lancet*, vol. 337, no. 8752, pp. 1235–1243, 1991.

[50] H. Ota, K. Takase, H. Rikimaru, *et al.*, "Quantitative vascular measurements in arterial occlusive disease," *Radiographics*, vol. 25, no. 5, pp. 1141–1158, 2005.

[51] R. Virmani, A. P. Burke, F. D. Kolodgie, and A. Farb, "Pathology of the thin-cap fibroatheroma: A type of vulnerable plaque," *Journal of interventional cardiology*, vol. 16, no. 3, pp. 267–272, 2003.

[52] K. I. Paraskevas, A. N. Nicolaides, J. S. Suri, and L. Saba, *Identifying the vulnerable carotid atherosclerotic plaque in patients with asymptomatic carotid stenosis*, 2021.

[53] J. Kamtchum-Tatuene, A. Wilman, M. Saqqur, A. Shuaib, and G. C. Jickling, "Carotid plaque with high-risk features in embolic stroke of undetermined source: Systematic review and meta-analysis," *Stroke*, vol. 51, no. 1, pp. 311–314, 2020.

[54] S. Carr, A. Farb, W. H. Pearce, R. Virmani, and J. S. Yao, "Atherosclerotic plaque rupture in symptomatic carotid artery stenosis," *Journal of vascular surgery*, vol. 23, no. 5, pp. 755–766, 1996.

[55] C.-M. Wahlgren, W. Zheng, W. Shaalan, J. Tang, and H. S. Bassiouny, "Human carotid plaque calcification and vulnerability," *Cerebrovascular diseases*, vol. 27, no. 2, pp. 193–200, 2009.

[56] E. L. Ritman and A. Lerman, "The dynamic vasa vasorum," *Cardiovascular research*, vol. 75, no. 4, pp. 649–658, 2007.

[57] J. Xu, X. Lu, and G.-P. Shi, "Vasa vasorum in atherosclerosis and clinical significance," *International journal of molecular sciences*, vol. 16, no. 5, pp. 11 574–11 608, 2015.

[58] M. Gabriela Espinosa, M. Catalin Staiculescu, J. Kim, E. Marin, and J. E. Wagenseil, "Elastic fibers and large artery mechanics in animal models of development and disease," *Journal of biomechanical engineering*, vol. 140, no. 2, p. 020 803, 2018.

[59] H. Wolinsky, "Comparison of medial growth of human thoracic and abdominal aortas," *Circulation research*, vol. 27, no. 4, pp. 531–538, 1970.

[60] P. Carmeliet, "Angiogenesis in health and disease," *Nature medicine*, vol. 9, no. 6, pp. 653–660, 2003.

[61] P. R. Moreno, K.-R. Purushothaman, M. Sirol, A. P. Levy, and V. Fuster, "Neovascularization in human atherosclerosis," *Circulation*, vol. 113, no. 18, pp. 2245–2252, 2006.

[62] V. W. van Hinsbergh, E. C. Eringa, and M. J. Daemen, "Neovascularization of the atherosclerotic plaque: Interplay between atherosclerotic lesion, adventitia-derived microvessels and perivascular fat," *Current opinion in lipidology*, vol. 26, no. 5, pp. 405–411, 2015.

[63] K. S. Moulton, "Areplaque angiogenesis and atherosclerosis," *Current atherosclerosis reports*, vol. 3, no. 3, pp. 225–233, 2001.

[64] A. van Veelen, N. M. van der Sangen, J. P. Henriques, and B. E. Claessen, "Identification and treatment of the vulnerable coronary plaque," *Reviews in cardiovascular medicine*, vol. 23, no. 1, p. 39, 2022.

[65] J. C. Sluimer, F. D. Kolodgie, A. P. Bijnens, *et al.*, "Thin-walled microvessels in human coronary atherosclerotic plaques show incomplete endothelial junctions: Relevance of compromised structural integrity for intraplaque microvascular leakage," *Journal of the American College of Cardiology*, vol. 53, no. 17, pp. 1517–1527, 2009.

[66] Z. He, J. Luo, M. Lv, *et al.*, "Characteristics and evaluation of atherosclerotic plaques: An overview of state-of-the-art techniques," *Frontiers in Neurology*, vol. 14, p. 1 159 288, 2023.

[67] C. Camaré, M. Pucelle, A. Nègre-Salvayre, and R. Salvayre, "Angiogenesis in the atherosclerotic plaque," *Redox biology*, vol. 12, pp. 18–34, 2017.

[68] K. D. O'Brien, M. D. Allen, T. O. McDonald, *et al.*, "Vascular cell-adhesion molecule-1 is expressed in human coronary atherosclerotic plaques: Implications for the mode of progression of advanced coronary atherosclerosis," *The Journal of Clinical Investigation*, vol. 92, no. 2, pp. 945–951, 1993.

[69] Y. Zhang, J. Cao, J. Zhou, *et al.*, "Plaque elasticity and intraplaque neovascularisation on carotid artery ultrasound: A comparative histological study," *European Journal of Vascular and Endovascular Surgery*, vol. 62, no. 3, pp. 358–366, 2021.

[70] B. Wang, Y. Chen, Q. Qiao, L. Dong, C. Xiao, and Z. Qi, "Evaluation of carotid plaque vulnerability with different echoes by shear wave elastography and ceus," *Journal of Stroke and Cerebrovascular Diseases*, vol. 32, no. 3, p. 106 941, 2023.

[71] L. Zhang, C. Jia, S. Gu, J. Chen, and R. Wu, "Intraplaque neovascularization combined with plaque elasticity for predicting ipsilateral stroke in patients with asymptomatic mild carotid stenosis," *Quantitative Imaging in Medicine and Surgery*, vol. 14, no. 7, p. 4815, 2024.

[72] Z. Teng, J. He, A. J. Degnan, *et al.*, "Critical mechanical conditions around neovessels in carotid atherosclerotic plaque may promote intraplaque hemorrhage," *Atherosclerosis*, vol. 223, no. 2, pp. 321–326, 2012.

[73] M. Tian, N. Mohamad, X. Gao, and N. M. Taib, "Quantitative characterisation of carotid atherosclerotic plaque neovascularisation using contrast-enhanced ultrasound imaging: A feasibility study," *The Medical journal of Malaysia*, vol. 80, no. 1, pp. 88–95, 2025.

[74] E. Marsch, T. L. Theelen, J. A. F. Demandt, *et al.*, "Reversal of hypoxia in murine atherosclerosis prevents necrotic core expansion by enhancing efferocytosis," *Arteriosclerosis, Thrombosis, and Vascular Biology*, vol. 34, no. 11, pp. 2545–2553, 2014.

[75] V. Nardi, J. Benson, M. C. Bois, *et al.*, "Carotid plaques from symptomatic patients with mild stenosis is associated with intraplaque hemorrhage," *Hypertension*, vol. 79, no. 1, pp. 271–282, 2022.

[76] J. Herrmann, L. O. Lerman, M. Rodriguez-Porcel, *et al.*, "Coronary vasa vasorum neovascularization precedes epicardial endothelial dysfunction in experimental hypercholesterolemia," *Cardiovascular Research*, vol. 51, no. 4, pp. 762–766, 2001.

[77] L. E. Savastano *et al.*, "Symptomatic nonstenotic carotids: A topical review," *Journal of the American College of Cardiology*, 2024.

[78] W. J. Rogers, J. W. Prichard, Y.-L. Hu, *et al.*, "Characterization of signal properties in atherosclerotic plaque components by intravascular mri," *Arteriosclerosis, thrombosis, and vascular biology*, vol. 20, no. 7, pp. 1824–1830, 2000.

[79] J. Narula, M. Nakano, R. Virmani, *et al.*, "Histopathologic characteristics of atherosclerotic coronary disease and implications of the findings for the invasive and noninvasive detection of vulnerable plaques," *Journal of the American College of Cardiology*, vol. 61, no. 10, pp. 1041–1051, 2013.

[80] M. Araki, S.-J. Park, H. L. Dauerman, *et al.*, "Optical coherence tomography in coronary atherosclerosis assessment and intervention," *Nature Reviews Cardiology*, vol. 19, no. 10, pp. 684–703, 2022.

[81] C. Noble, K. D. Carlson, E. Neumann, *et al.*, "Patient specific characterization of artery and plaque material properties in peripheral artery disease," *Journal of the mechanical behavior of biomedical materials*, vol. 101, p. 103 453, 2020.

[82] A. Nair, B. D. Kuban, E. M. Tuzcu, P. Schoenhagen, S. E. Nissen, and D. G. Vince, "Coronary plaque classification with intravascular ultrasound radiofrequency data analysis," *Circulation*, vol. 106, no. 17, pp. 2200–2206, 2002.

[83] M. B. Syed, A. J. Fletcher, R. O. Forsythe, *et al.*, "Emerging techniques in atherosclerosis imaging," *The British journal of radiology*, vol. 92, no. 1103, p. 20 180 309, 2019.

[84] S. Josephson, S. Bryant, H. Mak, S. Johnston, W. Dillon, and W. Smith, "Evaluation of carotid stenosis using ct angiography in the initial evaluation of stroke and tia," *Neurology*, vol. 63, no. 3, pp. 457–460, 2004.

[85] A. Den Hartog, S. Bovens, W. Koning, *et al.*, "Current status of clinical magnetic resonance imaging for plaque characterisation in patients with carotid artery stenosis," *European Journal of Vascular and Endovascular Surgery*, vol. 45, no. 1, pp. 7–21, 2013.

[86] T. Saam, T. S. Hatsukami, N. Takaya, *et al.*, "The vulnerable, or high-risk, atherosclerotic plaque: Noninvasive mr imaging for characterization and assessment," *Radiology*, vol. 244, no. 1, pp. 64–77, 2007.

[87] C. Otto, "Principles of echocardiographic image acquisition and doppler analysis," *Otto CM: Textbook of clinical echocardiography. WB Saunders, Philadelphia*, pp. 1–3, 2000.

[88] A. Fedak, K. Ciuk, and A. Urbanik, "Ultrasonography of vulnerable atherosclerotic plaque in the carotid arteries: B-mode imaging," *Journal of Ultrasonography*, vol. 20, pp. 155–164, 2020.

[89] E. Cave, N. Pugh, R. Wilson, G. Sissons, and J. Woodcock, "Carotid artery duplex scanning: Does plaque echogenicity correlate with patient symptoms?" *European Journal of Vascular and Endovascular Surgery*, vol. 10, no. 1, pp. 77–81, 1995.

[90] M.-L. M. Grønholdt *et al.*, "Ultrasonic echolucent carotid plaques predict future strokes," *Circulation*, vol. 104, pp. 68–73, 2001.

[91] R. Sztajzel, "Ultrasonographic assessment of the morphological characteristics of the carotid plaque," *Swiss Medical Weekly*, vol. 135, no. 45-46, pp. 635–643, 2005.

[92] R. D. Park, T. G. Nyland, J. C. Lattimer, C. W. Miller, and J. L. Lebel, "B-mode gray-scale ultrasound: Imaging artifacts and interpretation principles," *Veterinary Radiology & Ultrasound*, vol. 22, no. 5, pp. 183–191, 1981.

[93] F. W. Kremkau and K. Taylor, "Artifacts in ultrasound imaging.," *Journal of ultrasound in medicine*, vol. 5, no. 4, pp. 227–237, 1986.

[94] L. H. Gimber and M. S. Taljanovic, "Ultrasound imaging artifacts," in *Musculoskeletal Ultrasound*, Springer, 2017.

[95] R. Kern, K. Szabo, M. Hennerici, and S. Meairs, "Characterization of carotid artery plaques using real-time compound b-mode ultrasound," *Stroke*, vol. 35, no. 4, pp. 870–875, 2004.

[96] F. Tranquart, N. Grenier, V. Eder, and L. Pourcelot, "Clinical use of ultrasound tissue harmonic imaging," *Ultrasound in medicine & biology*, vol. 25, no. 6, pp. 889–894, 1999.

[97] C.-L. Yen, H.-Y. Chang, S.-Y. Huang, Y.-C. Huang, and C.-M. Jeng, "Combination of tissue harmonic sonography, real-time spatial compound sonography and adaptive image processing technique for the detection of carotid plaques and intima-medial thickness," *European journal of radiology*, vol. 71, no. 1, pp. 11–16, 2009.

[98] J. Bercoff, M. Tanter, and M. Fink, "Supersonic shear imaging: A new technique for soft tissue elasticity mapping," *IEEE transactions on ultrasonics, ferroelectrics, and frequency control*, vol. 51, no. 4, pp. 396–409, 2004.

[99] K. V. Ramnarine, J. W. Garrard, B. Kanber, S. Nduwayo, T. C. Hartshorne, and T. G. Robinson, "Shear wave elastography imaging of carotid plaques: Feasible, reproducible and of clinical potential," *Cardiovascular ultrasound*, vol. 12, no. 1, pp. 1–9, 2014.

[100] E. Widman, E. Maksuti, D. Larsson, *et al.*, "Feasibility of shear wave elastography for plaque characterization," in *2014 IEEE International Ultrasonics Symposium*, IEEE, 2014, pp. 1818–1821.

[101] P. L. Mellucci Filho, M. Bertanha, R. G. Jaldin, W. B. Yoshida, and M. L. Sobreira, "Shear wave elastography for extracranial carotid atherosclerotic plaques: Technical principles and how to do it," *Jornal Vascular Brasileiro*, vol. 22, e20220082, 2023.

[102] J.-M. Cai, T. S. Hatsukami, M. S. Ferguson, R. Small, N. L. Polissar, and C. Yuan, "Classification of human carotid atherosclerotic lesions with in vivo multicontrast magnetic resonance imaging," *Circulation*, vol. 106, no. 11, pp. 1368–1373, 2002.

[103] D. Marlevi, S. L. Mulvagh, R. Huang, *et al.*, "Combined spatiotemporal and frequency-dependent shear wave elastography enables detection of vulnerable carotid plaques as validated by mri," *Scientific reports*, vol. 10, no. 1, p. 403, 2020.

[104] H. H. Hansen, M. Pernot, S. Chatelin, M. Tanter, and C. L. de Korte, "Shear wave elastography for lipid content detection in transverse arterial cross-sections," in *2015 IEEE International Ultrasonics Symposium (IUS)*, IEEE, 2015, pp. 1–4.

[105] A. Tjan, I. G. R. Widiana, E. D. Martadiani, I. M. D. Ayusta, M. W. Asih, and F. P. Sitanggang, "Carotid artery stiffness measured by strain elastography ultrasound is a stroke risk factor," *Clinical Epidemiology and Global Health*, vol. 12, p. 100 850, 2021.

[106] A. Davidhi, V. Rafailidis, E. Destanis, P. Prassopoulos, and S. Foinitsis, "Ultrasound elastography: Another piece in the puzzle of carotid plaque vulnerability?" *Medical Ultrasonography*, vol. 24, no. 3, pp. 356–363, 2022.

[107] J. T. Pruijssen, F. H. Schreuder, J. Wilbers, J. H. Kaanders, C. L. de Korte, and H. H. Hansen, "Performance evaluation of commercial and non-commercial shear wave elastography implementations for vascular applications," *Ultrasonics*, vol. 140, p. 107 312, 2024.

[108] X. Wang, J. Zhu, J. Gao, *et al.*, "Assessment of ultrasound shear wave elastography within muscles using different region of interest sizes, manufacturers, probes and acquisition angles: An ex vivo study," *Quantitative imaging in medicine and surgery*, vol. 12, no. 6, p. 3227, 2022.

[109] A. I. Alrashed and A. M. Alfuraih, "Reproducibility of shear wave elastography among operators, machines, and probes in an elasticity phantom," *Ultrasonography*, vol. 40, no. 1, p. 158, 2021.

[110] J. Ophir, I. Cespedes, H. Ponnekanti, Y. Yazdi, and X. Li, "Elastography: A quantitative method for imaging the elasticity of biological tissues," *Ultrasonic imaging*, vol. 13, no. 2, pp. 111–134, 1991.

[111] R. G. P. Lopata, *2D and 3D ultrasound strain imaging. Methods and in vivo applications*. [Sl: sn], 2010.

[112] P. Khavari, A. Asif, M. Boily, and H. Rivaz, "Nonlocal coherent denoising of rf data for ultrasound elastography," *Journal of Healthcare Engineering*, vol. 2018, no. 1, p. 7 979 528, 2018.

[113] M. Omidyeganeh, Y. Xiao, M. O. Ahmad, and H. Rivaz, "Estimation of strain elastography from ultrasound radio-frequency data by utilizing analytic gradient of the similarity metric," *IEEE transactions on medical imaging*, vol. 36, no. 6, pp. 1347–1358, 2017.

[114] R. Delaunay, Y. Hu, and T. Vercauteren, "An unsupervised approach to ultrasound elastography with end-to-end strain regularisation," in *Medical Image Computing and Computer Assisted Intervention–MICCAI 2020: 23rd International Conference, Lima, Peru, October 4–8, 2020, Proceedings, Part III 23*, Springer, 2020, pp. 573–582.

[115] M. Averkiou, M. Bruce, J. Powers, P. S. Sheeran, and P. Burns, "Imaging methods for ultrasound contrast agents," *Ultrasound in Medicine Biology*, vol. 45, no. 12, pp. 3446–3458, 2019.

[116] Q. Lyu, X. Tian, Y. Ding, *et al.*, "Evaluation of carotid plaque rupture and neovascularization by contrast-enhanced ultrasound imaging: An exploratory study based on histopathology," *Translational Stroke Research*, vol. 12, pp. 49–56, 2021.

[117] Y. Cheng, A. Wu, M. Ying, and X. Chen, "The updated roles of new ultrasound imaging techniques in assessing carotid vulnerable plaques," *WFUMB Ultrasound Open*, p. 100 023, 2023.

[118] S. B. Feinstein, "Contrast ultrasound imaging of the carotid artery vasa vasorum and atherosclerotic plaque neovascularization," *Journal of the American College of Cardiology*, vol. 48, no. 2, pp. 236–243, 2006.

[119] S. Coli, M. Magnoni, G. Sangiorgi, *et al.*, "Contrast-enhanced ultrasound imaging of intraplaque neovascularization in carotid arteries: Correlation with histology and plaque echogenicity," *Journal of the American College of Cardiology*, vol. 52, no. 3, pp. 223–230, 2008.

[120] A. Hoogi, D. Adam, A. Hoffman, H. Kerner, S. Reisner, and D. Gaitini, "Carotid plaque vulnerability: Quantification of neovascularization on contrast-enhanced ultrasound with histopathologic correlation," *American Journal of Roentgenology*, vol. 196, no. 2, pp. 431–436, 2011.

[121] F. Shah, P. Balan, M. Weinberg, *et al.*, "Contrast-enhanced ultrasound imaging of atherosclerotic carotid plaque neovascularization: A new surrogate marker of atherosclerosis?" *Vascular medicine*, vol. 12, no. 4, pp. 291–297, 2007.

[122] Q. Zhang, C. Li, H. Han, L. Yang, Y. Wang, and W. Wang, "Computer-aided quantification of contrast agent spatial distribution within atherosclerotic plaque in contrast-enhanced ultrasound image sequences," *Biomedical Signal Processing and Control*, vol. 13, pp. 50–61, 2014.

[123] S.-P. Joo, S.-W. Lee, Y.-H. Cho, *et al.*, "Vasa vasorum densities in human carotid atherosclerosis is associated with plaque development and vulnerability," *Journal of Korean Neurosurgical Society*, vol. 63, no. 2, pp. 178–187, 2020.

[124] A. Alonso, D. Artemis, and M. G. Hennerici, "Molecular imaging of carotid plaque vulnerability," *Cerebrovascular diseases*, vol. 39, no. 1, pp. 5–12, 2015.

[125] B. Ning, D. Zhang, W. He, L. S. Wang, and Z. Q. Jin, "A study on distribution features of neovascularization in atherosclerotic carotid artery plaques: Comparing contrast-enhanced ultrasound with histopathology," *Ultrasonic Imaging*, vol. 41, no. 2, pp. 115–125, 2019.

[126] F. Che, D. Mi, A. Wang, *et al.*, "Extracranial carotid plaque hemorrhage predicts ipsilateral stroke recurrence in patients with carotid atherosclerosis–a study based on high-resolution vessel wall imaging mri," *BMC neurology*, vol. 22, no. 1, p. 237, 2022.

[127] X. Chen, H. Wang, Y. Jiang, *et al.*, "Neovascularization in carotid atherosclerotic plaques can be effectively evaluated by superb microvascular imaging (smi): Initial experience," *Vascular Medicine*, vol. 25, no. 4, pp. 328–333, 2020.

[128] G. Goudot, A. Jimenez, N. Mohamedi, *et al.*, "Assessment of takayasu's arteritis activity by ultrasound localization microscopy," *EBioMedicine*, vol. 90, 2023.

[129] H. Leroy, L. Z. Wang, A. Jimenez, *et al.*, "Assessment of microvascular flow in human atherosclerotic carotid plaques using ultrasound localization microscopy," *EBioMedicine*, vol. 111, 2025.

[130] Y. Guo, X. Wang, L. Wang, *et al.*, "The value of superb microvascular imaging and contrast-enhanced ultrasound for the evaluation of neovascularization in carotid artery plaques," *Academic Radiology*, vol. 30, no. 3, pp. 403–411, 2023.

[131] M. Zamani, K. Skagen, H. Scott, B. Lindberg, D. Russell, and M. Skjelland, "Carotid plaque neovascularization detected with superb microvascular imaging ultrasound without using contrast media," *Stroke*, vol. 50, no. 11, pp. 3121–3127, 2019.

[132] Q. Meng, X. Xie, L. Li, *et al.*, "Assessment of neovascularization of carotid artery atherosclerotic plaques using superb microvascular imaging: A comparison with contrast-enhanced ultrasound imaging and histology," *Quantitative Imaging in Medicine and Surgery*, vol. 11, no. 5, p. 1958, 2021.

[133] K. Oura, T. Kato, H. Ohba, and Y. Terayama, "Evaluation of intraplaque neovascularization using superb microvascular imaging and contrast-enhanced ultrasonography," *Journal of Stroke and Cerebrovascular Diseases*, vol. 27, no. 9, pp. 2348–2353, 2018.

[134] C. Cano, C. Matos, A. Gholampour, M. van Sambeek, R. Lopata, and M. Wu, "Blind spectral unmixing for characterization of plaque composition based on multispectral photoacoustic imaging," *Scientific Reports*, vol. 13, no. 1, p. 4119, 2023.

[135] J. D. Spence and G. Parraga, "Three-dimensional ultrasound of carotid plaque," *Neuroimaging Clinics*, vol. 26, no. 1, pp. 69–80, 2016.

[136] J. Baun, "The efficacy of emerging ultrasound applications in characterizing vulnerable carotid plaques," *Journal of Diagnostic Medical Sonography*, p. 87 564 793 241 311 545, 2025.

[137] A. J. Malone, S. Cournane, I. G. Naydenova, A. J. Fagan, and J. E. Browne, "Polyvinyl alcohol cryogel based vessel mimicking material for modelling the progression of atherosclerosis," *Physica Medica*, vol. 69, pp. 1–8, 2020.

[138] M. Sotiriou, M. Yiannakou, and C. Damianou, "Investigating atherosclerotic plaque phantoms for ultrasound therapy," *Journal of Ultrasound*, vol. 25, no. 3, pp. 709–720, 2022.

[139] J. Fromageau, E. Brusseau, D. Vray, G. Gimenez, and P. Delachartre, "Characterization of pva cryogel for intravascular ultrasound elasticity imaging," *IEEE transactions on ultrasonics, ferroelectrics, and frequency control*, vol. 50, no. 10, pp. 1318–1324, 2003.

[140] K. Surry, H. Austin, A. Fenster, and T. Peters, "Poly (vinyl alcohol) cryogel phantoms for use in ultrasound and mr imaging," *Physics in Medicine & Biology*, vol. 49, no. 24, p. 5529, 2004.

[141] D. M. King, C. M. Moran, J. D. McNamara, A. J. Fagan, and J. E. Browne, "Development of a vessel-mimicking material for use in anatomically realistic doppler flow phantoms," *Ultrasound in medicine & biology*, vol. 37, no. 5, pp. 813–826, 2011.

[142] R. W. Boekhoven, M. C. Rutten, F. N. van de Vosse, and R. Lopata, "Design of a fatty plaque phantom for validation of strain imaging," in *2014 IEEE International Ultrasonics Symposium*, IEEE, 2014, pp. 2619–2622.

[143] J. Porée, B. Chayer, G. Soulez, J. Ohayon, and G. Cloutier, "Noninvasive vascular modulography method for imaging the local elasticity of atherosclerotic plaques: Simulation and in vitro vessel phantom study," *IEEE transactions on ultrasonics, ferroelectrics, and frequency control*, vol. 64, no. 12, pp. 1805–1817, 2017.

[144] A. J. Chee, B. Y. Yiu, C. K. Ho, and C. Alfred, "Arterial phantoms with regional variations in wall stiffness and thickness," *Ultrasound in Medicine & Biology*, vol. 44, no. 4, pp. 872–883, 2018.

[145] B. Chayer, M. Van den Hoven, M.-H. R. Cardinal, *et al.*, "Atherosclerotic carotid bifurcation phantoms with stenotic soft inclusions for ultrasound flow and vessel wall elastography imaging," *Physics in Medicine & Biology*, vol. 64, no. 9, p. 095 025, 2019.

[146] V. Gatti, P. Nauleau, G. M. Karageorgos, J. J. Shim, G. A. Ateshian, and E. E. Konofagou, "Modeling pulse wave propagation through a stenotic artery with fluid structure interaction: A validation study using ultrasound pulse wave imaging," *Journal of Biomechanical Engineering*, vol. 143, no. 3, p. 031 005, 2021.

[147] H. Crielaard, T. B. Wissing, S. G. Torun, *et al.*, "Local characterization of collagen architecture and mechanical properties of tissue engineered atherosclerotic plaque cap analogs," *Acta Biomaterialia*, 2025.

[148] S. Le Floc'h, G. Cloutier, G. Finet, P. Tracqui, R. I. Pettigrew, and J. Ohayon, "On the potential of a new ivus elasticity modulus imaging approach for detecting vulnerable atherosclerotic coronary plaques: In vitro vessel phantom study," *Physics in Medicine & Biology*, vol. 55, no. 19, p. 5701, 2010.

[149] V. Pazos, R. Mongrain, and J.-C. Tardif, "Mechanical characterization of atherosclerotic arteries using finite-element modeling: Feasibility study on mock arteries," *IEEE transactions on biomedical engineering*, vol. 57, no. 6, pp. 1520–1528, 2010.

[150] W. Nafo and A. Al-Mayah, "Characterization of pva hydrogels' hyperelastic properties by uniaxial tension and cavity expansion tests," *International Journal of Non-Linear Mechanics*, vol. 124, p. 103 515, 2020.

[151] H. Hansen, A. Saris, N. Vaka, M. Nillesen, and C. De Korte, "Ultrafast vascular strain compounding using plane wave transmission," *Journal of biomechanics*, vol. 47, no. 4, pp. 815–823, 2014.

[152] Z. Teng, J. Yuan, J. Feng, *et al.*, "The influence of constitutive law choice used to characterise atherosclerotic tissue material properties on computing stress values in human carotid plaques," *Journal of biomechanics*, vol. 48, no. 14, pp. 3912–3921, 2015.

[153] S. Barrett, M. Sutcliffe, S. Howarth, Z.-.-Y. Li, and J. Gillard, "Experimental measurement of the mechanical properties of carotid atherothrombotic plaque fibrous cap," *Journal of biomechanics*, vol. 42, no. 11, pp. 1650–1655, 2009.

[154] C.-K. Chai, A. C. Akyildiz, L. Speelman, *et al.*, "Local axial compressive mechanical properties of human carotid atherosclerotic plaques—characterisation by indentation test and inverse finite element analysis," *Journal of biomechanics*, vol. 46, no. 10, pp. 1759–1766, 2013.

[155] G. A. Holzapfel, G. Sommer, and P. Regitnig, "Anisotropic mechanical properties of tissue components in human atherosclerotic plaques," *J. Biomech. Eng.*, vol. 126, no. 5, pp. 657–665, 2004.

[156] J. Mulvihill, E. Cunnane, S. McHugh, E. Kavanagh, S. Walsh, and M. Walsh, "Mechanical, biological and structural characterization of in vitro ruptured human carotid plaque tissue," *Acta biomaterialia*, vol. 9, no. 11, pp. 9027–9035, 2013.

[157] R. W. Boekhoven, M. C. Rutten, M. R. van Sambeek, F. N. van de Vosse, and R. G. Lopata, "Towards mechanical characterization of intact endarterectomy samples of carotid arteries during inflation using echo-ct," *Journal of biomechanics*, vol. 47, no. 4, pp. 805–814, 2014.

[158] S. N. Sanders, R. G. Lopata, L. C. van Breemen, F. N. van de Vosse, and M. C. Rutten, "A novel technique for the assessment of mechanical properties of vascular tissue," *Biomechanics and modeling in mechanobiology*, vol. 19, no. 5, pp. 1585–1594, 2020.

[159] U. Sadat, Z. Teng, and J. H. Gillard, "Biomechanical structural stresses of atherosclerotic plaques," *Expert review of cardiovascular therapy*, vol. 8, no. 10, pp. 1469–1481, 2010.

[160] P. Martins, R. Natal Jorge, and A. Ferreira, "A comparative study of several material models for prediction of hyperelastic properties: Application to silicone-rubber and soft tissues," *Strain*, vol. 42, no. 3, pp. 135–147, 2006.

[161] R. Rivlin, "Large elastic deformations of isotropic materials. i. fundamental concepts," *Philosophical Transactions of the Royal Society of London. Series A, Mathematical and Physical Sciences*, vol. 240, no. 822, pp. 459–490, 1948.

[162] R. W. Ogden, "Large deformation isotropic elasticity–on the correlation of theory and experiment for incompressible rubberlike solids," *Proceedings of the Royal Society of London. A. Mathematical and Physical Sciences*, vol. 326, no. 1567, pp. 565–584, 1972.

[163] A. Delfino, N. Stergiopulos, J. Moore Jr, and J.-J. Meister, "Residual strain effects on the stress field in a thick wall finite element model of the human carotid bifurcation," *Journal of biomechanics*, vol. 30, no. 8, pp. 777–786, 1997.

[164] G. A. Holzapfel and R. W. Ogden, "Constitutive modelling of arteries," *Proceedings of the Royal Society A: Mathematical, Physical and Engineering Sciences*, vol. 466, no. 2118, pp. 1551–1597, 2010.

[165] P. D. Richardson, M. Davies, and G. Born, "Influence of plaque configuration and stress distribution on fissuring of coronary atherosclerotic plaques," *The Lancet*, vol. 334, no. 8669, pp. 941–944, 1989.

[166] S. Williamson, Y. Lam, H. Younis, H. Huang, S. Patel, R. Kamm, *et al.*, "On the sensitivity of wall stresses in diseased arteries to variable material properties," *Journal of biomechanical engineering*, vol. 125, no. 1, pp. 147–155, 2003.

[167] H. M. Loree, R. Kamm, R. Stringfellow, and R. T. Lee, "Effects of fibrous cap thickness on peak circumferential stress in model atherosclerotic vessels.," *Circulation research*, vol. 71, no. 4, pp. 850–858, 1992.

[168] G. Finet, J. Ohayon, and G. Rioufol, "Biomechanical interaction between cap thickness, lipid core composition and blood pressure in vulnerable coronary plaque: Impact on stability or instability," *Coronary artery disease*, vol. 15, no. 1, pp. 13–20, 2004.

[169] Z.-Y. Li, S. Howarth, R. A. Trivedi, *et al.*, "Stress analysis of carotid plaque rupture based on in vivo high resolution mri," *Journal of biomechanics*, vol. 39, no. 14, pp. 2611–2622, 2006.

[170] J. Ohayon, G. Finet, F. Treyve, G. Rioufol, and O. Dubreuil, "A three-dimensional finite element analysis of stress distribution in a coronary atherosclerotic plaque: In-vivo prediction of plaque rupture location," *Biomechanics applied to computer assisted surgery*, vol. 37, no. 2, pp. 225–241, 2005.

[171] D. Lee and J. Chiu, "Intimal thickening under shear in a carotid bifurcation—a numerical study," *Journal of biomechanics*, vol. 29, no. 1, pp. 1–11, 1996.

[172] Z. Teng, G. Canton, C. Yuan, *et al.*, "3d critical plaque wall stress is a better predictor of carotid plaque rupture sites than flow shear stress: An in vivo mri-based 3d fsi study," 2010.

[173] L. Cardoso, A. Kelly-Arnold, N. Maldonado, D. Laudier, and S. Weinbaum, "Effect of tissue properties, shape and orientation of microcalcifications on vulnerable cap stability using different hyperelastic constitutive models," *Journal of biomechanics*, vol. 47, no. 4, pp. 870–877, 2014.

[174] R. Karimi, T. Zhu, B. E. Bouma, and M. R. K. Mofrad, "Estimation of nonlinear mechanical properties of vascular tissues via elastography," *Cardiovascular Engineering*, vol. 8, no. 4, pp. 191–202, 2008.

[175] H. Nieuwstadt, S. Fekkes, H. Hansen, *et al.*, "Carotid plaque elasticity estimation using ultrasound elastography, mri, and inverse fea–a numerical feasibility study," *Medical engineering & physics*, vol. 37, no. 8, pp. 801–807, 2015.

[176] R. G. Lopata, M. M. Nillesen, H. H. Hansen, I. H. Gerrits, J. M. Thijssen, and C. L. De Korte, "Performance evaluation of methods for two-dimensional displacement and strain estimation using ultrasound radio frequency data," *Ultrasound in medicine & biology*, vol. 35, no. 5, pp. 796–812, 2009.

[177] L. Horn, T. Adámek, and M. Kulvajtová, "A comparison of age-related changes in axial prestretch in human carotid arteries and in human abdominal aorta," *Biomechanics and modeling in mechanobiology*, vol. 16, no. 1, pp. 375–383, 2017.

[178] B. Narayanan, M. L. Olender, F. R. Nezami, E. R. Edelman, and D. Marlevi, "In vitro validation of a novel image-based inverse method for mechanical characterization of vessels," in *2021 IEEE EMBS International Conference on Biomedical and Health Informatics (BHI)*, IEEE, 2021, pp. 1–4.

[179] E. Maher, A. Creane, S. Sultan, N. Hynes, C. Lally, and D. J. Kelly, "Tensile and compressive properties of fresh human carotid atherosclerotic plaques," *Journal of biomechanics*, vol. 42, no. 16, pp. 2760–2767, 2009.

[180] Z. Teng, D. Tang, J. Zheng, P. K. Woodard, and A. H. Hoffman, "An experimental study on the ultimate strength of the adventitia and media of human atherosclerotic carotid arteries in circumferential and axial directions," *Journal of biomechanics*, vol. 42, no. 15, pp. 2535–2539, 2009.

[181] Z. Teng, Y. Zhang, Y. Huang, *et al.*, "Material properties of components in human carotid atherosclerotic plaques: A uniaxial extension study," *Acta biomaterialia*, vol. 10, no. 12, pp. 5055–5063, 2014.

[182] M. H. Kural, M. Cai, D. Tang, T. Gwyther, J. Zheng, and K. L. Billiar, "Planar biaxial characterization of diseased human coronary and carotid arteries for computational modeling," *Journal of biomechanics*, vol. 45, no. 5, pp. 790–798, 2012.

[183] B. Narayanan, M. L. Olender, D. Marlevi, E. R. Edelman, and F. R. Nezami, "An inverse method for mechanical characterization of heterogeneous diseased arteries using intravascular imaging," *Scientific Reports*, vol. 11, no. 1, p. 22 540, 2021.

[184] A. Malone, "The use of fluid haemodynamics in the diagnosis of cardiovascular disease," 2019.

[185] Z. Xu, Y. Chen, Y. Wang, *et al.*, "Matrix stiffness, endothelial dysfunction and atherosclerosis," *Molecular Biology Reports*, vol. 50, no. 8, pp. 7027–7041, 2023.

[186] H. S. Nam, J. W. Song, S.-J. Jang, *et al.*, "Characterization of lipid-rich plaques using spectroscopic optical coherence tomography," *Journal of biomedical optics*, vol. 21, no. 7, pp. 075 004–075 004, 2016.

[187] R. Mahutga, C. Schoephoerster, and V. Barocas, "The ring-pull assay for mechanical properties of fibrous soft tissues–an analysis of the uniaxial approximation and a correction for nonlinear thick-walled tissues," *Experimental mechanics*, vol. 61, pp. 53–66, 2021.

[188] Y. Chen, J. Li, J. Lu, M. Ding, and Y. Chen, "Synthesis and properties of poly (vinyl alcohol) hydrogels with high strength and toughness," *Polymer Testing*, vol. 108, p. 107 516, 2022.

[189] R. A. Macrae, K. Miller, and B. J. Doyle, "Methods in mechanical testing of arterial tissue: A review," *Strain*, vol. 52, no. 5, pp. 380–399, 2016.

[190] K. L. Fegan, N. C. Green, M. M. Britton, A. J. Iqbal, and L. E. Thomas-Seale, "Design and simulation of the biomechanics of multi-layered composite poly (vinyl alcohol) coronary artery grafts," *Frontiers in cardiovascular medicine*, vol. 9, p. 883 179, 2022.

[191] S. S. Brunke, M. F. Insana, J. J. Dahl, C. Hansen, M. Ashfaq, and H. Ermert, "An ultrasound research interface for a clinical system.," *IEEE transactions on ultrasonics, ferroelectrics, and frequency control*, vol. 54, no. 1, pp. 198–210, 2007.

[192] S. Guvenir Torun, H. M. Torun, H. H. Hansen, *et al.*, "Multicomponent mechanical characterization of atherosclerotic human coronary arteries: An experimental and computational hybrid approach," *Frontiers in Physiology*, vol. 12, p. 733 009, 2021.

[193] T. Khamdaeng, J. Luo, J. Vappou, P. Terdtoon, and E. Konofagou, "Arterial stiffness identification of the human carotid artery using the stress–strain relationship in vivo," *Ultrasonics*, vol. 52, no. 3, pp. 402–411, 2012.

[194] A. Franquet, S. Avril, R. Le Riche, *et al.*, "Identification of the in vivo elastic properties of common carotid arteries from mri: A study on subjects with and without atherosclerosis," *Journal of the mechanical behavior of biomedical materials*, vol. 27, pp. 184–203, 2013.

[195] J. Vychytil, F. Moravec, P. Kochová, J. Kuncová, and J. Švíglerová, "Modelling of the mechanical behaviour of porcine carotid artery undergoing inflation-deflation test," 2010.

[196] R. W. Boekhoven, M. F. Peters, M. C. Rutten, M. R. van Sambeek, F. N. van de Vosse, and R. G. Lopata, "Inflation and bi-axial tensile testing of healthy porcineácarotid arteries," *Ultrasound in Medicine & Biology*, vol. 42, no. 2, pp. 574–585, 2016.

[197] L. A. Davis, S. E. Stewart, C. G. Carsten III, B. A. Snyder, M. A. Sutton, and S. M. Lessner, "Characterization of fracture behavior of human atherosclerotic fibrous caps using a miniature single edge notched tensile test," *Acta biomaterialia*, vol. 43, pp. 101–111, 2016.

[198] C. P. Loizou, M. Pantzaris, E. Kyriacou, A. N. Nicolaides, and C. S. Pattichis, "Effect of the internal carotid artery degree of stenosis on wall and plaque distensibility," *Biomedical Signal Processing and Control*, vol. 68, p. 102 572, 2021.

[199] M. Ghasemi, D. R. Nolan, and C. Lally, "Assessment of mechanical indicators of carotid plaque vulnerability: Geometrical curvature metric, plaque stresses and damage in tissue fibres," *Journal of the Mechanical Behavior of Biomedical Materials*, vol. 103, p. 103 573, 2020.

[200] E. Soleimani, M. Mokhtari-Dizaji, N. Fatouraee, and H. Saberi, "Stress distribution analysis in healthy and stenosed carotid artery models reconstructed from in vivo ultrasonography," *Ultrasonography*, vol. 40, no. 3, p. 428, 2021.

[201] S. Sarkar, C. Hillery, A. Seifalian, and G. Hamilton, "Critical parameter of burst pressure measurement in development of bypass grafts is highly dependent on methodology used," *Journal of vascular surgery*, vol. 44, no. 4, pp. 846–852, 2006.

[202] V. Laterreur, J. Ruel, F. A. Auger, *et al.*, "Comparison of the direct burst pressure and the ring tensile test methods for mechanical characterization of tissue-engineered vascular substitutes," *Journal of the mechanical behavior of biomedical materials*, vol. 34, pp. 253–263, 2014.

[203] Á. T. Latorre, M. A. Martínez, M. Cilla, J. Ohayon, and E. Peña, "Atherosclerotic plaque segmentation based on strain gradients: A theoretical framework," *Mathematics*, vol. 10, no. 21, p. 4020, 2022.

[204] A. S. Federici, B. Tornifoglio, C. Lally, O. Garcia, D. J. Kelly, and D. A. Hoey, "Melt electrowritten scaffold architectures to mimic vasculature mechanics and control neo-tissue orientation," *bioRxiv*, pp. 2023–04, 2023.

[205] S. Chatelin, M. Bernal, T. Deffieux, *et al.*, "Anisotropic polyvinyl alcohol hydrogel phantom for shear wave elastography in fibrous biological soft tissue: A multimodality characterization," *Physics in Medicine & Biology*, vol. 59, no. 22, p. 6923, 2014.

[206] M. Bernal, J. Saldarriaga, C. Cabeza, C. Negreira, J. Bustamante, and J. Brum, "Development and evaluation of anisotropic and nonlinear aortic models made from clinical images for in vitro experimentation," *Physics in Medicine & Biology*, vol. 64, no. 16, p. 165 006, 2019.

[207] F. Diana, S. Peschillo, M. Requena, *et al.*, "Correlation between intravascular pressure gradients and ultrasound velocities in carotid artery stenosis: An exploratory study," *Interventional Neuroradiology*, p. 15 910 199 231 224 007, 2023.

[208] C. T. Rueden, J. Schindelin, M. C. Hiner, *et al.*, "Imagej2: Imagej for the next generation of scientific image data," *BMC bioinformatics*, vol. 18, pp. 1–26, 2017.

[209] S.-h. Hsu and H. Karnbic, "On matching compliance between canine carotid arteries and polyurethane grafts," *Artificial organs*, vol. 21, no. 12, pp. 1247–1254, 1997.

[210] M. J. Williams, R. A. Stewart, C. J. Low, and G. T. Wilkins, "Assessment of the mechanical properties of coronary arteries using intravascular ultrasound: An in vivo study," *The International Journal of Cardiac Imaging*, vol. 15, pp. 287–294, 1999.

[211] B. Syeda, M. Gottsauner-Wolf, S. Denk, P. Pichler, A. Khorsand, and D. Glogar, "Arterial compliance: A diagnostic marker for atherosclerotic plaque burden?" *American journal of hypertension*, vol. 16, no. 5, pp. 356–362, 2003.

[212] B. A. Haluska, L. Jeffries, S. Carlier, and T. H. Marwick, "Measurement of arterial distensibility and compliance to assess prognosis," *Atherosclerosis*, vol. 209, no. 2, pp. 474–480, 2010.

[213] N. M. Van Popele, D. E. Grobbee, M. L. Bots, *et al.*, "Association between arterial stiffness and atherosclerosis: The rotterdam study," *Stroke*, vol. 32, no. 2, pp. 454–460, 2001.

[214] M. E. Boesen, D. Singh, B. K. Menon, and R. Frayne, "A systematic literature review of the effect of carotid atherosclerosis on local vessel stiffness and elasticity," *Atherosclerosis*, vol. 243, no. 1, pp. 211–222, 2015.

[215] R. W. Boekhoven, R. G. Lopata, M. R. van Sambeek, F. N. van de Vosse, and M. C. Rutten, "A novel experimental approach for three-dimensional geometry assessment of calcified human stenotic arteries in vitro," *Ultrasound in Medicine & Biology*, vol. 39, no. 10, pp. 1875–1886, 2013.

[216] R. W. Boekhoven, M. C. Rutten, M. R. van Sambeek, F. N. van de Vosse, and R. G. Lopata, "Echo-computed tomography strain imaging of healthy and diseased carotid specimens," *Ultrasound in medicine & biology*, vol. 40, no. 6, pp. 1329–1342, 2014.

[217] J. E. Hasson, J. Megerman, and W. M. Abbott, "Suture technique and para-anastomotic compliance," *Journal of vascular surgery*, vol. 3, no. 4, pp. 591–598, 1986.

[218] P. Bankhead, M. B. Loughrey, J. A. Fernández, *et al.*, "Qupath: Open source software for digital pathology image analysis," *Scientific reports*, vol. 7, no. 1, pp. 1–7, 2017.

[219] C. Robertson, A. E. Heidari, Z. Chen, and S. C. George, "Mechanical analysis of arterial plaques in native geometry with oct wall motion analysis," *Journal of biomechanics*, vol. 47, no. 3, pp. 755–758, 2014.

[220] M. Walsh, E. Cunnane, J. Mulvihill, A. Akyildiz, F. Gijsen, and G. A. Holzapfel, "Uniaxial tensile testing approaches for characterisation of atherosclerotic plaques," *Journal of biomechanics*, vol. 47, no. 4, pp. 793–804, 2014.

[221] J. A. Schaar, C. L. De Korte, F. Mastik, *et al.*, "Characterizing vulnerable plaque features with intravascular elastography," *Circulation*, vol. 108, no. 21, pp. 2636–2641, 2003.

[222] H. Zahedmanesh and C. Lally, "Determination of the influence of stent strut thickness using the finite element method: Implications for vascular injury and in-stent restenosis," *Medical & biological engineering & computing*, vol. 47, pp. 385–393, 2009.

[223] Z. Allum Saib, F. Abed, M. H. Ghayesh, and M. Amabili, "Interaction of a self-expandable stent with the arterial wall in the presence of hypocellular and calcified plaques," *Biomechanics and Modeling in Mechanobiology*, pp. 1–15, 2024.

[224] Z. Li, Y. Wang, X. Wu, *et al.*, "Studying the factors of human carotid atherosclerotic plaque rupture, by calculating stress/strain in the plaque, based on ceus images: A numerical study," *Frontiers in Neuroinformatics*, vol. 14, p. 596 340, 2020.

[225] T. Ma, X. Shi, C. Yuan, *et al.*, "Contrast-enhanced ultrasound combined with 2d strain imaging and histopathological multimodal assessment of carotid plaque vulnerability," *Ultrasound in Medicine & Biology*, vol. 49, no. 7, pp. 1595–1601, 2023.

[226] C.-K. Chai, A. C. Akyildiz, L. Speelman, *et al.*, "Local anisotropic mechanical properties of human carotid atherosclerotic plaques–characterisation by micro-indentation and inverse finite element analysis," *Journal of the mechanical behavior of biomedical materials*, vol. 43, pp. 59–68, 2015.

[227] A. Hegner, H. L. Cebull, A. J. Gámez, C. Blase, C. J. Goergen, and A. Wittek, "Biomechanical characterization of tissue types in murine dissecting aneurysms based on histology and 4d ultrasound-derived strain," *Biomechanics and Modeling in Mechanobiology*, vol. 22, no. 5, pp. 1773–1788, 2023.

[228] M. Stefanati, A. Corti, V. D. Corino, *et al.*, "Effect of variability of mechanical properties on the predictive capabilities of vulnerable coronary plaques," *Computer Methods and Programs in Biomedicine*, vol. 254, p. 108 271, 2024.

[229] P.-t. Huang, F.-g. Huang, C.-p. Zou, *et al.*, "Contrast-enhanced sonographic characteristics of neovascularization in carotid atherosclerotic plaques," *Journal of Clinical Ultrasound*, vol. 36, no. 6, pp. 346–351, 2008.

[230] B. N. Shah, D. M. Gujral, N. S. Chahal, K. J. Harrington, C. M. Nutting, and R. Senior, "Plaque neovascularization is increased in human carotid atherosclerosis related to prior neck radiotherapy: A contrast-enhanced ultrasound study," *JACC: Cardiovascular Imaging*, vol. 9, no. 6, pp. 668–675, 2016.

[231] H. M. Loree, A. J. Grodzinsky, S. Y. Park, L. J. Gibson, and R. T. Lee, "Static circumferential tangential modulus of human atherosclerotic tissue," *Journal of biomechanics*, vol. 27, no. 2, pp. 195–204, 1994.

[232] M. G. Lawlor, M. R. O'Donnell, B. M. O'Connell, and M. T. Walsh, "Experimental determination of circumferential properties of fresh carotid artery plaques," *Journal of biomechanics*, vol. 44, no. 9, pp. 1709–1715, 2011.

[233] M. Catalano, A. Lamberti-Castronuovo, A. Catalano, D. Filocamo, and C. Zimbalatti, "Two-dimensional speckle-tracking strain imaging in the assessment of mechanical properties of carotid arteries: Feasibility and comparison with conventional markers of subclinical atherosclerosis," *European Journal of Echocardiography*, vol. 12, no. 7, pp. 528–535, 2011.

[234] A. A. Khan, S. Sikdar, T. Hatsukami, *et al.*, "Noninvasive characterization of carotid plaque strain," *Journal of vascular surgery*, vol. 65, no. 6, pp. 1653–1663, 2017.

[235] F. Demeure, C. Bouzin, V. Roelants, *et al.*, "Head-to-head comparison of inflammation and neovascularization in human carotid plaques: Implications for the imaging of vulnerable plaques," *Circulation: Cardiovascular Imaging*, vol. 10, no. 5, e005846, 2017.

[236] E. Widman, E. Maksuti, D. Larsson, M. Urban, A. Bjällmark, and M. Larsson, "Shear wave elastography plaque characterization with mechanical testing validation: A phantom study," *Physics in Medicine & Biology*, vol. 60, no. 8, p. 3151, 2015.

[237] S. Rogers, A. Phair, J. Carriera, J. Ghosh, F. Bowling, and C. McCollum, "Feasibility and accuracy of measuring carotid plaque volume (burden) with contrast-enhanced tomographic 3d ultrasound and ultrasound image fusion," *Annals of Vascular Surgery*, vol. 91, pp. 168–175, 2023.

Appendix A

Chapter 3

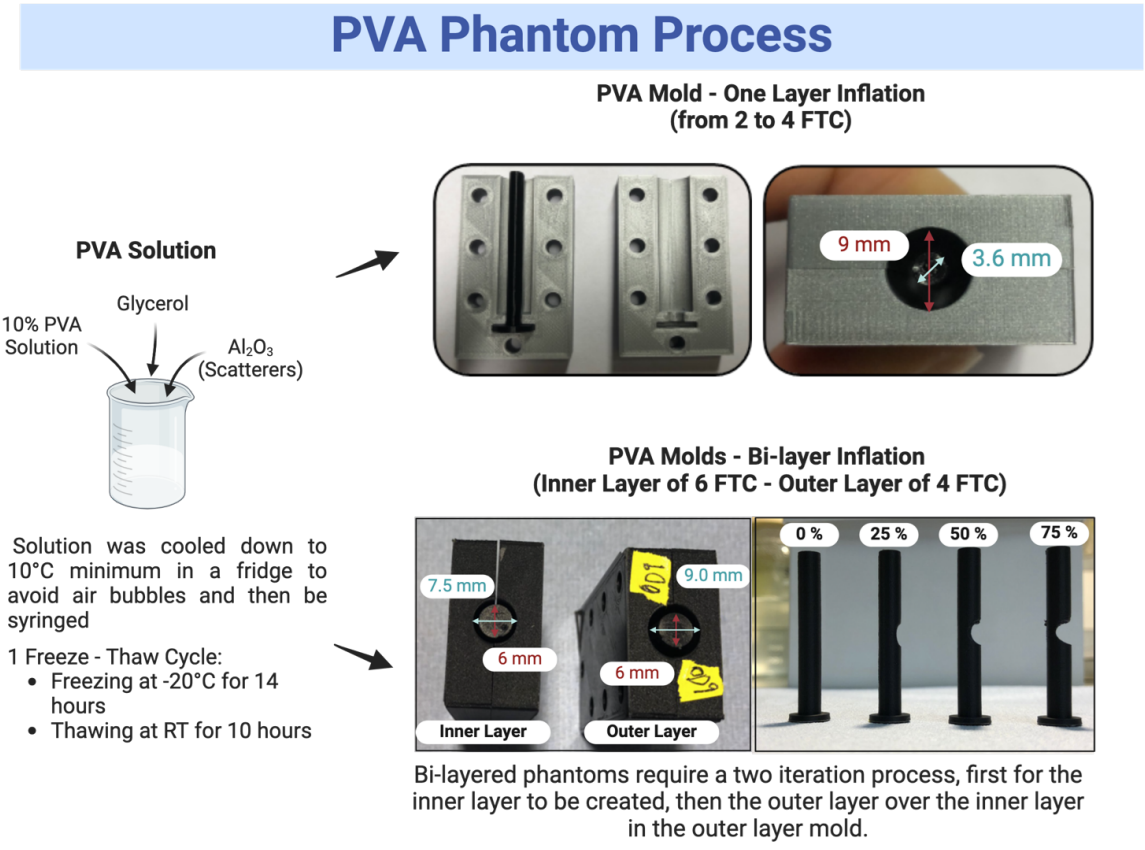

Figure A.1: PVA Phantom Fabrication Process

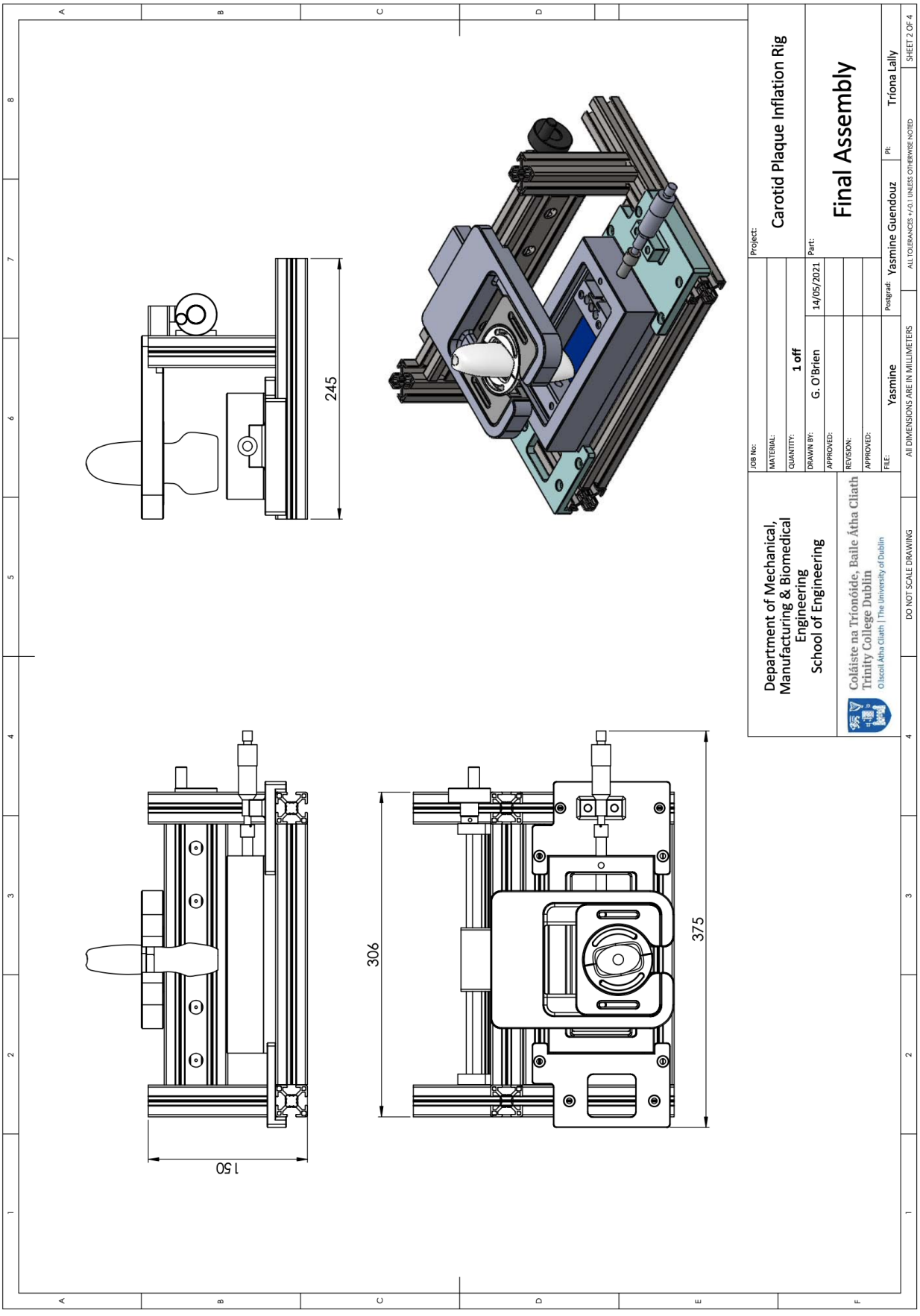

Figure A.2: CAD drawing of the assembled inflation testing rig.

Ultrasound Parameters				
Depth	Frequency	Mode	Frame Rate	Focal Depth
3 cm	9 MHz	2D	60 fps	1 cm

Table A.1: Supplementary table of ultrasound acquisition parameters during inflation testing.

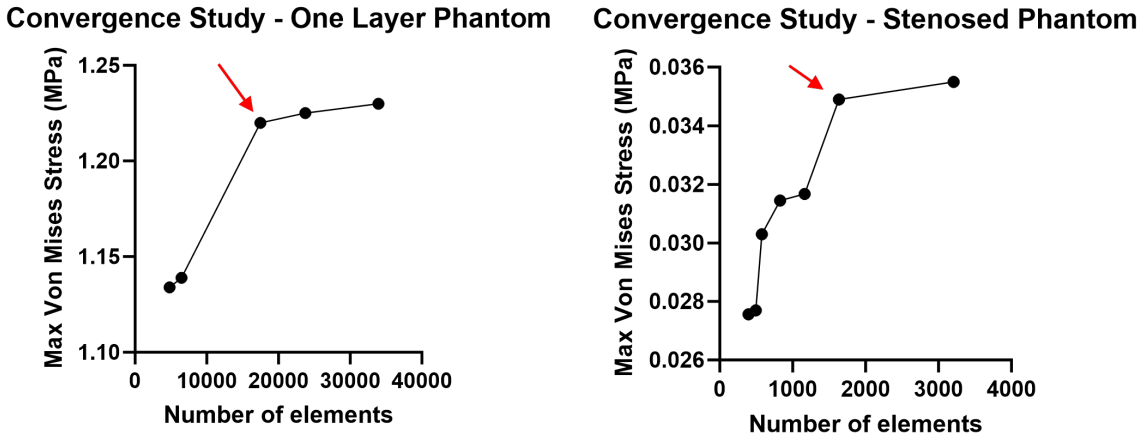

Figure A.3: Convergence studies made for each model (3D one layered and 2D stenosed phantom) are seen below showing that the number of elements was selected as a good compromise between computational cost and accuracy. Red arrow shows the chosen number of elements for the finite element modelling.

The same fixed initial material properties were consistently applied to all stenotic phantoms to maintain uniformity in the analysis and ensure comparability of results. Below is a table detailing the initial guesses for the parameters, their sources, as well as the upper and lower bounds, if present. Isight 5.9 (Dassault Systèmes Simulia corporations, Vélizy-Villacoublay, France) was employed to implement an inverse FE algorithm that adjusted these parameters to match the inflation testing data. By varying the parameters within these specified bounds, the optimized material properties that best matched the experimental observations were identified.

Parameter	Initial Guess	Source	Upper Bound	Lower Bound
Lipid pool C_{10}	1 kPa	Guvenir et al., 2021	NA	0.0
μ_{1wall}	171 kPa	One layered 4 FTC phantom	NA	0.0
α_{1wall}	4	One layered 4 FTC phantom	NA	0.0

Table A.2: Boundary Matching iFEM Parameters.

Parameter	2 FTC	3 FTC	4 FTC	5 FTC	6 FTC	Method
Mean Elastic Modulus (kPa ± SD	331 ± 21	510 ± 43	630 ± 110	662 ± 110	957 ± 147	Ring tensile testing
First Order Ogden Parameters						
μ_1**(kPa)**	90	122	171	188	235	Ring tensile testing
α_1	4.8	4.8	4.0	4.1	4.1	
Diameter Matching iFEM						
μ_1**(kPa)**	40	82	191	NA	NA	Inflation of one-layered phantoms and diameter matching based iFEM
α_1	6.7	9.7	9.2	NA	NA	

Figure A.4: Summary of findings from mechanical testing and iFEM analyses.

Boundary Matching iFEM					
Parameter	**0 % stenosis**	**25 % stenosis**	**50 % stenosis**	**75 % stenosis**	**Method**
μ_{1wall} **(kPa)**	41	29	53	27	Inflation of bi-layered phantoms and boundary based iFEM
α_{1wall}	1.86	1.39	1.76	3.89	
Lipid pool C_{10}**(kPa)**	NA	0.1	0.38	NA	

Figure A.5: Summary of findings from iFEM boundary matching.

Appendix B

Chapter 5

This appendix presents additional histological images of atherosclerotic plaque samples stained for neovascularisation assessment. These images provide a closer look at the plaques' neovessel density.

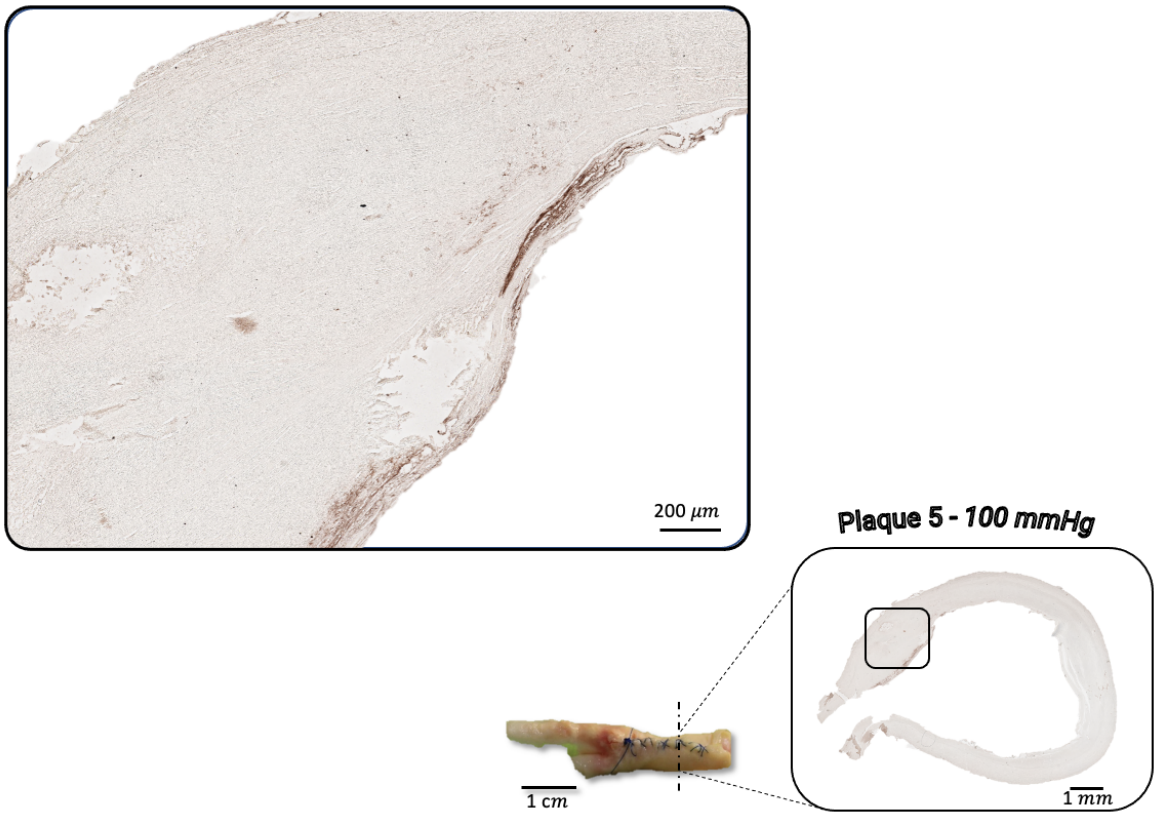

Figure B.1: Representative histological section of Plaque 5 inflated until 100 mmHg, showing the presence of elongated neovessels on the luminal side.

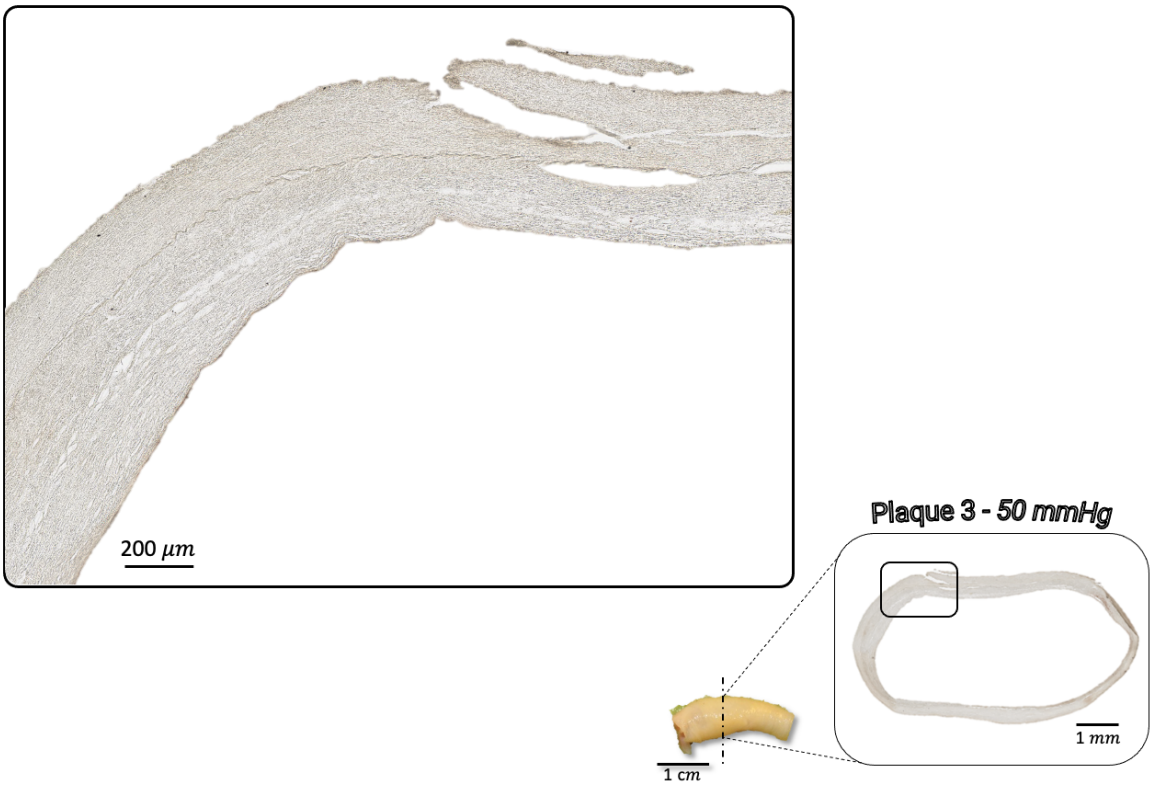

Figure B.2: Representative histological section of Plaque 3 at 50 mmHg, no CD31-positive neovessels are visible in this section.

Appendix C

Chapter 6

The relationship between UT stress and localised DIC-L strain at failure is illustrated in Figure C.1. Each plaque strip is represented as an individual data point, with the corresponding strain maps visually confirming the location of rupture (circled in red). Notably, strain maps revealed that rupture locations coincided with regions of maximum localised strain in $n = 20$ out of the total $n = 25$ tested strips, emphasising the role of localised strain concentration in mechanical failure. Note that the colour of each data point represents its plaque of origin, while the strain map colour bar represents engineering strain magnitude in percent.

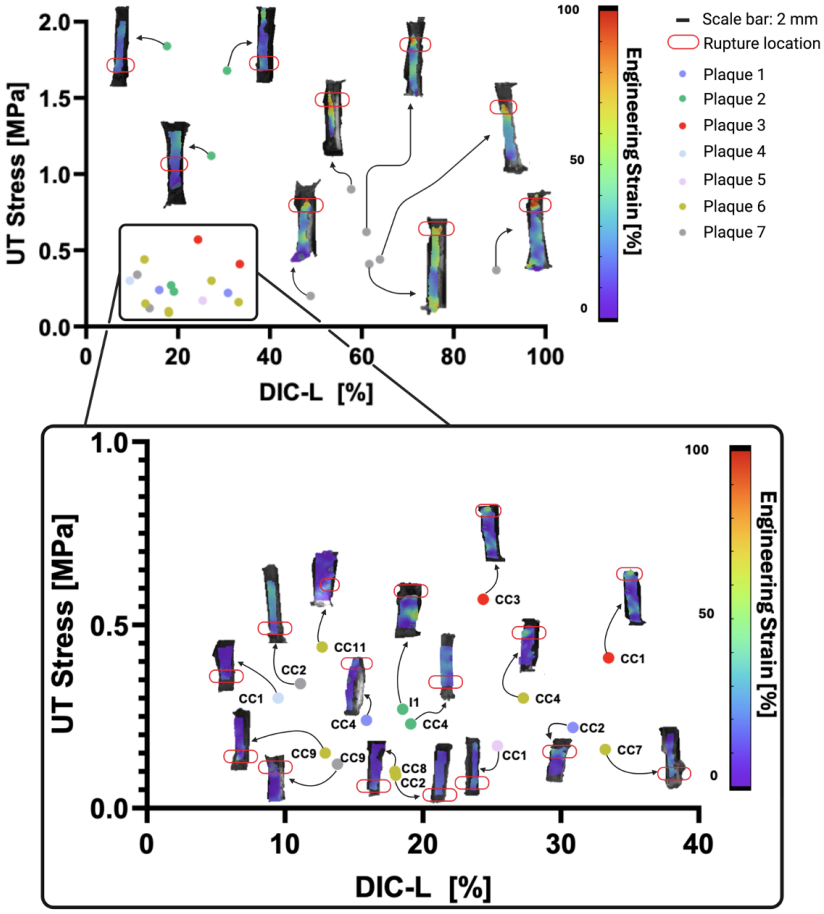

Figure C.1: (A) Scatter plot of UT stress versus DIC-L for each strip specimen. (B) Zoomed-in view of lower strain regions. The colour map represents engineering strain percentages, highlighting strain distributions across each tested sample. The corresponding DIC strain maps highlight the rupture locations (red outlines) for each sample. Scale bar: 2 mm.

To determine the optimal feature combination for k-means clustering, different sets of mechanical parameters were evaluated. The baseline clustering was performed using UT stress and UT strain only, and additional features such as DIC-L were subsequently tested. The number of clusters was varied between $k = 2$, $k = 3$, and $k = 4$, and the clustering performance was assessed using multiple evaluation metrics, including the elbow score, silhouette score, and gap statistic. As shown in Figure C.2, the best clustering performance was observed when using UT stress and UT strain alone, particularly for $k = 2$ and $k = 3$, with high silhouette scores (0.843 for $k = 2$ and 0.812 for $k = 3$). Increasing to $k = 4$ led to a reduction in clustering quality. When DIC-L was introduced as an additional feature, the clustering performance deteriorated, as indicated by lower silhouette scores (0.698 for $k = 2$ and 0.694 for $k = 3$), suggesting that adding this feature did not improve the clustering structure. These findings support the selection of UT stress and UT strain as the primary clustering features, as they provided the most robust separation between clusters.

```
Evaluating baseline (UT stress and UT strain only)...
Evaluating combinations with additional features...
Top 5 Results:
Best result #1:
Feature combination: UT_stress & UT_strain only
Optimal number of clusters (k): 2
Elbow Score (Sum of Squared Distances): 1439.3724
Silhouette Score: 0.84321
Gap Statistic: -6.6022
----------------------------------
Best result #2:
Feature combination: UT_stress & UT_strain only
Optimal number of clusters (k): 3
Elbow Score (Sum of Squared Distances): 585.9948
Silhouette Score: 0.81203
Gap Statistic: -6.296
----------------------------------
Best result #3:
Feature combination: UT_stress & UT_strain only
Optimal number of clusters (k): 4
Elbow Score (Sum of Squared Distances): 360.2766
Silhouette Score: 0.77463
Gap Statistic: -6.2967
----------------------------------
Best result #4:
Feature combination: DIC_L
Optimal number of clusters (k): 2
Elbow Score (Sum of Squared Distances): 6638.9826
Silhouette Score: 0.69806
Gap Statistic: -7.5165
----------------------------------
Best result #5:
Feature combination: DIC_L
Optimal number of clusters (k): 3
Elbow Score (Sum of Squared Distances): 3183.2672
Silhouette Score: 0.69491
Gap Statistic: -7.2304
----------------------------------
```

Figure C.2: Evaluation of different feature combinations for k-means clustering, considering UT stress, UT strain, and DIC-L. The optimal number of clusters (k) was tested between 2 and 4, with clustering performance assessed using elbow scores, silhouette scores, and gap statistics. UT stress and UT strain alone provided the highest clustering performance at $k = 2$ and $k = 3$, while adding DIC-L resulted in lower silhouette scores and worse clustering separation.

To determine the optimal number of clusters (k) for k-means clustering, multiple clustering metrics were computed for k values ranging from 2 to 4. Based on the combined evaluation of these metrics, $k = 2$ was selected as the optimal number of clusters.

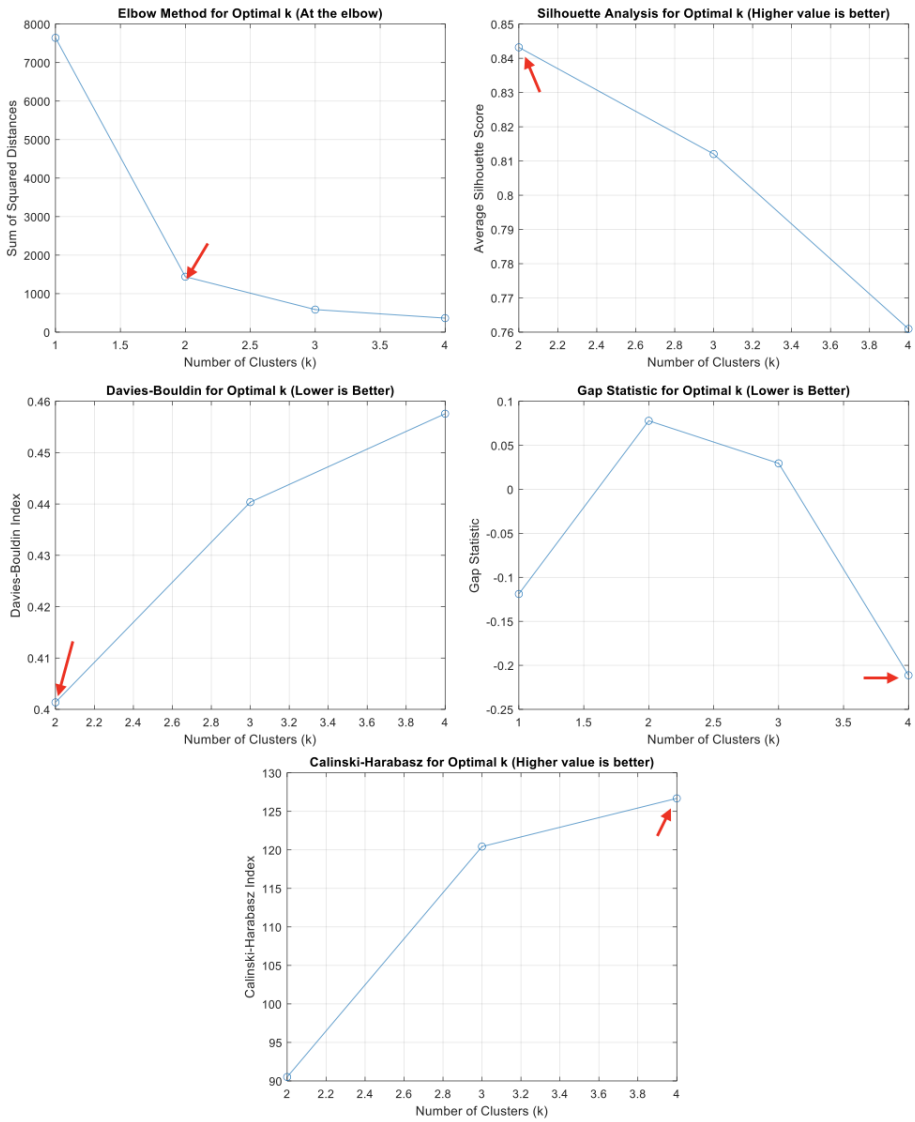

Figure C.3: Evaluation of the optimal number of clusters (k) using multiple clustering validity indices. The elbow method, silhouette analysis, Davies-Bouldin index, gap statistic, and Calinski-Harabasz index were calculated for k values between 2 and 4. The best cluster number is indicated by the red arrows in each plot with ($k = 2$) performing better overall.

Figure C.4 presents a comparison of neovascularisation percentage, localised strain at failure (DIC-L), final elastic modulus, and initial elastic modulus between cluster 1 (red) and cluster 2 (blue). Outliers, shown in grey, were identified but not included in the statistical analysis to ensure robust comparisons.

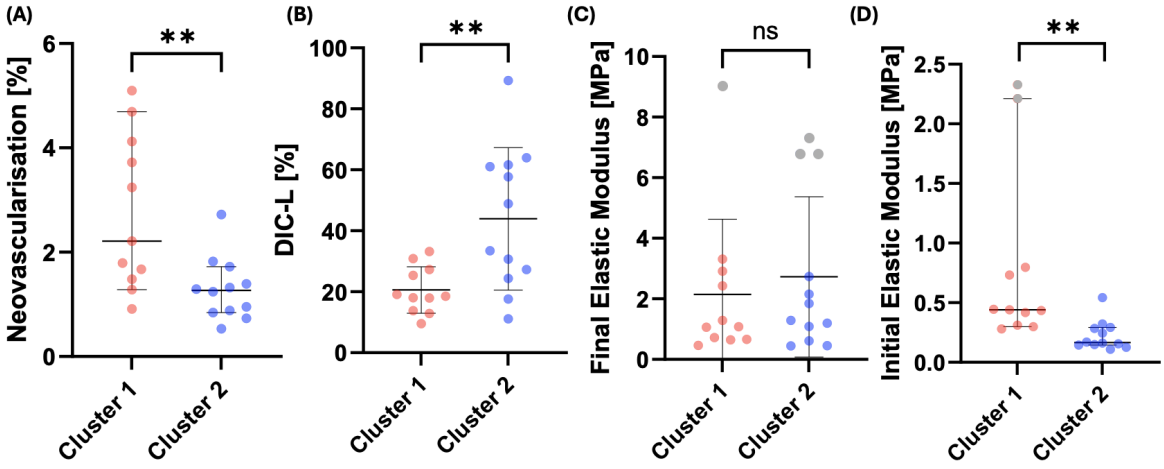

Figure C.4: Comparison of mechanical and structural properties between Cluster 1 (red) and Cluster 2 (blue). (A) Neovascularisation percentage, analysed using the Mann-Whitney test (**$p < 0.01$), reported as median with 95% CI. (B) Localised strain at failure (DIC-L), analysed using a t-test (**$p < 0.01$), reported as mean ± SD. (C) Final elastic modulus, analysed using a t-test (*ns*, $p = 0.74$), reported as mean ± SD. (D) Initial elastic modulus, analysed using the Mann-Whitney test (**$p < 0.01$), reported as median with 95% CI. Outliers (shown in grey) were not included in the statistical analysis but are displayed for completeness. Black horizontal lines indicate either median or mean values, depending on the statistical test used.

Supplementary Fig. C.5 further integrates k-means clustering results with histological observations, providing additional examples of plaque heterogeneity. Representative histological sections (H&E and CD31 staining) are shown for two additional strips located closest to their respective cluster centroids. The H&E staining highlights structural heterogeneity within a strip from Cluster 1. CD31 staining reveals increased neovascularisation, with dense brown staining indicative of endothelial cells. In contrast, a representative strip from cluster 2 exhibits a more homogeneous tissue structure, with H&E staining revealing well-organised layers and CD31 staining confirming reduced neovascularisation. Red rectangles highlight magnified zones, allowing a closer examination of neovessel distribution. Notably, in the strip from Cluster 2, no neovascularisation was observed at the rupture site. These observations align with findings in the main dataset, supporting the association between increased neovascularisation and localised mechanical instability in Cluster 1.

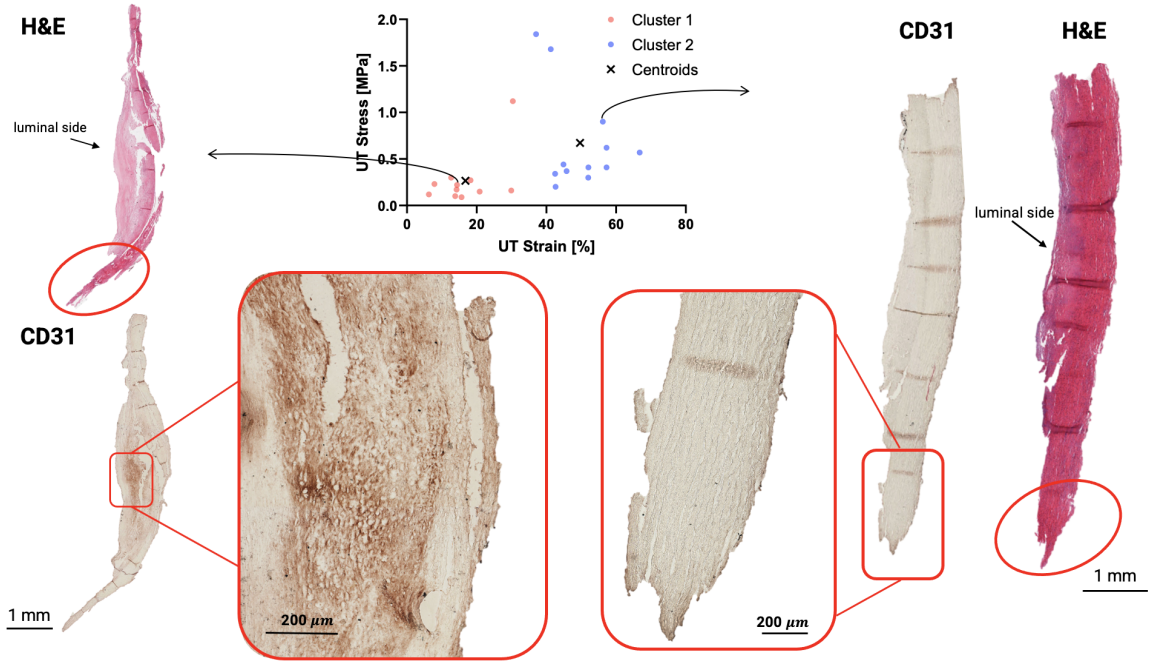

Figure C.5: Supplementary figure integrating k-means clustering with histological data. Representative histological sections (*H&E* and *CD31* staining) for two additional strips closest to their cluster centroids. The scatter plot presents two clusters (Cluster 1: red, Cluster 2: blue), with centroids marked as black crosses. Red rectangles indicate magnified zones for detailed visualisation of tissue structure and neovascularisation.

This is also highlighted in Figure C.6.

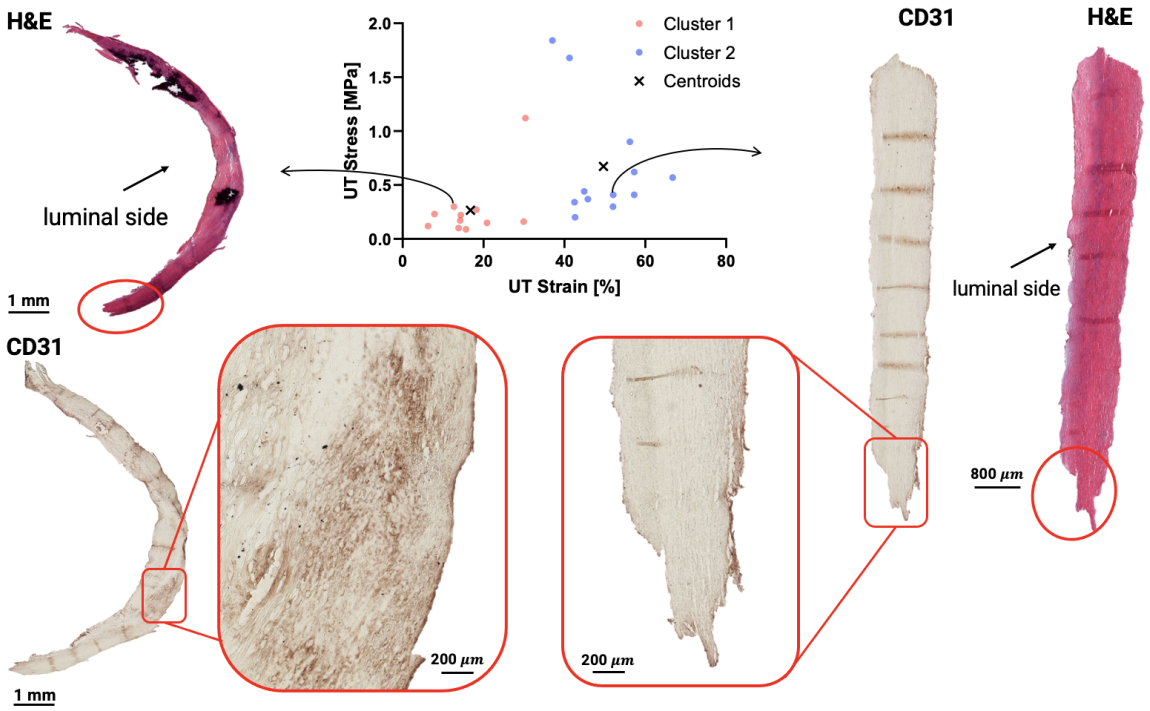

Figure C.6: Integration of k-means clustering results with histological data. Representative histological sections (*H&E* and *CD31* staining) for two additional strips closest to their cluster centroids. The scatter plot presents two clusters (Cluster 1: red, Cluster 2: blue), with centroids marked as black crosses. *H&E* staining highlights structural heterogeneity and rupture location (circled) in a strip from Cluster 1, while *CD31* staining reveals increased neovascularisation (brown staining) in the same region. Conversely, a strip from Cluster 2 exhibits well-organised tissue layers with no observable neovascularisation at the rupture site. Red rectangles indicate magnified zones for detailed visualisation of neovessel distribution. Scale bars indicate 1 mm, 800 μm, and 200 μm for respective images.